Davis, E. E., Mottl, M. J., Fisher, A. T., et al., 1992
Proceedings of the Ocean Drilling Program, Initial Reports, Vol. 139

8. SITE 858[1]

Shipboard Scientific Party[2]

HOLE 858A

Date occupied: 10 August 1991

Date departed: 13 August 1991

Time on hole: 3 days, 4 hr

Position: 48°27.413′N, 128°42.708′W

Bottom felt (drill-pipe measurement from rig floor, m): 2420.1

Distance between rig floor and sea level (m): 11.00

Water depth (drill-pipe measurement from sea level, m): 2409.1

Total depth (rig floor, m): 2759.20

Penetration (m): 339.10

Number of cores (including cores with no recovery): 39

Total length of cored section (m): 339.10

Total core recovered (m): 97.77

Core recovery (%): 28

Oldest sediment cored:
Depth below seafloor (m): 332.57
Nature: sandstone, siltstone, and silty claystone
Earliest age: Pleistocene (14X-CC, 110.6 mbsf)
Latest age: Holocene
Measured velocity (km/s): 2.035 (31X-1)

HOLE 858B

Date occupied: 13 August 1991

Date departed: 14 August 1991

Time on hole: 1 day, 1 hr

Position: 48°27.336′N, 128°42.545′W

Bottom felt (drill-pipe measurement from rig floor, m): 2420.3

Distance between rig floor and sea level (m): 11.00

Water depth (drill-pipe measurement from sea level, m): 2409.3

Total depth (rig floor, m): 2458.90

Penetration (m): 38.60

Number of cores (including cores with no recovery): 9

Total length of cored section (m): 38.60

Total core recovered (m): 31.67

Core recovery (%): 82

Oldest sediment cored:
Depth below seafloor (m): 35.33
Nature: hydrothermally altered claystone
Earliest age: Pleistocene (1H-CC, 7.2 mbsf)
Latest age: Holocene
Measured velocity (km/s): 1.526 (2H-1)

Comments: Velocities could not be measured on cores in aluminum liners.

HOLE 858C

Date occupied: 14 August 1991

Date departed: 15 August 1991

Time on hole: 22 hr

Position: 48°27.336′N, 128°42.660′W

Bottom felt (drill-pipe measurement from rig floor, m): 2428.0

Distance between rig floor and sea level (m): 11.10

Water depth (drill-pipe measurement from sea level, m): 2416.9

Total depth (rig floor, m): 2521.10

Penetration (m): 93.10

Number of cores (including cores with no recovery): 14

Total length of cored section (m): 91.60

Total core recovered (m): 55.50

Core recovery (%): 60

Oldest sediment cored:
Depth below seafloor (m): 84.67
Nature: claystone, silty claystone, sandstone
Earliest age: Pleistocene (5H-CC, 33.0 mbsf)
Measured velocity (km/s): 1.823 (14X-1)

HOLE 858D

Date occupied: 15 August 1991

Date departed: 15 August 1991

Time on hole: 16 hr, 30 min

Position: 48°27.374′N, 128°42.530′W

Bottom felt (drill-pipe measurement from rig floor, m): 2426.2

Distance between rig floor and sea level (m): 11.10

Water depth (drill-pipe measurement from sea level, m): 2415.1

Total depth (rig floor, m): 2466.90

Penetration (m): 40.70

Number of cores (including cores with no recovery): 7

Total length of cored section (m): 40.70

Total core recovered (m): 30.43

Core recovery (%): 74

Oldest sediment cored:
Depth below seafloor (m): 37.45
Nature: siltstone, claystone
Earliest age: Pleistocene (1H-CC, 9.8 mbsf)
Latest age: Holocene?
Measured velocity (km/s): 2.587 (6X-CC)

---

[1] Davis, E. E., Mottl, M. J., Fisher, A. T., et al., 1992. *Proc. ODP, Init. Repts.,* 139: College Station, TX (Ocean Drilling Program).
[2] Shipboard Scientific Party is as given in the list of participants preceding the contents.

HOLE 858E

Date occupied: 15 August 1991

Date departed: 16 August 1991

Time on hole: 10 hr

Position: 48°27.368′N, 128°42.531′W

Bottom felt (drill-pipe measurement from rig floor, m): 2426.2

Distance between rig floor and sea level (m): 11.10

Water depth (drill-pipe measurement from sea level, m): 2415.1

Total depth (rig floor, m): 2464.70

Penetration (m): 38.50

Number of cores (including cores with no recovery): 1

Total length of cored section (m): 38.50

Total core recovered (m): 4.70

Core recovery (%): 12

Comments: Inadvertently reentered Hole 858D.

HOLE 858F

Date occupied: 16 August 1991

Date departed: 20 August 1991

Time on hole: 4 days, 13 hr, 30 min

Position: 48°27.369′N, 128°42.527′W

Bottom felt (drill-pipe measurement from rig floor, m): 2426.2

Distance between rig floor and sea level (m): 11.10

Water depth (drill-pipe measurement from sea level, m): 2415.1

Total depth (rig floor, m): 2723.10

Penetration (m): 296.90

Number of cores (including cores with no recovery): 29

Total length of cored section (m): 269.1

Total core recovered (m): 10.02

Core recovery (%): 4

Oldest sediment cored:
Depth below seafloor (m): 249.56
Nature: silty claystone, siltstone
Earliest age: no fossil data
Measured velocity (km/s): 2.742 (25R-1)

Hard rock:
Depth below seafloor (m): 296.90
Nature: basalt
Measured velocity (km/s): 5.226 (29R-1)

HOLE 858G

Date occupied: 20 August 1991

Date departed: 10 September 1991 (end of second time)

Time on hole: 2 days, 6 hr, 30 min (first time); 6 days, 19 hr, 30 min (second time)

Position: 48°27.360′N, 128°42.531′W

Bottom felt (drill-pipe measurement from rig floor, m): 2426.2

Distance between rig floor and sea level (m): 11.1

Water depth (drill-pipe measurement from sea level, m): 2415.1

Total depth (rig floor, m): 2858.8

Penetration (m): 432.60

Number of cores (including cores with no recovery): 16

Total length of cored section (m): 155.80

Total core recovered (m): 6.86

Core recovery (%): 4

Oldest sediment cored: none

Hard rock:
Depth below seafloor (m): 432.60
Nature: basalt

Comments: Reentry hole. First time: 2230 hr, 20 August, to 0500 hr, 23 August. Second time: 1730 hr, 3 September, to 1300 hr, 10 September.

Principal results: Site 858 is located 1.6 km north of Site 857, over an active hydrothermal vent field that extends about 800 m along and 400 m across the strike of Middle Valley. The regional structural setting of Site 858 is similar to that at Site 857; they are both situated about 6 km east of the axis of the rift valley over an uplifted but fully buried basement fault-block. Sediment thickness in the vicinity of Site 858 ranges from 400 to 700 milliseconds two-way traveltime (ms TWT). The vent field lies above what appears to be a local basement edifice. Several shallow (<300 ms TWT), bright reflectors are seen in both single- and multichannel seismic profiles beneath the site, and the more regional layered seismic stratigraphy is disrupted throughout the section. The amplitude of the seafloor reflection within the vent field is two to three times higher than that from the surrounding seafloor. Heat flow through the seafloor surrounding the site is typically about 1.0–1.5 W/m^2, slightly higher than that at Site 857. Measured values increase over a distance of a few hundred meters, from 4 W/m^2 to more than 20 W/m^2 within the field itself. Numerous vent sites have been observed from a manned submersible; fluid temperatures of most vents range between 255° and 265°C.

Four advanced piston corer/extended core barrel (APC/XCB) holes were drilled in an array crossing the field and onto the flank of the associated thermal anomaly (Table 1). These four holes (858A–858D) were drilled in order to document the local fluid-flow and thermal regimes, and the associated sediment alteration beneath and around the vent field. A rotary core barrel (RCB) exploratory hole (858F) and a deep reentry hole (858G) were drilled approximately in the center of the field in order to characterize the deeper hydrothermal and geologic structure in the upflow zone and within the upper igneous crust lying beneath the area of discharge.

Table 1. Summary of hole depths and locations.

Hole	Depth[a] (mbrf)	Offset from beacon (in meters)	GPS location
858A	2420.1	170 N, 118 W	48°27.413′ N, 128°42.708′ W
858B	2420.3	30 N, 82 E	48°27.336′ N, 128°42.545′ W
858C	2428.0	30 N, 58 W	48°27.336′ N, 128°42.660′ W
858D	2426.2	100 N, 102 E	48°27.374′ N, 128°42.530′ W
858F	2426.2	90 N, 102 E	48°27.369′ N, 128°42.527′ W
858G	2426.2	80 N, 102 E	48°27.360′ N, 128°42.531′ W

[a]Depths given in meters below rig floor. Depths below sea level can be calculated by subtracting height of rig floor above water line at this site: Holes 858A and 858B = 11.0 m, Holes 858C–858G = 11.1 m.

Hole 858A was drilled with continuous APC coring to 62.5 mbsf and XCB coring to 339 mbsf (Table 2). Drilling ended when the penetration rate and recovery dropped below acceptable levels. The hole is located about 100 m west of the vent field area (as defined by seismic, 3.5-kHz, and acoustic side-scan data), and about 150 m west of the nearest currently active vents. Temperatures measured in the upper 110 m of the hole show the thermal regime to be conductive; the thermal gradient is 1.7°C/m.

The next hole in the transect, Hole 858C, was drilled within the distal part of the vent field area (again as defined by high acoustic backscatter and the locally depressed topography), 70 m west of the nearest known vent. Measurements define a temperature gradient of about 3°C/m. APC/XCB cores were collected to a depth of 93 mbsf, by which point the penetration rate

Table 2. Site 858 coring summary.

Core	Date (1991)	Time (UTC)	Depth interval (mbsf)	Cored (m)	Recovered (m)	Recovery (%)
139-858A-						
1H	10 Aug.	1030	0.0–2.4	2.4	2.33	97.1
2H	10 Aug.	1130	2.4–11.9	9.5	9.93	104.0
3H	10 Aug.	1220	11.9–21.4	9.5	9.72	102.0
4H	10 Aug.	1340	21.4–30.9	9.5	9.97	105.0
5H	10 Aug.	1430	30.9–40.4	9.5	9.65	101.0
6H	10 Aug.	1530	40.4–49.9	9.5	4.71	49.6
7H	10 Aug.	1700	49.9–58.9	9.0	9.09	101.0
8H	10 Aug.	1830	58.9–62.5	3.6	3.64	101.0
9X	10 Aug.	1945	62.5–71.9	9.4	9.59	102.0
10P	10 Aug.	2100	71.9–72.9	1.0	0.46	46.0
11X	10 Aug.	2345	72.9–81.6	8.7	1.06	12.2
12X	11 Aug.	0045	81.6–91.3	9.7	0.69	7.1
13X	11 Aug.	0245	91.3–101.0	9.7	0.00	0.0
14X	11 Aug.	0410	101.0–110.6	9.6	0.33	3.4
15X	11 Aug.	0645	110.6–120.3	9.7	1.19	12.2
16X	11 Aug.	0810	120.3–129.9	9.6	0.76	7.9
17X	11 Aug.	0930	129.9–139.6	9.7	0.80	8.3
18X	11 Aug.	1045	139.6–149.3	9.7	3.73	38.4
19X	11 Aug.	1220	149.3–159.0	9.7	0.48	5.0
20X	11 Aug.	1400	159.0–168.6	9.6	6.13	63.8
21X	11 Aug.	1530	168.6–178.2	9.6	3.97	41.3
22X	11 Aug.	1645	178.2–187.9	9.7	0.42	4.3
23X	11 Aug.	1745	187.9–197.6	9.7	1.49	15.3
24X	11 Aug.	1900	197.6–207.3	9.7	1.10	11.3
25X	11 Aug.	2040	207.3–216.9	9.6	0.81	8.4
26X	11 Aug.	2215	216.9–226.6	9.7	0.25	2.6
27X	12 Aug.	0010	226.6–236.2	9.6	0.88	9.2
28X	12 Aug.	0115	236.2–245.9	9.7	0.29	3.0
29X	12 Aug.	0345	245.9–255.6	9.7	0.50	5.2
30X	12 Aug.	0515	255.6–265.3	9.7	1.24	12.8
31X	12 Aug.	0655	265.3–274.5	9.2	1.26	13.7
32X	12 Aug.	0815	274.5–281.7	7.2	0.29	4.0
33X	12 Aug.	0950	281.7–291.5	9.8	0.00	0.0
34X	12 Aug.	1130	291.5–301.4	9.9	0.24	2.4
35X	12 Aug.	1330	301.4–311.2	9.8	0.16	1.6
36X	12 Aug.	1500	311.2–315.2	4.0	0.08	2.0
37X	12 Aug.	1730	315.2–322.7	7.5	0.21	2.8
38X	12 Aug.	2100	322.7–332.4	9.7	0.15	1.5
39X	12 Aug.	2355	332.4–339.1	6.7	0.17	2.5
			Coring totals	339.1	97.77	28.8
139-838B-						
1H	13 Aug.	1530	0.0–7.2	7.2	7.12	98.9
2H	13 Aug.	1615	7.2–16.7	9.5	9.70	102.0
3H	13 Aug.	1700	16.7–18.4	1.7	1.73	102.0
4X	13 Aug.	2000	18.4–23.9	5.5	0.01	0.2
5H	13 Aug.	2100	23.9–31.5	7.6	6.43	84.6
6H	13 Aug.	2200	31.5–32.5	1.0	0.82	82.0
7X	13 Aug.	2315	32.5–32.7	0.2	0.00	0.0
8X	14 Aug.	0200	32.7–35.1	2.4	5.63	234.0
9X	14 Aug.	0505	35.1–38.6	3.5	0.23	6.6
			Coring totals	38.6	31.67	82.0
139-858C-						
1H	14 Aug.	0845	0.0–3.5	3.5	3.50	100.0
2H	14 Aug.	1035	3.5–13.0	9.5	9.68	102.0
3H	14 Aug.	1130	13.0–22.5	9.5	9.80	103.0
4P	14 Aug.	1230	22.5–23.5	1.0	0.00	0.0
5H	14 Aug.	1545	23.5–33.0	9.5	9.74	102.0
6H	14 Aug.	1645	33.0–41.5	8.5	8.48	99.7
7H	14 Aug.	1740	41.5–46.5	5.0	4.88	97.6
8H	14 Aug.	2030	46.5–47.5	1.0	0.91	91.0
9H	14 Aug.	2130	49.0–49.3	0.3	0.27	90.0
10X	14 Aug.	2300	49.3–54.5	5.2	0.61	11.7
11X	15 Aug.	0015	54.5–64.0	9.5	1.32	13.9
12X	15 Aug.	0130	64.0–73.7	9.7	4.42	45.5
13X	15 Aug.	0250	73.7–83.4	9.7	0.62	6.4
14X	15 Aug.	0430	83.4–93.1	9.7	1.27	13.1
			Coring totals	91.6	55.50	60.6
			Drilled between 139-858C-8H and -9H			1.5

Table 2 (continued).

Core	Date (1991)	Time (UTC)	Depth interval (mbsf)	Cored (m)	Recovered (m)	Recovery (%)
139-858D-						
1H	15 Aug.	0740	0.0–9.3	9.3	9.31	100.0
2H	15 Aug.	0845	9.3–18.8	9.5	10.09	106.2
3P	15 Aug.	1000	18.8–19.8	1.0	0.56	56.0
4H	15 Aug.	1210	19.8–28.3	8.5	8.37	98.5
5H	15 Aug.	1300	28.3–28.8	0.5	0.49	98.0
6X	15 Aug.	1545	28.8–37.2	8.4	1.36	16.2
7X	15 Aug.	1800	37.2–40.7	3.5	0.25	7.1
			Coring totals	40.7	30.43	74.8
139-858E-1W	16 Aug.	0710	0.0–38.5	38.5	4.70	(wash core)
			Coring totals	0.0	0.0	
			Washing total		38.5	4.70
			Combined total		38.5	4.70
139-858F-						
1W	16 Aug.	0915	0.0–27.8	27.8	1.85	(wash core)
2R	16 Aug.	1100	27.8–37.0	9.2	0.10	1.1
3R	16 Aug.	1320	37.0–46.5	9.5	0.00	0.0
4R	16 Aug.	1500	46.5–56.0	9.5	0.27	2.8
5R	16 Aug.	1600	56.0–65.6	9.6	0.02	0.2
6R	16 Aug.	1945	65.6–75.1	9.5	0.09	1.0
7R	16 Aug.	2045	75.1–84.7	9.6	0.07	0.7
8R	16 Aug.	2145	84.7–94.2	9.5	0.15	1.6
9R	17 Aug.	0015	94.2–103.9	9.7	0.23	2.4
10R	17 Aug.	0115	103.9–113.6	9.7	0.02	0.2
11R	17 Aug.	0300	113.6–123.3	9.7	0.52	5.4
12R	17 Aug.	0410	123.3–132.9	9.6	0.07	0.7
13R	17 Aug.	0530	132.9–142.6	9.7	0.19	2.0
14R	17 Aug.	0645	142.6–152.2	9.6	0.30	3.1
15R	17 Aug.	0800	152.2–161.9	9.7	0.16	1.7
16R	17 Aug.	0910	161.9–171.6	9.7	0.04	0.4
17R	17 Aug.	1030	171.6–181.3	9.7	0.20	2.1
18R	17 Aug.	1145	181.3–190.9	9.6	0.94	9.8
19R	17 Aug.	1330	190.9–200.6	9.7	0.39	4.0
20R	17 Aug.	1445	200.6–210.3	9.7	0.15	1.5
21R	17 Aug.	1600	210.3–220.0	9.7	0.34	3.5
22R	17 Aug.	1700	220.0–229.6	9.6	0.14	1.5
23R	17 Aug.	1815	229.6–239.3	9.7	0.17	1.8
24R	17 Aug.	1930	239.3–248.9	9.6	0.18	1.9
25R	17 Aug.	2100	248.9–258.6	9.7	1.02	10.5
26R	17 Aug.	2330	258.6–267.8	9.2	0.94	10.2
27R	18 Aug.	0145	267.8–277.5	9.7	0.23	2.4
28R	18 Aug.	0430	277.5–287.2	9.7	0.34	3.5
29R	18 Aug.	0705	287.2–296.9	9.7	0.90	9.3
			Coring totals	269.1	8.17	3.0
			Washing totals		27.8	1.85
			Combined totals		296.9	10.02
139-858G-						
1R	4 Sept.	1300	276.8–286.5	9.7	0.50	5.2
2R	4 Sept.	1600	286.5–296.1	9.6	0.58	6.0
3R	4 Sept.	1845	296.1–305.8	9.7	0.17	1.8
4R	4 Sept.	2115	305.8–315.4	9.6	0.57	5.9
5R	4 Sept.	2300	315.4–325.1	9.7	0.48	5.0
6R	5 Sept.	0110	325.1–334.8	9.7	0.36	3.7
7R	5 Sept.	0340	334.8–344.5	9.7	0.55	5.7
8R	5 Sept.	0545	344.5–354.1	9.6	0.30	3.1
9R	5 Sept.	2045	354.1–364.9	10.8	0.11	1.0
10R	5 Sept.	2330	364.9–374.5	9.6	0.95	9.9
11R	6 Sept.	0215	374.5–384.2	9.7	0.20	2.1
12R	6 Sept.	0440	384.2–393.9	9.7	0.45	4.6
13R	6 Sept.	0700	393.9–403.6	9.7	0.39	4.0
14R	6 Sept.	1035	403.6–413.3	9.7	0.28	2.9
15R	6 Sept.	1330	413.3–422.9	9.6	0.27	2.8
16R	6 Sept.	1600	422.9–432.6	9.7	0.70	7.2
			Coring totals	155.8	6.86	4.4

and core recovery had deteriorated and drilling was terminated. No indications of focused fluid flow were observed, although a considerable amount of dispersed pyrite and some brecciation were encountered.

Hole 858B, the next hole in the transect, was drilled 140 m east of Hole 858C and only a few meters away from a 276°C hydrothermal vent. A temperature of 197°C was measured at 19.5 m depth in the hole, indicating that the flow feeding the vent is very localized. The hole was drilled to a depth of 39 mbsf, where the core recovery and rate of penetration dropped below acceptable levels. Highly silicified sediment was encountered near the bottom of the hole.

Hole 858D was drilled at the center of the vent area, about 70 m northeast of the nearest vent (in Hole 858B). Twenty-nine meters of sediment were recovered with APC coring; an *in-situ* temperature of at least 208°C at 18.8 mbsf was determined with the water-sampler temperature probe (WSTP). Hard drilling and low XCB recovery began at about 30 mbsf, and drilling was terminated at 41 mbsf. Deep drilling began at this location with RCB Hole 858F, which penetrated 258 m of sediment and into extrusive basalt. Penetration of basalt flows continued in reentry Hole 858G to a total depth of 432.6 mbsf.

Unfortunately, recovery was poor with all coring systems but the APC. Recovery in the sedimentary section from Hole 858F averaged about 3%, and in the igneous section from Hole 858G averaged less than 5%.

Sediment in all holes at this site is hydrothermally altered, as reflected in mineral assemblages, bulk chemical composition, and physical and magnetic properties. The degree of alteration varies laterally and with depth in a way that is consistent with the thermal structure defined by the surface heat flow and downhole temperature measurements. The lateral boundary of the upflow system is very sharp, and upward flow of pore fluid at a rate that can be detected thermally or geochemically is limited to the area beneath the vent field itself. Conditions are thermally conductive, and chemically diffusive or reactive, in Holes 858A and 858C. Within the vent field, it is inferred that the section is virtually isothermal and chemically dominated by advection deeper than a few tens of meters. Lateral flow appears to be significant at various levels in all holes. Extreme alteration may have resulted in the formation of a cap of indurated sediment intersected at 30 mbsf in Holes 858B, 858F, and 858G. This cap may represent a fundamental hydrologic unit beneath the field. Unfortunately, very little of this material was recovered. Electrical resistivity logging in Hole 858F imaged a sequence of turbidite layers that correlates remarkably well with a similar sequence logged in Hole 857C, 1.6 km distant. This is remarkable, in light of the vast difference in thermal and chemical regimes at the two sites, for two reasons: the porosity signature of the turbidite layers has survived hydrothermal induration, and the section has been vertically compressed by less than 10% in the process. Clear correlations can also be drawn between the sections in Hole 858A and Holes 857A and 857C, based on lithologic and biostratigraphic boundaries.

Igneous basement at Site 858 comprises a relatively uniform sequence of basalt flows. Units are defined primarily on the basis of textural variation. Low core recovery limits the degree to which individual flow units could be recognized, although typically one to two chilled margins were recovered in a given core. Chemical analysis indicates that the flows may be genetically related to the sills drilled at Site 857. The rocks are highly altered, but vein- and dispersed-mineral assemblages show little indication of the passage of high-temperature (>38°C) hydrothermal fluids. Injection tests showed that this basaltic basement is highly permeable. Measurements with a flow-meter in Hole 858G during a steady injection test showed that most of the flow entered the formation in a discrete layer. Temperature measurements showed clear evidence that downhole flow, forced "naturally" by the cold, high-density water in the hole, entered the formation at the same depth and cooled it. Temperature measurements in Hole 858G indicate as well that drawdown into the sediment section may have been stimulated where Hole 858F penetrated the cap rock.

After completion of all operations at this site, an instrumented hydrologic seal (CORK) was installed to obviate downhole circulation and to monitor temperature and pressure as the formation returns to equilibrium.

BACKGROUND AND OBJECTIVES

Site 858 is centered over a large hydrothermal vent field in the eastern part of Middle Valley where fluids discharge through the seafloor at temperatures of up to 276°C. Sediment thickness in the vicinity of the site ranges from 500 to over 700 ms TWT; a strong reflector lies at a depth of 120 ms TWT directly beneath the vent field, and it was suspected that the discharge was controlled by this local basement topography and the local reduction in sediment thickness. A number of objectives were to be addressed by drilling and downhole measurements in this active upflow and discharge zone.

Most importantly, it was anticipated that observations made at this site could be coupled with the information provided by the deep hole at Site 857 to answer several fundamental questions about the fluid flow regime in the upper crust in this sedimented rift environment. For example, what controls the location, rate, and nature of upflow and discharge? How rapid is the rate of discharge relative to the conductive heat loss in the upflow zone beneath the vent field? How efficiently does the sediment cover thermally insulate and hydrologically isolate the underlying igneous crust? And how efficiently do hydrothermal fluids transport heat and chemical species laterally from one part of the crust to another beneath the sediment "seal?"

Important questions also could be answered about the detailed aspects of upflow at this site. Is there a regional "hydrothermal fluid reservoir" beneath the sediment section that is tapped by the discharge zone, or do fluids ascend from greater depth? How focused is the ascending flow? To what degree do fluids react with the adjacent rock and sediment during their ascent? How much heat is lost during ascent? Is there significant diffuse fluid flow that results in significant alteration of and possibly mineralization within the sediments in the vicinity of the vent field? Does a discharge area such as this host significant subsurface mineralization?

Other more site-specific questions to be addressed by this drilling concern the history of hydrothermal discharge as recorded in the sedimentary section, the influence of high temperatures on diagenesis, hydrocarbon maturation, and sediment and igneous rock physical and magnetic properties, and the nature and composition of the igneous rock that underlies this site.

It was anticipated that all of these questions could be addressed with the combination of an array of relatively shallow holes across the vent field, and a deep reentry hole sited as close to the center of the area of discharge as logistically possible. In addition to drilling and coring, operations would include fluid sampling, discrete and continuous downhole measurements and logging, formation permeability testing, and long-term observations of temperatures and pressures in the formation.

SITE GEOPHYSICS AND GEOLOGY

Structural Setting

Site 858 is centered over a vent field located roughly 6 km east of the current axis of Middle Valley, and about the same distance west of the valley-bounding normal fault that creates the topographic and hydrologic boundary to the valley along its eastern side (Figs. 1 to 3; see also maps and profiles in the back pocket of this volume). The approximate age of the underlying igneous crust, as estimated from the combination of the distance to the eastern Brunhes magnetic chron and the spreading rate of the ridge, is about 250,000 yr (Davis and Villinger, this volume). The general structural setting of this site is similar to that of Site 857; a large-offset synsedimentary normal fault or localized fault zone separates both sites from the current structural axis of the rift. This fault is well developed farther north in the valley; at one location, the fault has produced a local scarp of 250 m relief (Davis and Villinger, this volume). Near the location of Site 858 the throw on the fault appears to have created a substantial offset in the

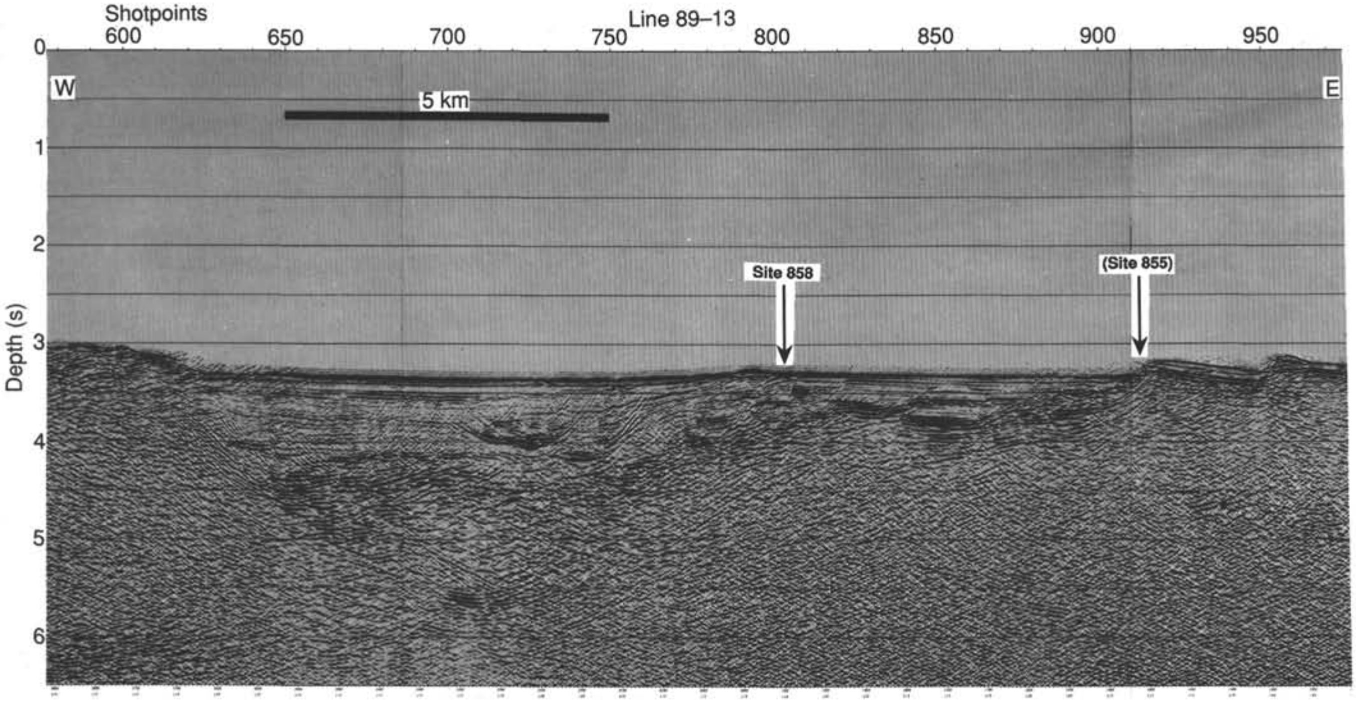

Figure 1. Multichannel seismic reflection profile 89-13, crossing Middle Valley and Site 858 (from Rohr et al., 1992). The location of Site 855 is shown for reference.

local depth to basement, but the seafloor relief produced by the fault is modest, only about 50 m (Figs. 2 and 4). Uplift of the foot-wall block has not been sufficient to have lifted the seafloor above the level of turbidite sedimentation until recently; at no location in the vicinity of the site does acoustic basement rise close to the seafloor along the fault.

The seismic structure directly beneath Site 858 is complex and probably three-dimensional (Fig. 5); the relatively simple structure that characterizes the foot-wall block of the fault seen at the location of Site 857 is disrupted locally beneath the vent field by a zone of incoherence that rises to the seafloor. A closer inspection of the multichannel reflection data (Fig. 6) shows that the seafloor reflection amplitude in the vent area itself is higher relative to the amplitude in the surrounding region by roughly a factor of two. This character contrasts with the highly scattered and low-amplitude reflection character seen in the 3.5-kHz echo-sounding profile (Fig. 4). Several bright but local reflectors are also present below the seafloor; one occurs at a depth of 130 ms TWT bsf, and another at a depth of 300 ms TWT bsf. Both of these are relatively singular, isolated events; the latter is inverted in its waveform relative to the seafloor reflection, implying that it marks a boundary where higher impedance material overlies lower. This depth corresponds quite closely to the depth of a local bright horizon that is seen in single-channel data to terminate against the higher-level zone of incoherence (Fig. 6D in Davis and Villinger, this volume). This difference probably indicates the small scale and the two-dimensionality of the structure, and suggests that the multichannel line crosses far enough off the center of the structure for the deeper reflector at 300 ms TWT bsf that may surround the vent area to appear to pass continuously beneath it.

Thermal Structure

The vent field is situated within the same axis-parallel thermal anomaly as Site 857 (Fig. 7; Davis and Villinger, this volume). Seafloor heat flow exceeds 800 mW/m^2 in a 1-km-wide zone that runs parallel to the valley about 1–2 km east of the primary rift-bounding normal fault. Near the perimeter of the vent field, heat flow increases sharply over a distance of a few hundred meters toward the perimeter of the vent field; within the field, heat flow is typically between 5 and 10 W/m^2, and exceeds 20 W/m^2 at some locations (Fig. 8). None of the measurements made within or in the vicinity of the field displays any nonuniformity in heat flow with depth, and this sets a limit on the rate of diffuse pore-fluid flux that might be passing through the seafloor at about 10^{-8} m/s (0.3 m/yr). Unfortunately, most measurements in this area were made without acoustic navigational control of the probe, and the inaccuracy of the positions of individual measurements is typically 100 m. Such inaccuracy does not allow the nature of the heat flow variability within the vent field to be defined, nor the position of the measurements relative to known vents or related seafloor structures to be determined.

Geology of the Vent Field

The detailed seafloor morphology of the vent field is characterized by 3.5-kHz echo-sounding profiles (Fig. 8), deep-towed side-scan imagery (Fig. 9), and submersible observations (Fig. 10). The field (referred to herein as the "Dead Dog" vent field) is situated in a local topographic depression that lies locally up to 10 ms (about 8 m) below the surrounding, undisturbed turbidite-sediment seafloor. The seafloor within the depression is acoustically rougher than that in the surrounding area; this is indicated by the local high-amplitude backscatter seen in both the 12-kHz and 30-kHz side-scan acoustic imagery of the area (Figs. 3 and 9) and in the 3.5-kHz echo-sounding profile as low-amplitude, highly scattered signal.

At least eight vent sites have been mapped in this area during deep-towed camera tows and submersible traverses; up to 18 are inferred to be present, on the basis of the acoustic imagery (Figs. 9 and 10). Each of the prominent vent sites consists of a mound, typically 5 to 15 m high and 25 to 35 m in diameter, that casts an acoustic shadow in the grazing-angle image of Figure 9. Each site has from one to five separate high-temperature vents situated at the top of the respective mound. Each vent consists of an anhydrite-pyrite chimney, 0.7–1.2 m high, where fluid discharges from several conduits. The chimneys are surrounded by aprons of anhydrite, about 2–5 m in diameter. The tops and sides of the mounds are underlain

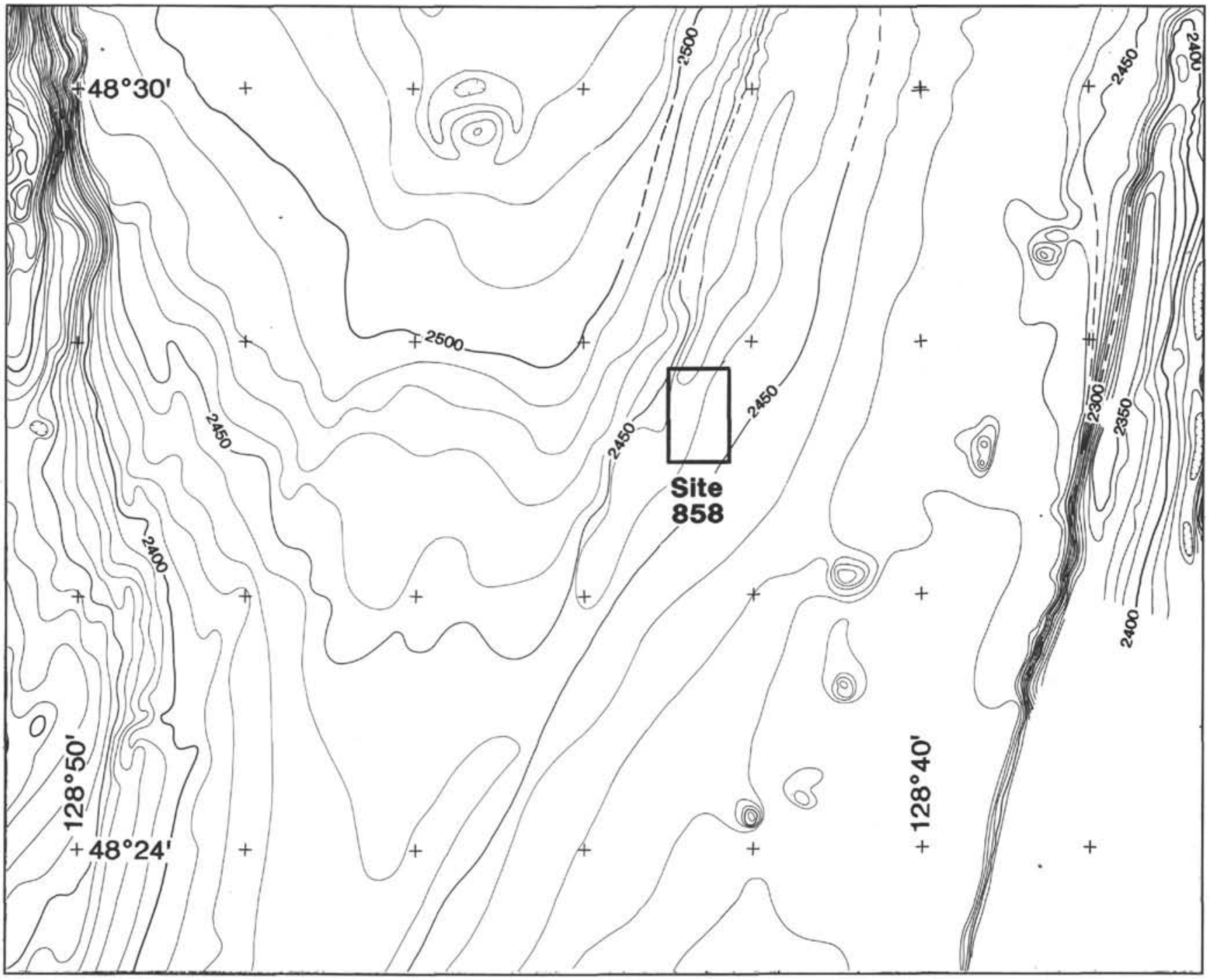

Figure 2. Bathymetry (in meters) of the part of Middle Valley occupied by Leg 139, based on continuous SeaBeam swath soundings. Depths are computed using a sonic velocity of 1500 m/s and contoured at 10-m intervals. The area of Site 858 included in Figures 8 and 9 is outlined.

by a well-indurated crust and highly altered sediment. Barite, anhydrite, pyrite, sphalerite, and chalcopyrite, as well as Mg-smectite and ferruginous clay are all present in the vicinity of the vents.

Vent-fluid temperatures range from 234° to 276°C; most fall between 254° and 276°C. The fluids have a pH of approximately 5.4, and a Ca (estimated end-member) concentration of 80 millimolar (mmol). End-member compositions are somewhat heterogeneous, with concentrations of most components being consistently lower than those in typical ridge-crest hydrothermal fluids. Metal contents are very low, near detection levels (J. Lydon, pers. comm., 1991). Isotopic data for carbon, oxygen, and hydrogen from these fluids indicate that CO_2 and methane are being generated by pyrolysis of organic material (Taylor, 1990). The pH values indicate the fluids have equilibrated with carbonate. The low metal content indicates that either the metalliferous components have precipitated in the subsurface, or that the fluids never reached sufficiently high temperature or low pH to contain abundant metals.

Sediments in the vent field but away from individual vent sites is highly altered; carbonate nodules are very common. Pore-water data collected from piston cores show high geochemical gradients, with the highest gradients present in the central part of the field. Most cores show a strong downward depletion in SO_4 and Mg, and up to a five-fold downward increase in Ba (J. Lydon, pers. comm., 1991). These trends are consistent with the observed increase in Mg-smectite and barite near the top of the cores (W. Goodfellow, pers. comm., 1991). Diffuse discharge is indicated, but at a rate lower than the limit indicated by the linearity of the thermal profiles.

OPERATIONS

Operations Outline

Operations began at Site 858 with the completion of a suite of four APC/XCB holes distributed across a hydrothermal vent field, drilled in part to provide the detailed information about depth to basement necessary to site a deep reentry hole as close to the zone of fluid upflow as possible. All holes were drilled until the rate of penetration or core recovery became very low. The relative positions of each of the holes was established with respect to previously studied local seafloor structures and vents in the field during a vibration-isolated television (VIT) deployment before spudding Hole 858B. A minicone was left in the deepest of these holes (858C) to allow later reentry and logging. A site in the center of the vent field near Hole 858D was chosen for the deep reentry hole, and an exploratory RCB hole was drilled to a depth of 297 m. Following a logging program, the hole

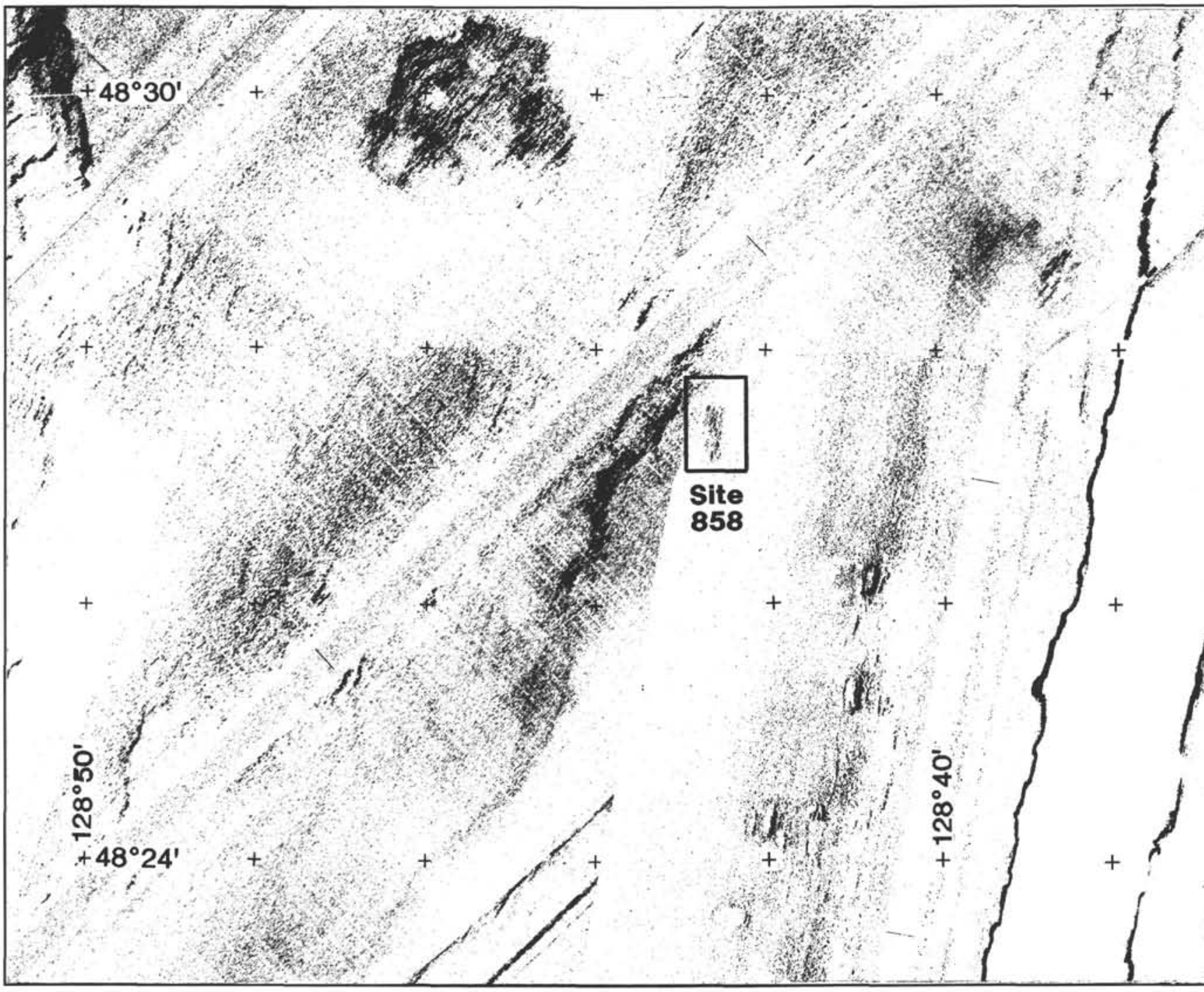

Figure 3. SeaMARC II (12 kHz) acoustic image mosaic of the same part of Middle Valley that is shown in Figure 2.

was cemented to prevent fluid from passing into or out of the formation, and the reentry Hole 858G was started. This hole was initially drilled to 276 mbsf, cased and cemented. Operations were then temporarily suspended to allow the hole to equilibrate with the formation while final operations at Site 857 were carried out.

Operations began again 11.5 days later with a temperature log in the cemented-in casing. The casing shoe and cement was then drilled from the bottom of the hole. Drilling continued with two bits to a total depth of 432.6 mbsf; igneous rock was recovered throughout the cored interval. A logging program was then completed that included two temperature logs, and an induction/porosity/natural gamma tool string. Operations at the site ended with a successful packer/flowmeter experiment and installation of a CORK instrumented hydrologic seal. A TV/sonar survey was then conducted in order to identify the exact position of the holes of this site with respect to nearby vents before the VIT frame and drill string were recovered for the last time.

Hole 858A

Operations began at Site 858 with APC/XCB coring in Hole 858A. A new beacon had to be dropped, as the beacon dropped previously at this site had failed to turn on. An initial APC core was shot from 2413 meters below rig floor (mbrf), 6 m above the depth of 2419 mbrf determined by the precision depth recorder (PDR). Water depth was established at 2420.1 mbrf on the basis of the core recovered. Heat flow measurements began with the APC heat flow shoe on every core as soon as the sediment could support enough bit weight for heave compensation; the first measurement was made at Core 139-858A-3H. Incomplete stroke of the corer began with Core 139-858A-5H, but coring continued on an advance-by-recovery basis. Core 139-858A-7H remained in the sediment for an extended period for temperature equilibration. The measured temperature was 92°C, and the butyrate core liner showed signs of high-temperature failure. Core 139-858A-8H was taken with a high-temperature "ultem" liner. The liner was shattered when the core was recovered, confirming that ultem is too brittle for APC coring. XCB coring then began at 63 m.

One XCB core then was recovered with full core recovery. Butyrate liner was again deployed; no problems were encountered, presumably because of the cooling efficiency of circulation. This core was followed by a successful pressure core sampler (PCS) core which yielded a half-meter core under pressure. After a WSTP run, XCB coring continued with WSTP runs after each second core to 111 mbsf. Circulating pressures for the XCB escalated on successive runs, indicating progressively more jet nozzles plugged, until all the circulation apparently was going through the ports of the cutter shoe. Two liners were collapsed (preventing core entry) by attempts to open the

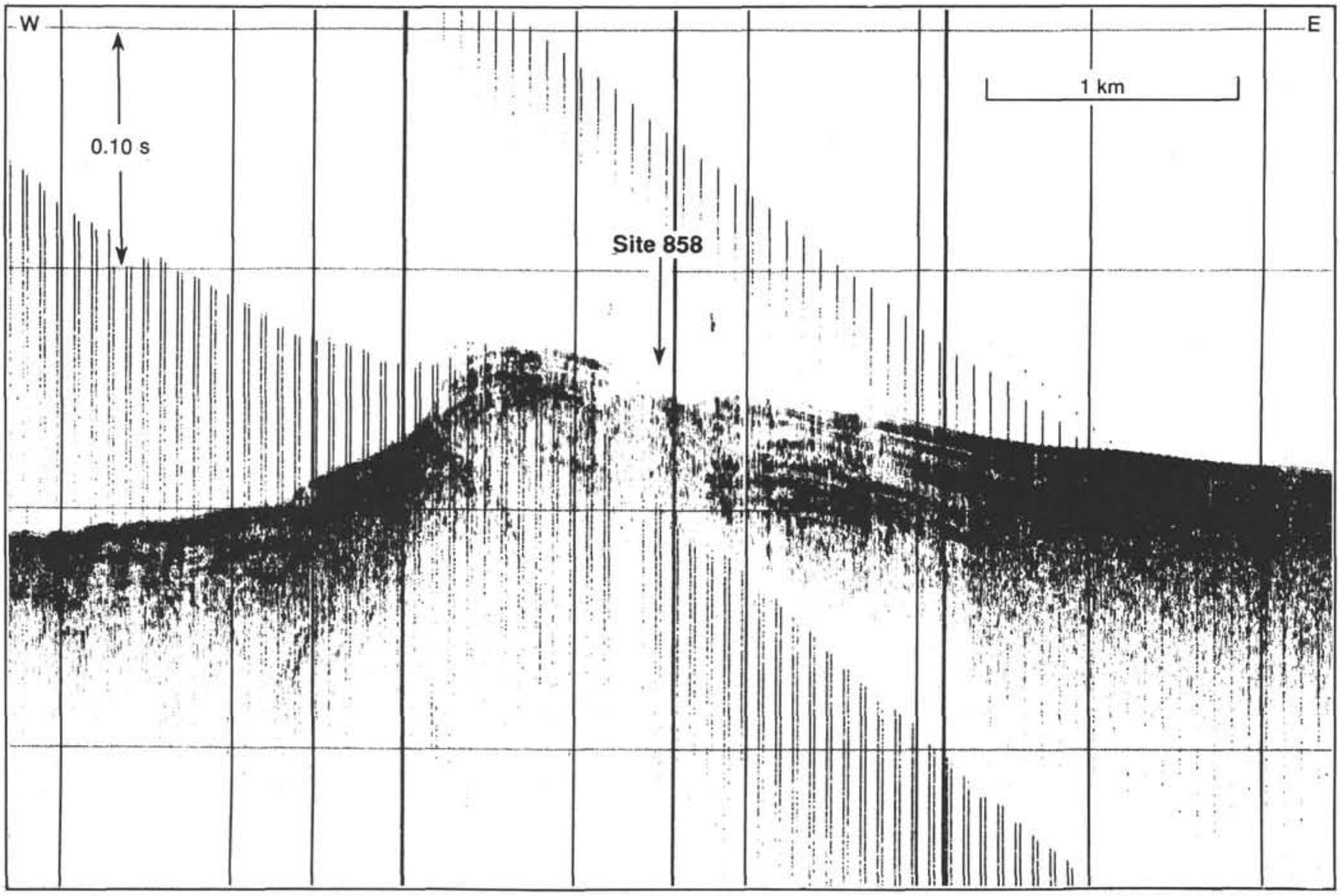

Figure 4. 3.5-kHz reflection profile crossing Site 858. The vertically exaggerated profile illustrates well the back-tilting of the fault block into which the holes were drilled at this site. The rough, highly scattering, and depressed seafloor of the vent field is also apparent.

jets with high circulating rates. The pressure was considerably reduced at the beginning of Core 139-858A-17X, indicating that at least some jet circulation had been regained.

XCB core recovery was low, with only an occasional high-percentage core despite excellent core quality in firm claystone/siltstone. The rate of penetration (ROP) dropped in more highly indurated sediment below about 312 mbsf; this, coupled with low recovery caused us to decide against further effort to reach the igneous basement target. Hole 858A was terminated at 339 mbsf.

As a temperature measurement was desired, the bit was pulled to 100 mbsf and the Sandia temperature tool was run on the coring line. While the log was in progress, a free-fall funnel (FFF) was assembled around the drill string and dropped so that a return could be made for further logging and/or deepening of the hole with the RCB system. The bit was pulled clear of the seafloor at 2330 hr UTC on 12 August.

Hole 858B

It was critical for all of the holes at this site to be well located with respect to various known features on the seafloor, including several hydrothermal vents. Toward this end, a systematic survey was completed in the vent field with the VIT camera and scanning sonar system. This 7-hr survey included one north-south and three east-west traverses. Several known vents and mounds were identified along these traverses, and on this basis final adjustments were made to the navigation of the side-scan/submersible map that was to be used to lay out the final position of all remaining holes. Hole 858B was positioned about 245 m southeast of Hole 858A, on the flank of a hydrothermal mound, about 10 m from an active vent. The pipe was lowered to touch the seafloor and mark the depth at 2419 m. The VIT then was recovered while preparations for spudding were made. Because the hole was more than 250 m from the positioning beacon used for 858A, it was necessary to launch a new beacon.

A "mudline" core measured the depth at 2420.3 m, indicating that the new hole actually was a bit downslope on the mound from the initial target located with the TV. The first core was recovered in a butyrate liner with no problems, but the special aluminum liners were used for subsequent APC cores because of the anticipated high temperatures. Incomplete stroke was encountered on Core 139-858B-3H; gravelly material was recovered in the catcher of a 1.7-m core.

After a WSTP probe recorded a temperature of 196°C, a short XCB core was tried. The ROP was high and only a trace of sediment was recovered, so we reverted to the APC. Core 5H apparently stroked out during the trip down the pipe, but 7.6 m of sediment was recovered. Core 6H recovered only 82 cm after an incomplete stroke.

The following XCB core had no recovery; in the next, hole-cleaning difficulties began and 5-1/2 m of drill cuttings were recovered in the liner. During the cutting Core 9X to 38.6 mbsf, pressure and torque began to increase, indicating that the hole was not being cleaned of cuttings. Coring was terminated at that point, due to poor conditions, low core recovery, and low ROP.

As the drill string was raised in preparation for retrieval of the final core, it began to stick and about 15 min were required to free it. The string was free with the bit positioned at 24 mbsf, and the Sandia temperature logging tool was run on the coring line. Despite the problems associated with the pipe sticking in the hole, the depth meter

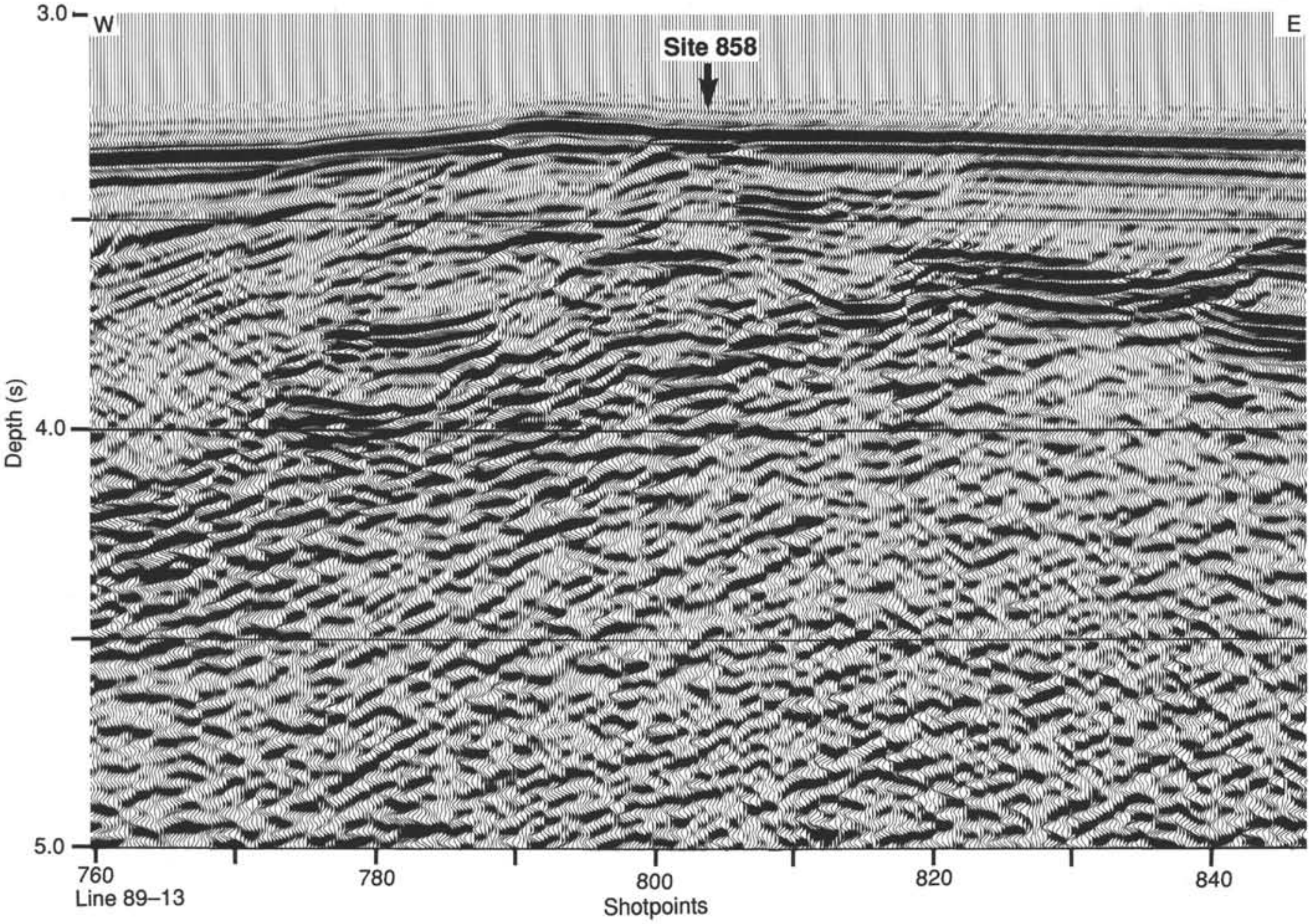

Figure 5. Detail of seismic profile 89-13, showing the local seismic structure in the vicinity of Site 858. Shotpoints are spaced 50 m apart.

showed that the lightweight logging tool descended to total depth. The recorded temperature of about 150°C indicated that hot formation water was not flowing into the hole.

Hole 858C

A positioning offset of 140 m west then was made to locate the next hole at an intermediate position between Hole 858A and 858B. The hole was spudded on 14 August, at 0130 hr, with an APC core that determined seafloor depth to be 2428.0 m. After two additional APC cores, the PCS was run at 22.5 mbsf. Only water was recovered, apparently because too much pump circulation was used in the soft sediment, but the chamber was pressurized when recovered. APC cores with heat flow shoes then were taken to 47.5 mbsf. All had incomplete stroke. WSTP probe runs were made at 24 and 47 mbsf. After Core 139-858C-8H recovered gravelly material, a 1.5-m interval was drilled in the hope of extending APC coring past the gravel or hard bed. Core 9H apparently made little penetration, however, recovering only 27 cm. XCB cores then were taken to 93 mbsf, where low ROP and poor core recovery caused us to terminate drilling.

Hole 858D

The vessel then was offset back to the hydrothermal discharge area to a point about 75 m north-northeast of Hole 858B. The depth determined from the first APC core was 2426.2 m. Upon recovery of Core 139-858D-2H, the upper half of the butyrate liner was found to be carbonized and partially melted. In addition, gas from a core-liner void sent a portable H_2S monitor off scale, generating a H_2S alert. A PCS core was taken next, and a sediment core was recovered under pressure with gases intact. A WSTP measurement was made at 18.8 mbsf and registered a temperature of 208°C. Two additional APC cores collected in aluminum liners achieved only incomplete stroke; XCB coring began at 29 mbsf. After two cores with low ROP and recovery, coring was terminated. It was decided that this site, located approximately in the center of the vent field, was geologically ideal, and logistically suitable for the reentry hole. A pipe trip was started to change to a RCB bottom-hole assembly (BHA) for the reentry exploratory hole.

"Hole" 858E

Because of the local variability in the geology of the area, it was desirable to minimize the offsets between the Hole 858D, the exploratory hole, and the reentry hole. Thus no change was made in the dynamic positioning offsets. Hole 858E was to begin with a jet-in test to determine the setting depth for conductor casing; water depth was checked by tagging bottom with no circulation. Weight was taken at about 2429 m, which was reasonable considering that 2–3 m of very soft sediment was noted in the first APC core of Hole 858D. Jetting then commenced at low pump rates to 20 mbsf, where the test was interrupted for a WSTP sample in an interval missed in the previous hole. Some circulation had to be maintained to cool the electronics, and the WSTP had to be "chased" about 10 m to the end of derrick travel as it continued to sink into the sediment. A new "wash barrel" was pumped into place and the jetting test continued. When progress

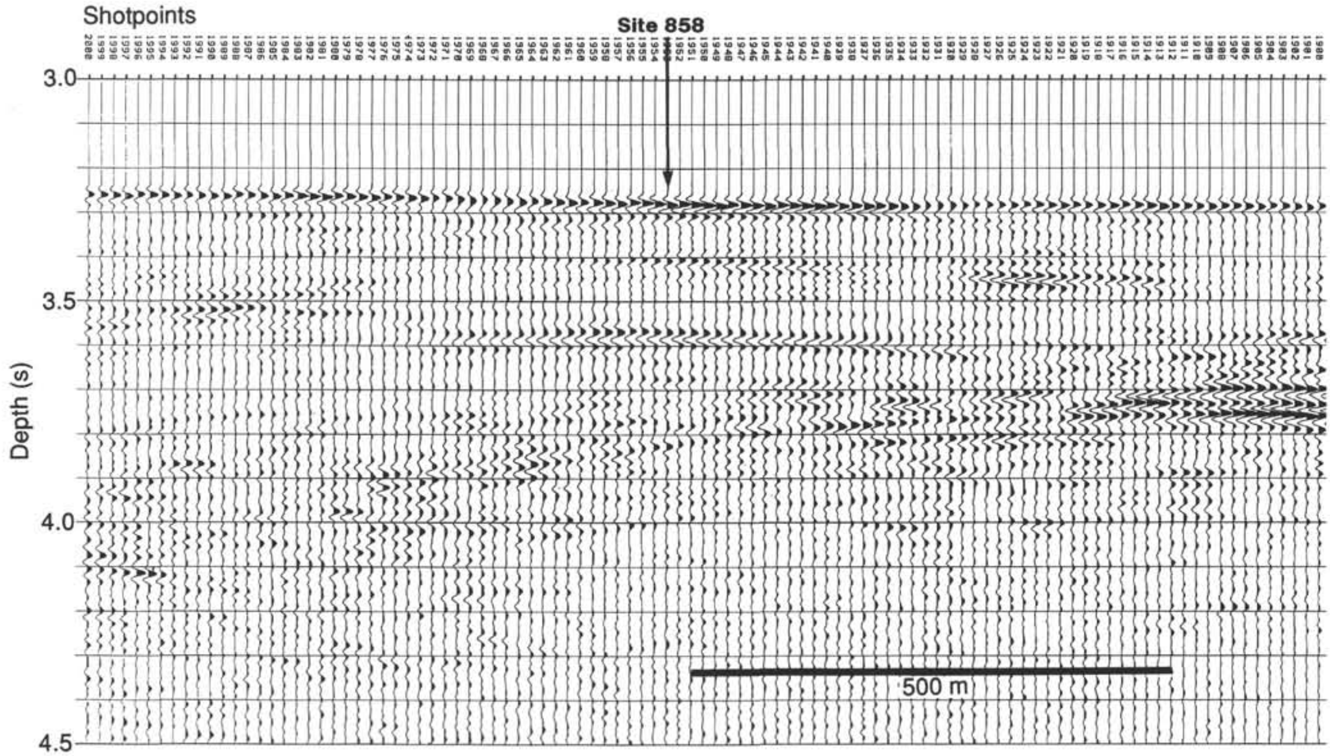

Figure 6. Near-trace display of multichannel line 89-13. Individual traces are spaced at 12.5 m apart.

failed to slow with depth, and the level of the first hard layers of Hole 858D were passed, it became apparent that Hole 858D had been reentered inadvertently and that the jetting and WSTP operation had been conducted in a hole containing cuttings and "fill." This reentry was confirmed when solid bottom was contacted at the total depth reached by Hole 858D.

As a correctly representative jet-in test was required for the reentry installation, and as Hole 858E was clearly bogus, the bit was pulled above the seafloor and a new hole was started.

Hole 858F

After a 10-m offset to the south, the jet-in test was repeated. Results indicated that up to 26 m of conductor casing could be emplaced. Although that would be a short string, it would be adequate to support a casing string up to the anticipated maximum length of 200 m.

Continuous RCB coring then began. ROP was very slow for the first two cores; drilling times were 50 and 70 min. Below that, drilling rates increased to 10 to 15 min per core, although core recovery did not improve. After Core 139-858F-5R had been retrieved from 66 mbsf, the bit became plugged as the new core barrel was pumped into place. Circulation could not be established, even after a wireline trip was made and the inner barrel was unseated. The bit was finally unplugged with fairly low pressure after the barrel was pulled close to the seafloor, probably because of the swabbing action of the wireline trip. Circulating pressure through the bit throat remained high, and high torque and drag indicated that the annulus was packing off around the BHA. When the hole did not clean up with the high circulating rate or with a mud flush, indications were that circulation was going into the formation without carrying the cuttings out of the hole. After a considerable period of working the pipe, the hole cleared and ultimately caused no further problems to total depth. One additional instance of plugged jets occurred, apparently because of a failed spring in the float valve. When the jets had been cleared, a higher circulating rate was used during wireline retrievals and there were no further problems.

The ROP continued to be high and recovery low, only 2%, down to 258 mbsf where altered igneous rock was encountered. Drilling times for cores increased to 80–100 min, and recovery improved, but only to about 7%. At 297 mbsf, sufficient penetration of competent rock had been made to confirm that a satisfactory casing seat was available. Forty meters of penetration into the igneous unit also provided an opportunity to log the sediment-igneous contact. The drilling objectives of the exploratory hole were declared accomplished and preparations for logging began.

Forty meters of fill was encountered upon return of the bit to total depth for the wiper trip. The fill was washed out easily without requiring rotation, and the hole was flushed with 50 bbl of high-viscosity mud. The pipe then was pulled back to logging depth at 46 mbsf for installation of the sidewall-entry sub (SES).

A temperature profile was desired before the hole was disturbed by logging with the SES to confirm whether there was a flow of water into or out of the hole. The self-contained Sandia temperature tool was run on the coring line for that purpose. The weight indicator registered setdown at 2690 m, 33 m short of total depth. After the log had been completed, the sinker bars were recovered, but without the logging tool attached. The 3/4-in. threaded connection had parted, leaving the entire dewared pressure case in the hole.

After an open-hole fishing attempt with an inner core barrel failed, runs were made with the Los Alamos water sampler and the JAPEX pressure-temperature-flowmeter (PTF) tool to gather more information about the hydrology of the hole before the standard logs were run. The PTF tool came to rest 25 m higher than the depth reached by the Sandia logging attempt.

As a trip to total depth for additional hole cleaning was needed, the cleanout effort was combined with a more serious attempt to recover the Sandia tool. Fortunately, the tool apparently came to rest standing free of the wall of the hole and the mechanical bit release (MBR) top connector washed over it. A fishing run with a 3-1/2-in. Bowen overshot on an inner core barrel was made when fill had been washed out to 2702 m. The grapple engaged the tool but recovered only the 2-1/4-in.-diameter

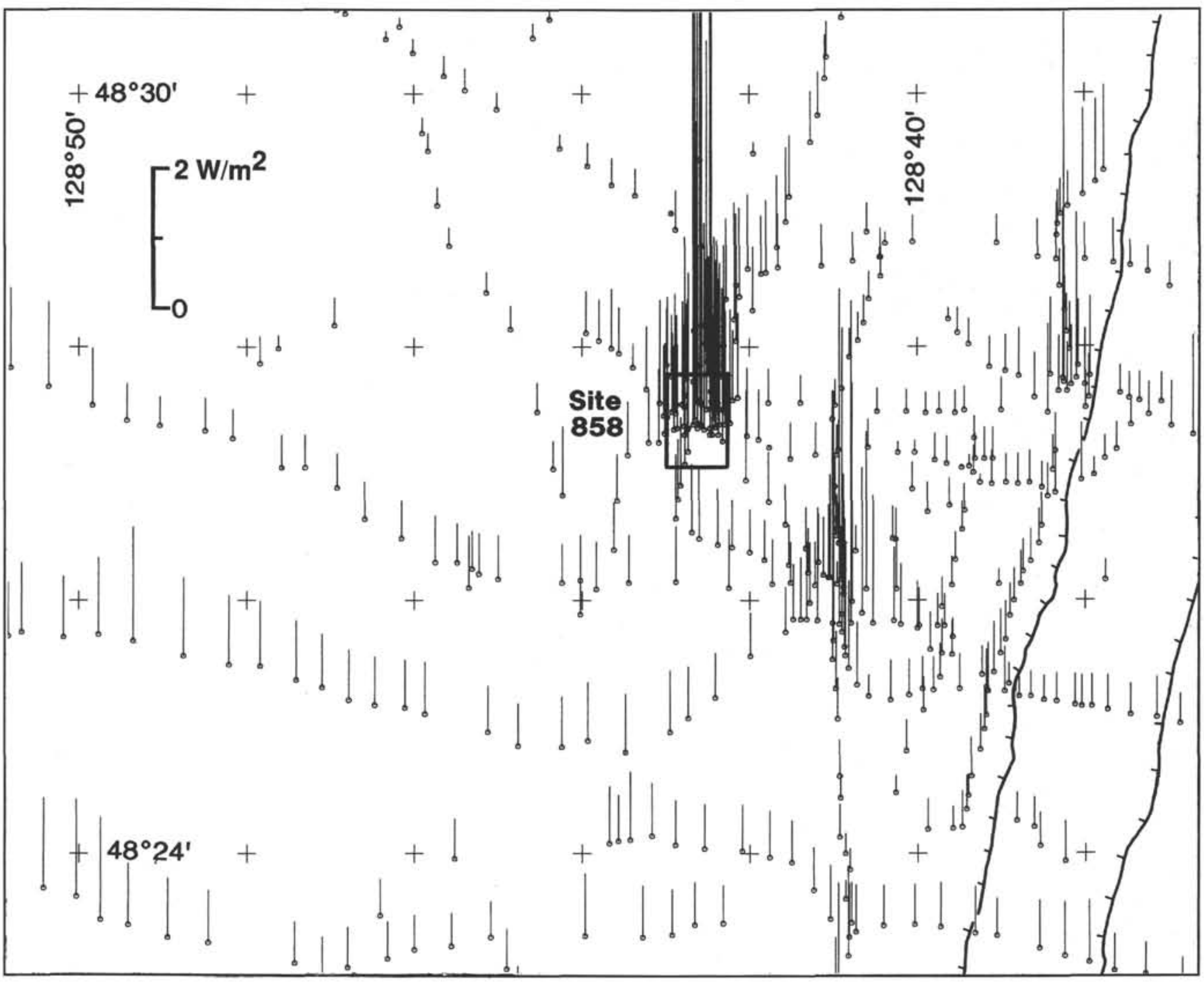

Figure 7. Regional heat flow variations in the same area shown in Figures 2 and 3. The area of Site 858 (shown in Fig. 8) is outlined.

shroud that had been attached to the top of the pressure case by set screws. A second run then was made with a "Larson" slip-type core catcher that had been modified for the reduced-diameter (2.007 in.) catch size. The tool was recovered, in good condition, completely inside the inner barrel (with 19-1/2 hr of temperature data contained in memory).

The remainder of the fill was washed from the hole and another mud sweep was circulated at total depth before the drill string was pulled back to logging depth for the Schlumberger logging program.

The seismic stratigraphy combination was the first major log to be run. Cablehead problems resulted in a delay of about 5 hr, but a good log eventually was recorded from about 12 m off total depth with an assist from the SES. A formation microscanner (FMS) log followed and reached essentially the same depth without SES circulation. The hole remained relatively cool and logging results were good. The geochemical tool was the third one deployed. The tool had been rigged through the SES and run to 800 m when it failed to function and had to be recovered. Because of the log time anticipated for either repair or replacement of the tool and a repeat calibration, the logging program was terminated.

When the SES and logging equipment had been rigged down, the pipe was run back to total depth. A 35-bbl cement plug was spotted from about 294 to 220 mbsf. The pipe was then raised to 2527 m and another 35-bbl plug was set at about 101–45 mbsf before the pipe was pulled out of the hole and flushed of cement.

Hole 858G

Upon completion of the pipe trip, the second reentry cone to be emplaced on Leg 139 was moved into place in the moonpool. The short (two-joint) conductor casing string and special BHA were made up and latched into the cone. The remainder of the drill string was assembled to lower the casing shoe to the seafloor, and Hole 858G was spudded at 0600 hr on 21 August on a 10-m offset south of Hole 858F.

Though the jetting test had found 26 m of soft sediment below the measured seafloor depth of 2426 m, jetting progress stopped with the mud plate of the cone 2.5 m shallower. The cone/casing assembly was released with the RST and drilling of the 14-3/4-in. hole began.

During a connection at 132 mbsf, the bit became completely plugged and all ability to circulate was lost. When repeated efforts to clear the bit were unsuccessful, the bit was pulled into the conductor casing in preparation for a round trip. A final attempt to circulate was made before the seafloor was cleared, and one jet was cleared.

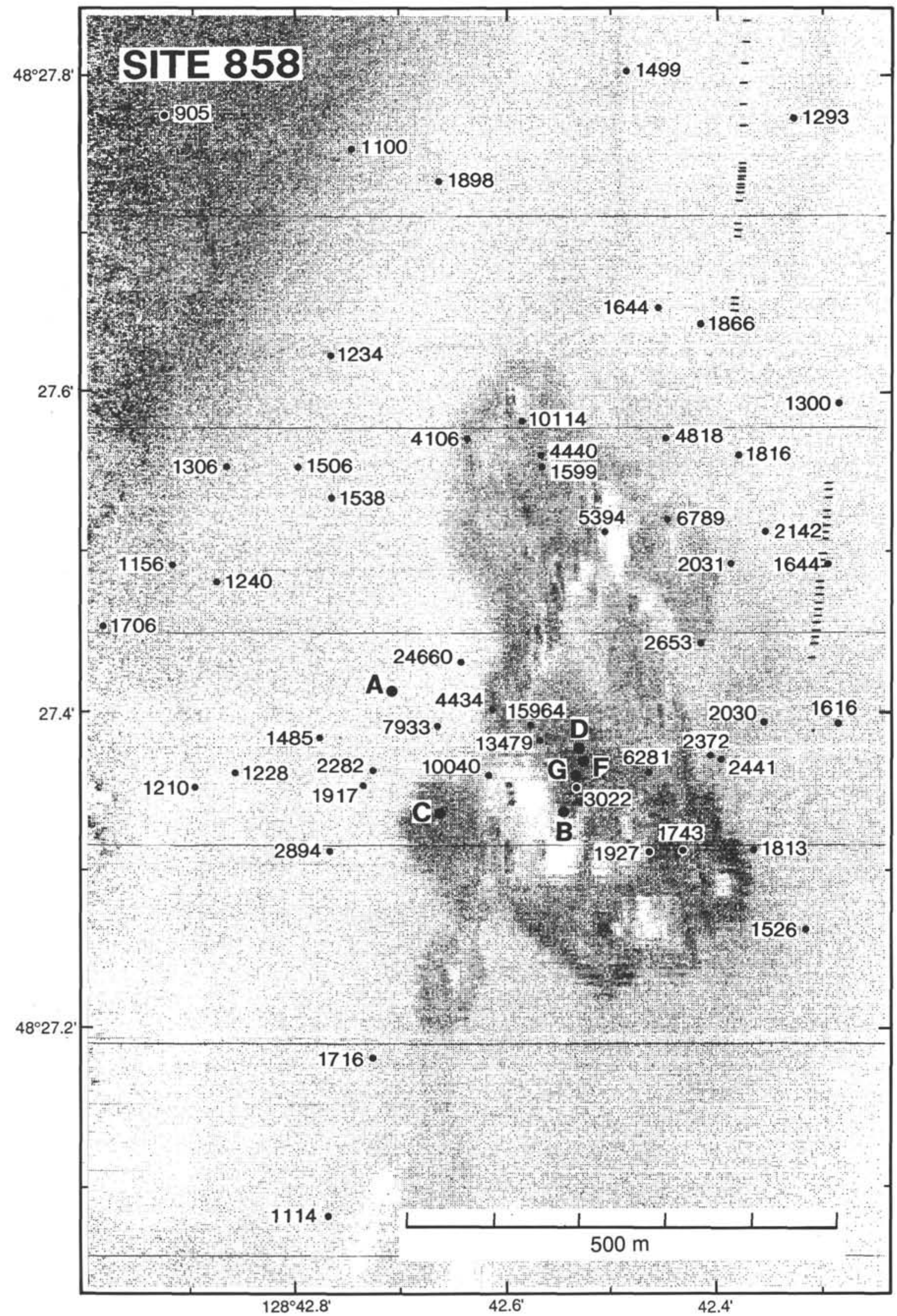

Figure 8. Seafloor heat flow measured within and in the immediate vicinity of the vent field where the holes of Site 858 are located. The uncertainty of most measurement locations is of the order of ±100 m.

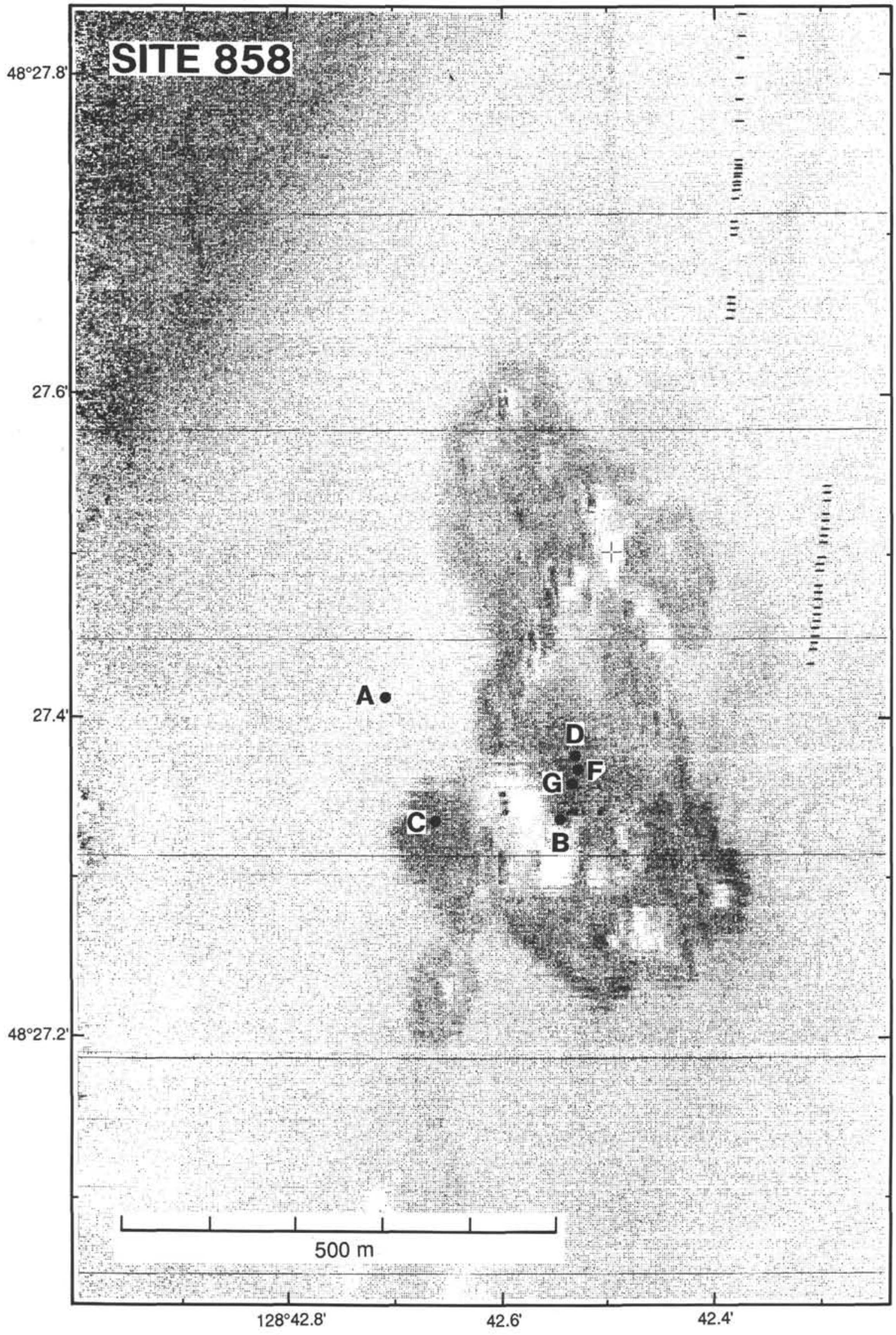

Figure 9. SeaMARC I (30 kHz) side-scan acoustic image of the vent field where Site 858 is located (from Johnson et al., in press), with positions of individual holes shown.

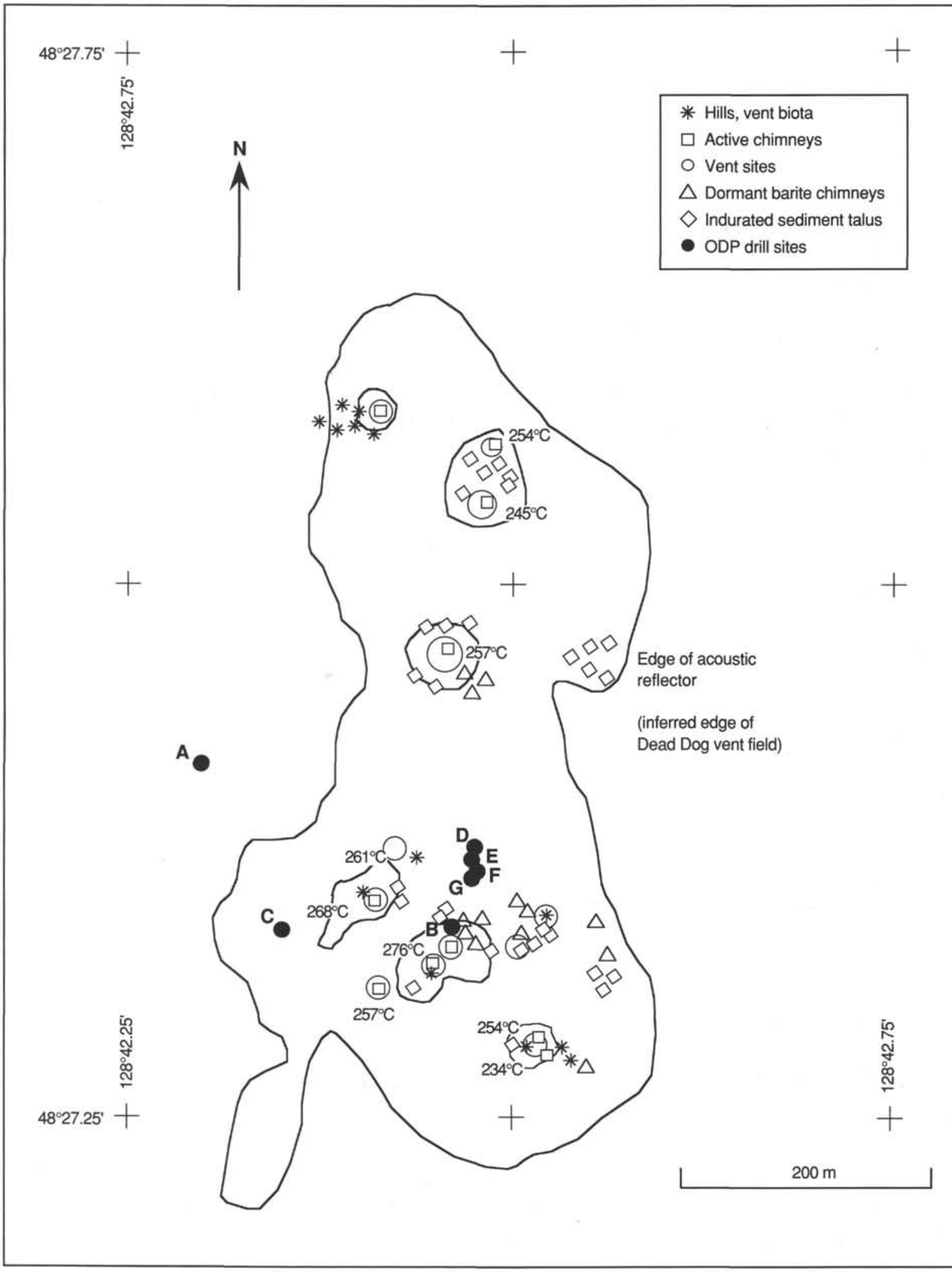

Figure 10. Geologic map of the Site 858 vent field, showing the location of known hydrothermal mounds and vents, and the temperatures of discharging water (J. Franklin, pers. comm., 1991).

Continued circulation cleared a second jet so that drilling could continue at acceptable flow rates. The hole then was flushed with mud as the bit was run back to total depth.

Drilling continued with frequent mud pills. The third and final jet nozzle cleared itself after drilling had resumed and circulating pressures returned to normal. The float valve in the bit sub continued to malfunction and to allow backflow on connections, but no further plugging occurred. (On recovery of the bit, the float valve was found to be held open by a piece of cement which apparently had broken loose from inside the standpipe plumbing.)

Hard drilling was encountered at the expected depth of 2684 m. Drilling of 14-3/4-in. hole was terminated at 2702 m to provide for setting surface casing approximately 11 m into hard rock and to leave about 7 m of "rathole." Because of the large hole diameter measured by caliper logs in Hole 858F and the earlier hole-cleaning problems in Hole 858G, a copious mud flush of 100 bbl was circulated through the hole and overdisplaced by more than 200 bbl of seawater in preparation for the casing string.

Following the pipe trip and disassembly of the BHA, the surface casing string of 21 joints of 11-3/4-in. casing was made up to the casing hanger and hung off in the moonpool. The cementing stinger was assembled and attached to the casing string by means of the casing running tool. The entire assembly was lowered on the drill string and reached reentry depth at 1815 hr on 22 August after a delay of about 1-1/2 hr to replace a malfunctioning reentry TV camera. While the casing operation and trip were in progress, good weather conditions were exploited to launch a new beacon, which was equipped with a strobe light for night recovery, and to retrieve the two existing unlighted beacons.

After a routine reentry, the casing shoe was lowered to 236 mbsf before the top drive was picked up to provide cooling circulation. Resistance was met by the casing string about 24 m short of the intended setting depth. The casing was "worked" with circulation for an additional 17 m through an apparent dogleg or series of ledges in the hole before it became immobilized both up and down. There was uncertainty as to whether the casing was stuck in the hole or had latched into the reentry cone and pipe depth. Because of the light weight of the cone and short conductor string, little pull could be exerted on the surface string to dislodge it without risk of lifting the cone/conductor. The VIT was deployed and the TV showed the running tool to be some distance above the cone and in approximate agreement with the pipe tally. Thus the driller was free to be "rougher" with the drill string, freeing the casing and eventually moving it downhole until the hanger latched into place.

The cement job was hampered by plugged shipping lines and difficulty in achieving a constant flow of dry cement to the mixer. After delays totaling about 2 hr, a good mix was attained and the slurry was mixed and displaced successfully. The cement plug was emplaced at 0330 hr on 23 August.

The drill string then was pulled out of the hole, the Site 858 beacon was switched to standby mode, and offsetting to Site 857 began. The cased and grouted Hole 858F was to be left thermally to reequilibrate.

Hole 858G (Return)

Plans called for a single bit run of a minimum of 100 m in Hole 858G before the final round of packer/logging/CORK work and departure for port. Because all experience of the leg indicated that bits and drill-string components could be kept below the maximum seal temperature of about 150°C by circulation in even the hottest holes, a sealed journal-bearing RBI C-4 bit was selected. A longer rotating life was projected for the journal bearing (so long as the seals were intact), and it was hoped that use of this bit would improve core recovery.

Following a routine reentry, the bit was lowered to only about 17 mbsf before the (resurrected) Sandia temperature logging tool was lowered on the coring line for a log of the undisturbed cased hole. This run began at 1800 hr on 3 September, 11.5 days after the last circulation in the hole. An obstruction in the casing stopped the tool at 162 mbsf. Upon recovery of the logging tool, the data were read out to show that the maximum temperature in the hole, 268°C, occurred at the level of the bit! The temperature declined with depth to about 105° at 60 mbsf before rising again to 250° at the deepest reading.

Because the bearing seals of the bit undoubtedly were destroyed, a reduced operating life was expected for the bit, and plans were changed to include two bit runs. Solid cement was encountered at 255 mbsf; the temperature tool had been stopped by a thin cement bridge. About 5-1/2 hr were required to drill out the cement, plug, and shoe 6 m of "rathole" and 1 m of new hole. The center bit was exchanged for a standard RCB core barrel, and coring commenced at 277 mbsf.

Unlike Site 857, all core recovered from the lower section in Holes 858G and 858H was igneous rock, primarily altered extrusive basalt. The rock was highly fractured, contributing to reasonably good ROP (4–15 m/hr), but poor core recovery (4.4% overall). Because projected coring time remaining in the leg was insufficient to wear out the second bit, the journal-bearing bit was pulled from 354 mbsf after just 14-1/2 rotating hr.

The round trip and reentry were routine. As expected, the bit-bearing seals were gone and one bearing was somewhat loose, so the trip was not premature. Only 1 m of fill was found at total depth. Coring then continued with a roller-bearing bit. The formation, ROP, and recovery were virtually unchanged from the first bit run. Some torquing of the drill string was noted after a drilling break at 399 mbsf, and the next connection found some fill or ledges. All indications cleared up after a mud pill on the ensuing core. Coring and drilling operations were terminated for the hole and the leg at 432.6 mbsf due to expiring operating time. The hole was swept with mud in preparation for the trip for the packer BHA.

Information on hole temperature was needed to finalize planning for the remainder of the leg, so a temperature log was run with the Sandia tool after the bit had been pulled to just below seafloor level. The temperature tool was stopped by an obstruction at 389 mbsf. The maximum temperature of only 76°C was recorded at that depth and there was no sign of the high-temperature zone recorded on the earlier log.

Because the obstruction was a few meters short of the open-hole depth needed for the planned thermistor string installation, a wiper trip was made back to total depth with the bit. A 15-m interval took 15,000–35,000 lb weight, but the resistance was cleared by circulating and working the pipe through the interval; it was not necessary to deploy the top drive. Another mud pill was circulated at total depth before the pipe was tripped.

The packer BHA was made up in the same configuration as was used in Hole 857D, but newer S-140 drill pipe replaced the S-135 that had been in service for the leg in an effort to reduce the threat of pipe rust to the packer operation. When the pipe reached reentry depth, a pig was pumped through it to remove rust scale. Following a routine reentry, the reentry/cleanout bit was run to 113 mbsf and the logging sheaves were rigged.

An induction/density/natural gamma log was then run; the tool again set down at 394 mbsf. A fairly good log was recorded from that depth up to the casing shoe, but a malfunction of the caliper arm prevented continuous coverage with the density log.

When the logging tool had been recovered, the drill string was repositioned slightly to place the center of the packer at 107 mbsf, a level found on previous temperature logs to be relatively cool. The go-devil was pumped into place for packer permeability tests. Initial pulse tests indicated fairly high permeability. Subsequent constant-rate injection tests gave high pressure readings at low circulating rates, suggesting low permeability values. When the go-devil and downhole pressure recorders were recovered, the downhole pressure readings were found to be too low in comparison with the surface readings, and rust was found in the go-devil passages.

While options were being considered for the remaining operating time, another Sandia temperature log was recorded. The tool reached 399 mbsf and recorded a maximum temperature of 158°C at that depth. An abrupt increase in gradient about 55 m below the casing shoe indicated downhole flow of cold water into the formation at that depth.

As the earlier packer-permeability results were highly suspect, the experiment was repeated after completion of the temperature log. The packer was set at the same point in the casing as before, and a "slug" test was followed by a series of constant-rate injection tests. The permeability indicated by the response of pressure to injection was much higher and injection rates of up to 400 gallons per minute (gpm) were used. Because high flow rates had been achieved, the go-devil was retrieved and replaced by the flowmeter and its special go-devil. A series of flowmeter tests then was conducted to determine the location of the permeable zones.

Upon successful completion of the flowmeter measurements, the drill string was tripped for the CORK assembly. Assembly and deployment proceeded smoothly; the installation took about 22 hr. The data logger was latched in at 0300 hr on 9 September, and the CORK was landed at 0417 hr. This provided slightly more than an hour of recording time to obtain a seafloor hydrostatic pressure reference before sealing into the formation.

After the submersible landing platform was dropped and inspected with the VIT and before the drill string was retrieved, a systematic TV/sonar survey of the area around Holes 858B–858G was completed, so that the exact position of the holes with respect to seafloor vents could be determined. The VIT, drill string, and beacon were then recovered, and the short transit to Victoria began.

LITHOSTRATIGRAPHY AND SEDIMENTOLOGY

Site 858 is situated adjacent to and over an active hydrothermal vent field. This location, the high temperatures present at relatively shallow depths ("Heat Flow" section, this chapter), and the associated difficulties with coring ("Operations" section, this chapter) resulted in widely varying depths of penetration and percentages of strata recovered among the six holes that comprise this site. Three of these holes (858A, 858B, and 858C) are arranged in a generally northwest-southeast transect across the site: Hole 858A is located approximately 100 m west of the active vent area, Hole 858C is located just within the western margin of the vent area, and Hole 858B is located only a few meters from a vent. Three additional holes (858D, 858E, and 858F) are located directly in an active vent area near the center of the field. Depths of penetration, type of coring, and average recovery for each of these six holes are shown in the site data given at the beginning of this chapter. These data are important to the lithostratigraphic evaluation of this site because unusual brecciated textures (of equivocal origins) are present in some of the APC cores and because turbiditic strata of varying degrees of induration and brittleness are interbedded throughout the stratigraphic sequence. In general, sand/sandstone and silt/siltstone intervals appear to be preferentially lost (broken up or washed away) during coring. Coring mechanics (drill-floor difficulties), recovery percentage, and type of strata recovered must therefore be considered in any attempt to attribute unusual textures, changes in turbidite thickness, or changes in number of turbidites present to any "real" sedimentological or geological phenomenon.

The most complete sedimentary sequences at Site 858 are found in Holes 858A (339.1 m drilled) and 858F (296.9 m drilled). Strata in Hole 858A constitute a "background" record of hemipelagic and turbiditic sedimentation. These strata are only slightly affected by the nearby hydrothermal activity. The hemipelagic and turbiditic strata in Hole 858F are hydrothermally altered from 27.80 mbsf to the base of the sedimentary section (249.7 mbsf). Hole 858D strata are hydrothermally altered throughout. Holes 858B and 858C contain semimassive sulfide and sulfide-rich brecciated strata at relatively shallow depths, presumably as a result of their proximity to active vents. Hole 858E was aborted after only one core; therefore it provides no useful stratigraphic data.

Strata recovered at Site 858 are divided into five lithostratigraphic units—four sedimentary units and one igneous unit (Table 3 and Fig. 11). Division of the sedimentary units is based on the percentage of turbidites present, on the degree of alteration, and on sulfide content. Lithologic Unit I consists of fine-grained hemipelagic sediments with only minor fine-grained turbidites, lithologic Unit II consists of interbedded hemipelagic and turbiditic strata, lithologic Unit III consist of oxidized metalliferous sediments, and lithologic Unit IV consists of semimassive sulfide. Lithologic Unit II is further divided into four subunits based on brecciation and degree of hydrothermal alteration. Lithologic Unit V consists of mafic igneous rocks. Each of these units is discussed in detail below.

Lithologic Unit I

Sections 139-858A-1H-1, 0 cm, to -3H-CC, 30 cm (0–21.40 mbsf); Sections 139-858B-1H-2, 47 cm, to -2H-3, 21 cm (1.97–10.41 mbsf), and Sections 139-858B-2H-4, 100 cm, to -5H-1, 141 cm (12.70–25.31 mbsf); Sections 139-858C-1H-1, 0 cm, to -3H-2, 35 cm (0–14.85 mbsf); Sections 139-858D-1H-1, 0 cm, to -2H-6, 150 cm (0–18.30 mbsf); Holocene–Pleistocene.

Lithologic Unit I is massive, greenish gray (5GY 5/1) to dark greenish gray (5GY 4/1) silty clay of Holocene to late Pleistocene age that ranges in thickness from 21.40 m in Hole 858A to 13.44 m in Hole 858B. Minor silty laminations (<1 cm thick) are present locally, but generally occur in frequencies of less than one lamination per meter. An exception to this is in Sections 139-858B-1H-4 and -1H-5, where 15 laminations are present within only 2.75 m of strata. These laminations are probably distal deposits of turbidity currents. They are composed of quartz, feldspar, mica, clay, and chlorite with trace amounts of epidote, calcite, hornblende, and pyrite. Pyrite is present as fine-grained disseminated crystals in Holes 858B and 858D.

Lithologic Unit I contains up to 25% carbonate. Small (<2 cm long) carbonate nodules are present in all holes in which this unit was encountered, and carbonate-filled burrows are common in Holes 858A and 858B. Dolomite is present as disseminated, euhedral, zoned crystals in Cores 139-858B-1H and -858D-2H. Many of the dolomite crystals seem to have replaced calcite; a few have central cores of calcite or protodolomite. Dolomite was also identified in X-ray diffraction (XRD) analysis in intervals 139-858C-2H-3, 25–27 cm (6.8 mbsf), and 139-858D-2H-1, 49–51 cm (9.8 mbsf). Sand-size barite crystals were found in washed and sieved paleontological samples from Sections 139-858B-1H-CC (7.0 mbsf) and -5H-CC (30.2 mbsf). XRD analysis indicates the presence of chlorite in all cores sampled in this subunit (see "Sediment Geochemistry and Alteration" section, this chapter) and saponite in Core 139-858A-1H.

A few pockets of pale yellow (2.5Y 8/4) distinctly layered, thick-walled shell fragments (mollusks?) are present in Sections 139-858A-2H-6 and -2H-7 (about 11 mbsf). These may be shells of the vent clam *Galyptogena.* Foraminifers and nannofossils are common biogenic components in this unit in most holes. Samples prepared for paleontological analysis from Holes 858B, 858C, and 858D, however, were barren of all microfossils below 13 mbsf and barren of calcareous nannofossils below 9.3 mbsf. Above 13 mbsf, all of the calcareous microfossils present are strongly recrystallized. Radiolarians are present in paleontological samples from Sections 139-858A-1H-CC, -858A-2H-CC, -858C-1H-1, and -858D-1H-1. At greater depths, biogenic silica is absent. Bioturbation is also common. *Zoophycus* burrows are present in discrete horizons in intervals 139-858C-2H-2, 33–74 cm, 139-858C-2H-4, 100–125 cm, and 139-858D-1H-5, 70–115 cm. The upper *Zoophycus* horizon in Hole 858C and the horizon

Table 3. Lithostratigraphic units for Site 858.

Unit	Description (age)	Interval	Top (mbsf)	Bottom (mbsf)	Thickness (m)
I	Fine-grained hemipelagic sediments with minor fine-grained turbidites (Holocene–late Pleistocene)	858A-1H-1, 0 cm, to 3H-CC, 30 cm	0.00	21.40	21.40
		858B-1H-2, 47 cm, to 2H-3, 21 cm	1.97	10.41	8.44
		and -2H-4, 100 cm, to 5H-1, 141 cm	12.70	25.31	4.00
		858C-1H-1, 0 cm, to 3H-2, 35 cm	0.00	14.85	14.85
		858D-1H-1, 0 cm, to 2H-6, 150 cm	0.00	18.30	18.30
IIA	Interbedded hemipelagic and turbiditic sediments (Pleistocene)	858A-4H-1, 0 cm, to 5H-5, 150 cm	21.40	38.40	17.00
		858D-2H-7, 0 cm, to 5H-1, 50 cm	18.30	28.80	10.50
		858F-1W-1, 0 cm, to 2R-CC, 5 cm	0.00	27.90	27.90
IIB	Brecciated, anhydrite- and carbonate-rich, hemipelagic and turbiditic sediments with local sulfide-rich zones (Pleistocene-Pleistocene?)	858B-5H-1, 141 cm, to 6H-1, 33 cm	25.31	31.83	15.13
		858C-3H-2, 35 cm, to 10X-CC, 41 cm	14.85	49.91	35.06
IIC	Moderately to well-indurated, interbedded hemipelagic and turbiditic strata (Pleistocene)	858A-5H-6, 0 cm, to 36X-CC, 8 cm	38.40	311.28	272.78
		858C-11X-1, 0 cm, to 14X-CC, 52 cm	49.91	84.67	37.76
IID	Silicified/hydrothermally altered, interbedded hemipelagic and turbiditic strata	858A-37X-CC, 0 cm, to 39X-CC, 17 cm	315.20	332.57	17.37
		858B-6H-1, 33 cm, to 9X-CC, 23 cm	31.83	35.33	3.50
		858D-6X-1, 0 cm, to 7X-CC, 25 cm	28.80	37.45	8.65
		858F-2R-CC, 5 cm, to 25R-1, 81 cm	27.80	249.71	221.91
III	Oxidized, metalliferous sediments (Holocene–late Pleistocene)	858B-1H-1, 0 cm, to 1H-2, 47 cm	0.00	1.97	1.97
IV	Semimassive sulfides	858B-2H-3, 21 cm, to 2H-4, 100 cm	10.41	12.70	2.31
V	Mafic igneous rocks (?)	858F-25R-1, 81 cm, to 29R-1, 124 cm	249.71	288.44	38.73

in Hole 858D may be correlative with the "*Zoophycus* marker bed" in interval 139-857A-1H-4, 36–75 cm (see "Lithostratigraphy and Sedimentology" section, "Site 857" chapter, this volume). Each of these horizons is about 40 cm thick and has a distinct maroonish gray (5Y 5/1) color. Furthermore, within a reasonable margin of error, they all occur at about the same depth. The top of the *Zoophycus* horizon in Hole 857A is at 6.49 mbsf, the top of the horizon in Hole 858C is at 5.33 mbsf, and the top of the horizon in Hole 858D is at 6.70 mbsf. On the basis of biostratigraphic data (see "Biostratigraphy" section, this chapter), these horizons are all late Pleistocene in age.

Lithologic Unit I is interpreted to be largely a hemipelagic sequence. A minor turbidite component is recorded by the silty intervals and by the occurrence of out-of-place (redeposited) neritic and upper bathyal fauna (see "Biostratigraphy" section, this chapter).

Lithologic Unit II

Lithologic Unit II is characterized by alternating hemipelagic and turbiditic sediments and is generally correlative to lithologic Unit II at all previous Leg 139 sites. At Site 858, lithologic Unit II is divided into four subunits on the basis of degree of induration, degree of hydrothermal alteration, and presence or absence of brecciation. Subunit IIA is nonaltered to weakly altered; Subunit IIC is moderately to well-indurated and altered; and Subunit IID is completely silicified, commonly fractured, and contains abundant authigenic silicate and sulfide minerals. These three subunits are lithologically similar to Subunits IIA, IIC, and IID at Site 856. A fourth subunit, Subunit IIB, is a brecciated, anhydrite- and carbonate-rich sequence that contains semimassive sulfide. Subunit IIB is in a stratigraphic position similar to that of the slumped(?) Subunit IIB at Site 856—below nonindurated turbiditic and hemipelagic sediments and above moderately to well-indurated turbiditic and hemipelagic sediments. Subunit IIB at Site 856 also contains sulfides. Even so, no direct correlation between the two subunits is implied. Original deposition of the interbedded turbidites and hemipelagic sediments comprising both units was similar, but the post-depositional events leading to their present-day textures were undoubtedly controlled by local phenomenon.

Subunit IIA

Sections 139-858A-4H-1, 0 cm, to -5H-5, 150 cm (21.40–38.40 mbsf); Sections 139-858D-2H-7, 0 cm, to -5H-1, 50 cm (18.30–28.80 mbsf); Sections 139-858F-1W-1, 0 cm, to -2R-CC, 5 cm (0–27.90 mbsf); Pleistocene.

Sediments from Subunit IIA are characterized by interbedded, carbonate-rich, gray (2.5Y 5/0) to dark gray (2.5Y 4/0 and N 5/) silty clay and dark gray (2.5Y 4/0) to dark greenish gray (5GY 4/1, 5/1) quartz-plagioclase silt, silty sand, and fine- to medium-grained sand. Quartz and plagioclase typically make up 90% of the grains identified in smear slides from this subunit (Section 4 of this volume). Chlorite is also present (up to 5%), as are trace amounts of mica, hematite, pyrite, hornblende, zircon, and zoisite. This subunit is similar to Subunit IIA at Sites 856 and 857.

The subunit commonly comprises stacked Tb-e or Tc-e turbiditic sequences with sharp basal contacts overlain by massive- to parallel-laminated fine sand that grades upward to hemipelagic silty clay. Bioturbation is locally pervasive. A zone of *Zoophycus* burrows is present in interval 139-858D-4H-6, 0–58 cm (26.5 mbsf), but most bioturbation in this subunit is preserved as a ubiquitous mottled texture that mixes the silt and silty clay intervals and destroys most of the primary textures and structures. Commonly, only the basal few centimeters of the coarsest portion of the turbiditic sequences show no direct evidence of burrowing.

An average of about three turbiditic sequences per meter of recovered core is present in this subunit. There is no systematic variation in the number of turbidite sequences with depth in these holes. The sand/mud ratio, however, typically becomes higher downcore. In Hole 858A, for example, the sand/mud ratio increases from about 10% at the top of the subunit to about 50% at the base. Also, amalgamated sand intervals are common near the base of the subunit but are rare near the top. These sand intervals commonly display

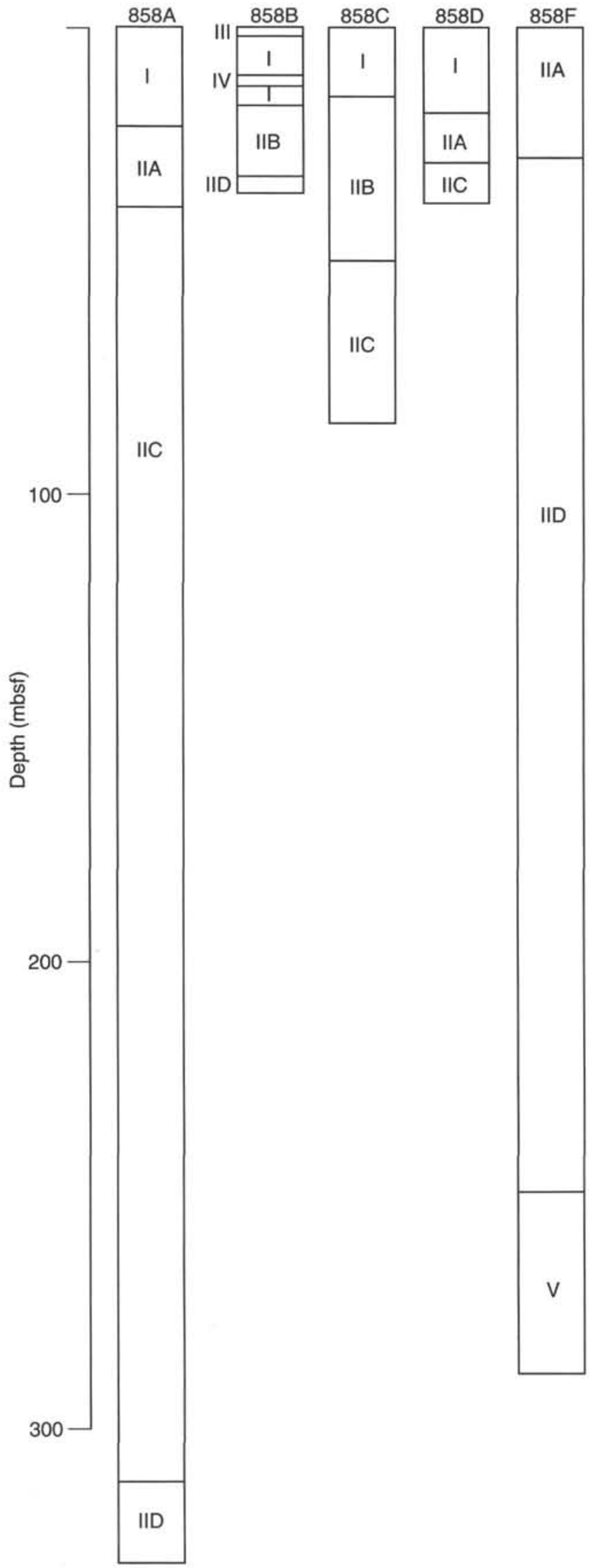

Figure 11. Hole-to-hole correlation of lithostratigraphic units at Site 858.

parallel and cross laminations and are generally nonburrowed. The coarse-grained (sand and silt) portions of individual turbidites range from 2 to 22 cm thick.

Biogenic components are present in the fine-grained intervals throughout Subunit IIA. Both foraminifers and nannofossils are present in trace amounts in smear slides examined from this subunit. All paleontological samples from holes other than Hole 858A, however, were completely barren in this and subsequent subunits. Reasons for the discrepancy between smear slide examination and paleontological examination are unclear.

Carbonate nodules and carbonate-filled burrows are common throughout this subunit and the entire subunit in generally carbonate-rich in many of the silty clay intervals. Carbonate nodules range in length from 5 mm to 3 cm and are most common in the fine-grained portions of the sequence. Carbonate-filled burrows occur as both straight, unbranched types and multiple-branch types. They are typically 3–5 cm long. In Hole 858D, Subunit IIA is also rich in anhydrite. The shallowest occurrence of anhydrite in Hole 858D is in Section 139-858D-4H-3 (22 mbsf). Anhydrite occurs as coarsely crystalline nodules, which may locally exhibit a radial, fibrous texture (Fig. 12). Anhydrite is also present in this subunit as bedding-parallel veins (for example, in Section 139-858D-4H-4, 24 mbsf). Gypsum was identified by XRD analysis in Section 139-858C-10X-CC (50 mbsf) and anhydrite was identified by XRD analysis in Sections 139-858D-4H-3 and -4H-4 (about 22 to 24 mbsf). XRD analysis also revealed the presence of calcite in Sections 139-858A-4H-1, -4H-2, and -5H-3 (about 21 to 33 mbsf); and Sections 139-858C-5H-4 and -5H-5 (about 29 to 30 mbsf). Chlorite was identified in Sections 139-858A-4H-1 through -5H-3 (about 21 to 33 mbsf); Sections 139-858C-3H-3 through -6H-3 (about 16 to 37 mbsf); and 139-858D-2H-7 through -4H-6 (about 19 to 27 mbsf).

Disseminated pyrite is present throughout Subunit IIA. In Hole 858D it is abundant and commonly occurs in coarse (up to 2 mm) euhedral crystals. Pyrite is also present as a minor component in some of the anhydrite veins. Sphalerite is present locally in Hole 858D. See the "Sulfide Petrology" section (this chapter) for further discussion of sulfide mineralogy and occurrence.

Subunit IIB

Sections 139-858B-5H-1, 141 cm, to -6H-1, 33 cm (25.31–31.83 mbsf); Sections 139-858C-3H-2, 35 cm, to -10X-CC, 41 cm (14.85–49.91 mbsf); Pleistocene–Pleistocene?

Subunit IIB consists of brecciated hemipelagic and turbiditic sediments. These sediments are typically anhydrite- and carbonate-

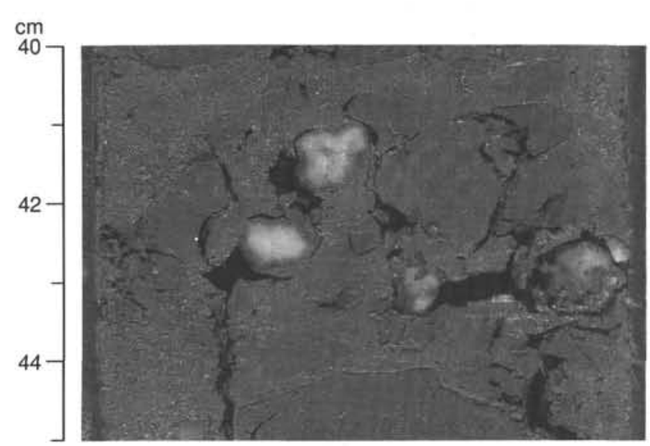

Figure 12. Radially fibrous anhydrite nodules in Subunit IIC at interval 139-858A-9X-5, 40–45 cm. Similar nodules are also present in Subunits IIA, IIC, and IID.

bearing and contain local concentrations of sulfide. The subunit displays several types of brecciation and the exact mechanism of brecciation is not clear. There is no agreement among the shipboard sedimentologists on the relative importance of core disturbance in these intervals. In Hole 858B operational problems during APC coring resulted in the buildup of extreme pressures in the core barrel. These mechanical problems may have induced some of the brecciation seen in the cores.

In Hole 858B the brecciated interval is present in six sections of disturbed Core 139-858B-5H. The interval is dominated by rounded mud-clast breccia (Fig. 13). This breccia is characterized by small (1–3 mm), well-rounded clasts of gray (N 5/) silty clay resting in a matrix of lighter gray (N 6/) silty clay and cemented with fine-grained talc(?) and anhydrite(?). Finely network-fractured intervals of silty clay are present in Section 139-858B-5H-3 (Fig. 14). Primary sedimentary and biogenic structures are well preserved between the fractured intervals.

Pyrite is abundant in both Holes 858B and 858C. It is present in the form of fine- to coarse-grained, euhedral crystals disseminated throughout the silty clay, as nodules, as bladed crystals with about 1:7 aspect ratios, and as a replacement after pyrrhotite. Locally, pyrite constitutes about 2% of the total sediment. Calcite is also common. It forms horizontal veins (1 to 3 mm wide) and is present as coarsely crystalline spar filling voids. Anhydrite(?) is present as disseminated crystals, veins, and layers. It appears in association with talc(?). XRD analysis reveals the presence of chlorite/smectite mixed-layer clays in Sections 139-858B-5H-3, -5H-4, and -5H-CC. No XRD analyses were done on samples from this subunit in Hole 858C.

The brecciated interval in Hole 858C is first encountered at 14.85 mbsf, where a limestone nodular breccia (Fig. 15) composed of rounded mud clasts (1–3 mm in diameter) within a calcite-cemented crust (interval 139-858C-3H-2, 35–135 cm, 17 mbsf) rests on a brecciated hemipelagic silty clay. Much of the primary stratification is preserved on the brecciated units below the carbonate-encrusted interval. Two types of breccia exist below this interval: rounded-mud-clast breccias (Fig. 13) and brecciated silt and sand contained within relatively undisturbed silty claystone (Fig. 16). In many cases, the undisturbed intervals exhibit pristine primary sedimentary and biogenic structures. All of the breccias appear to be "strata bound." The geometry of the breccia in both Holes 858B and 858C suggests that the fluids which were responsible for brecciation flowed laterally along bedding planes and through permeable zones. The mud clasts may have been rounded by these fluids moving through cohesive, clay-rich sediments. Brecciation of such sediment may have been caused by the buildup and subsequent catastrophic(?) release of fluid pressures high enough to break through these porous but relatively impermeable sediments. The presence of sulfide and the mineralization associated with veining suggests that the fluids must have been hot. The calcite-encrusted interval at the top of this subunit in Hole 858C may have been formed by post-brecciation cementation at or near the sediment-water interface. If this is the case, the age of the calcite crust and the stratigraphic position of this interval in the core could provide an age for the formation of the breccias.

Subunit IIC

Sections 139-858A-5H-6, 0 cm, to -36X-CC, 8 cm (38.40–311.28 mbsf); Sections 139-858C-11X-1, 0 cm, to -14X-CC, 52 cm (49.91–84.67 mbsf); Pleistocene.

Strata from Subunit IIC were recovered from Holes 858A and 858C, the two coolest holes at this site. The subunit is characterized by moderately to well-indurated, carbonate-bearing, gray (N 5/) to dark gray (N 4/) silty claystone and light gray (N 6/ to N 7/) to gray (N 5/) siltstone, silty sandstone, and medium- to fine-grained sandstone. They are distinguished from Subunit IIA solely on the basis of induration. This change in induration is a gradational one and is largely the result of carbonate cementation. The upper boundary of

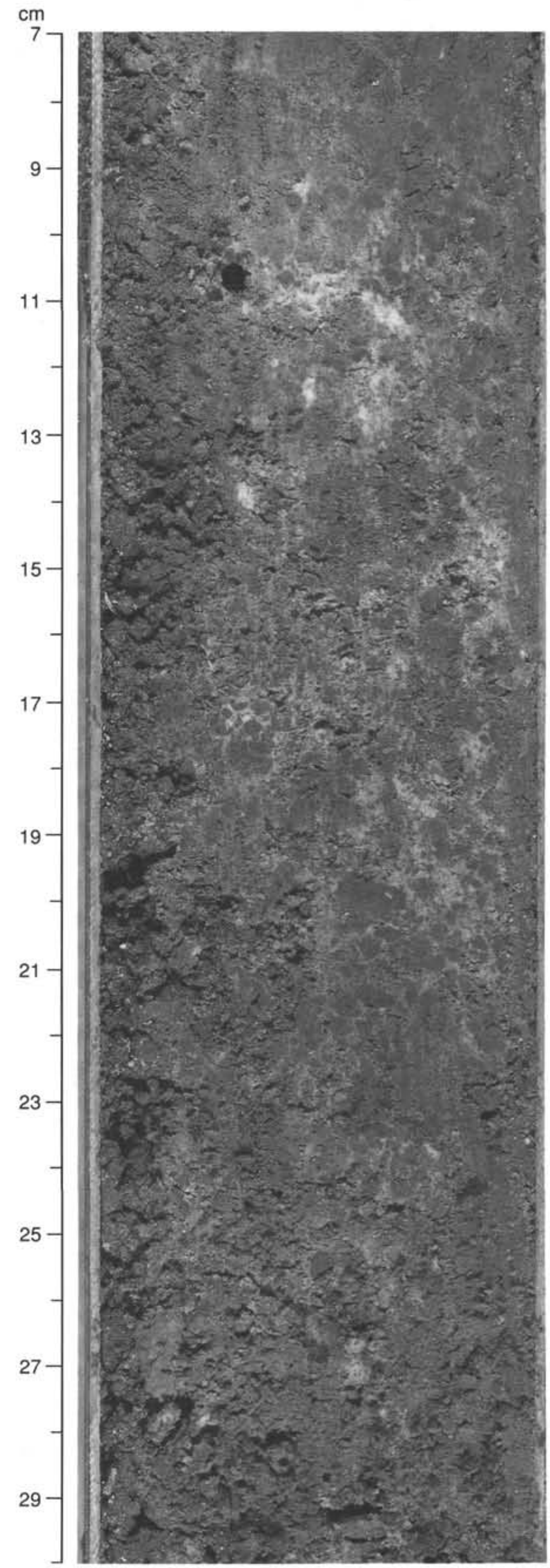

Figure 13. Rounded-mud-clast breccia in Subunit IIB at interval 139-858B-5H-2, 7–30 cm. Breccias of this type are characteristic of Subunit IIB in both Holes 858B and 858C.

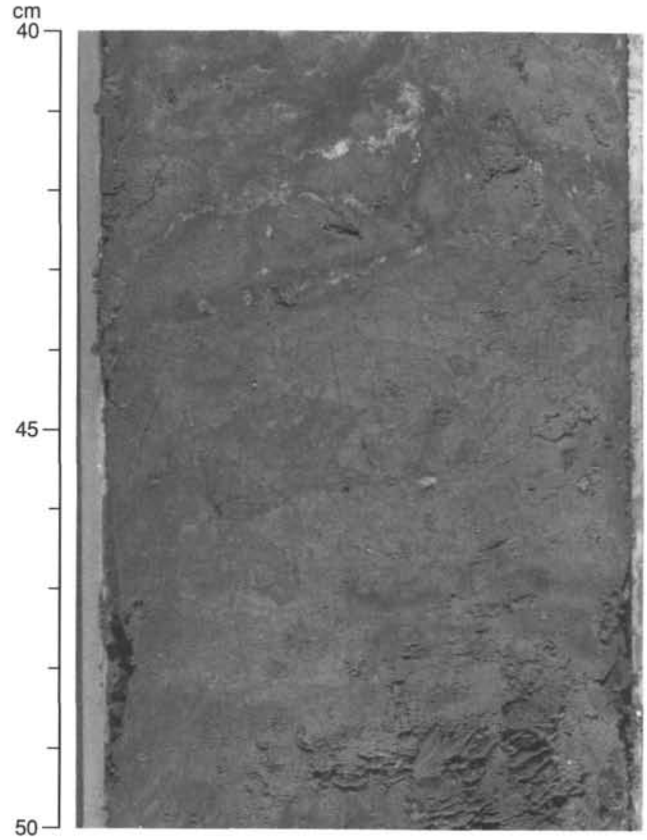

Figure 14. Fine-scale network-fractured silty clay with disturbed anhydrite(?) layers from interval 139-858B-5H-3, 40–50 cm. This type of fracturing is common in Subunit IIB of Holes 858B and 858C.

Subunit IIC is placed where carbonate-cemented strata become volumetrically more important than noncemented strata. This subunit is generally correlative with Subunit IIC at Site 856 and Subunit IIB at Site 857.

Quartz and plagioclase typically make up 70% to 90% of the grains identified in smear slides from this subunit (see Section 4 of this volume). Chlorite and anhydrite are also present throughout the subunit (up to 15% in individual samples). Calcite is present locally in abundances up to 20%. Biotite, zircon, epidote, hematite, amphibole, and pyrite are present in trace amounts throughout the subunit.

The strata of this subunit are interpreted as interbedded hemipelagic and turbiditic deposits. The turbiditic intervals commonly consist of stacked Ta-e and Tb-e sequences with sharp to scoured basal contacts overlain by massive to parallel-laminated (Fig. 17) and locally convolute-bedded (Fig. 18), medium-grained sandstone that grades upward into cross-laminated and cross-bedded (1–6 cm sets of cross strata; Fig. 19), fine- to medium-grained sandstone. These sandstone layers, in turn, grade upward into interbedded, planar-laminated, and locally convolute-bedded (Fig. 20) fine-grained sandstone and siltstone which, finally, grade into massive to bioturbated siltstone and silty claystone. Mud rip-up clasts are present locally (Sections 139-858A-17X-CC, 131 mbsf; and 139-858A-24X-1, 198 mbsf) at the bases of individual fining-upward sequences.

In Hole 858A, where this subunit is most dominant, the percentage of sandstone plus siltstone in the turbiditic sequences increases downward through the subunit, reaching a local maximum at Section 139-858A-20X-3 (163 mbsf; Table 4). Extrapolating beyond this depth is tenuous because silty claystones are recovered preferentially over more easily fractured sandstones during XCB coring and because recovery was poor below this interval. Thicknesses of individual turbidite sequences range from a few centimeters to 166 cm. Multiple scours within the coarse-grained portion of many of the

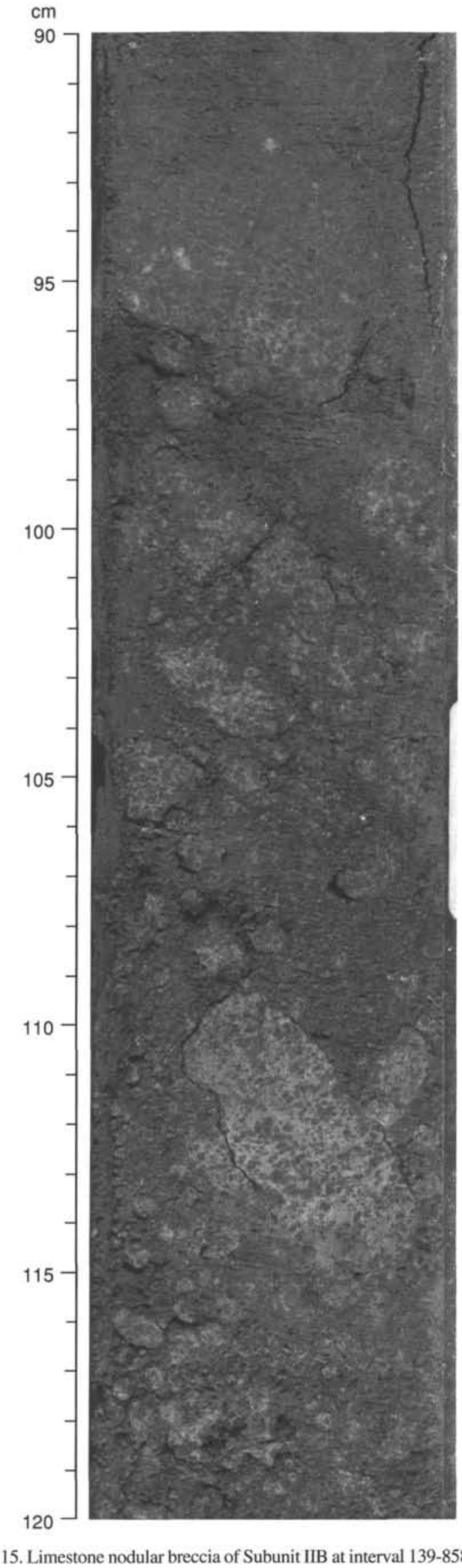

Figure 15. Limestone nodular breccia of Subunit IIB at interval 139-858C-3H-2, 90–120 cm. The well-rounded gray mud clasts in this breccia are cemented by crusty, white calcite.

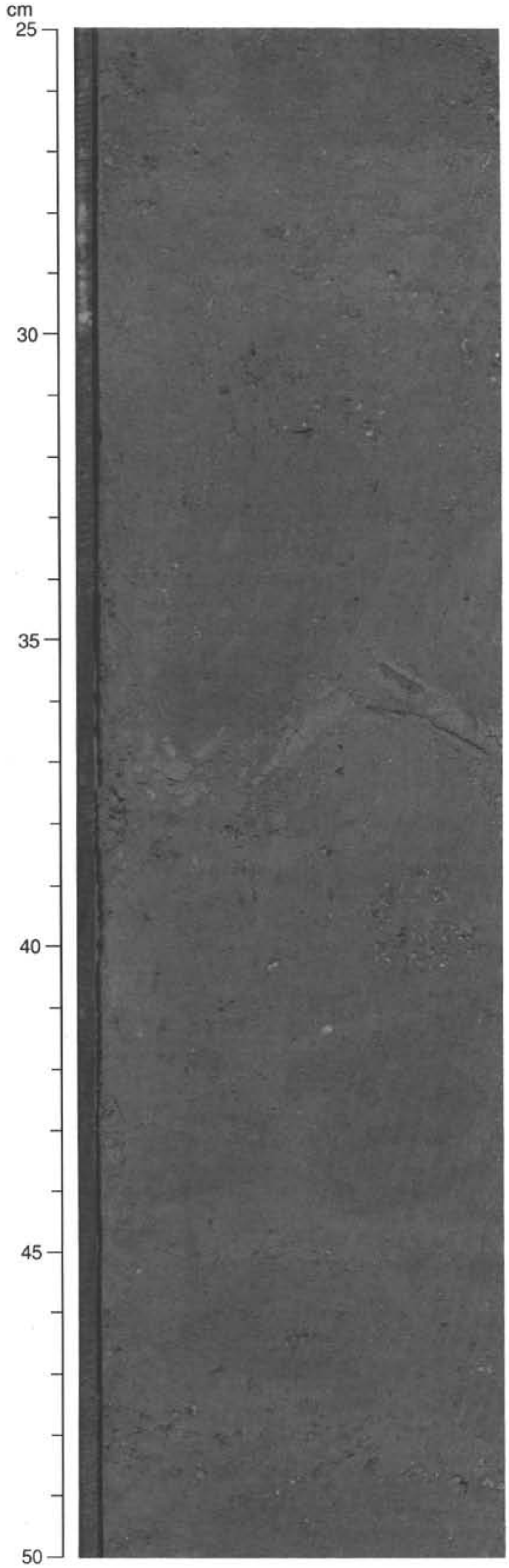

Figure 16. Brecciated, fine-grained sand and silt layers resting on relatively undisturbed (note preserved burrows and continous layers of pyrite) silty clay. This type of breccia is common in Subunit IIB in Hole 858C. Photo is from interval 139-858C-5H-3, 25–50 cm.

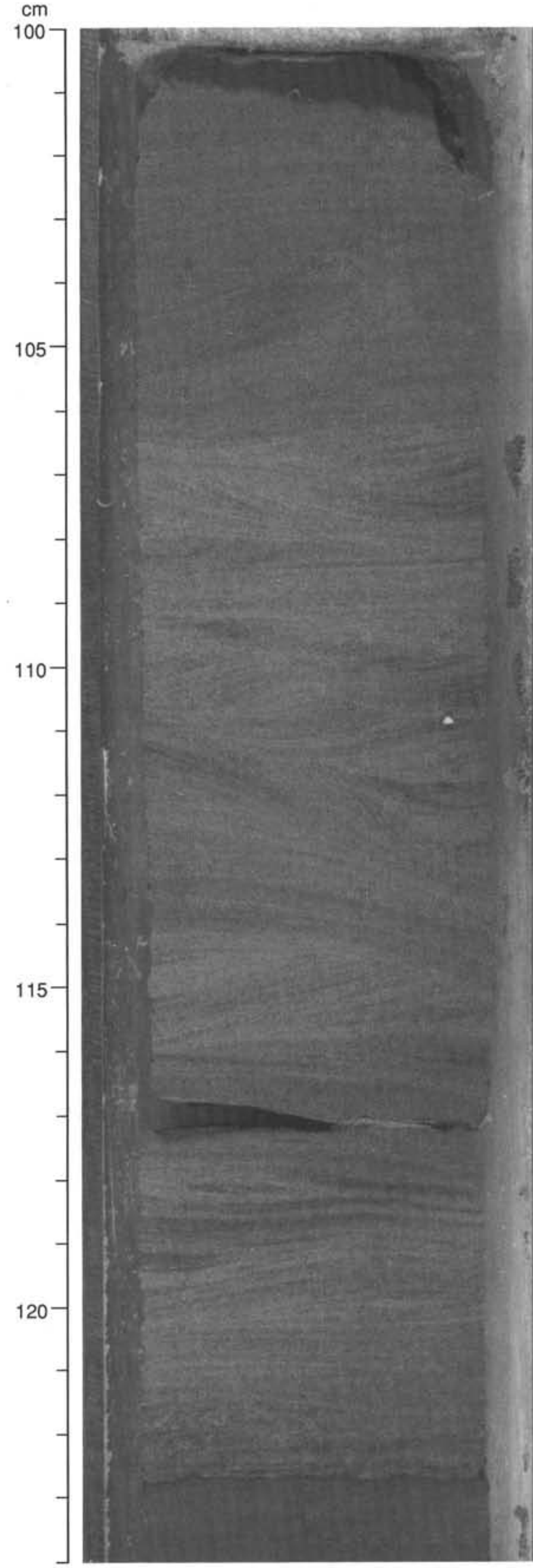

Figure 17. Scoured basal contact at base of Subunit IIC turbiditic sequence. Scour is overlain by massive medium-grained sandstone and then by parallel-laminated and rippled medium- to fine-grained sandstone. Photo is from interval 139-858A-21X-2, 100–124 cm.

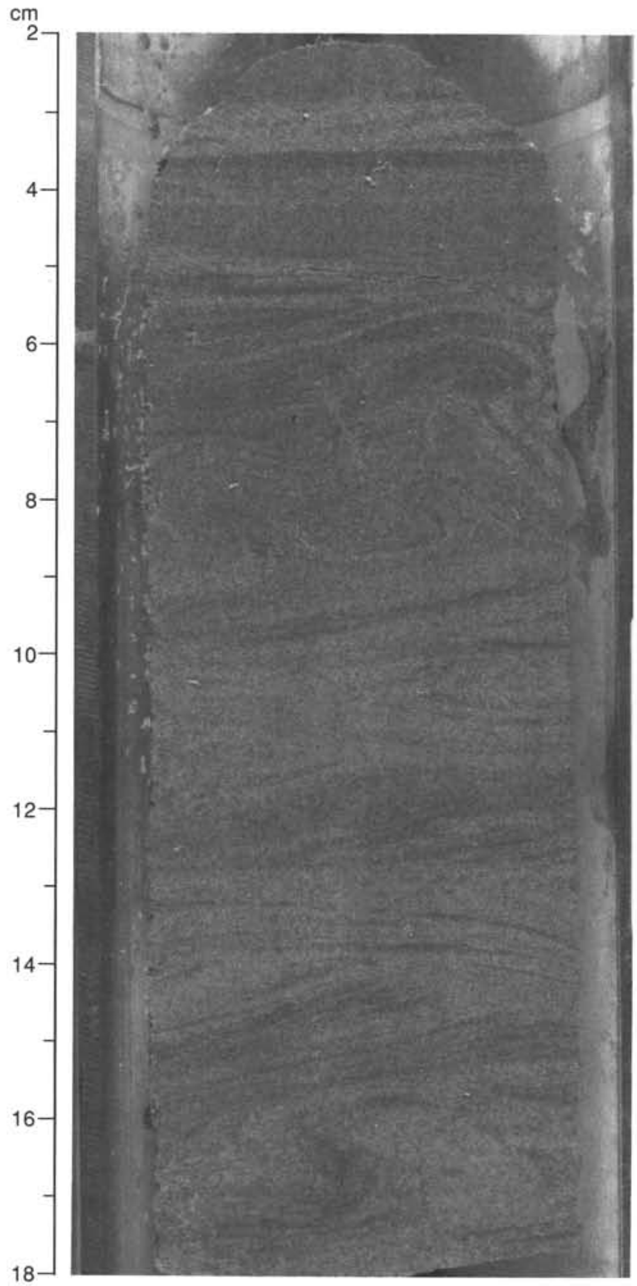

Figure 18. Convolute bedding in medium-grained sandstone from Subunit IIC. Photo is from interval 139-858-20X-1, 2–18 cm.

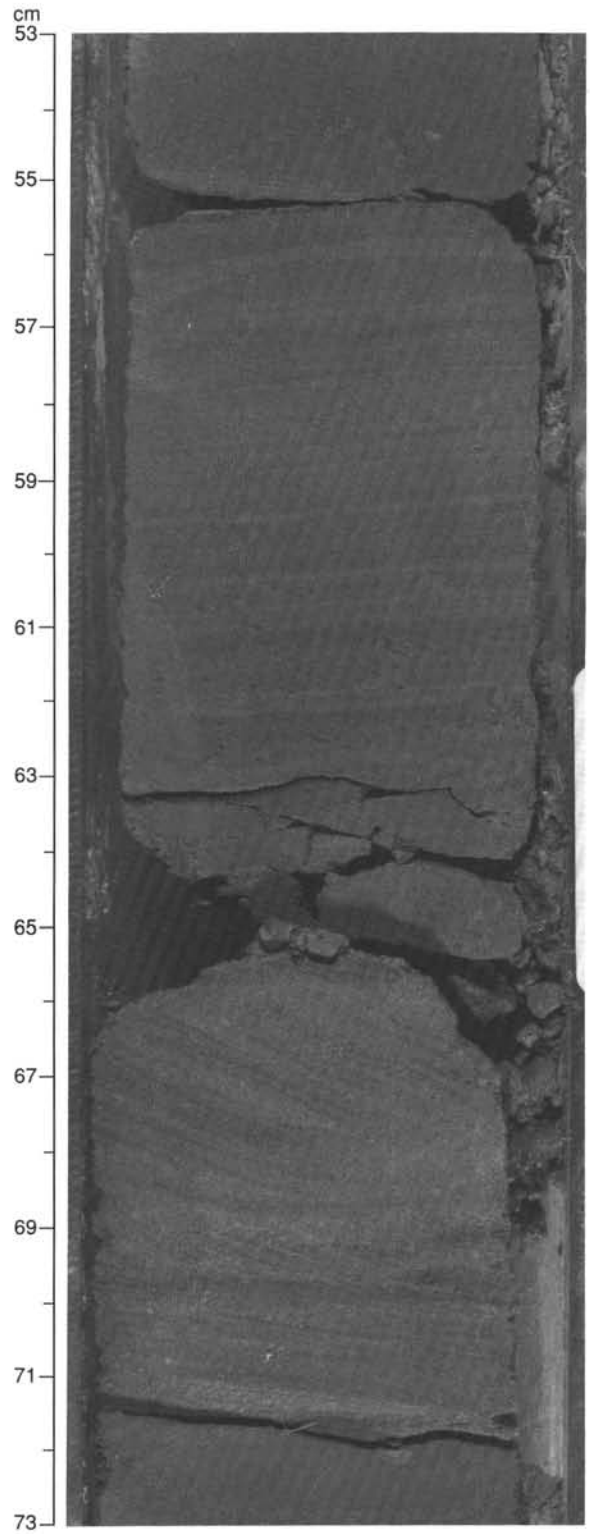

Figure 19. Large- and small-scale ripple laminations in turbiditic sequence from Subunit IIC. Photo is from interval 139-858A-20X-4, 53–73 cm.

turbidite sequences (especially in the interval between Cores 139-858A-18X and -24X; 140 to 199 mbsf), some with mud rip-up clasts resting on the scours (e.g., Section 139-858A-24X-1, 198 mbsf), suggest multiple pulses of the episodic turbidity currents and erosion of any hemipelagic sediment that may have been deposited. The thickest turbidite sequence recovered in this subunit is from Sections 139-858A-20X-2 and -20X-3 (162 mbsf); this sequence contains 33 cm of sandstone.

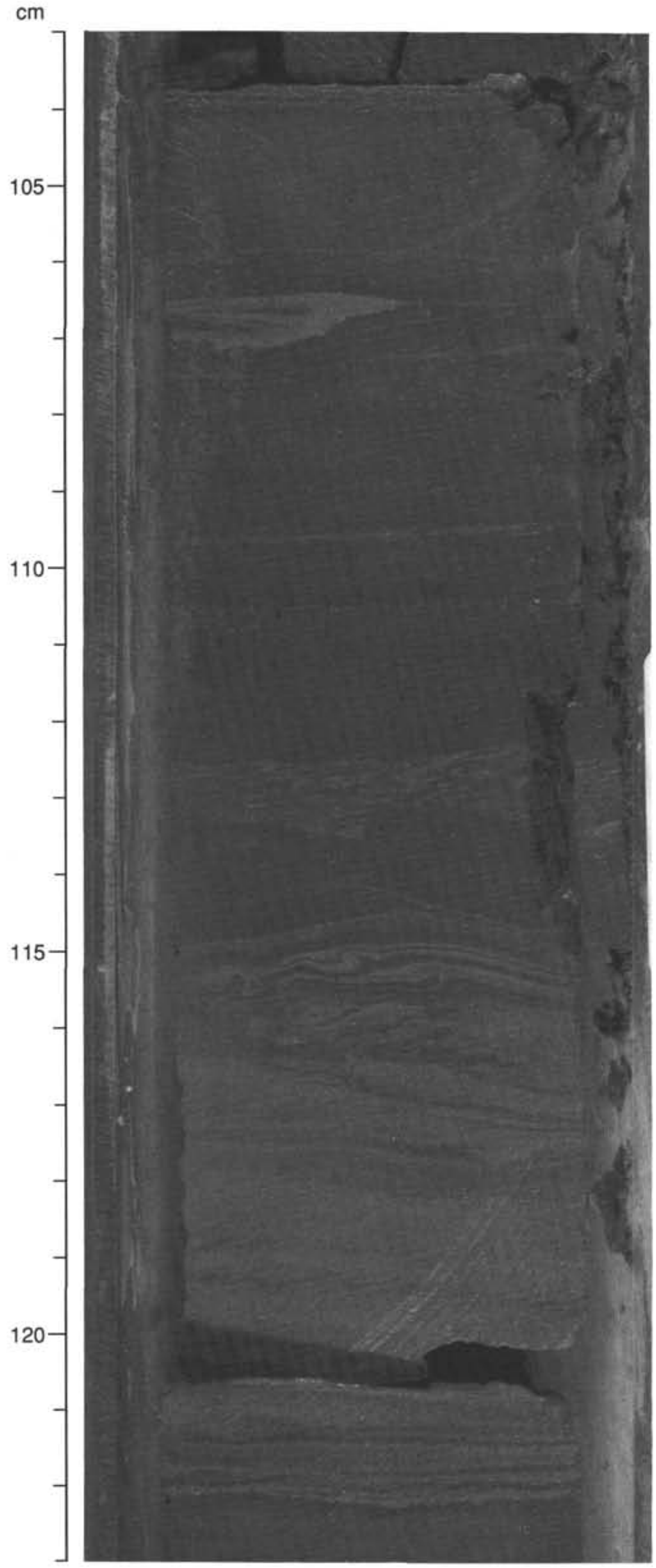

Figure 20. Convolutely bedded siltstone and silty claystone (in the interval from 112.5 to 116.5 cm) in a turbiditic sequence from Subunit IIC. Also note scour-base, small-scale cross laminations, isolated scour-and-fill structure, and anhydrite laths. Photo is from interval 139-858A-18X-2, 103–123 cm.

In this subunit, biogenic constituents are only present in Hole 858A, where both foraminifers and nannofossils are present to 110 mbsf. From Sections 139-858A-5H-6 to -8H-3 (38 to 61 mbsf), medium-sand-size foraminifers form local, discrete laminations which occur dispersed through the silty claystone portions of turbiditic and hemipelagic sequences and are rarely present as rims around carbonate nodules. These foraminifers are highly recrystallized and give the strata a distinct, bumpy surface texture. Bioturbation is prevalent throughout the fine-grained intervals of this subunit. An assemblage of trace fossils common to many turbiditic sequences is present here: *Zoophycus, Teichichnus, Planolites,* and *Chondrites*. *Zoophycus* is present rarely in the silty claystone intervals. *Teichichnus, Planolites,* and *Chondrites* commonly occur within the coarser turbidite intervals and they usually occur in a predictable order. Figure 21 shows such a typical succession of trace fossils in a turbidite in Subunit IIC.

Carbonate nodules, carbonate-filled burrows, and carbonate cements are common throughout this subunit. Carbonate nodules range from 3 mm to 8 cm long and are most common in the fine-

Table 4. Volume percentage of sand plus silt in the total thickness of recovered strata in lithologic Units I, IIA, IIC, and IID in Hole 858A.

Core	Sand content (%)
139-858A-	
1H	5
2H	4
3P	2
4H	19
5H	17
6H	pr
7H	27
8H	pr
9X	10
10P	pr
11X	(50)
12X	(30)
13X	(10)
14X	(20)
15X	42
16X	(30)
17X	(67)
18X	41
19X	(25)
20X	47
21X	34
22X	(10)
23X	27
24X	(14)
25X	(22)
26X	pr
27X	(37)
28X	pr
29X	(100)
30X	2
31X	(3)
32X	(20)
33X	nr
34X	pr
35X	(100)
36X	pr
37X	(100)
38X	(30)
39X	(20)

Note: Percentages are estimated from visual core examination and from core photographs. The abbreviations "pr" = poor recovery and "nr" = no recovery. Parentheses indicate that the core is less than 100 cm long.

grained portions of the subunit. Many of the nodules are zoned and some are overgrown by anhydrite(?). Anhydrite is also common in Subunit IIC. In Hole 858A, anhydrite occurs as lath-shaped crystals in silty claystone (from Sections 139-858A-15X-1 to -23X-CC, 111 to 189 mbsf; Fig. 22), as rims around carbonate nodules (intervals 139-858A-20X-2, 130 cm, 161.7 mbsf; and -20X-3, 135 cm, 163.3 mbsf; Fig. 23), as coarsely crystalline nodules (Fig. 24), as radially textured nodules (interval 139-858A-9X-5, 40–45 cm, 68.9 mbsf, Fig. 12), and as burrow-fill (interval 139-858C-21X-3, 49 cm, 171.9 mbsf). Anhydrite molds, similar to those present in Subunit IIC at Site 856, are present in this site in Sections 139-858A-31X-1 (266 mbsf), 139-858C-12X-1 (64 mbsf), and 139-858A-12X-2 (66 mbsf). Anhydrite laminations are present in Section 139-858C-12X-CC (68 mbsf). Washed and sieved paleontological samples from Sections 139-858A-15X-CC (112 mbsf), 139-858A-18X-CC (143 mbsf), 139-858A-23X-CC (189 mbsf), and 139-858C-14X-CC (84 mbsf) also contained anhydrite. Disseminated pyrite is present throughout the subunit. Pyrite nodules and burrow-fills are also common.

Subunit IID

Sections 139-858A-37X-CC, 0 cm, to -39X-CC, 17 cm (315.20–332.57 mbsf); Sections 139-858B-6H-1, 33 cm, to -9X-CC, 23 cm (31.83–35.33 mbsf); Sections 139-858D-6X-1, 0 cm, to -7X-CC, 25 cm (28.80–37.45 mbsf); Sections 139-858F-2R-CC, 5 cm, to -25R-1, 81 cm (27.80–249.71 mbsf), indeterminate age.

Subunit IID is characterized by silicified and hydrothermally altered, interbedded hemipelagic and turbiditic strata. Recovery was poor in this subunit and core disturbance is locally severe. As a result, only small, out-of-place pieces of broken rock were recovered in most holes and complete sedimentary sequences are not preserved. Smear slide analysis of the rock pieces (see Section 4 of this volume) reveals they are composed primarily of quartz (35%–45%) and feldspar (20%–40%). Mica (5%–15%), zeolite (5%–20%), chlorite (5%–20%), and pyrite (trace–5%) are also common constituents. Sphalerite, zoisite, and epidote are present locally in trace amounts.

Micropaleontological samples were barren throughout the entire subunit, presumably because the high temperatures at these sub-bottom depths promote calcite and silica dissolution. One small (fine-sand size), silicified microfossil was observed in an altered sandstone clast from Section 139-858F-9R-CC, but more precise identification was not possible.

Reconstruction of individual sedimentary sequences is difficult in this subunit, but examination of the pieces of drilling breccia reveals the presence of sedimentary structures similar to those preserved in other subunits of Unit II. Massive to planar- and cross-laminated gray (N 5/ to N 6/) siltstone and medium- to fine-grained sandstone, bioturbated and locally laminated gray (N 5/) to dark gray (N 4/) silty claystone, and locally preserved scour contacts and convolute bedding are all present in this subunit. The preserved pieces suggest that Bouma Ta-e and Tb-e sequences are present and that these strata are depositionally identical to strata of Subunit IIC.

The primary sediments of Subunit IID are characteristically well indurated. They become more silicified downcore and have undergone hydrothermal alteration that resulted in several types of mineralization. Quartz and zeolites are, by far, the most common alteration minerals present. They occur separately as replacement products within the sandstone and siltstone interbeds throughout the subunit and together as euhedral fracture- and vug-filling minerals (Cores 139-858A-37X to -39X, 315 to 332 mbsf; Cores 139-858B-8X to -9X, 33 to 35 mbsf; and Cores 139-858F-4R to -10R, 46 to 104 mbsf). Spots (0.1 mm) of gray silicification produce a distinctive alteration texture that is pervasive in the sandstone and siltstone intervals of Hole 858F from Core 139-858F-4R downward (below 46 mbsf).

Zeolites are present both as elongated, euhedral crystals with about a 10:1 aspect ratio and as equant, euhedral crystals. They occur as fracture fill alone and with quartz (as mentioned above), pyrite, and sphalerite (throughout Hole 858F and locally in Hole 858A, 858B, and 858D). Smear slide analysis suggests that zeolites are also present in the matrix of some sandstone intervals (e.g., Section 139-858F-8R-CC).

Anhydrite is present as euhedral crystals in vugs (Section 139-858B-9X-CC, 35.3 mbsf), as nodules (Sections 139-858F-13R-CC, 133.0 mbsf; and 139-858F-16R-CC, 161.9 mbsf), and as a fracture-lining mineral (Sections 139-858F-14R-CC, 142.9 mbsf; -15R-CC, 152.3 mbsf;

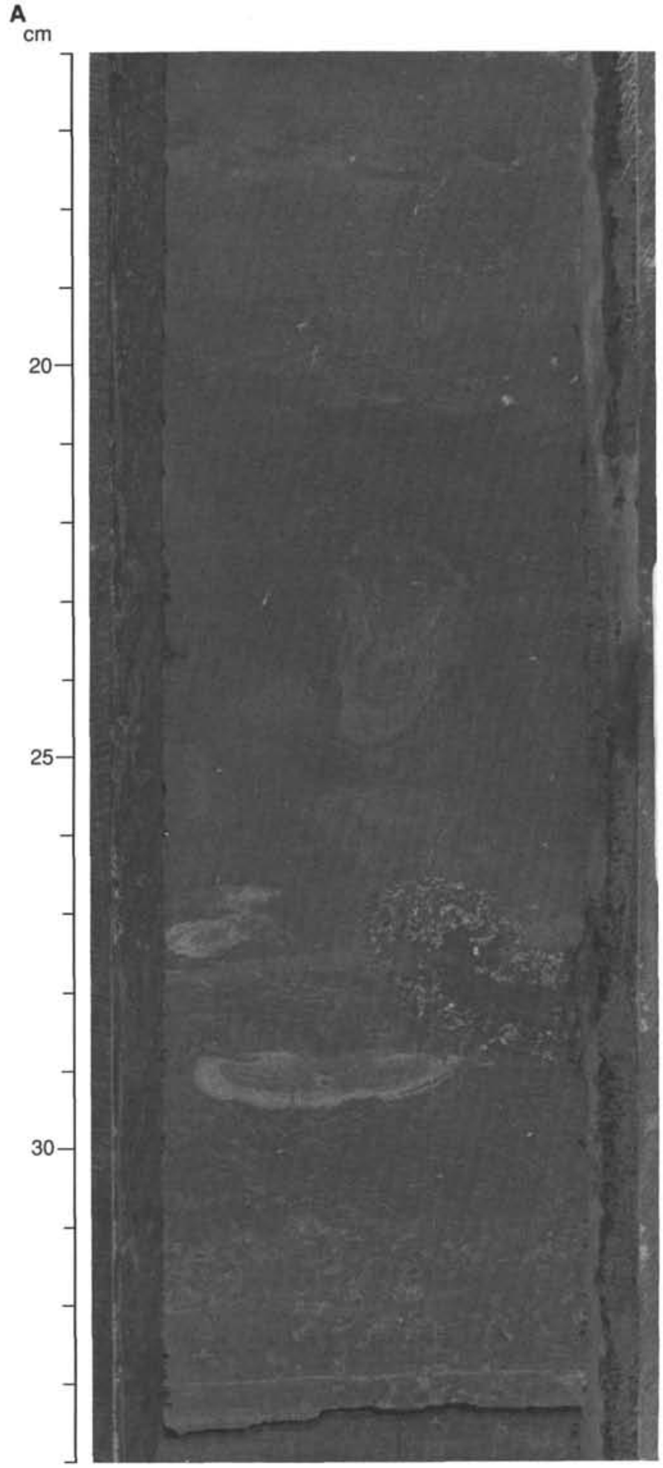

Figure 21. **A.** Typical sequence of trace fossils in turbiditic sequence from Subunit IIC. Photo is from interval 139-858A-21X-2, 16–34 cm. **B.** Sketch of Subunit IIC trace fossil assemblage and its relationship to turbidite stratigraphy.

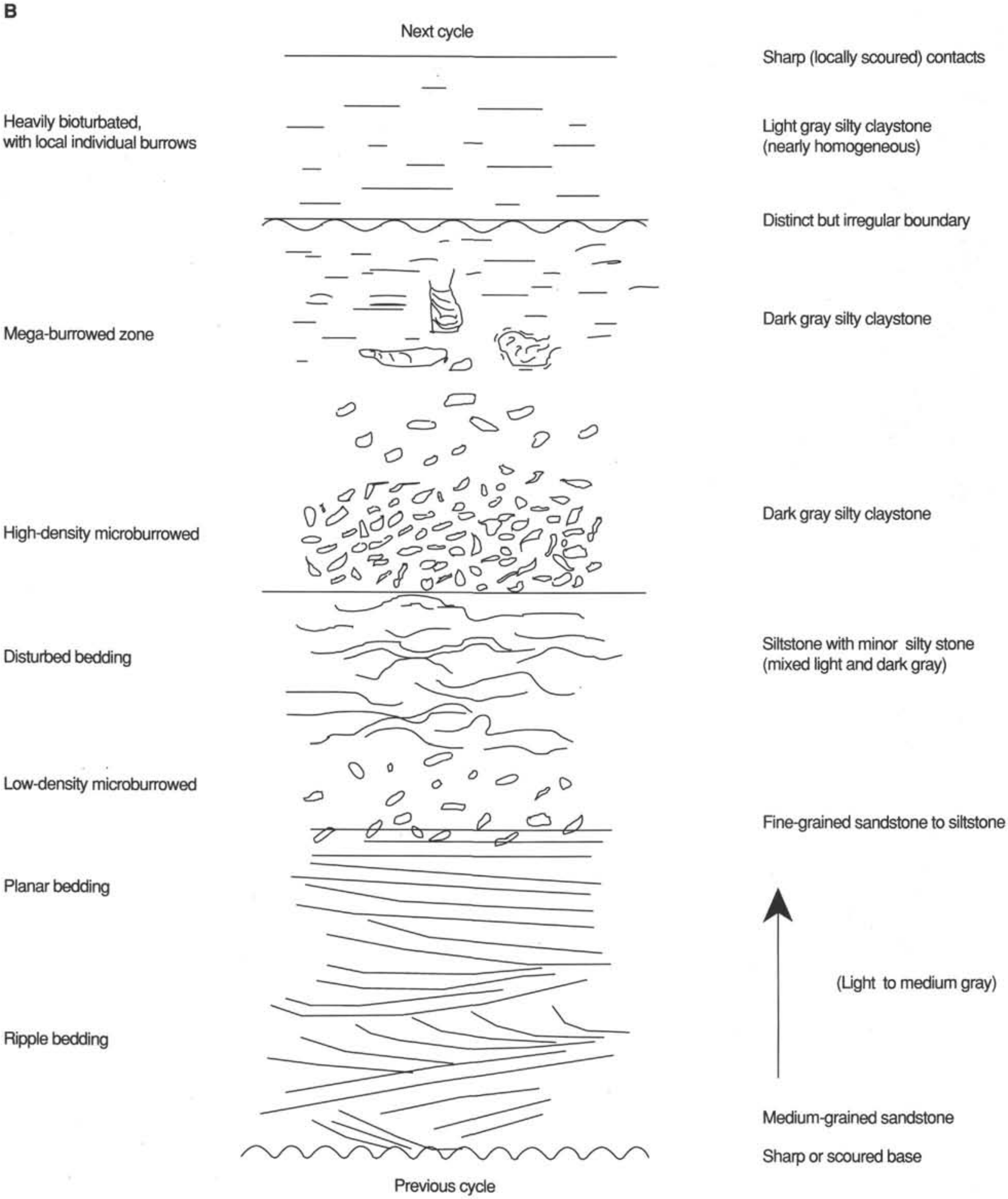

Figure 21 (continued).

-17R-CC, 171.7 mbsf; -19R-1, 191.1 mbsf; and -25R-1, 250 mbsf). In Section 139-858F-11R-CC (114.1 mbsf) anhydrite is present with pyrite and chalcopyrite as a fracture-filling material. Anhydrite was also recognized in washed and sieved paleontological samples from Sections 139-858A-39X-CC (332.5 mbsf) and -7X-CC (37.3 mbsf).

Sulfide minerals are ubiquitous in this subunit. Pyrite occurs as a trace constituent in vein- and fracture-filling assemblages and is present as fine to coarse (up to 1 mm cubes), disseminated, euhedral crystals in the sandstone, siltstone, and silty claystone interbeds. Sphalerite is also present as an accessory mineral in vein- and fracture-filling assemblages. In addition, it occurs locally (e.g., Section 139-858F-10R-CC, 103.9 mbsf) as large (up to 3 mm) euhedral crystals in siltstone. Chalcopyrite occurs in trace amounts in veins in Section 139-858D-6X-1 (29 mbsf) and Sections 139-858A-37X-CC (315.3 mbsf),

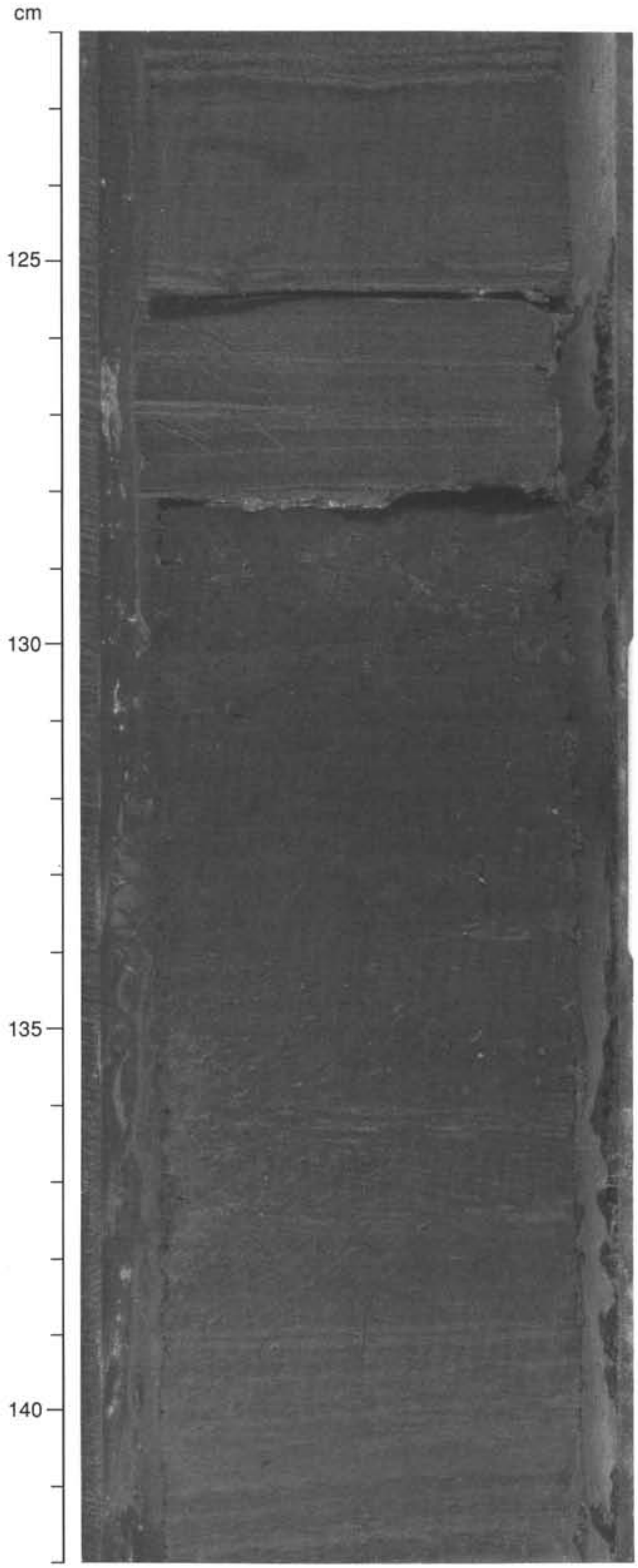

Figure 22. Lath-shaped anhydrite crystals in silty claystone of Subunit IIC. Photo is from interval 139-858A-18X-2, 122–142 cm.

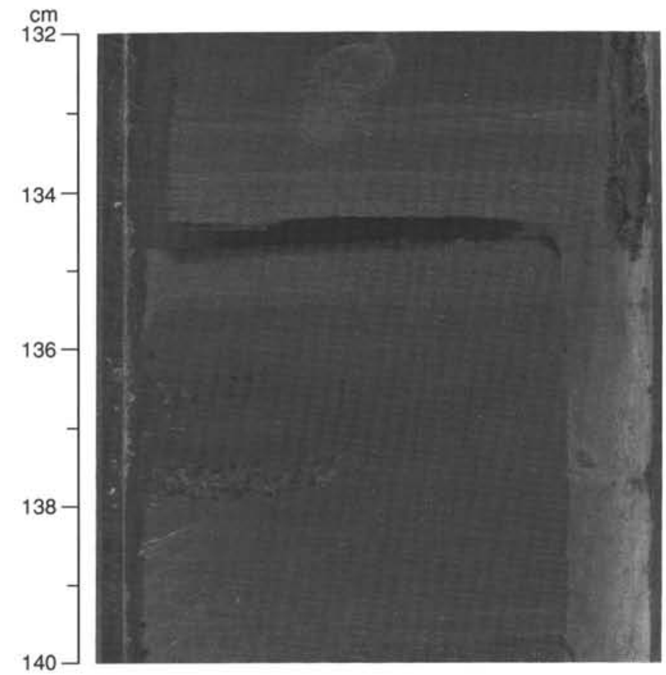

Figure 23. Coarsely crystalline anhydrite rim around zoned carbonate nodule in Subunit IIC. Photo is from interval 139-858A-20X-3, 132–140 cm.

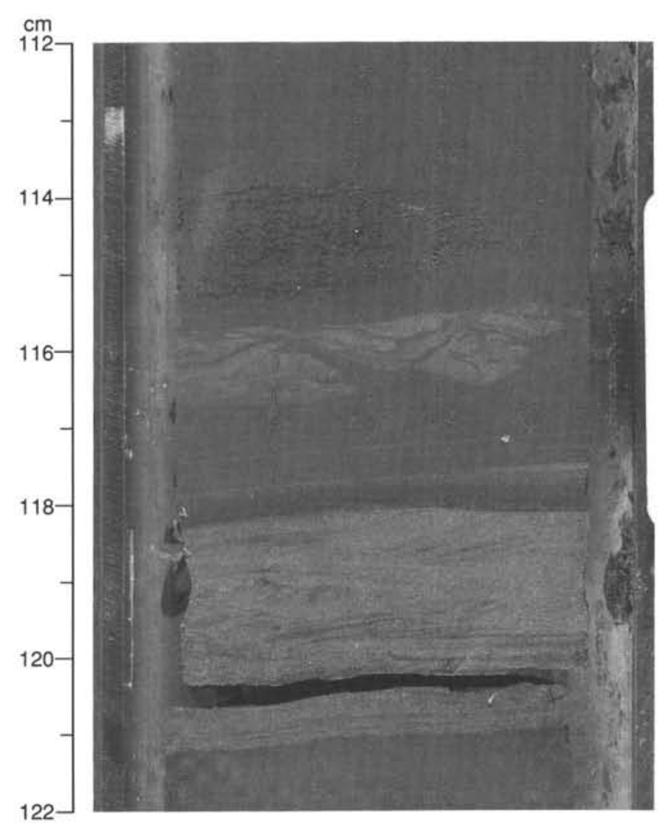

Figure 24. Coarsely crystalline anhydrite nodule in Subunit IIC. Also note the scour-based turbidite sequence and the isolated scour-and-fill structure with internal convolute bedding. Photo is from interval 139-858A-20X-1, 112–122 cm.

-38X-CC (322.8 mbsf), and -39X-CC (332.5 mbsf). Freshly broken surfaces from Hole 858F give off a faint odor of H_2S below Core 139-858F-5R (below 65 mbsf).

Olive green (5GY 3/5) Mg-rich smectite, chlorite/smectite mixed-layer clays, and talc(?) are common in Subunit IID. Chlorite was identified in all XRD analyses from this subunit and a chlorite/smectite mixed layer clay was identified from Section 139-858B-6H-CC (32.3 mbsf). Analcime and wairakite were identified in XRD analyses of samples from Sections 139-858F-8R-CC (84.8 mbsf), -9R-CC (94.3 mbsf), and -11R-CC (114.1 mbsf). Tentative visual identification of talc in Sections 139-858B-8X-3 (35 mbsf) and -9X-CC (35.2 mbsf) and smectite in Sections 139-858B-8X-1 (33 mbsf), -8X-CC (38.2 mbsf), and -16R-CC (161.9 mbsf) suggests that alteration is pervasive in this subunit.

Lithologic Unit III

Sections 139-858B-1H-1, 0 cm, to -1H-2, 47 cm (0–1.97 mbsf); Holocene–late Pleistocene.

Lithologic Unit III consists of metalliferous, oxidized, surficial sediment that overlies strata containing semimassive sulfide (lithologic Unit IV). The Unit is characterized by varicolored—blue-green (5GY 4/1) to dark olive green (5GY 3/4) to grayish olive green (5GY 3/2) to yellow green—silty, Mg-rich smectite (?) that is interlayered with black, clay-rich, pyrite beds. This sediment may record the initiation of active venting at this location. It is probably the result of *in-situ* alteration of warm sediments at the seafloor by interaction among hemipelagic sediment, locally derived sulfide sediment, seawater, and hydrothermal fluids from the nearby vent (see "Sediment Geochemistry and Alteration" section, this chapter). This unit is similar to Unit III at Site 856.

Lithologic Unit IV

Sections 139-858B-2H-3, 21 cm, to -2H-4, 100 cm (10.41–12.70 mbsf).

Lithologic Unit IV consists of strata-bound semimassive sulfide confined to the coarse portions of fining-upward turbidite sequences in the upper part of Hole 858B. This sulfide probably represents precipitation from sulfide-rich pore fluids moving laterally along permeable horizons. The sulfide in lithologic Unit IV, along with the sulfide accumulations in Subunits IIB and III, is discussed in detail in the "Sulfide Petrology" section (this chapter).

Lithologic Unit V

Sections 139-858F-25R-1, 81 cm, to -29R-1, 124 cm (249.71–288.44 mbsf).

Lithologic Unit V consists of mafic extrusive rock recovered at the base of Holes 858F and 858G. This unit is discussed in the "Igneous Petrology" section (this chapter).

BIOSTRATIGRAPHY

Six holes were drilled at Site 858: Holes 858B to 858G lie within a zone of hydrothermal discharge and Hole 858A lies adjacent to the zone. Microfossils are preserved to a depth of 72 mbsf outside the discharge zone, and absent from sediments deeper than 13 mbsf within the zone. Fossils at the surface of Hole 858B are rare in contrast to their abundance in other surficial samples at this site. This surface sample is dominated by anhydrite crystals typical of those which form chimneys in this region (W. Goodfellow, pers. comm., 1991). It is unclear whether the sparse fossil population is due to dilution or to lack of preservation. Hydrothermal sediment was also observed in the surficial sediment of Hole 858C and 858D. Recrystallized fossils occur below the surfacemost samples in Holes 858A, 858B, 858C, and 858D, and sand-size barite, anhydrite, and calcite crystal masses are associated with the altered fossils. No foraminifers or calcareous nannofossils were preserved in Hole 858F, but a radiolarian-like form was observed in the quartzite of core-catcher Section 139-858F-9R-CC.

Poor preservation interfered with placement of biostratigraphic boundaries defined by calcareous nannofossils. The preserved bases of the *Emiliania huxleyi* Acme Zone and Zone NN21 may be shallower than their true bases due to destruction of the marker species. Placement of biostratigraphic boundaries based on foraminifers appears unaffected by poor preservation. The Holocene-Pleistocene boundary, which is defined as the base of planktonic foraminiferal Zone CD1, was recognized within the first cores of Holes 858A, 858B, 858C, and 858D as it has been at all other sites. Shore-based study will determine if Zone CD3 lies near 27 mbsf in Hole 858A as it does in Hole 857A.

Foraminifers

Both high heat flow and hydrothermal circulation altered and removed foraminifers from the thick sequence of Pleistocene turbidites and hemipelagites. Of 67 samples examined, only 20 near-surface samples contain foraminifers. Hole 858A, which lies near the zone of hydrothermal discharge, bears foraminifers to a depth of 110 mbsf, but holes within the zone bear foraminifers no deeper than about 13 mbsf (Table 5). The preservation state of the fossils ranges from moderate to poor, and all those from depths greater than a few meters below seafloor are recrystallized (Table 6). The recrystallized tests are overgrown with calcite protuberances, and some are chalky in appearance. Recrystallized foraminifers grade in color from pale yellow near the top of the sequence (11.9 mbsf in Hole 858A) to deep golden brown at depth (110.6 mbsf in Hole 858A).

The planktonic foraminiferal fauna (Table 6) bears species typical of subarctic waters and includes *Globigerina bulloides* d'Orbigny, *Globigerinita glutinata* (Egger), *Globigerinita minuta* (Natland), *Globigerinita uvula* (Ehrenberg), sinistral and dextral *Neogloboquadrina pachyderma* (Ehrenberg), and *Turborotalita quinqueloba* (Natland). The transitional species *Globorotalia scitula* (Brady) is few to rare in abundance, and the subtropical species *Globorotalia theyeri* Fleisher is also few to rare in abundance (see Thunell and Reynolds, 1984, and Sautter and Thunell, 1991, for comments on environment of this species).

Holocene-age sediment was observed at the surface of four of five holes, and in all four holes where a mudline core was taken (Holes 858A, 858B, 858C, and 858D). Holocene-age samples were recognized based on the relative frequency of dextral to sinistral *Neogloboquadrina pachyderma* (Bandy, 1960; Table 6). Dextral coiling forms are greater in frequency than sinistral forms in this region of the North Pacific Ocean during interglacial climatic intervals. The dextral form occurs commonly relative to the sinistral form in Samples 139-858A-1H-1, 0–1 cm; 139-858B-1H-1, 0–1 cm; 139-858C-1H-1, 0–1 cm; and 139-858D-1H-1, 0–1 cm. The samples are assigned to Zone CD1 of Lagoe and Thompson (1988).

Pleistocene-age sediment was encountered at the base of the first core from Holes 858A, 858B, 858C, and 858D and recognized based on the dominance of sinistral *Neogloboquadrina pachyderma* relative to the dextral form (Bandy, 1960; Table 6). The interval is tentatively assigned to Zone CD2 of Lagoe and Thompson (1988). Shore-based study of the sequence in Hole 858A will determine if Zone CD3, the penultimate interglacial period, lies near 27 mbsf as it does at Site 857. The Holocene-Pleistocene boundary lies within the first cores of these four holes.

The benthic foraminiferal assemblage consists of species from depth zones ranging from neritic to lower bathyal (Table 6). Lower and lower middle bathyal species are intermixed with neritic and upper bathyal species which were transported to the site by turbidity currents. Prominent members of the *in-situ* depth fauna include *Bulimina barbata, Cibicides wuellerstorfi, Gyroidina altiformis, Gyroidina planulata, Melonis pompilioides, Pullenia bulloides,*

Table 5. Comparison of abundances of calcareous nannofossils, planktonic foraminifers, and benthic foraminifers to lithology of sample.

Sample (cm)	Lithology	Nannofossils	Benthic foraminifers	Planktonic foraminifers
139-858A-				
1H-1, 0–1	Clay	C	C	C
1H-CC	Clay	C	C	A
2H-CC	Silty clay	F	A	F
3H-CC	Silty clay	C	A	A
4H-CC	Silt laminations	F	A	A
5H-CC	Claystone	F	—	—
6H-CC	Silt- and sandstone	F	F	C
7H-CC	Silty claystone	F	F	F
8H-CC	Drilling breccia	R	C	A
9X-CC	Claystone	C	A	A
11X-CC	Sandstone	R	C	R
13X-CC	No description	R	—	—
14X-CC	Silt- and sandstone	R	F	R
15X-CC	Silty claystone	B	B	B
16X-CC	Sandstone	B	B	B
17X-CC	Sandstone?	B	B	B
18X-CC	Laminated sandstone	B	B	B
19X-CC	No description	B	B	B
20X-CC	Clay	B	B	B
21X-CC	Clay	B	B	B
22X-CC	Siltstone	B	B	B
23X-CC	Siltstone	B	B	B
24X-CC	Medium sandstone	B	B	B
25X-CC	Silty claystone	B	B	B
26X-CC	Claystone	B	B	B
27X-CC	Coarse siltstone	B	B	B
28X-CC	Siltstone	B	B	B
29X-CC	Sandstone	B	B	B
30X-CC	Laminated claystone	B	B	B
31X-CC	Claystone	B	B	B
32X-CC	Claystone	B	B	B
34X-CC	Claystone	B	B	B
35X-CC	Sandstone	B	B	B
36X-CC	Claystone	B	B	B
37X-CC	Siltstone	B	B	B
38X-CC	Siltstone	B	B	B
39X-CC	Silty claystone	B	B	B
139-858B-				
1H-1, 0–1	Clay	B	R	R
1H-1, 128	Clay	R	—	—
1H-2, 30	Clay	C	—	—
1H-2, 138	Clay	C	—	—
1H-3, 54	Clay	C	—	—
1H-3, 146	Clay	R	—	—
1H-CC	Clay	R	R	R
2H-CC	Clay	B	B	B
3H-CC	Clay	B	B	B
4X-CC	Clay	B	—	—
5H-CC	Claystone	B	B	B
6H-CC	Silty claystone	B	B	B
8X-CC	Claystone	B	B	B
9X-CC	Claystone	B	—	—
139-858C-				
1H-1, 0–1	Clay	C	C	F
1H-CC	Clay	C	C	A
2H-CC	Silty clay	F	A	A
3H-CC	Sand and silt	R	B	B
5H-CC	Disturbed silty clay	R	B	B
6H-CC	Disturbed silty clay	B	B	B
7H-CC	Disturbed silty clay	B	B	B
8H-CC	Disturbed silty clay	B	B	B
9H-CC	Lithified pebbles	B	B	B
10X-CC	Silty claystone	B	B	B
11X-CC	Claystone	B	B	B
12X-CC	Silty claystone	B	B	B
13X-CC	Siltstone	B	B	B
14X-CC	Drilling breccia	—	B	B

Table 5 (continued).

Sample (cm)	Lithology	Nannofossils	Benthic foraminifers	Planktonic foraminifers
139-858D-				
1H-1, 0–1	Silty clay	R	F	F
1H-1, 97	Clay	A	—	—
1H-1, 116	Clay	A	—	—
1H-2, 12	Clay	A	—	—
1H-4, 17	Clay	A	—	—
1H-5, 120	Clay	A	—	—
1H-6, 6	Clay	C	—	—
1H-6, 144	Clay	B	—	—
1H-CC	Silty clay	R	R	F
2H-3, 3	Clay	B	—	—
2H-CC	Silty clay	R	C	F
4H-CC	Disturbed silty clay	R	B	B
5H-CC	Disturbed sandy clay	B	B	B
6X-CC	Sandstone	B	B	B
7X-CC	Sandstone	B	B	B
139-858E-1W-CC	Clay	F	—	—
139-858F-				
1W-CC	Clay	B	—	—
2R-CC	Sandstone	B	B	B
4R-CC	Sandstone	B	B	R
5R-CC	Siltstone	—	B	B
9R-CC	Siltstone	B	—	—
12R-CC	Siltstone	B	—	—
17R-CC	Siltstone	B	—	—
18R-CC	Sandstone	B	—	—
21R-CC	Siltstone	B	—	—
22R-CC	Siltstone	B	—	—
23R-CC	Siltstone	B	—	—
24R-CC	Siltstone	B	—	—

Notes: A = abundant, C = common, F = few, R = rare, B = barren, — = sample not prepared.

Sphaeroidina bulloides, and *Uvigerina senticosa.* Species from neritic and upper bathyal depths (Bergen and O'Neil, 1979; R. Patterson, unpubl. data, 1991) are mixed with middle and lower bathyal species. Upper bathyal species include *Bolivina pacifica, Buliminella tenuata, Globobulimina affinis, Oridorsalis tener, Pullenia quinqueloba,* and *Stainforthia complanata.* Neritic taxa include *Buliminella elegantissima, Elphidium, Globobulimina pacifica, Nonion, Nonionella, Pullenia salisburyi,* and *Rosalina.*

The topmost samples from Holes 858A through 858D bear agglutinated foraminifers not observed in deeper samples. This observation is true of most surficial samples at all four sites (855, 856, 857, and 858). The taxa were tentatively identified to genus and include three species of *Ammodiscus,* two species of *Eggerella,* one species each of *Karreriella, Hormosina, Saccammina,* and several species of *Cribrostomoides.* Fragments from several different tube-shaped agglutinated species were also observed, some in great abundance. Shore-based quantitative work will determine if the faunas from the vent field are different from those outside the vent field.

Calcareous Nannofossils

Calcareous nannofossils at Site 858 are low in abundance and species diversity because of high heat flow and thermal alteration. Only 38 of 90 samples examined contain nannofossils (42.2% of the total), and all samples from Hole 858F are completely barren of nannofossils (Tables 7 and 8). Nannofossils are abundant to rare, with six to eight species in these 38 samples. The preservation is generally poor, and moderately well-preserved fossil assemblages occur only in samples from the topmost cores of Hole 858B and 858D. Fossil abundance and species diversity decrease with depth, and preservation state deteriorates with depth as well. The marker of Zone NN21 (Martini, 1971), *Emiliania huxleyi,* occurs in most samples where nannofossils are present. Zone NN21 can therefore be recognized in all holes but Hole 858F, where nannofossils do not occur in any samples.

Nannofossils have their deepest occurrence at 110.6 mbsf in Hole 858A, where thermal alteration is less intense than at any other hole of Site 858 (Table 7). The *Emiliania huxleyi* Acme Zone (Gartner, 1977) cannot be detected, suggesting that some part of the uppermost Pleistocene may be missing in this hole. On Table 7 a dashed line was drawn between Samples 139-858A-4H-CC and -3H-CC, where *E. huxleyi* has its deepest occurrence, indicating the uncertainty of the base of Zone NN21. *E. huxleyi,* which has a delicate structure, may have its first appearance datum (FAD) below Sample 139-858A-4H-CC and was perhaps selectively removed by thermal alteration. Calcareous nannofossils are absent from all samples below Sample 139-858A-14X-CC.

The *Emiliania huxleyi* Acme Zone was observed in Hole 858B. The base of the zone was placed tentatively between Samples 139-858B-1H-3, 146 cm, and 139-858B-1H-3, 54 cm (Table 7), because we think that both the low abundance in Sample 139-858A-1H-3, 54 cm, and the absence of this species in samples below result from thermal alteration which removed some of the more delicate *Emiliania huxleyi* from the original nannofossil floras. Shore-based scanning electron microscope (SEM) study of nannofossils from the sequence in Hole 858B may help find the relationships between fossil abundance, preservation, and thermal alteration. The acme zone may start deeper in the sequence than we now assume, although it may occur deeper and we may not be able to locate it. Likewise, the section between Samples 139-858A-1H-3, 146 cm, and 139-858A-1H-CC cannot be dated because of the removal of *E. huxleyi* by the thermal alteration.

The base of the *Emiliania huxleyi* Acme Zone in Hole 858C was placed tentatively between Samples 138-858C-3H-CC and -2H-CC. Shore-based SEM study of nannofossils from the section may help find the true base of the zone. Below Sample 139-858C-3H-CC, nannofossils are very rare, with one to two poorly preserved *Coccolithus pelagicus* per 100 fields. The interval of barren samples in Hole 858C starts below 41.5 mbsf, about 80 m shallower than in Hole 858A, presumably because Hole 858C is located within the vent field area, whereas Hole 858A is located beyond this vent field area (see site summary at the beginning of this chapter). In addition, the heat flow and temperatures are significantly higher in Hole 858C than in Hole 858A (see "Heat Flow" section, this chapter).

In Hole 858D nannofossils occur mainly in samples from the first core, which may be assigned to the *Emiliania huxleyi* Acme Zone on the basis of the abundant occurrence of *Emiliania huxleyi.* The low abundance and even absence of the species in some samples of Core 139-858D-1H may be attributed to the removal of *Emiliania huxleyi* from the original floras by thermal alteration.

Eleven samples from Hole 858F were investigated. All of them are completely barren of nannofossils because of the intense thermal alteration. As shown at the other three sites, the subarctic species *Coccolithus pelagicus* proved to be the species most resistant to thermal alteration.

PALEOMAGNETISM

Site 858 is located over an active hydrothermal vent field that extends several hundred meters along and across the strike of Middle Valley. Seven holes were drilled in an array crossing the field and on the flank of the associated thermal anomaly. Paleomagnetic studies were carried out on cores from Holes 858A, 858B, 858C, and 858D. Hole 858A was drilled with continuous APC coring to 62.5 mbsf and XCB coring to 339 mbsf. Temperature measurements in the upper 110 mbsf of the hole reveal a thermal gradient of 1.7°C/m. An extrapolation of this gradient to the bottom of the hole yields an estimated temperature near 300°C ("Heat Flow" section, this chapter). Hole 858B was drilled with APC/XCB to 38.6 mbsf. A temperature of 197°C was measured at 19.5 mbsf ("Heat Flow" section, this chapter). Because of the high temperature inside the hole, aluminum core liners were used instead of plastic liners for several APC cores in Holes 858B and 858D. These high-temperature liners present several problems for magnetic measurements, which are discussed later. Hole 858C was drilled with APC/XCB to 93 mbsf, within the distal part of the vent field area. Temperature measurements define a temperature gradient of about 3°C/m ("Heat Flow" section, this chapter). Holes 858D, 858E, 858F, and 858G were drilled in the center of the vent area. Hole 858D was drilled with the APC/XCB coring system, Hole 858E was washed down to 38 mbsf and Hole 858F was drilled with the RCB coring system to 210 mbsf and had low recovery. Hole 858E and most parts of Hole 858F were not suitable for paleomagnetic measurements. Hole 858G was drilled with the RCB to 432.6 mbsf. The recovery was too low to get reliable paleomagnetic results.

The archive halves of Holes 858A, 858B, 858C, and 858D were measured with the pass-through cryogenic magnetometer. Each section was demagnetized in peak alternating fields (AF) of 10 and 15 milliTesla (mT). Intervals of the pass-through measurements were 2 cm after 15-mT demagnetization and 10 cm for the other measurements.

Forty-five oriented, discrete samples of sediment were taken from the working half from Holes 858A, 858B, 858C, 858D, and 858F, and were progressively demagnetized at 5, 10, 15, 20, 30, 40, 50, 65, 80, and 95 mT using the Schonstedt demagnetizer. Two oriented, discrete samples of igneous rocks from Hole 858F were demagnetized and measured in the same way. Magnetic susceptibility of all cores was measured using the multisensor track (MST) at 2-cm intervals before splitting.

Results

Hole 858A

The intensities of the sediments range between 0.1 and 1000 mA/m for natural remanent magnetization (NRM) and are generally higher in the upper part of the hole (0–80 mbsf) than in the lower part. After AF demagnetization at 15 mT, the intensity ranges between 0.1 and 100 mA/m (Fig. 25). Discrete samples, shown by open circles in Figure 25, show an average value of 9 ± 13 mA/m above 82 mbsf and 0.4 ± 0.3 mA/m between 82 and 316 mbsf for the intensity after demagnetization with 15-mT peak alternating field. Because of the low recovery below 80 mbsf, our discussion will be confined to the upper part of the hole. Figure 26 shows the inclination, intensity, and susceptibility for NRM and after 15-mT demagnetization for 0–80 mbsf.

The difference between NRM intensity and intensity after 15-mT demagnetization may be in part an indicator of the sensitivity of samples to overprinting by the fields associated with the drilling operation. The peak alternating field of 15 mT, which is the maximum field of the demagnetizer with the pass-through cryogenic magnetometer on board, does not change significantly the magnetic directions and magnetic intensity at 15–17 mbsf, 20–21 mbsf, and 31–38 mbsf.

The evidence for stable magnetization and stable direction led us to consider possible real reversed directions at 15–17 mbsf and at 20–21 mbsf. To confirm the results of the pass-through measurements, we measured several discrete samples from the working halves with the Molspin magnetometer and demagnetized them until the magnetization was completely destroyed or became unstable. The results are listed in Table 9 and are shown by open circles in Figure 26. We noticed a stable negative inclination only for Sample 139-858A-3H-3, 100–102 cm, at a depth of 15.7 mbsf (see Fig. 27). The other discrete samples show stable positive inclinations after AF demagnetization. The observed difference between archive-half and discrete working-half measurements is thought to be caused by the difference in drilling disturbance between the outer part and inner part of the core. This difference was observed also at other sites of this leg (see "Paleomagnetism" sections, "Site 856" and "Site 857" chapters, this volume).

The susceptibility of the upper 80 mbsf seems to be divided in two ranges of values, about 2×10^{-4} SI and about 2×10^{-3} SI. We observe several changes in susceptibility with sharp boundaries between higher and lower values. The decrease at 23 mbsf might be associated with an increase in carbonate nodules (see "Sediment Geochemistry and Alteration" section, this chapter). No clear correlation between the susceptibility and the magnetic intensity measured on the whole-core sections is immediately evident, especially for the depth between 23 and 36 mbsf, where the susceptibility is low and constant. The magnetic intensity measured on the archive half is not constant in this

Table 6. Range chart of planktonic and benthic foraminifers, their abundance and preservation, and abundance of other major constituents of the sand-size fraction.

	Abundance of benthic foraminifers	Abundance of planktonic foraminifers	Preservation of foraminifers	*Globigerina bulloides*	*Globigerinita glutinata*	*Globigerinita minuta*	*Globigerinita uvula*	*Globorotalia scitula*	*Globorotalia theyeri*	*Neogloboquadrina pachyderma* (dex.)	*Neogloboquadrina pachyderma* (sin.)	*Turborotalita quinqueloba*	*Ammodiscus* sp. A	*Eggerella bradyi*	*Eggerella* spp.	*Hormosina* sp. A	*Textularia* sp. A	*Pyrgo murrhina*	*Triloculina* sp. A	*Bolivina pacifica*	*Bolivina seminuda*	*Bulimina barbata*	*Buliminella elegantissima*	*Buliminella tenuata*	*Cassidulina laevigata carinata*	*Chilostomella oolina*	*Cibicides kullenbergi*	*Cibicides wuellerstorfi*	*Elphidium* spp.	*Globobulimina affinis*	*Globobulimina ovula*	*Globobulimina pacifica*	*Globocassidulina* spp.
139-858A-																																	
1H-1, 0–1	C	C	M	X	·	·	·	·	·	X	X	X	X	X	·	X	·	·	·	·	X	·	·	·	·	X	·	X	·	X	X	X	·
1H-CC	C	A	M	X	X	X	X	·	·	·	X	X	·	·	·	·	·	·	X	·	·	·	·	·	·	X	X	X	·	X	X	X	X
2H-CC	A	F	P	X	·	·	·	·	·	·	X	·	·	·	·	·	·	·	·	·	·	X	·	·	·	·	·	X	·	X	·	·	·
3H-CC	A	A	P	A	F	·	·	R	·	R	A	F	·	X	·	·	·	X	X	X	X	·	·	X	·	·	·	X	·	X	·	X	X
4H-CC	A	A	P	X	·	·	·	X	X	·	X	X	·	·	X	·	·	·	X	·	·	·	·	·	·	·	·	X	·	·	X	·	·
6H-CC	F	C	P	X	·	·	·	·	·	·	X	·	·	·	·	·	·	·	·	·	·	·	·	·	·	·	·	·	·	·	·	·	·
7H-CC	F	F	P	X	·	·	·	·	·	·	X	·	·	·	·	·	·	·	·	·	·	·	·	·	·	·	·	·	·	·	·	·	·
8H-CC	C	A	M	X	X	·	·	X	·	·	X	X	·	·	·	·	·	·	X	X	X	·	·	·	·	·	·	·	X	·	X	·	X
9X-CC	A	A	P	A	·	·	·	·	·	·	A	·	·	·	·	·	X	·	X	·	·	·	·	·	·	X	X	X	·	X	·	·	·
11X-CC	C	R	P	·	·	·	·	·	·	·	·	·	·	·	·	·	·	·	·	·	·	·	·	·	·	·	·	·	·	·	·	·	·
12X-CC	C	R	P	·	·	·	·	·	·	·	X	·	·	·	·	·	·	·	·	·	·	·	X	·	·	·	·	·	·	·	·	·	·
14X-CC	F	R	P	·	·	·	·	·	·	·	X	·	·	·	·	·	·	·	·	·	·	·	·	·	?	·	·	·	·	·	·	·	·
15X-CC	B	B	·	·	·	·	·	·	·	·	·	·	·	·	·	·	·	·	·	·	·	·	·	·	·	·	·	·	·	·	·	·	·
16X-CC	B	B	·	·	·	·	·	·	·	·	·	·	·	·	·	·	·	·	·	·	·	·	·	·	·	·	·	·	·	·	·	·	·
17X-CC	B	B	·	·	·	·	·	·	·	·	·	·	·	·	·	·	·	·	·	·	·	·	·	·	·	·	·	·	·	·	·	·	·
18X-CC	B	B	·	·	·	·	·	·	·	·	·	·	·	·	·	·	·	·	·	·	·	·	·	·	·	·	·	·	·	·	·	·	·
19X-CC	B	B	·	·	·	·	·	·	·	·	·	·	·	·	·	·	·	·	·	·	·	·	·	·	·	·	·	·	·	·	·	·	·
20X-CC	B	B	·	·	·	·	·	·	·	·	·	·	·	·	·	·	·	·	·	·	·	·	·	·	·	·	·	·	·	·	·	·	·
21X-CC	B	B	·	·	·	·	·	·	·	·	·	·	·	·	·	·	·	·	·	·	·	·	·	·	·	·	·	·	·	·	·	·	·
22X-CC	B	B	·	·	·	·	·	·	·	·	·	·	·	·	·	·	·	·	·	·	·	·	·	·	·	·	·	·	·	·	·	·	·
23X-CC	B	B	·	·	·	·	·	·	·	·	·	·	·	·	·	·	·	·	·	·	·	·	·	·	·	·	·	·	·	·	·	·	·
24X-CC	B	B	·	·	·	·	·	·	·	·	·	·	·	·	·	·	·	·	·	·	·	·	·	·	·	·	·	·	·	·	·	·	·
25X-CC	B	B	·	·	·	·	·	·	·	·	·	·	·	·	·	·	·	·	·	·	·	·	·	·	·	·	·	·	·	·	·	·	·
26X-CC	B	B	·	·	·	·	·	·	·	·	·	·	·	·	·	·	·	·	·	·	·	·	·	·	·	·	·	·	·	·	·	·	·
27X-CC	B	B	·	·	·	·	·	·	·	·	·	·	·	·	·	·	·	·	·	·	·	·	·	·	·	·	·	·	·	·	·	·	·
28X-CC	B	B	·	·	·	·	·	·	·	·	·	·	·	·	·	·	·	·	·	·	·	·	·	·	·	·	·	·	·	·	·	·	·
29X-CC	B	B	·	·	·	·	·	·	·	·	·	·	·	·	·	·	·	·	·	·	·	·	·	·	·	·	·	·	·	·	·	·	·
30X-CC	B	B	·	·	·	·	·	·	·	·	·	·	·	·	·	·	·	·	·	·	·	·	·	·	·	·	·	·	·	·	·	·	·
31X-CC	B	B	·	·	·	·	·	·	·	·	·	·	·	·	·	·	·	·	·	·	·	·	·	·	·	·	·	·	·	·	·	·	·
32X-CC	B	B	·	·	·	·	·	·	·	·	·	·	·	·	·	·	·	·	·	·	·	·	·	·	·	·	·	·	·	·	·	·	·
33X-CC	B	B	·	·	·	·	·	·	·	·	·	·	·	·	·	·	·	·	·	·	·	·	·	·	·	·	·	·	·	·	·	·	·
34X-CC	B	B	·	·	·	·	·	·	·	·	·	·	·	·	·	·	·	·	·	·	·	·	·	·	·	·	·	·	·	·	·	·	·
35X-CC	B	B	·	·	·	·	·	·	·	·	·	·	·	·	·	·	·	·	·	·	·	·	·	·	·	·	·	·	·	·	·	·	·
36X-CC	B	B	·	·	·	·	·	·	·	·	·	·	·	·	·	·	·	·	·	·	·	·	·	·	·	·	·	·	·	·	·	·	·
37X-CC	B	B	·	·	·	·	·	·	·	·	·	·	·	·	·	·	·	·	·	·	·	·	·	·	·	·	·	·	·	·	·	·	·
38X-CC	B	B	·	·	·	·	·	·	·	·	·	·	·	·	·	·	·	·	·	·	·	·	·	·	·	·	·	·	·	·	·	·	·
39X-CC	B	B	·	·	·	·	·	·	·	·	·	·	·	·	·	·	·	·	·	·	·	·	·	·	·	·	·	·	·	·	·	·	·

Table 6 (continued).

	Gyroidina altiformis	*Gyroidina* sp. A	*Gyroidina* spp.	*Hoeglundina elegans*	Lagenids	*Melonis barleeanum*	*Melonis pompilioides*	Nodosarids	*Nonion labradorica*	*Nonion* spp.	*Nonionella* spp.	*Pullenia bulloides*	*Pullenia salisburyi*	*Rosalina* sp. A	*Rutherfordoides* sp. A	*Sphaeroidina bulloides*	*Stainforthia complanata*	*Uvigerina dirupta*	*Uvigerina senticosa*	*Uvigerina* spp.	*Valvulineria* spp.	Indeterminate	Others:	Agglutinated taxa	Anhydrite and/or gypsum	Cemented clay lumps	Diatoms	Mica	Mineral grains	Radiolarians	Recrystallized foraminifers	Sulfides	Test fragments
139-858A-																																	
1H-1, 0–1	X	X	·	·	X	·	X	·	·	·	·	X	X	·	·	X	·	X	X	·	·	X		X	·	·	·	·	·	A	·	·	·
1H-CC	X	X	·	X	·	·	·	·	·	·	·	·	·	·	·	·	X	·	X	·	X	X		·	·	·	·	·	·	X	·	·	·
2H-CC	X	X	·	·	X	·	X	X	X	·	·	·	X	·	·	·	·	·	X	·	·	X		·	·	·	X	·	·	X	X	·	·
3H-CC	·	·	·	·	X	·	X	X	·	X	·	X	·	X	·	·	X	·	X	·	·	X		X	·	·	·	·	·	·	A	A	A
4H-CC	·	·	·	·	·	·	·	·	·	·	X	·	·	·	·	X	·	·	X	·	·	·		A	·	·	·	·	·	·	A	·	·
6H-CC	·	·	·	·	·	·	·	·	·	·	·	·	·	·	·	·	·	·	·	·	·	X		·	·	·	·	·	A	·	·	·	·
7H-CC	·	·	·	·	·	·	·	·	·	·	·	·	·	·	·	·	·	·	·	X	·	·		·	·	A	·	A	A	·	F	C	·
8H-CC	·	·	X	·	·	X	·	·	·	X	·	·	X	·	·	X	X	·	X	·	·	·		·	·	A	·	·	·	·	A	·	·
9X-CC	X	·	·	·	X	·	X	·	·	·	·	·	·	·	·	·	X	X	X	·	·	·		·	X	·	·	·	·	·	A	X	·
11X-CC	·	·	·	·	·	·	·	·	X	·	·	·	·	·	X	·	X	·	·	·	·	X		·	·	A	·	·	·	·	·	A	·
12X-CC	·	·	·	·	·	·	·	·	·	·	·	·	·	·	X	·	X	·	·	·	·	X		·	·	A	·	·	·	·	X	X	·
14X-CC	·	·	·	·	·	·	·	·	?	·	·	·	·	·	·	·	·	·	·	·	·	X		·	X	X	·	·	·	·	X	·	·
15X-CC	·	·	·	·	·	·	·	·	·	·	·	·	·	·	·	·	·	·	·	·	·	·		·	A	A	·	·	·	·	·	·	·
16X-CC	·	·	·	·	·	·	·	·	·	·	·	·	·	·	·	·	·	·	·	·	·	·		·	·	A	·	·	·	·	·	X	·
17X-CC	·	·	·	·	·	·	·	·	·	·	·	·	·	·	·	·	·	·	·	·	·	·		·	·	·	·	·	A	·	·	·	·
18X-CC	·	·	·	·	·	·	·	·	·	·	·	·	·	·	·	·	·	·	·	·	·	·		·	C	·	·	·	A	·	·	·	·
19X-CC	·	·	·	·	·	·	·	·	·	·	·	·	·	·	·	·	·	·	·	·	·	·		·	·	·	·	A	A	·	·	·	·
20X-CC	·	·	·	·	·	·	·	·	·	·	·	·	·	·	·	·	·	·	·	·	·	·		·	·	A	·	·	·	·	·	·	·
21X-CC	·	·	·	·	·	·	·	·	·	·	·	·	·	·	·	·	·	·	·	·	·	·		·	X	A	·	·	·	·	·	X	·
22X-CC	·	·	·	·	·	·	·	·	·	·	·	·	·	·	·	·	·	·	·	·	·	·		·	·	A	·	·	·	·	·	X	·
23X-CC	·	·	·	·	·	·	·	·	·	·	·	·	·	·	·	·	·	·	·	·	·	·		·	X	A	·	·	·	·	·	X	·
24X-CC	·	·	·	·	·	·	·	·	·	·	·	·	·	·	·	·	·	·	·	·	·	·		·	·	A	·	·	·	·	·	X	·
25X-CC	·	·	·	·	·	·	·	·	·	·	·	·	·	·	·	·	·	·	·	·	·	·		·	·	A	·	·	·	·	·	·	·
26X-CC	·	·	·	·	·	·	·	·	·	·	·	·	·	·	·	·	·	·	·	·	·	·		·	·	A	·	·	·	·	·	X	·
27X-CC	·	·	·	·	·	·	·	·	·	·	·	·	·	·	·	·	·	·	·	·	·	·		·	·	C	·	·	A	·	·	·	·
28X-CC	·	·	·	·	·	·	·	·	·	·	·	·	·	·	·	·	·	·	·	·	·	·		·	·	A	·	·	·	·	·	·	·
29X-CC	·	·	·	·	·	·	·	·	·	·	·	·	·	·	·	·	·	·	·	·	·	·		·	·	·	·	·	A	·	·	X	·
30X-CC	·	·	·	·	·	·	·	·	·	·	·	·	·	·	·	·	·	·	·	·	·	·		·	·	A	·	·	·	·	·	X	·
31X-CC	·	·	·	·	·	·	·	·	·	·	·	·	·	·	·	·	·	·	·	·	·	·		·	·	A	·	·	A	·	·	X	·
32X-CC	·	·	·	·	·	·	·	·	·	·	·	·	·	·	·	·	·	·	·	·	·	·		·	·	A	·	·	·	·	·	·	·
33X-CC	·	·	·	·	·	·	·	·	·	·	·	·	·	·	·	·	·	·	·	·	·	·		·	·	A	·	·	·	·	·	X	·
34X-CC	·	·	·	·	·	·	·	·	·	·	·	·	·	·	·	·	·	·	·	·	·	·		·	·	A	·	·	·	·	·	R	·
35X-CC	·	·	·	·	·	·	·	·	·	·	·	·	·	·	·	·	·	·	·	·	·	·		·	·	A	·	·	·	·	·	·	·
36X-CC	·	·	·	·	·	·	·	·	·	·	·	·	·	·	·	·	·	·	·	·	·	·		·	·	A	·	·	A	·	·	·	·
37X-CC	·	·	·	·	·	·	·	·	·	·	·	·	·	·	·	·	·	·	·	·	·	·		·	X	A	·	·	·	·	·	R	·
38X-CC	·	·	·	·	·	·	·	·	·	·	·	·	·	·	·	·	·	·	·	·	·	·		·	X	A	·	·	·	·	·	R	·
39X-CC	·	·	·	·	·	·	·	·	·	·	·	·	·	·	·	·	·	·	·	·	·	·		·	A	X	·	·	·	·	·	R	·

Table 6 (continued).

	Abundance of benthic foraminifers	Abundance of planktonic foraminifers	Preservation of foraminifers	*Globigerina bulloides*	*Globigerinita glutinata*	*Globigerinita minuta*	*Globorotalia scitula*	*Neogloboquadrina pachyderma* (dex.)	*Neogloboquadrina pachyderma* (sin.)	*Tenuitella parkerae*	*Turborotalita quinqueloba*	*Ammodiscus* sp. A	*Cribrostomoides* sp. A	*Eggerella* spp.	*Hormosina* sp. A	*Karreriella* sp. A	*Saccammina* sp. A	*Textularia* sp. A	*Pyrgo murrhina*	*Triloculina* sp. A	*Bolivina pacifica*	*Bolivina seminuda*	*Bulimina* cf. *B. inflata*	*Cassidulina laevigata carinata*	*Chilostomella oolina*	*Chilostomellina fimbriata*	*Cibicides kullenbergi*	*Cibicides wuellerstorfi*	*Eponides turgida*	*Globobulimina affinis*	*Globobulimina ovala*	*Globobulimina* spp.	*Globocassidulina* spp.
139-858B-																																	
1H-1, 0–1	R	R	M	X	·	·	·	·	X	·	·	·	·	·	·	·	·	·	·	·	·	·	·	·	·	·	·	·	·	·	·	·	·
1H-CC	R	R	P	X	·	·	·	·	X	·	X	·	·	X	·	·	·	·	·	·	·	·	·	·	·	·	·	·	·	·	·	X	·
2H-CC	B	B	·	·	·	·	·	·	·	·	·	·	·	·	·	·	·	·	·	·	·	·	·	·	·	·	·	·	·	·	·	·	·
3H-CC	B	B	·	·	·	·	·	·	·	·	·	·	·	·	·	·	·	·	·	·	·	·	·	·	·	·	·	·	·	·	·	·	·
5H-CC	B	B	·	·	·	·	·	·	·	·	·	·	·	·	·	·	·	·	·	·	·	·	·	·	·	·	·	·	·	·	·	·	·
6H-CC	B	B	·	·	·	·	·	·	·	·	·	·	·	·	·	·	·	·	·	·	·	·	·	·	·	·	·	·	·	·	·	·	·
8X-CC	C	B	·	·	·	·	·	·	·	·	·	·	·	·	·	·	·	·	·	·	·	·	·	·	·	·	·	·	·	·	·	·	·
139-858C-																																	
1H-1, 0–1	C	F	M	F	·	·	·	R	R	·	·	X	X	X	X	X	X	·	X	·	·	X	·	·	·	·	·	·	X	·	X	·	·
1H-CC	C	A	M	A	X	X	X	R	A	·	X	·	·	·	·	·	·	·	X	X	X	X	X	·	X	·	·	X	X	X	X	·	X
2H-CC	A	A	P	A	X	X	·	X	A	·	·	·	·	·	·	X	·	X	·	X	X	·	·	X	X	X	·	X	·	X	·	·	·
3H-CC	B	B	·	·	·	·	·	·	·	·	·	·	·	·	·	·	·	·	·	·	·	·	·	·	·	·	·	·	·	·	·	·	·
5H-CC	B	B	·	·	·	·	·	·	·	·	·	·	·	·	·	·	·	·	·	·	·	·	·	·	·	·	·	·	·	·	·	·	·
6H-CC	B	B	·	·	·	·	·	·	·	·	·	·	·	·	·	·	·	·	·	·	·	·	·	·	·	·	·	·	·	·	·	·	·
7H-CC	B	B	·	·	·	·	·	·	·	·	·	·	·	·	·	·	·	·	·	·	·	·	·	·	·	·	·	·	·	·	·	·	·
8H-CC	B	B	·	·	·	·	·	·	·	·	·	·	·	·	·	·	·	·	·	·	·	·	·	·	·	·	·	·	·	·	·	·	·
9H-CC	B	B	·	·	·	·	·	·	·	·	·	·	·	·	·	·	·	·	·	·	·	·	·	·	·	·	·	·	·	·	·	·	·
10X-CC	B	B	·	·	·	·	·	·	·	·	·	·	·	·	·	·	·	·	·	·	·	·	·	·	·	·	·	·	·	·	·	·	·
11X-CC	B	B	·	·	·	·	·	·	·	·	·	·	·	·	·	·	·	·	·	·	·	·	·	·	·	·	·	·	·	·	·	·	·
12X-CC	B	B	·	·	·	·	·	·	·	·	·	·	·	·	·	·	·	·	·	·	·	·	·	·	·	·	·	·	·	·	·	·	·
13X-CC	B	B	·	·	·	·	·	·	·	·	·	·	·	·	·	·	·	·	·	·	·	·	·	·	·	·	·	·	·	·	·	·	·
14X-CC	B	B	·	·	·	·	·	·	·	·	·	·	·	·	·	·	·	·	·	·	·	·	·	·	·	·	·	·	·	·	·	·	·
139-858D-																																	
1H-1, 0–1	F	F	M	X	·	·	X	X	X	·	·	X	X	X	X	·	X	·	·	·	·	·	·	·	·	·	X	·	X	·	·	·	·
1H-CC	R	F	P	X	X	·	X	·	X	X	X	·	·	·	·	·	·	·	·	·	·	·	·	·	·	·	·	·	X	·	·	·	X
2H-CC	C	F	P	X	X	X	·	·	X	·	·	·	·	·	·	·	·	·	·	·	·	·	·	·	·	·	·	·	·	·	·	·	·
4H-CC	B	B	·	·	·	·	·	·	·	·	·	·	·	·	·	·	·	·	·	·	·	·	·	·	·	·	·	·	·	·	·	·	·
5H-CC	B	B	·	·	·	·	·	·	·	·	·	·	·	·	·	·	·	·	·	·	·	·	·	·	·	·	·	·	·	·	·	·	·
6X-CC	B	B	·	·	·	·	·	·	·	·	·	·	·	·	·	·	·	·	·	·	·	·	·	·	·	·	·	·	·	·	·	·	·
7X-CC	B	R	·	·	·	·	·	·	·	·	·	·	·	·	·	·	·	·	·	·	·	·	·	·	·	·	·	·	·	·	·	·	·
139-858F-																																	
2R-CC	B	B	·	·	·	·	·	·	·	·	·	·	·	·	·	·	·	·	·	·	·	·	·	·	·	·	·	·	·	·	·	·	·
4R-CC	B	R	P	X	·	·	·	·	·	·	·	·	·	·	·	·	·	·	·	·	·	·	·	·	·	·	·	·	·	·	·	·	·
5R-CC	B	B	·	·	·	·	·	·	·	·	·	·	·	·	·	·	·	·	·	·	·	·	·	·	·	·	·	·	·	·	·	·	·

Table 6 (continued).

	Gyroidina altiformis	*Gyroidina planulata*	*Gyroidina* sp. A	*Gyroidina* spp.	Lagenids	*Melonis barleeanum*	*Melonis pompilioides*	*Nonion labradorica*	*Nonionella digitata*	*Oridorsalis tener*	*Pullenia bulloides*	*Pullenia quinqueloba*	*Pullenia salisburyi*	*Sphaeroidina bulloides*	*Stainforthia complanata*	*Uvigerina dirupta*	*Uvigerina hispida*	*Uvigerina senticosa*	*Uvigerina* spp.	*Valvulineria inequalis*	*Valvulineria laevigata*	*Valvulineria* spp.	Indeterminate	Others:	Agglutinated taxa	Anhydrite and/or gypsum	Barite	Calcite masses or crystals	Cemented clay lumps	Diatoms	Dolomite nodule	Mineral grains	Radiolarians	Recrystallized foraminifers	Sulfides	Test fragments
139-858B-																																				
1H-1, 0–1	·	·	·	·	·	·	·	·	·	·	·	·	·	·	·	·	·	·	·	·	·	·	·		X	·	·	·	·	·	·	·	·	·	·	·
1H-CC	·	·	·	·	·	·	·	·	·	·	·	·	·	·	·	·	·	·	·	·	·	·	·		X	·	A	·	·	·	·	·	R	·	·	·
2H-CC	·	·	·	·	·	·	·	·	·	·	·	·	·	·	·	·	·	·	·	·	·	·	·		·	·	·	·	A	·	·	·	·	·	X	·
3H-CC	·	·	·	·	·	·	·	·	·	·	·	·	·	·	·	·	·	·	·	·	·	·	·		·	A	·	·	·	·	·	·	·	·	X	·
5H-CC	·	·	·	·	·	·	·	·	·	·	·	·	·	·	·	·	·	·	·	·	·	·	·		·	X	·	·	X	·	·	·	·	·	X	·
6H-CC	·	·	·	·	·	·	·	·	·	·	·	·	·	·	·	·	·	·	·	·	·	·	·		·	·	·	·	A	·	·	·	·	·	·	·
8X-CC	·	·	·	·	·	·	·	·	·	·	·	·	·	·	·	·	·	·	·	·	·	·	·		·	·	·	·	A	·	·	·	·	·	·	·
139-858C-																																				
1H-1, 0–1	·	·	X	·	·	X	·	·	·	·	·	·	X	X	·	·	X	X	·	·	·	·	X		X	A	·	·	·	A	·	·	A	·	·	·
1H-CC	X	X	X	·	X	X	X	·	·	X	·	·	·	·	X	X	·	X	·	X	X	X	·		·	·	·	·	·	·	·	·	·	R	·	A
2H-CC	·	·	X	·	X	X	X	X	X	X	X	·	X	·	X	·	·	X	·	·	·	·	X		X	·	·	·	·	·	·	·	·	R	X	·
3H-CC	·	·	·	·	·	·	·	·	·	·	·	·	·	·	·	·	·	·	·	·	·	·	·		·	·	·	·	A	·	·	·	·	·	A	·
5H-CC	·	·	·	·	·	·	·	·	·	·	·	·	·	·	·	·	·	·	·	·	·	·	·		·	X	·	·	A	·	·	·	·	·	X	·
6H-CC	·	·	·	·	·	·	·	·	·	·	·	·	·	·	·	·	·	·	·	·	·	·	·		·	R	·	·	A	·	·	·	·	·	R	·
7H-CC	·	·	·	·	·	·	·	·	·	·	·	·	·	·	·	·	·	·	·	·	·	·	·		·	·	·	·	A	·	·	·	·	·	X	·
8H-CC	·	·	·	·	·	·	·	·	·	·	·	·	·	·	·	·	·	·	·	·	·	·	·		·	·	·	·	A	·	·	·	·	·	X	·
9H-CC	·	·	·	·	·	·	·	·	·	·	·	·	·	·	·	·	·	·	·	·	·	·	·		·	A	·	A	A	·	·	·	·	·	X	·
10X-CC	·	·	·	·	·	·	·	·	·	·	·	·	·	·	·	·	·	·	·	·	·	·	·		·	·	·	·	X	·	·	·	·	·	X	·
11X-CC	·	·	·	·	·	·	·	·	·	·	·	·	·	·	·	·	·	·	·	·	·	·	·		·	·	·	·	A	·	·	·	·	·	X	·
12X-CC	·	·	·	·	·	·	·	·	·	·	·	·	·	·	·	·	·	·	·	·	·	·	·		·	·	·	·	A	·	·	A	·	·	·	·
13X-CC	·	·	·	·	·	·	·	·	·	·	·	·	·	·	·	·	·	·	·	·	·	·	·		·	X	·	·	X	·	·	·	·	·	X	·
14X-CC	·	·	·	·	·	·	·	·	·	·	·	·	·	·	·	·	·	·	·	·	·	·	·		·	X	·	·	A	·	·	·	·	·	·	·
139-858D-																																				
1H-1, 0–1	·	·	·	X	·	X	·	·	·	·	·	X	·	·	·	·	·	·	X	·	·	·	X		X	·	·	·	·	A	·	·	A	·	·	·
1H-CC	·	·	·	·	X	·	·	·	·	·	·	·	·	·	·	·	·	X	·	·	·	·	X		X	·	·	X	·	X	·	·	X	R	·	·
2H-CC	·	·	·	·	·	·	·	·	·	·	·	·	·	·	·	·	·	·	·	·	·	·	·		X	A	·	·	·	·	·	·	·	R	·	A
4H-CC	·	·	·	·	·	·	·	·	·	·	·	·	·	·	·	·	·	·	·	·	·	·	·		·	·	·	·	A	·	·	·	·	·	·	·
5H-CC	·	·	·	·	·	·	·	·	·	·	·	·	·	·	·	·	·	·	·	·	·	·	·		·	·	·	·	A	·	·	·	·	·	·	·
6X-CC	·	·	·	·	·	·	·	·	·	·	·	·	·	·	·	·	·	·	·	·	·	·	·		·	·	·	·	A	·	X	·	·	·	·	·
7X-CC	·	·	·	·	·	·	·	·	·	·	·	·	·	·	·	·	·	·	·	·	·	·	X		·	X	·	·	A	·	·	·	·	·	X	·
139-858F-																																				
2R-CC	·	·	·	·	·	·	·	·	·	·	·	·	·	·	·	·	·	·	·	·	·	·	·		·	·	·	·	A	·	·	·	·	·	X	·
4R-CC	·	·	·	·	·	·	·	·	·	·	·	·	·	·	·	·	·	·	·	·	·	·	X		·	·	·	·	A	·	·	·	·	R	·	·
5R-CC	·	·	·	·	·	·	·	·	·	·	·	·	·	·	·	·	·	·	·	·	·	·	·		·	·	·	·	A	·	·	·	·	·	·	·

Notes: A = abundant, C = common, F = few, R = rare, B = barren, G = good preservation, M = moderately good preservation, P = poor preservation.

Table 7. Range chart of calcareous nannofossils and their abundance and preservation.

Hole 858A Sample (cm)	Depth (mbsf)	Age	Nannofossil zonation	Abundance	Preservation	*Braarudosphaera bigelowii*	*Calciduscus leptoporus*	*Coccolithus pelagicus*	*Emiliania huxleyi*	*Emiliania pujosae*	small *Gephyrocapsa*	*Gephyrocapsa* sp.	*Pontosphaera* sp.
1H-1, 0–1	0.1	l. Pleis. –Holo.	NN21	C	P		F	F	F		C		R
1H-CC	2.4			C	P	R	R	C	F		C		
2H-CC	11.9			F	P			R	R		F		
3H-CC	21.4			C	P		R	F	F	R	C		
4H-CC	30.9	Pleistocene	NN21 ?	F	P	R		F			R		
5H-CC	40.4			F	P	F		F				R	
6H-CC	49.9			F	P	R		F			F		
7H-CC	58.9			F	P			R				R	
8H-CC	62.5			R	P	R		F			R		
9X-CC	71.9			C	P			C					
11X-CC	81.6			R	P			R					
13X-CC	101.0			R	P			R				R	
14X-CC	110.6			R	P			R					
15X-CC – 39X-CC	120.3– 339.1	?	?	B	—								

Hole 858B Sample (cm)	Depth (mbsf)	Age	Nannofossil zonation		Abundance	Preservation	*Calciduscus leptoporus*	*Coccolithus pelagicus*	*Emiliania huxleyi*	*Gephyrocapsa oceanica*	small *Gephyrocapsa sp.*	*Reiiticulofenestra sp.*
1H-1, 0–1	0.1	l. Pleis. -Holocene	NN21	*Emiliania huxleyi* Acme	B	—						
1H-1,128	1.28				R	P	R		R	R	R	
1H-2, 30	1.8				C	P	F	R	C	C		
1H-2,138	2.88				C	M		C	F	C		
1H-3, 54	3.54				C	P		C	R	F	F	R
1H-3,146	4.46	Pleis.	NN21 ?		R	P		R			R	
1H-CC	7.2				R	P		R				
2H-CC	16.7	?	?		B	—						
3H-CC	18.4											
4X-CC	23.9											
5H-CC	31.5											
6H-CC	32.5											
8X-CC	35.1											
9X-CC	38.6											

Hole 858C Sample (cm)	Depth (mbsf)	Age	Nannofossil zonation		Abundance	Preservation	*Calcidiscus leptoporus*	*Coccolithus pelagicus*	*Emiliania huxleyi*	*Emiliania pujosae*	small *Gephyrocapsa*	*Gephyrocapsa* sp.	*Pontosphaera* sp.	*Syrocosphaera pulchra*
1H-1, 0–1	0.1	l. Pleis. - Holo.	NN21	*E. hux.* Acme	C	P	F	R	R	R	C			R
1H-CC	3.5				C	P		C	C	R	C		R	
2H-CC	13.0				C	P	R	F	F	R	C			
3H-CC	22.5	Pleis.	NN21?		R	P					R			
5H-CC	33.0				R	P						R		
6H-CC– 13X-CC	41.5– 83.4	?	?		B	-								

Table 7 (continued).

Hole 858D Sample (cm)	Depth (mbsf)	Age	Nannofossil zonation		Abundance	Preservation	*Braarudosphaera bigelowii*	*Calcidiscus leptoporus*	*Coccolithus pelagicus*	*Emiliania huxleyi*	*Emiliania pujosae*	small *Gephyrocapsa*	*Gephyrocapsa caribbeanica*	*Pontosphaera japonica*	*Pontosphaera* sp.
1H-1, 0–1	0.1	l. Pleistocene–Holocene	NN21	*E. hux.* Acme	R	P		R		R		R			
1H-1, 97	0.9				A	M	F		C	C		A			
1H-1, 116	1.2				A	M	F		C	C		A			R
1H-2, 12	1.6				A	M	F		C	F		A		R	
1H-4, 17	4.7				A	M			C	R		A	R		R
1H-5, 120	7.2				A	M			C	C	F	C	R		
1H-6, 6	7.5				C	P			F	R	R	F			
1H-6, 144	9.0				B	—									
1H-CC	9.3				R	P			R	R		R			
2H-3, 3	12.3	?	?		B	—									
2H-CC	18.8				R	P			R						
4H-CC	28.3				R	P			R						
5H-CC	28.8				B	—									
6X-CC	37.2				B	—									

Hole 858E Sample (cm)	Depth (mbsf)	Age	Nannofossil zonation	Abundance	Preservation	*Calcidiscus leptoporus*	*Emiliania huxleyi*	small *Gephyrocapsa*
1W-CC	38.5	l. Pleis. –Holo.	NN21	F	P	F	R	F

Hole 858F Sample (cm)	Depth (mbsf)	Age	Nannofossil zonation	Abundance
1W-CC	27.8	?	?	Barren
2R-CC	37.0			
4R-CC	56.0			
9R-CC	103.9			
12R-CC	132.9			
17R-CC	181.3			
18R-CC	190.9			
21R-CC	220.0			
22R-CC	229.6			
23R-CC	239.3			
24R-CC	248.9			

Note: A = abundant, C = common, F = few, R = rare, B = barren, G = good preservation, M = moderately good preservation, P = poor preservation.

range and shows a jump at 30 mbsf from higher to lower values. However, discrete samples which provide more reliable results than the whole cores, show lower intensities between 24 and 30 mbsf, indicating that in this part the pattern of the intensity seem to be similar to the susceptibility. One of the goals of later rock magnetic investigations is to determine why some sediments are more influenced by drilling than others.

Hole 858B

Because of the poor recovery in the lower part of the hole, paleomagnetic measurements were taken only for Cores 139-858B-1H, -2H and -5H. The core liner of Core 139-858B-3H was damaged and Core 139-858B-4X had no recovery. The measured temperature at 19.5 mbsf was about 200°C, so that aluminum core liners were used

Table 8. Comparison of sequences zoned by calcareous nannofossils (Martini, 1971; Gartner, 1977) and planktonic foraminifers (Lagoe and Thompson, 1988).

Hole 858A Sample (cm)	Depth (mbsf)	Age	Foraminifer zone	Nannofossil zone
1H-1, 0–1	0.0	Holo.	CD1	NN21
1H-CC	2.4	late Pleist.	CD2?	
2H-CC	11.9			
3H-CC	21.4	Pleistocene		NN21?
4H-CC	30.9			
5H-CC	40.4			
6H-CC	49.9			
7H-CC	58.9			
8H-CC	62.5			
9X-CC	71.9			
10P-CC	72.9			
11X-CC	81.6			
12X-CC	91.3	?	?	?
13X-CC	101.0			
14X-CC	110.6			
15X-CC	120.3			
16X-CC	129.9			
17X-CC	139.6			
18X-CC	149.3			
19X-CC	159.0			
20X-CC	168.6			
21X-CC	178.2			
22X-CC	187.9			
23X-CC	197.6			
24X-CC	207.3			
25X-CC	216.9			
26X-CC	226.6			
27X-CC	236.2			
28X-CC	245.9			
29X-CC	255.6			
30X-CC	265.3			
31X-CC	274.5			
32X-CC	281.7			
33X-CC	291.5			
34X-CC	301.4			
35X-CC	311.2			
36X-CC	315.2			
37X-CC	322.7			
38X-CC	332.4			
39X-CC	339.1			

Hole 858B Sample (cm)	Depth (mbsf)	Age	Foraminifer zone	Nannofossil zone	
1H-1, 0–1	0.0	Holo.	CD1	NN21	*E. hux.* Acme
1H-1,128	1.3	l. Pleisto.	CD2		
1H-2, 30	1.8				
1H-2,138	2.9				
1H-3, 54	3.5			NN21?	
1H-3,146	4.5	Pleist.			
1H-CC	7.2	?	?	?	
2H-CC	16.7				
3H-CC	18.4				
4X-CC	23.9				
5H-CC	31.5				
6H-CC	32.5				
7X-CC	32.7				
8X-CC	35.1				
9X-CC	38.6				

Hole 858C Sample (cm)	Depth (mbsf)	Age	Foraminifer zone	Nannofossil zone	
1R-1, 0–1	0.0	Holo.	CD1	NN21	*E. hux.* Acme
1H-CC	3.5	l. Pleist.	CD2		
2H-CC	13.0	?	?	?	
3H-CC	22.5				
4P-CC	23.5				
5H-CC	33.0				
6H-CC	41.5				
7H-CC	46.5				
8H-CC	47.5				
9H-CC	49.3				
10X-CC	54.5				
11X-CC	64.0				
12X-CC	73.7				
13X-CC	83.4				
14X-CC	93.1				

Hole 858D Sample (cm)	Depth (mbsf)	Age	Foraminifer zone	Nannofossil zone	
1H-1, 0–1	0.0	Holo.	CD1	NN21	*E. hux.* Acme
1H-CC	9.3	l. Pleist.	CD2		
2H-CC	18.8	?	?	?	
3H-CC	19.8				
4X-CC	28.3				
5H-CC	28.8				
6H-CC	37.2				
7X-CC	40.7				

Hole 858F Sample (cm)	Depth (mbsf)	Age	Foraminifer zone	Nannofossil zone
1W-CC	27.8	?	?	?
2R-CC	37.0			
4R-CC	56.0			
9R-CC	103.9			
12R-CC	132.9			
17R-CC	181.3			
18R-CC	190.9			
21R-CC	220.0			
22R-CC	229.6			
23R-CC	239.3			
24R-CC	248.9			

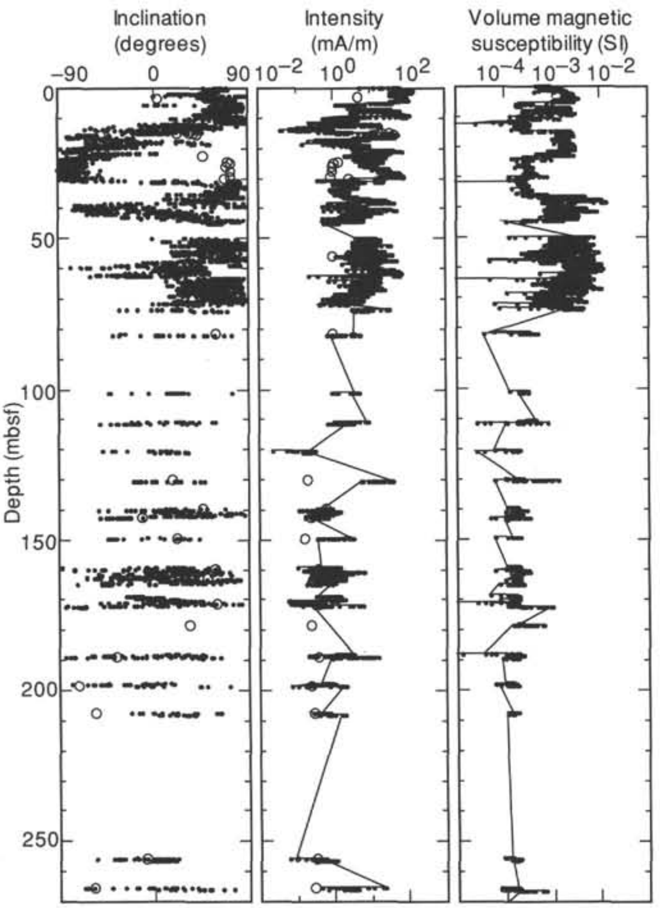

Figure 25. Inclination, intensity, and volume magnetic susceptibility after demagnetization at 15-mT peak alternating field vs. depth from Hole 858A. The intensity and the stable inclination obtained from stepwise AF demagnetization for sediment cube samples are shown by open circles.

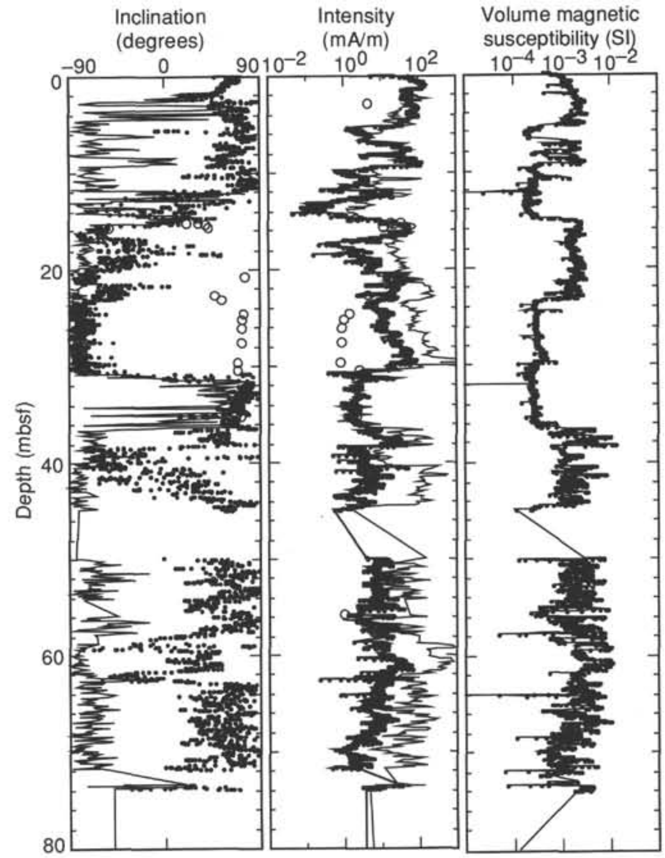

Figure 26. Inclination, intensity, and volume magnetic susceptibility vs. depth of Cores 139-858A-1H through -11X. NRM inclination and NRM intensity are shown by thin lines, inclination and intensity after demagnetization at 15-mT alternating field are shown by solid circles, and discrete samples are represented by open circles.

instead of the normal plastic liner for Cores 139-858B-2H and -5H. We used wrought aluminum alloy (6063) with a nominal addition of 0.4% Si and 0.7% Mg. It turned out that these liners were not suitable for susceptibility measurements and moderately acceptable for magnetic measurements in the pass-through magnetometer. To determine the magnetic influence of this material we measured an empty aluminum liner (divided into two halves) in the pass-through magnetometer and also examined the magnetic behavior after demagnetization. Figure 28 shows the intensity plot before and after demagnetization for one half of the core. The intensity of the aluminum liner lies between 0 and 5 mA/m and thus in the same order as the sediment. Nevertheless, the intensity of Core 139-858B-2H seems to be reliable (Fig. 29, 7.2–16.7 mbsf), although this observation is based only on one core and must be considered with caution. Susceptibility measurements of this core could not be taken because of strong disturbance by induced currents over the aluminum liner during the measurement on the MST. As in Hole 858A, the NRM intensities lie between 0.1 and 1000 mA/m, and decrease to intensities between 0.1 and 100 mA/m after 15-mT demagnetization (Fig. 29). We observe again sections with stable magnetization and those with unstable magnetization, independent of the different kinds of core liners. At 24 mbsf we observe a small zone with high and stable magnetic intensity. This high intensity of magnetization is confined to 0–80 cm in Section 139-858B-5H-1. Unfortunately, Core 139-858B-4X had no recovery and the high intensity part is at the top of the next core. We do not really know whether this signal is real or whether material which has fallen down in the borehole from a higher layer has influenced the results.

Hole 858C

Hole 858C was drilled using the APC coring system to a depth 49.3 mbsf and was finished with the XCB coring system at a depth of 93 mbsf. The recovery to 42 mbsf was good and magnetic measurements could be taken. Below 42 mbsf the recovery of the drilled sediment was too low to get reliable paleomagnetic results. Only Core 139-858C-12X (64 to 68 mbsf) had sufficient recovery for pass-through measurements. One discrete sample was taken from this core and demagnetized.

The NRM intensity, the intensity after demagnetization at 15 mT, and susceptibility are of the same order as in the other holes at Site 858. The stable inclination of discrete samples and the magnetic results from the archive halves are shown in Figure 30. The susceptibility is generally consistent with the other holes of Site 858 and the other holes from Leg 139, although we observe values between 10^{-5} and 10^{-4} SI from 13 to 18 mbsf which are the lowest measured during Leg 139. This depth range (13–22 mbsf) is described as a hydrothermal carbonate cap (see "Lithostratigraphy and Sedimentology" section, this chapter).

At 23 mbsf we observe an abrupt increase in magnetic intensity and susceptibility. This high-intensity interval is not seen in Hole 858A but is thought to correspond to similar intervals of high intensity in Holes 858B and 858D. As in Hole 858B, the interval of high intensity is at the top of a core; the preceding core (139-858C-4P) had no recovery. It is possible that high-intensity material is fallen from a higher part of the hole, but then we should have observed sections with similarly high intensity, magnetic stability, and structure above 23 mbsf.

Table 9. Paleomagnetic results of progressive demagnetization experiments on sediments from Holes 858A, 858B, 858C, 858D, and 858F.

Core, section, interval (cm)	Depth (mbsf)	I (degrees)	J_0 (mA/m)	MDF (mT)	Lithology
139-858A-					
2H-1, 46–48	2.86	61	35	9 (?)	Silty clay
3H-3, 49–51	15.16	33	22	35	Silty clay
3H-3, 57–59	15.24	22	44	27	Silty clay
3H-3, 68–70	15.35	39	24	30	Silty clay
3h-3, 96–98	15.63	42	56	30	Silty clay
3H-3, 100–102	15.67	–52	25	15	Silty clay
3H-7, 13–15	20.80	76	4 (9)	46 (32)	Silty clay
4H-1, 133–135	22.73	48	16 (8)	5 (16)	Silty clay
4H-2, 17–19	23.07	54	9 (8)	18 (27)	Silty clay
4H-3, 17–19	24.57	75	1.3 (3.6)	39 (14)	Silty clay
4H-3, 89–91	25.29	74	0.71	80	Silty clay
4H-4, 26–28	26.16	73	1.2 (?)	63	Silty clay
4H-5, 25–27	27.65	74	0.77	50	Silty clay
4H-6, 79–81	29.69	70	1.3	18	Silty clay
4H-7, 6–8	30.46	70	14	3	Silty clay
5H-3, 136–138	35.26	72	3.3	24	Silty clay
6H-2, 98–100	42.88	56 (Unstable)	30	3	Silty clay
7H-4, 137–139	55.77	72	1.8	18	Silty clay
12X-CC, 5–7	81.85	61	3.5	7	Bedded sandstone
17X-1, 24–26	130.14	Unstable	2.0	3	Medium-grained sandstone
18X-1, 17–19	139.77	–10 (Unstable)	0.96	7	Medium-grained sandstone
18X-3, 14–16	142.74	–9	0.95	6	Silty claystone
19X-1, 28–30	149.58	Unstable	0.42	10	Bioturbated clay
20X-1, 62–64	159.62	55	0.25	38	Silty claystone (bioturbated)
20X-3, 65–67	162.58	53	0.96	32	Mmedium to fine-grained sandstone
21X-2, 128–130	171.38	62	0.46	29	Medium-grained sandstone
22X-1, 12–14	178.32	34	0.5	4 (?)	Claystone
23X-1, 113–115	189.03	Unstable	1.5	5	Claystone with laminated fine sand
25X-1, 46–48	207.76	Unstable	1.8	5	Silty claystone
30X-1, 36–38	255.96	Unstable	0.7?	10	Silty claystone
31X-1, 21–23	265.51	Unstable	0.74	12	Silty claystone
37X-CC, 14–16	315.34	65	1.54	32	Coarse-grained sandstone
139-858B-					
1H-3, 68–70	3.68	50	104	31	Silty clay
1H-4, 46–48	4.96	40	4	40	Silty clay
2H-6, 7–9	14.77	Unstable	32	?	Clay
2H 6, 13–15	14.83	Unstable	123	?	Clay
139-858C-					
2H-3, 110–112	7.60	64	32	20	Silty clay
3H-1, 96–98	13.96	69	0.90	20	Clay
3H-1, 113–115	14.13	73	1.3	30	Clay
3H-4, 81–83	18.31	Unstable	126	?	Microbreccia of silty mudstone
7H-1, 49–51	41.99	45	1.2	10	Claystone
12X-1, 75–77	65.75	62	1.0	15	Silty claystone
139-858D-					
2H-5, 102–104	16.32	Unstable	3.7	15	Silty clay
2H-7, 5–7	18.35	70	0.62	27	Silty clay
139-858F-25R-1, 40–42	249.30	Unstable	0.28	36	Silty claystone

Hole 858D

Hole 858D was drilled at the center of the vent area using the APC coring system to 28 mbsf and the XCB coring system to 37 mbsf. The NRM and intensity after demagnetization at 15 mT ranges between 0.8 and 8000 mA/m and shows a complicated pattern with increasing depth (Fig. 31). We observe a stable intensity interval (~100 mA/m) from 2 to 9 mbsf. From 9.0 to 11.5 mbsf the intensity decreases and shows values of about 3 mA/m. Below this depth the intensity increases constantly to values of 8000 mA/m and remains high to 19 mbsf. The outside of the butyrate core liners of Sections 139-858D-2H-4 through -2H-7 (13.8–18.8 mbsf) were melted by high *in-situ* temperatures. The surfaces of the liners were rough and the color was changed from transparent to brown during coring. We were dubious of the high magnetic intensity values, so we investigated the contaminated plastic liners. We scraped and collected some fragments from the outside of the core liner and examined the material with a magnet and under a microscope. This inspection revealed the cause of the high intensities—iron fragments from the core barrel had fused into the outer part of the plastic liners.

Below 19 mbsf we observe an abrupt decrease in susceptibility. This core was collected with the pressure core sampler and the usual diameter of the core is only 42 mm. The diameter of APC cores is

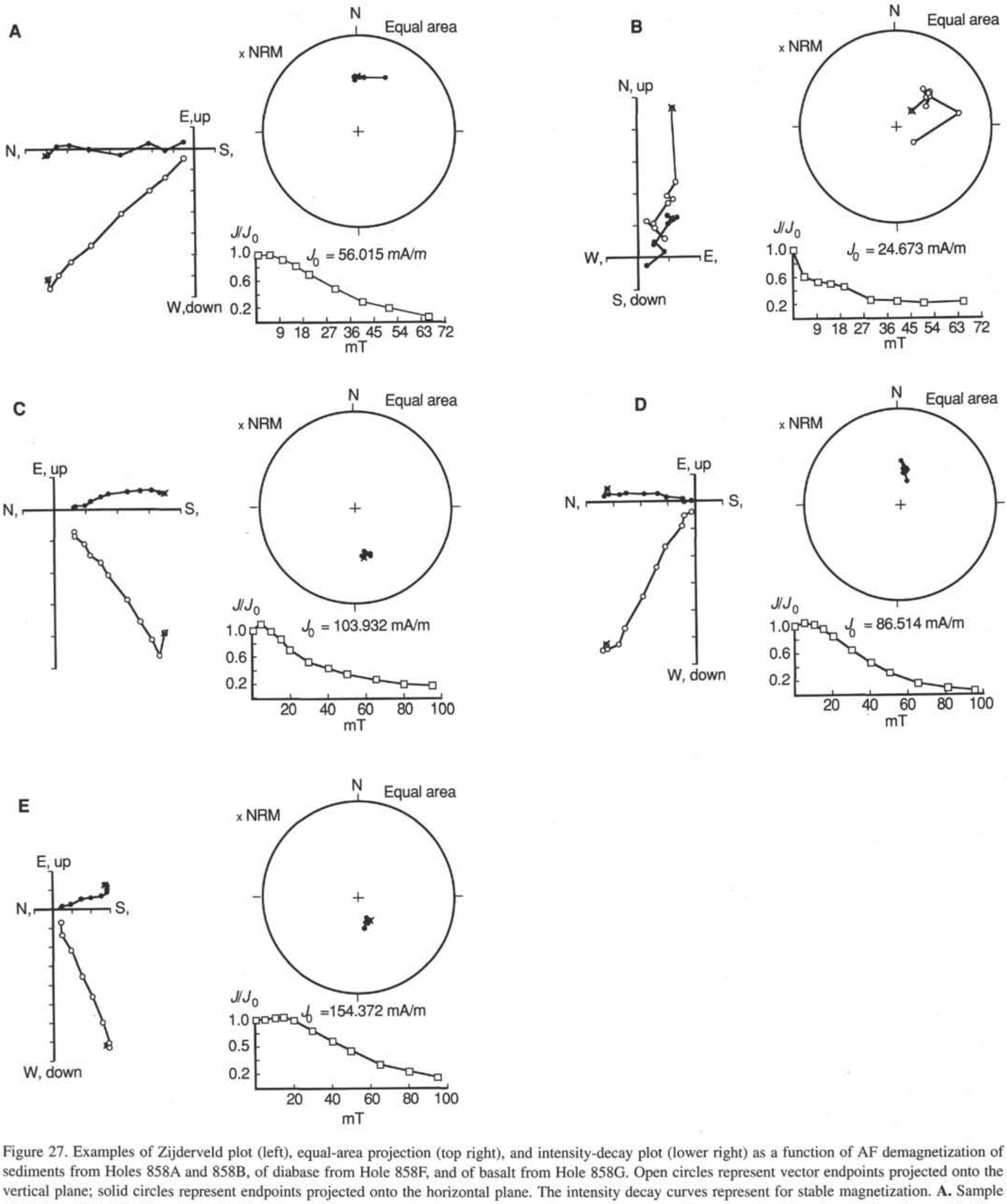

Figure 27. Examples of Zijderveld plot (left), equal-area projection (top right), and intensity-decay plot (lower right) as a function of AF demagnetization of sediments from Holes 858A and 858B, of diabase from Hole 858F, and of basalt from Hole 858G. Open circles represent vector endpoints projected onto the vertical plane; solid circles represent endpoints projected onto the horizontal plane. The intensity decay curves represent for stable magnetization. **A.** Sample 139-858A-3H-3, 96–98 cm, 0 to 65 mT, scale = 6.00 mA/m per division. **B.** Sample 139-858A-3H-3, 100–102 cm, 0 to 65 mT, scale = 5.00 mA/m per division. **C.** Sample 139-858A-1H-3, 68–70 cm, 0 to 95 mT, scale = 20.00 mA/m per division. **D.** Sample 139-858F-26R-1, 63–65 cm, 0 to 95 mT, scale = 14.00 mA/m per division. **E.** Sample 139-858G-12R-1, 57–59 cm, 0 to 95 mT, scale = 20.00 mA/m per division.

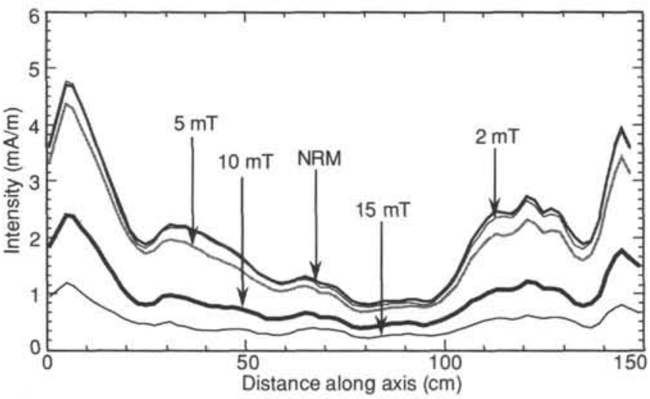

Figure 28. NRM intensity and intensity after demagnetization in a 2-, 5-, 10-, and 15-mT alternating peak field of an empty aluminum liner.

usually 66 mm. So the volume of a pressure core is about 40% of the volume of an APC core if both cores are filled completely. However, this explanation alone cannot explain the strong decrease in the susceptibility. Unfortunately, we do not have pass-through intensity data from this depth range. At 20 mbsf the susceptibility seems to increase again. Down to this depth we had used normal plastic liners but changed there to aluminum liners. As discussed in the case of Hole 858B, we could not use aluminum liners for susceptibility measurements and the reliability for magnetization measurements is also doubtful. Nevertheless, we measured the archive half of Core 139-858D-4H in the pass-through cryogenic magnetometer and observed again a decrease in NRM intensity. At 28.5 mbsf we observe a short increase in intensity followed by a decrease. The interval of high intensity might have the same origin as in Holes 858B and 858C. However, as in the other holes, the preceding core had no recovery and the consistency of the trend is unclear.

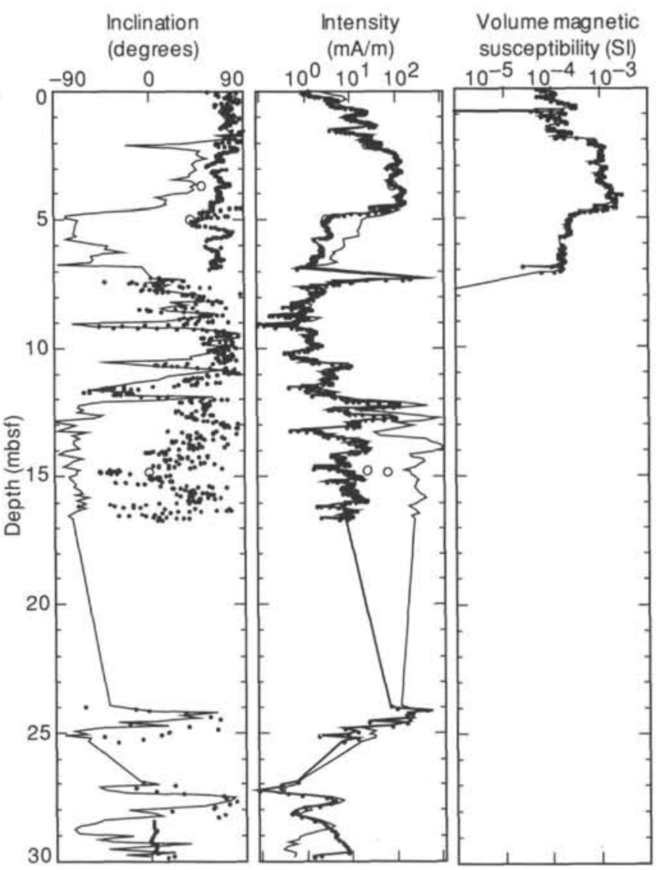

Figure 29. Inclination, intensity, and volume magnetic susceptibility vs. depth of Cores 139-858B-1H through -6H. NRM inclination and NRM intensity are shown by thin lines, inclination and intensity after demagnetization at 15-mT alternating field are shown by solid circles, and discrete samples are represented by open circles.

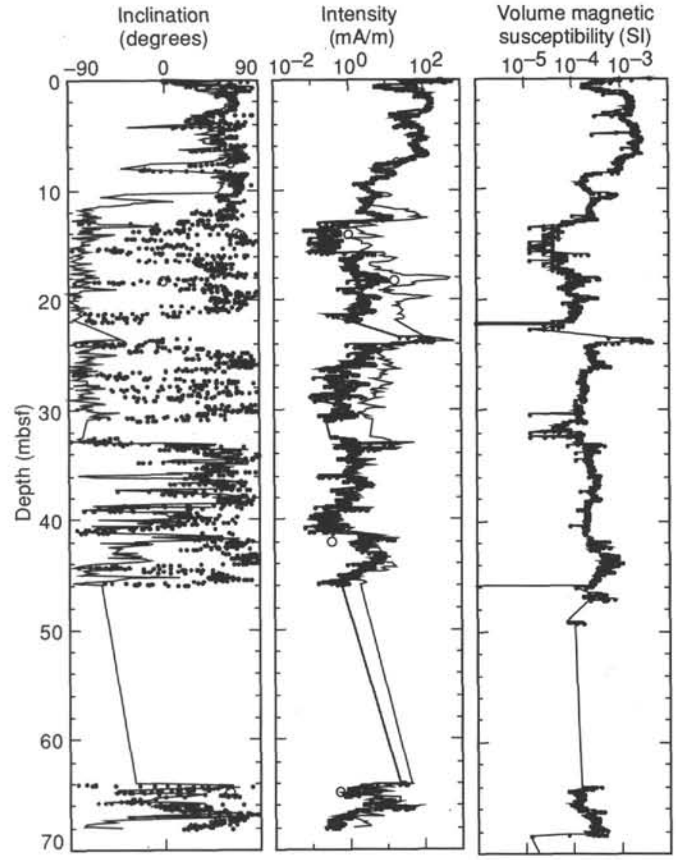

Figure 30. Inclination, intensity, and volume magnetic susceptibility vs. depth of Cores 139-858C-1H through -12X. NRM inclination and NRM intensity are shown by thin lines, inclination and intensity after demagnetization at 15-mT alternating field are shown by solid circles, and discrete samples are represented by open circles.

The inclination before and after demagnetization shows similar behavior as the inclination in Hole 858A. The stable negative inclination between 14 and 18 mbsf can be explained with the contamination of rust in the core liner. This explanation is confirmed by the results of discrete samples, which show much lower intensities than the archive half and have positive inclinations (Fig. 31).

Holes 858F and 858G

Holes 858F and 858G were drilled with RCB drilling system but the paleomagnetic measurements for the archive halves are not reliable because of the low recovery. We demagnetized one discrete sample of sediment from Hole 858F and eight discrete samples of igneous rocks from Hole 858F and Hole 858G in the Schonstedt demagnetizer and measured them in the Molspin Spinner magnetometer. The results are shown in Tables 9 and 10. Examples of two Zijderveld diagrams are shown in Figure 27.

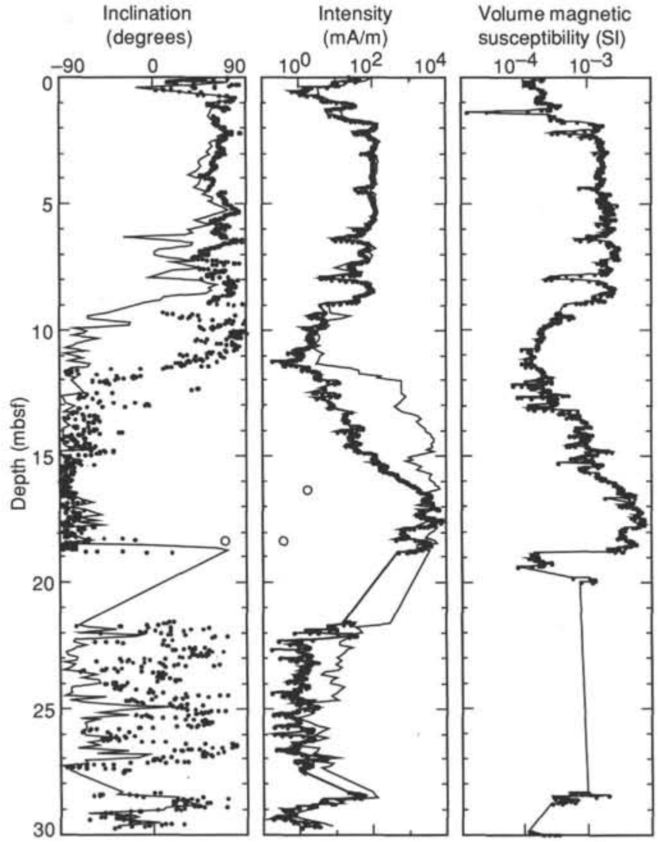

Figure 31. Inclination, intensity, and volume magnetic susceptibility vs. depth of Cores 139-858D-1H through -6X. NRM inclination and NRM intensity are shown by thin lines, inclination and intensity after demagnetization at 15-mT alternating field are shown by solid circles, and discrete samples are represented by open circles.

FLUID GEOCHEMISTRY

Seven holes were drilled at Site 858 within and near a hydrothermal discharge zone where the conductive heat flow locally exceeds 20 W/m^2. Hole 858B was drilled within 5 to 20 m of a vent that is discharging clear water at a temperature of 276°C. Holes 858D, 858E, 858F, and 858G were drilled about 60 m north of this vent and Hole 858C was drilled 140 m west of it. These six holes are located within a region of high backscatter in side-scan sonar records that defines the hydrothermal upflow zone. Hole 858A was drilled 100 m west of this reflective area, 250 m northwest of the vent near Hole 858B and 170 m northwest of the nearest high-temperature vent.

Interstitial water was obtained from six of the seven holes at Site 858. (Hole 858E was abandoned when it was discovered that the drill string had reentered Hole 858D.) Pore water was obtained by squeezing sediment from whole-round samples taken from Holes 858A, 858B, 858C, 858D, and 858F (Table 11). These samples were squeezed immediately upon retrieval of the cores. Additional samples were taken several days later from intervals of steep chemical gradients in Holes 858B and 858D. These samples were taken as quarter-rounds because the cores had already been split. These samples exhibit spuriously high chlorinity and low alkalinity as a result of evaporation and calcium carbonate precipitation. In Figures 32 to 34, all concentrations in these samples have been adjusted downward by 2.6% to correct for evaporation.

Interstitial water also was obtained using the water-sampler temperature probe, the pressure core sampler, and the ground rock interstitial normative determination (GRIND) technique (Table 12). The Los Alamos sampler, designed to collect water from an open borehole, was used once, in Hole 858F. The sample obtained is largely surface seawater which was pumped into the hole during drilling. Twenty-two samples of pore water were obtained using the GRIND technique on lithified sediment and basalt (see "Fluid Geochemistry" section, "Explanatory Notes" chapter, this volume). Ten of these samples were collected immediately adjacent to rock that yielded water upon squeezing. As at Site 857, the pore water obtained by the GRIND technique closely resembles that obtained by squeezing of whole-rounds, when normalized to the same chlorinity. In Figures 32 to 34, all GRIND samples have been corrected to the chlorinity of a nearby squeezed sample or, where none was available, to 566 mmol/kg.

Several samples are believed to be contaminated with surface seawater used as drilling fluid, or to be otherwise affected by sampling artifacts. Samples 139-858A-34X-1, 8–15 cm, and -858F-11R-1, 0–3 cm, are diluted with surface seawater, as evidenced by their high sulfate concentration and low chlorinity. Sample 139-858D-4H-2, 56–80 cm, was taken from a soupy section of core that contained many carbonate nodules. This core may have been disturbed by drilling and the sample contaminated with drilling fluid. Alternatively, the soupy consistency of the core may have been produced by lateral flow of pore water through this interval. Two samples, 139-858A-21X-2, 90–100 cm, and -858-10X-1, 30–35 cm, have exceptionally high concentrations of sulfate which are believed to result from dissolution of anhydrite upon recovery. Anhydrite is present in the sediments of each of these samples. Sample 139-858C-10X-1, 30–35 cm, had a dark rind on the outside of the whole-round. This rind is organic-rich and appears to have formed during the drilling process. A similar organic-rich rind is evident in the squeeze cakes of several sediment samples that have been squeezed at pressures of 2.8 MPa for several hours. This organic-rich rind is believed to form by migration of

Table 10. Inclination of stable component (I), intensity of natural remanent magnetization (J_0), median destructive field (MDF), volume magnetic susceptibility (χ), and Q-ratio for igneous rock samples.

Core, section, interval (cm)	Depth (mbsf)	I (degrees)	J_0 (mA/m)	MDF (mT)	χ_0 ($\times 10^{-4}$ SI)	Q-ratio	Lithology
139-858F-							
25R-1, 111–113	250.01	−70	6	40	2.9	0.46	Fine-grained basalt
26R-1, 63–65	259.23	60	87	38	7.4	2.65	Fine-grained diabase
139-858G-							
1R-1, 12–14	276.92	61	28	62	4.9	1.29	Variolitic fine-grained basalt
2R-1, 34–36	286.84	67	1293	32	183	1.58	Variolitic basalt
7R-1, 40–42	335.20	55	347	84	4.6	16.79	Variolitic basalt
10R-1, 68–70	365.58	69	30	60	8.1	0.83	Variolitic basalt
12R-1, 57–59	384.77	67	154	51	3.97	8.7	Variolitic basalt
16R-1, 62–64	423.52	Unstable	3	60	3.71	0.18	Spherulitic diabase

Table 11. Composition of pore water from sediment at Site 858.

Sample[a]	Core, section, interval (cm)	Depth (mbsf)	Volume (mL)	Squeeze pressure (psi)	pH	Alkalinity (meq/kg)	Chlorinity (mmol/kg)	Sulfate (mmol/kg)	Na[b] (mmol/kg)	K (mmol/kg)	Mg[c] (mmol/kg)	Ca[c] (mmol/kg)	Si (µmol/kg)	NH_4 (µmol/kg)	Phosphate (µmol/kg)	H_2S (mmol/kg)
Surface seawater (9 August 91)							497.6	25.73	425.3	10.7	48.25	9.36	0	0	0.0	
Bottom seawater (collected by *Alvin*, 6 August 91)							540.2	27.73	461.1	10.5	52.95	10.24	183	0	2.5	
	139-858A-															
IW-1	1H-1, 144–150	1.47	45	10,000	7.86	3.203	541.6	27.74	468.1	11.2	50.49	9.96	473	59	5.3	
IW-2	2H-2, 144–150	5.37	46	12,000	7.89	4.030	542.6	27.29	465.1	11.8	51.59	10.44	774	210	20.6	
IW-3	2H-3, 144–150	6.87	35	10,000	7.89	4.085	544.5	27.42	467.3	10.6	52.04	10.63	668	234	17.5	
IW-4	2H-5, 144–150	9.87	35	10,000	7.92	4.446	541.0	27.45	462.2	11.1	52.39	11.01	738	254	10.8	
IW-5	3H-4, 140–150	17.62	40	10,000	7.94	5.120	543.6	26.75	462.5	9.8	52.89	11.88	1054	351	3.2	
IW-6	4H-4, 140–150	27.35	48	9,000	7.93	5.446	545.5	25.79	462.7	9.9	51.71	13.03	272	507	0.0	
IW-7	5H-4, 140–150	36.85	49	9,000	7.91	5.156	549.4	25.54	469.5	8.6	48.95	14.50	272	659	0.0	
IW-8	6H-2, 140–150	43.35	50	12,000	7.93	5.422	552.3	26.04	472.6	8.8	46.38	17.50	439	678	0.0	
IW-9	7H-2, 140–150	52.85	50	13,000	7.89	5.556	554.2	21.72	463.2	9.4	38.83	26.20	459	605	0.0	
IW-10	9X-2, 0–10	64.05	32	20,000	7.99	6.825	556.2	20.44	460.2	7.6	37.14	30.61	511	571	0.0	
IW-11	9X-5, 140–150	69.95	38	18,000	7.96	8.009	558.1	15.67	465.4	8.5	32.77	28.70	665	673	0.0	
IW-12	10P-1, 0–8	71.94	28	20,000	7.89	8.300	560.0	14.97	466.2	8.2	30.38	31.19	822	702	0.3	
IW-12	10P-1, 0–8	71.94	999	—	7.89	2.258	498.1	25.52	424.8	10.8	48.56	9.35	0		0.1	
BC-13	11I-1, 74–97	73.76	10	—	8.05	2.610	499.0	25.83	423.2	10.8	48.10	11.46	56	141		
[d]BO-13	11I-1, 74–97	73.76	425	—	7.94	5.138	461.9	23.53	424.0	11.2	41.17	16.80	305		0.1	
IW-14	11X-1, 43–53	73.38	36	20,000	7.96	8.016	555.2	14.72	462.3	8.1	30.84	29.98	627	644	0.2	
IW-15	15X-1, 84–98	111.51	48	20,000	7.88	7.196	566.9	5.96	452.4	14.6	8.65	50.37	974	912	0.0	
IW-16	16X-1, 52–62	120.87	40	30,000	7.79	8.427	562.0	13.47	448.4	14.5	8.75	58.02	1112	886	1.0	
IW-17	18X-1, 137–147	141.02	35	36,000	7.88	6.893	544.0	17.39	449.9	16.7	8.05	51.24	1288	493		
IW-18	20X-1, 138–150	160.37	30	35,000	7.88	4.316	549.4	19.65	454.0	12.4	10.90	52.24	1259	288		
IW-19	21X-2, 90–100	171.05	26	35,000	7.85	5.549	546.5	28.38	450.2	13.2	13.13	59.39	1337	371		
IW-20	23X-1, 22–31	188.17	16	38,000	7.91	7.697	546.5	8.81	442.7	15.5	9.15	47.40	1473	502		
IW-21	25X-1, 0–10	207.35	17	38,000	7.89	8.859	538.7	4.96	432.4	16.0	10.46	43.79	1200	590		
IW-22	27X-1, 3–13	226.68	6	40,000	7.87	6.326	544.5	5.08	427.9	16.2	12.27	45.78	878	795		
IW-23	29X-1, 39–46	246.33	6	40,000	7.73	5.034	575.5	5.88	392.3	18.1	11.70	78.33	1698	1873		
IW-24	30X-1, 90–102	256.56	9	40,000	7.84	5.186	578.4	5.34	398.3	16.3	13.69	75.29	783	1673		
IW-25	31X-1, 69–84	266.07	8	40,000	7.74	5.666	581.3	4.04	396.8	17.9	12.84	76.56	822	1556		
IW-26	32X-1, 15–22	274.69	5	40,000	7.78	5.414	578.4	5.22	397.1	18.8	14.32	74.02	1005	1678		
IW-27	34X-1, 8–15	291.62	8	40,000	7.79	5.108	556.5	14.99	401.0	14.6	20.77	66.63		1259		
	139-858B-															
IW-1	1H-1, 140–150	1.45	50	4,000	7.93	3.296	542.6	27.65	462.3	11.9	52.87	10.58	615	63	4.5	0
IQ-2	1H-2, 73–79	2.26	27	15,000	7.79	3.062	563.5	27.77	478.4	10.7	55.06	11.44				
IW-3	1H-2, 140–150	2.95	50	4,000	7.80	3.934	548.4	27.17	464.0	10.8	53.17	12.70	669	190	1.9	0
IQ-4	1H-3, 118–129	4.24	26	15,000	7.83	1.296	573.2	27.09	481.1	10.6	54.17	14.34				
IQ-5	1H-4, 38–44	4.91	30	20,000	7.84	1.081	576.2	26.50	481.0	10.7	52.52	16.73				
IW-6	1H-4, 140–150	5.95	38	10,000	7.98	3.762	552.1	21.75	448.3	9.4	50.31	20.30	500	351	2.0	0.130
IQ-7	2H-1, 41–73	7.77	20	22,000	7.28	0.799	576.2	28.42	458.6	10.5	55.03	27.32				
IQ-8	2H-2, 7–21	8.84	24	20,000	7.56	0.478	569.4	26.47	465.0	10.2	47.08	26.68				
IQ-9	2H-2, 129–141	10.05	29	22,000	7.51	1.353	572.3	18.08	449.1	11.9	44.89	29.51				
IW-10	2H-4, 140–150	13.15	50	2,000	7.50	3.428	589.4	2.51	406.3	17.0	12.72	73.46	1502	2195	1.3	0.11
IQ-11	2H-5, 75–87	14.01	32	22,000	7.25	0.787	606.3	8.77	402.9	14.9	13.59	89.84				
IQ-12	2H-6, 17–32	14.95	35	25,000	7.61	0.813	579.1	4.29	392.1	16.7	11.08	78.79				
IQ-13	2H-6, 110–124	15.87	33	25,000	7.94	0.997	578.1	1.47	392.2	18.2	11.61	74.23				
IW-14	3H-1, 3–13	16.78	50	5,000	7.76	4.842	557.4	5.90	373.7	15.9	14.53	76.57	1366	2254	3.8	0.141
BC-15	4I-1, 74–97	19.26	10	—	7.41	3.294	603.5	2.49	414.5	21.5	8.28	77.69	1502	3824		0.190
[d]BO-15	4I-1, 74–97	19.26	110	—	7.87	4.906	517.5	6.74	530.3	8.3	16.75	24.92	878		0.0	
IQ-16	5H-1, 125–138	25.22	9	35,000	7.48	1.857	622.9	6.47	364.3	15.9	13.63	115.09				
IW-17	5H-2, 143–150	26.87	11	40,000	7.79	2.630	631.1	0.00	347.0	15.3	8.70	126.10	2098	1844	1.1	0.09
IW-18	5H-3, 140–150	28.35	18	40,000	7.53	4.492	616.6	0.00	354.4	14.2	9.12	116.10	1854	2039	1.1	0

Table 11 (continued).

Sample[a]	Core, section, interval (cm)	Depth (mbsf)	Volume (mL)	Squeeze pressure (psi)	pH	Alkalinity (meq/kg)	Chlorinity (mmol/kg)	Sulfate (mmol/kg)	Na[b] (mmol/kg)	K (mmol/kg)	Mg[c] (mmol/kg)	Ca[c] (mmol/kg)	Si (µmol/kg)	NH_4 (µmol/kg)	Phosphate (µmol/kg)	H_2S (mmol/kg)
	139-858C-															
IW-1	1H-1, 144–150	1.47	50	1,000	7.82	3.387	543.6	27.62	466.6	12.5	51.39	10.08	428	98	3.6	
IW-2	1H-2, 144–150	2.97	50	3,000	7.84	3.332	545.5	27.73	468.0	11.8	51.67	10.54	520	93	2.3	
IW-3	2H-2, 144–150	6.47	50	5,000	7.84	3.675	546.5	27.73	467.4	9.7	53.03	11.18	312	107	0.0	
IW-4	2H-3, 140–150	7.95	50	12,000	7.89	3.612	546.5	27.87	466.1	9.3	53.44	11.72	290	117	0.0	
IW-5	2H-5, 144–150	10.97	50	12,000	7.89	4.129	549.4	27.79	463.4	9.1	55.02	13.19	222	180	0.0	
IW-6	3H-3, 144–150	17.47	40	32,000	7.83	4.614	556.2	29.23	469.9	9.9	49.15	20.44	698	273	3.9	
IW-7	3H-5, 144–150	20.47	38	32,000	7.82	6.380	556.2	30.30	469.6	10.0	49.17	22.48	322	288	1.0	
BC-8	5 I-1, 74–97	24.36	11	—	7.83	4.975	533.8	28.41	456.4	10.7	46.28	17.83	475	254		
[d]BO-8	5 I-1, 74–97	24.36	999	—	7.84	5.117	502.6	27.70	456.3	10.3	45.98	17.89	421		0.0	
IW-9	5H-4, 140–150	29.45	53	5,000	7.80	4.593	547.0	28.24	462.7	9.2	43.85	24.15	533	117	0.0	
IW-10	6H-3, 140–150	37.45	54	20,000	7.87	4.336	547.5	33.80	465.1	8.5	50.58	22.28	649	122	0.3	
IW-11	7H-1, 140–150	42.95	51	30,000	7.80	3.353	550.6	27.28	467.2	8.4	47.50	18.82	758	234	0.8	
IW-12	10aX-1, 20–25	49.53	6	40,000	7.79	3.498	546.5	20.34	455.6	10.6	45.87	16.16	1141	400	0.0	
IW-12	10bX-1, 20–25	49.53	12	40,000	7.85	3.648	549.4	20.33	460.2	10.1	45.50	16.00	914	385	0.0	
IW-12	10X-1, 30–35	49.63	5	40,000	7.74	3.684	546.5	43.35	463.7	11.4	48.67	32.01	795	385	0.2	
IW-13	11X-1, 5–15	54.60	27	40,000	7.82	3.255	546.5	16.32	455.3	10.1	45.50	12.84	820	302		
IW-14	12X-1, 131–145	65.38	46	40,000	7.82	2.991	547.5	12.59	463.5	8.6	39.57	12.03	971	337	0.0	
IW-15	13X-1, 41–46	74.14	16	40,000	7.91	6.136	545.5	6.35	466.2	10.2	9.93	33.78	1307	537	0.0	
IW-16	14X-1, 68–78	84.13	42	20,000	7.86	5.168	556.2	3.45	466.8	12.5	5.82	38.41	1356	551	0.2	
	139-858D-															
IW-1	1H-1, 144–150	1.47	40	10,000	7.78	5.053	596.1	7.62	470.4	13.0	37.33	28.75	985	824	2.4	
IQ-2	1H-3, 3–12	3.08	30	20,000	7.35	1.092	666.7	1.25	491.5	15.6	30.23	51.34				
IW-3	1H-3, 144–150	4.47	50	5,000	7.47	2.886	655.7	1.44	468.7	14.2	27.40	60.89	770	1980	0.4	
IQ-4	1H-4, 103–117	5.60	30	20,000	7.34	0.690	675.4	0.44	475.7	16.9	24.93	67.26				
IW-5	1H-5, 144–150	7.47	50	5,000	7.37	1.804	660.3	0.00	452.7	12.8	22.88	73.72	400	3317	4.1	0
IQ-6	1H-6, 128–142	8.85	30	20,000	7.58	0.871	656.0	0.21	450.2	15.9	21.52	74.06				
IQ-7	2H-2, 2–16	10.89	30	20,000	7.66	0.986	638.5	1.86	440.3	14.0	20.53	73.88				
IQ-8	2H-2, 120–133	12.07	30	20,000	7.38	0.589	638.3	2.18	433.6	13.3	20.05	78.17				
IW-9	2H-3, 144–150	13.77	50	10,000	7.66	3.301	596.3	0.91	399.1	15.9	10.53	81.02	903	3356	2.7	0
IQ-10	2H-4, 133–147	15.20	30	20,000	7.42	1.445	629.7	0.94	423.5	14.6	15.06	82.42				
IW-11	2H-5, 144–150	16.77	48	26,000	7.68	3.129	621.1	0.90	407.6	11.9	17.09	85.20	451	1932	3.4	0
IQ-12	2H-6, 133–147	18.20	32	20,000	7.46	2.101	596.6	2.33	396.1	16.8	9.79	85.47				
IW-13	3P-1, 0–13	18.87	48	8,000	7.47	3.912	580.0	2.79	390.0	15.9	10.76	79.95	960	2224	0.3	
PO-13	3P-1, 0–13	18.87	12	—	7.84	2.891	512.5	25.54	434.3	15.3	22.50	35.90	0		0.0	
BC-14	4 I-1, 74–97	20.66	5	—	7.54	2.346	569.8	2.59	398.1	19.1	7.21	70.97	2556	3766		1.09
[d]BO-14	4 I-1, 74–97	20.66	999	—	7.54	2.789	532.9	2.54	396.2	22.6	8.89	70.56	4830		0.0	
IQ-15	4H-2, 56–80	20.72	16	20,000	7.69	2.089	579.1	21.40	462.6	12.9	39.45	34.77			0.080	
IW-16	4H-2, 144–150	21.51	50	8,000	7.70	4.496	562.3	8.05	401.0	15.4	17.31	65.08	1483	1654	3.2	
IQ-17	4H-3, 100–107	22.58	12	20,000	7.61	1.536	600.5	3.49	409.5	17.7	10.36	80.57				
IW-18	4H-4, 104–118	24.15	20	25,000	7.24	1.047	598.6	5.08	402.9	16.3	8.81	86.45				
IW-19	4H-5, 144–150	26.01	50	17,000	7.54	4.213	585.4	0.69	390.3	17.3	6.70	84.11	1307	1776	2.6	0
IQ-20	4H-6, 134–149	27.46	32	25,000	7.63	2.541	566.4	3.85	390.7	17.9	10.95	73.10				
IW-21	6X-1, 96–105	38.21	30	38,000	7.63	5.801	569.1	6.01	391.5	16.8	15.90	72.49	1298	1893	0.4	
	139-858F-															
IW-1	9R-CC, 0–1	94.21	1	38,000			570.7	4.79	398.1	16.9	12.80	71.21	2107	2210		
IW-2	11R-1, 0–3	113.62	5	38,000	7.79	4.721	530.0	16.73	411.6	12.4	30.48	41.16	750	912		
IW-3	14R-1, 0–3	142.62	5	39,000	7.61	5.605	570.7	4.69	399.5	16.5	13.92	69.88	2312	2117		
IW-4	17R-1, 0–3	171.62	3	39,500	7.73	4.756	561.5	4.90	388.4	19.1	13.02	70.14	1707	2215		
IW-5	18R-1, 67–72	182.00	2	39,500			567.8	6.57	399.7	17.8	16.85	66.42	1102	1834		
IW-6	19R-1, 9–12	191.01	3	39,500			565.8	6.95	401.9	17.3	17.60	64.19	1151	1971		

Table 11 (continued).

Sample[a]	Core, section, interval (cm)	Depth (mbsf)	Volume (mL)	Squeeze pressure (psi)	pH	Alkalinity (meq/kg)	Chlorinity (mmol/kg)	Sulfate (mmol/kg)	Na[b] (mmol/kg)	K (mmol/kg)	Mg[c] (mmol/kg)	Ca[c] (mmol/kg)	Si (µmol/kg)	NH_4 (µmol/kg)	Phosphate (µmol/kg)	H_2S (mmol/kg)
IW-7	21R-1, 9–13	210.41	6	39,500	7.86	6.632	565.8	7.22	399.8	17.5	17.65	66.25	743	1839		
IW-8	24R-CC, 0–4	239.32	4	39,000	7.75	6.541	567.8	3.68	399.6	18.5	11.25	69.31	1444	2459		
IW-9	25R-1, 2–8	248.95	6	39,000	7.86	7.247	566.8	5.62	400.7	17.8	14.53	67.92	702	1922		
LA-1	858F	101.80	999		8.00	3.174	502.6	26.06		9.9						

Notes: All concentrations are uncorrected for evaporation.
[a]IW = interstitial water sample squeezed from whole round of core; IQ = interstitial water sample squeezed from quarter round of core; BC = interstitial water sample taken *in situ* with the WSTP; BO = overflow aliquot from the WSTP (diluted with distilled water); LA = borehole water sampler from Los Alamos National Laboratory; PO = overflow from pressure core sampler.
[b]In calculating Na, alkalinity was assumed to be 5 meq/kg if not measured.
[c]Ca and Mg have been corrected using the equations of Gieskes and Peretsman (1986).
[d]Concentrations in mmol/kg measured in overflow aliquots have been adjusted to the chlorinity of the prime aliquot.

organic matter out of the sediment, in the same way that pore fluid is expelled during squeezing.

Several sediment samples from the upper 30 mbsf in Holes 858B and 858D were "slushy." This texture may reflect drilling disturbance; however, the concentration of hydrogen sulfide in these samples is as high as that in adjacent samples, implying that the sediment may have local zones with a naturally high water content. Alternatively, these layers may have even higher concentrations of hydrogen sulfide that were diluted by drilling fluid when the cores were disturbed.

Hydrogen sulfide was measured both colorimetrically on squeezed samples and electrochemically on basified pore water that was still in contact with sediment (Table 13) (see "Explanatory Notes" chapter, this volume). Measurements of hydrogen sulfide by the latter method yielded higher concentrations than did colorimetric determination on pore water squeezed from sediment, probably because of oxidation of hydrogen sulfide during squeezing. The WSTP sample from Hole 858D has a sulfide concentration of the same order of magnitude as concentrations determined on these basified sediment slurries in contact with the electrochemical cell.

Results and Discussion

Profiles of pore-water composition with depth at Site 858 are shown in Figures 32 to 34. In the following discussion we divide the holes into three types. The first type includes Holes 858B, 858D, 858F, and 858G. These holes are closest to the vents; among them they cover the depth range from shallow (Holes 858B and 858D) to deep (Holes 858F and 858G). Holes 858A and 858C are distinctive and constitute the other two types. They are located farther from the active vents and therefore have less-steep thermal gradients. All of these holes have pore-water profiles that are defined by a complex history of reaction, diffusion, and advection.

Hole 858A

The geochemistry of pore water from Hole 858A, the farthest from the vents, can be described conveniently in three distinct depth intervals as defined by chlorinity: 0–120 mbsf, 120–240 mbsf, and 240–292 mbsf. In the upper interval the chlorinity increases linearly with depth, indicative of control by diffusion. The chlorinity in the intermediate depth interval returns abruptly to a value similar to that in bottom seawater and remains more or less uniform throughout the interval. In the lower depth interval chlorinity again increases, especially between 230 and 250 mbsf, to a value of about 580 mmol/kg. Below 250 mbsf it remains uniform with depth, except for the deepest sample, which we suspect is contaminated by drilling fluid based on its anomalous concentrations of sulfate, magnesium, and potassium. The shape of the chlorinity profile almost certainly requires lateral flow of seawater, because it is unlikely that sufficient amounts of mineral hydration or dehydration could have occurred locally. If lateral flow is or was occurring at this hole, the chlorinity profile could be explained equally well by either of two alternatives: flow of high-chlorinity waters centered at depths of about 110 and 270 mbsf, or flow of a water of seawater chlorinity centered at about 180 mbsf. These flows may not be steady-state. We are presently unable to distinguish between these alternatives.

The concentration of dissolved calcium increases with depth from that in seawater to as high as 78 mmol/kg. Magnesium decreases with depth to a minimum concentration of 9 mmol/kg at about 110 mbsf. At depths greater than 110 mbsf, magnesium increases again slightly. These trends are most likely due to *in-situ* alteration of detrital silicate minerals or basalt, coupled with the transport processes mentioned above.

Within the upper 40 mbsf in Hole 858A, the slight decrease in dissolved sulfate and the increases in alkalinity, ammonium, and phosphate are probably caused by bacterial degradation of organic matter. The rapid increase in temperature with depth (153°C was measured at 111 mbsf) probably precludes bacterial metabolism at depths greater than about 60 or 70 mbsf. Below about 50 mbsf there

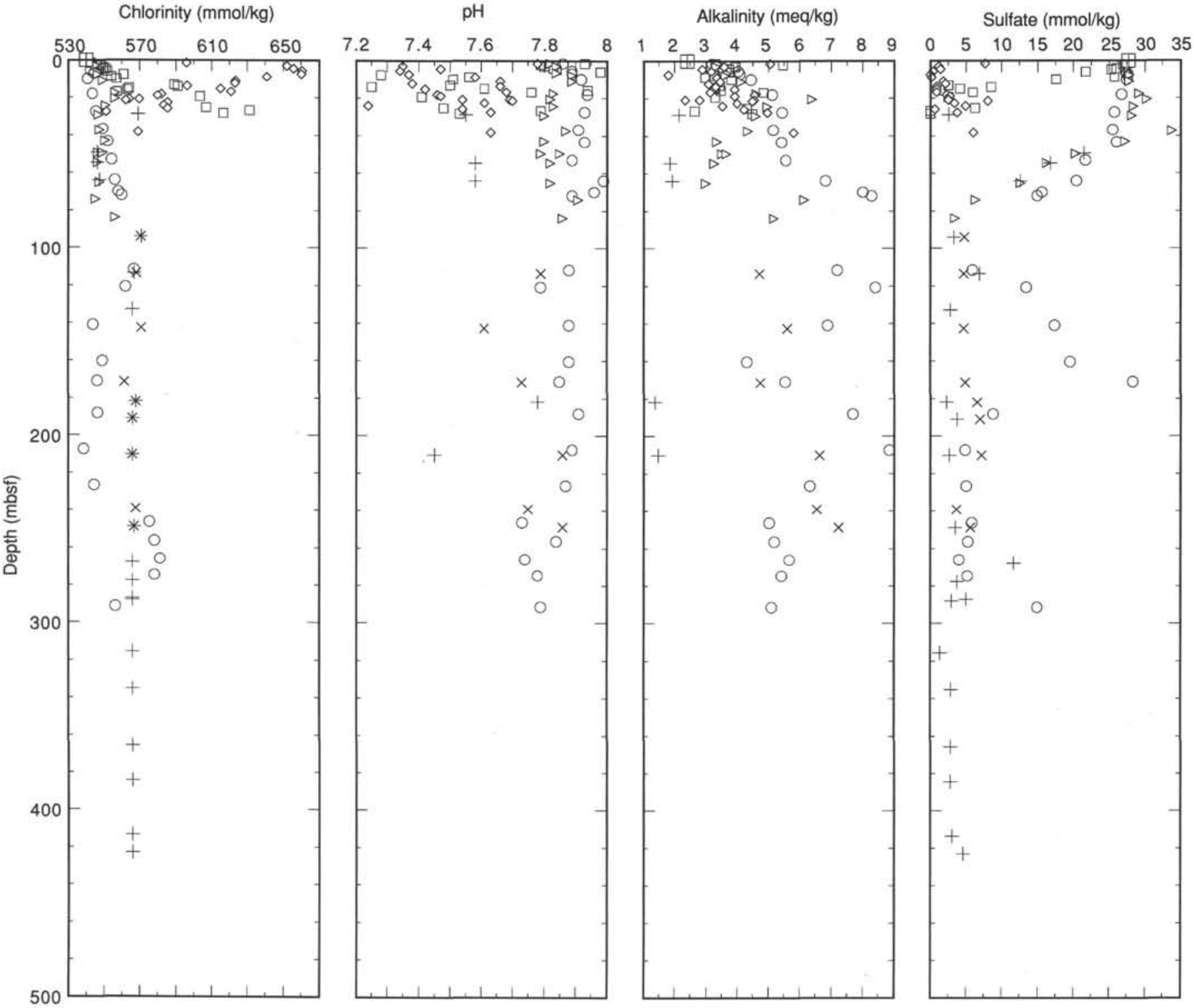

Figure 32. Composition of pore water from sediment and basalt at Site 858. Circles = Hole 858A; squares = Hole 858B, triangles = Hole 858C, diamonds = Hole 858D, x's = Hole 858F, and pluses = GRIND samples. The plus inside a square at 0 mbsf denotes bottom seawater. GRIND and quarter-round samples have been corrected for dilution and evaporation, respectively (see text).

is a large decrease in dissolved sulfate that correlates with the large increase in dissolved calcium and probably results from calcium sulfate precipitation. Anhydrite and gypsum are reported in Hole 858A between 69 and 333 mbsf (see "Lithostratigraphy and Sedimentology" section, this chapter).

If we assume that the pore waters are in equilibrium with anhydrite below 69 mbsf, then any anhydrite or gypsum in the sediment would be subject to dissolution during retrieval and pore-water extraction. This artifact has apparently produced elevated concentrations of dissolved sulfate in several samples which were confirmed by XRD to contain either gypsum or anhydrite. Calcium sulfate dissolution by itself would produce equimolar concentrations of calcium. In pore waters already in equilibrium with calcium carbonate (calcium carbonate nodules and cements are common throughout Hole 858A; see "Lithostratigraphy and Sedimentology" section, this chapter), this addition of dissolved calcium would cause calcium carbonate to precipitate and hence alkalinity to decrease. The two samples from 160 mbsf and 171 mbsf that have the most elevated sulfate concentrations also have anomalously low alkalinities. We conclude that both may be sampling artifacts. This conclusion awaits further analysis of the squeezed sediments by XRD.

Despite these possible artifacts, there remains the question of why alkalinity is so high at depth in Hole 858A. Below 100 mbsf calcium concentrations are 4 to 8 times that in seawater, pH ranges from 7.73 and 7.91, and alkalinity varies from 5 to 9 meq/kg. At the prevailing temperatures in excess of 150°C measured in this hole, the pore water would appear to be supersaturated with calcium carbonate. Carbon isotopic analyses of the dissolved inorganic carbon should clarify the possible sources of carbon and indicate whether the measured alkalinity is mainly bicarbonate.

Dissolved silica increases rapidly with depth to over 1 mmol/kg at 18 mbsf and may reflect saturation with amorphous silica over this depth interval. Biogenic silica was observed only between 0 and 15 mbsf (see "Lithostratigraphy and Sedimentology" section, this chapter). Dissolved silica then decreases steeply with depth between 18 and 27 mbsf to about 0.27 mmol/kg, before climbing slowly back to concentrations over 1 mmol/kg at depths greater than 120 mbsf. The steep decrease probably results from the exhaustion of biogenic silica

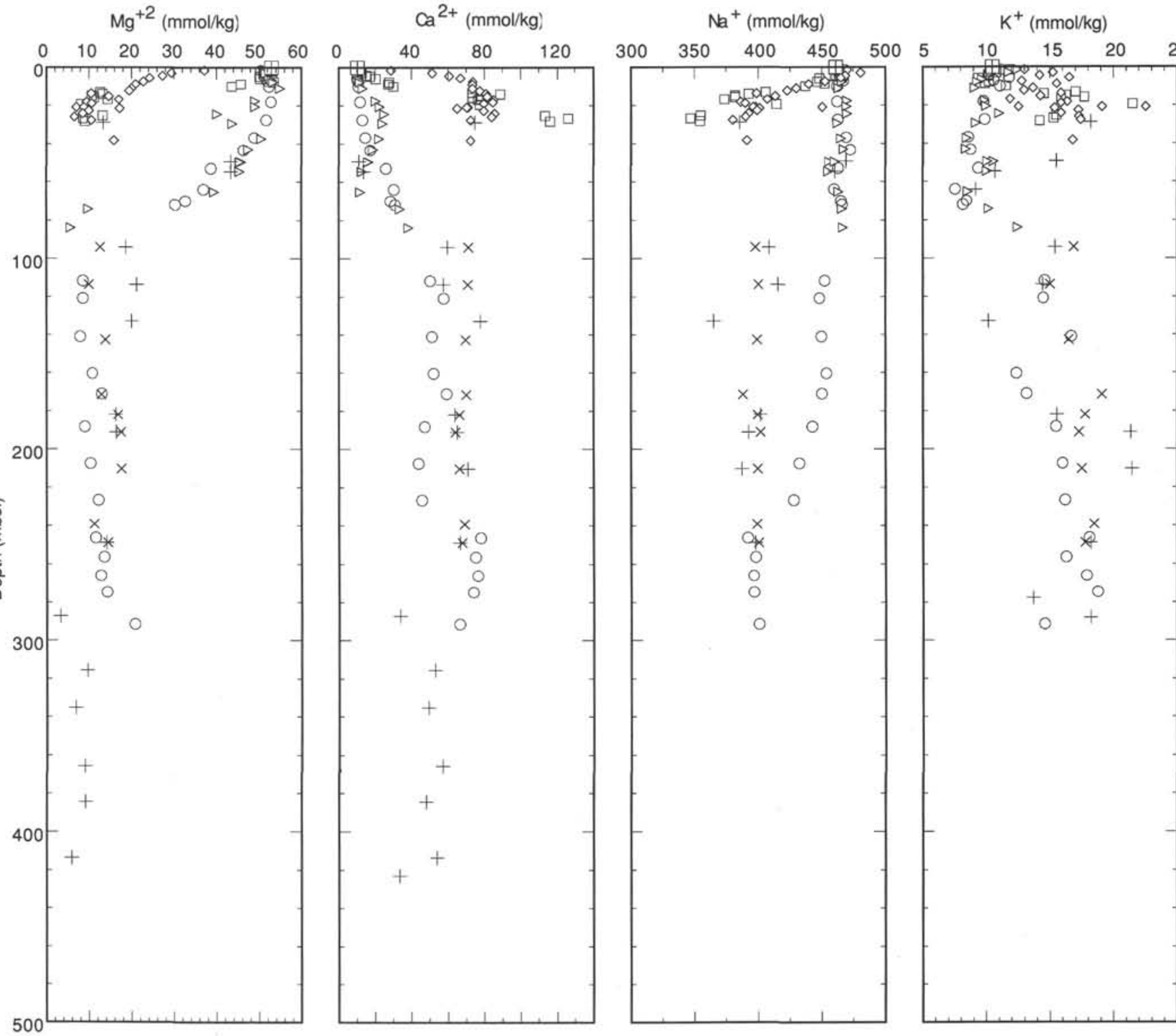

Figure 33. Composition of pore water from sediment and basalt at Site 858. See Figure 32 caption for key to symbols. GRIND and quarter-round samples have been corrected for dilution and evaporation, respectively (see text).

in the sediments. The increased concentration with depth below that correlates with increasing temperature. Quartz is very common as cement and vein fillings near the bottom of Hole 858A.

Dissolved potassium in Hole 858A decreases slightly from the seawater concentration to about 8 mmol/kg at 80 mbsf. At greater depths potassium increases again to about 15 mmol/kg. The potassium profile in Hole 858A is similar to that at Site 857, and reflects the transition from potassium uptake into clay minerals at low temperature to its release into solution at high temperature. The sodium concentration decreases by about 20% with depth in Hole 858A, probably by formation of albite and analcime. The latter commonly fills veins at depth in this hole.

Hole 858C

Pore-water profiles from Hole 858C are similar to those in the upper 100 mbsf of Hole 858A, except for chlorinity, calcium, and alkalinity. Chlorinity increases from the bottom-seawater value to a maximum of 556 mmol/kg at about 19 mbsf, then decreases to 546 mmol/kg at about 50 mbsf. In the interval from 50 to 74 mbsf, chlorinity is uniform with depth. Only one sample was taken below 74 mbsf and that sample has a chlorinity of 556 mmol/kg, about 11 mmol/kg lower than the chlorinity maximum at 112 mbsf. The shallow chlorinity maximum nearly coincides with a maximum in calcium of about 24 mmol/kg and in alkalinity, centered at about 30 mbsf. This coincidence suggests that lateral flow may be occurring, or may have occurred, at this shallow level. A second possibility is that the calcium and chloride maxima result from two unrelated processes: calcite dissolution and diffusive transport of chlorinity from Pleistocene bottom water (see "Fluid Geochemistry" section, "Site 855" chapter, this volume).

Holes 858B and 858D

Holes 858B and 858D are located less than 20 and 70 m, respectively, from hydrothermal vents that are discharging water at 276°C. The most obvious effect of this hydrothermal discharge is the chlorinity maximum of 660 mmol/kg at 3 to 7 mbsf in Hole 858D, and the

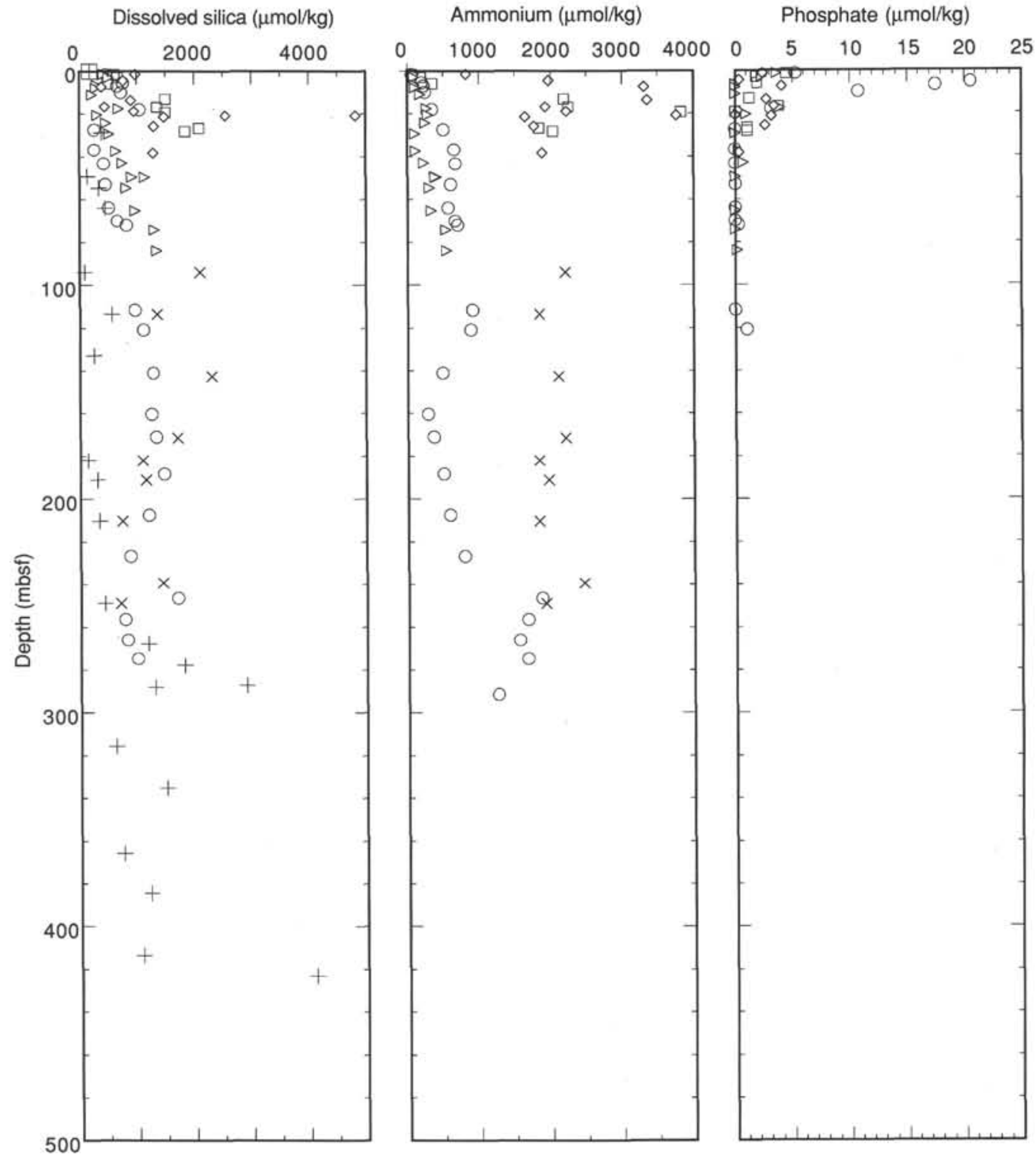

Figure 34. Composition of pore water from sediment and basalt at Site 858. See Figure 32 caption for key to symbols. GRIND and quarter-round samples have been corrected for dilution and evaporation, respectively (see text).

general increase in chlorinity with depth to about 620 mmol/kg at 28 mbsf in Hole 858B (Fig. 35). Because chlorinity at the maximum is about 100 mmol/kg greater than that either 20 m above or below, the only mechanism that can generate this profile is lateral flow. The source of the high-chlorinity pore water must be ascending hydro-thermal solutions that are diverted laterally by an impermeable or less permeable layer. The actual flow pattern must be complex, as the chlorinity profiles from the two holes are quite different from one another and may show local minima as well as maxima. The minima, if real, would suggest that both bottom seawater and hydrothermal vent water are flowing laterally at different depth intervals. Mixing of these two solutions in the intervening intervals would cause anhydrite to precipitate; mixing could also cause other reactions to occur that would affect the concentrations of various dissolved species. One likely interval where lateral flow may occur is that between 14 and 17 mbsf in Hole 858B; this interval lies just below a 1.5-m-thick layer of metalliferous sediment. The chlorinity of the pore water at 3 to 7 mbsf in Hole 858D is higher than any other measured during Leg 139, and must therefore derive from a different source. It is possible that this high-chlorinity solution is the most pristine example of deep basement water sampled during the leg.

The concentrations of other ions in the high-chlorinity pore water from Hole 858D are similar to those in water that discharges from the 276°C vents. Both waters contain about 80 mmol/kg calcium, 0 mmol/kg sulfate, several mmol/kg hydrogen sulfide, 14 to 18 mmol/kg potassium, and 400 mmol/kg sodium. Concentrations of dissolved silica, ammonium, and phosphate in the vent water are unknown at present. Pore water from Hole 857C in the depth interval 300 to 400 mbsf has similar concentrations of these ions as well, except for slightly higher sulfate. The pore water from Hole 858D differs from the vent water in having about 10 mmol/kg magnesium, much more than in the vent water. This discrepancy may result from dissolution of dolomite into the pore waters; dolomite has been identified in the uppermost cores from Holes 858B and 858D (see "Lithostratigraphy and Sedimentology" section, this chapter).

Table 12. Composition of water extracted from lithified sediment and altered basalt or diabase from Site 858 using the GRIND technique.

Sample	Core, section, interval (cm)	Depth (mbsf)	Volume (mL)	Squeeze pressure (psi)	pH	Alkalinity (meq/kg)	Chlorinity (mmol/kg)	Sulfate (mmol/kg)	Na[a] (mmol/kg)	K (µmol/kg)	Mg[b] (mmol/kg)	Ca[b] (mmol/kg)	Si (µmol/kg)
Sediment:													
	139-858C-												
G-10	10X-CC, 30–35	49.63	1.7				278.1	19.070	239.8	7.9	22.10	12.67	72
G-11	11R-1, 0–10	54.55	5.2		7.58	1.180	347.1	10.692	292.8	6.8	27.62	7.45	217
G-6	12X-1, 131–145	65.38	6		7.58	1.302	369.5	8.522		6.2			305
	139-858D-												
G-5	6X-1, 96–105	29.81	5		7.55	1.364	362.7	1.675	245.8	11.6	8.55	46.47	253
	139-858F-												
G-8	7R-CC, 0–6	75.13	0.5				94.3	0.153					
G-13	9R-CC, 3–5	94.24	2.2				295.6	1.721	212.6	8.0	9.73	30.01	48
G-9	11R-1, 0–3	113.62	7		7.76	2.376	360.8	4.366	264.7	9.2	13.53	35.47	356
G-4	13R-CC, 0–2	132.91	2.3				172.1	22.456	112.7	3.1	6.12	45.00	75
G-12	18R-1, 65–72	181.99	4.2		7.78	0.720	295.6	1.169	209.2	8.1	8.48	32.21	72
G-2	19R-1, 9–12	191.01	4.6				307.3	2.056	214.4	11.6	8.92	34.29	164
G-15	21R-1, 9–13	210.41	4		7.45	0.832	318.9	1.525	218.3	12.1	7.28	38.92	190
G-7	25R-1, 2–8	248.95	2				311.2	1.925	219.5	10.0	7.79	35.48	232
Basalt or diabase:													
	139-858F-												
G-16	27R-1, 21–24	268.03	2.5				65.3	1.350		10.2			137
G-17	28R-1, 28–32	277.80	1.5				53.8	0.355		1.3			173
G-14	29R-1, 85–87	288.06	2				68.4	3.594		2.2			158
	139-858G-												
G-1	2R-1, 56–58	287.07	2.3	30,000			38.4	0.338			0.23	2.30	197
G-2	5R-1, 15–18	315.57	2.5	3,000			83.7	0.195			1.42	7.82	91
G-3	7R-1, 55–58	335.37	2.8	3,000			57.3	0.294			0.70	4.97	152
G-4	10R-1, 90–91	365.81	2.5	3,000			82.1	0.412			1.31	8.28	109
G-5	12R-1, 12–15	384.34	2.8	35,000			61.5	0.305			1.00	5.22	133
G-6	15R-1, 20–24	413.52	2.2	35,000			75.6	0.409			0.79	7.21	145
G-7	16R-1, 18–22	423.10	2.5	35,000			37.4	0.307				2.20	271

Note: Concentrations are those measured on diluted samples.
[a]In calculating Na, alkalinity was assumed to be 1 meq/kg if not measured.
[b]Ca and Mg have been corrected using the equations of Gieskes and Peretsman (1986).

Table 13. Concentration of hydrogen sulfide in pore water from Site 858, as determined by leaching of sediment with NaOH (0.01M) + NaCl (0.55M).

Core, section, interval (cm)	Depth (mbsf)	H_2S (mmol/kg)
139-858A-		
1H-1, 0–3	0.02	0.0027
2H-3, 0–3	5.42	0.0027
139-858B-		
1H-1, 140–150	1.45	0.14
1H-4, 140–150	5.95	1.5
2H-4, 140–150	13.15	1.3
3H-1, 3–13	16.78	0.63
5H-2, 0–32	25.42	1.1
139-858C-		
1H-2, 0–5	1.53	0.20
2H-3, 0–5	6.53	0.002

The composition of pore water from Hole 858B is similar to that at less than 10 mbsf in Hole 858D, where the chlorinity maximum occurs, except for chlorinity, sodium, calcium, and dissolved silica. Chlorinity, sodium, and dissolved silica are lower in Hole 858B than in Hole 858D, and calcium is about 50% higher. Profiles of the ratios of calcium to chlorinity and magnesium to chlorinity also differ in the two holes (Fig. 36).

Holes 858F and 858G

Holes 858F and 858G were drilled to greater depths adjacent to Hole 858D. Pore water retrieved from below 90 mbsf has a similar composition to that in the interval of 10 to 30 mbsf in Hole 858D, with the exception of chlorinity, sulfate, pH, and alkalinity. The chlorinity in Hole 858F is uniform throughout the sampled section at about 566 mmol/kg. This is about 100 mmol/kg less than at the chlorinity maximum in Hole 858D. The concentration of sulfate in Hole 858F is about 5 mmol/kg, while the alkalinity averages about 2 meq/kg greater in Hole 858F than in Hole 858D. Differences between these two holes may reflect the degree of reaction between a fluid from basement and sediment.

The concentration of dissolved silica in Holes 858B, 858D, and 858F is at least 1.5 mmol/kg (Fig. 34). A maximum of about 5 mmol/kg is observed in Hole 858D at about 15 mbsf. Concentrations of phosphate in pore water from Holes 858B and 858D are several millimolar per kilogram in the upper 40 mbsf, indicating that diagenesis of organic matter produces more phosphate than is being taken up on manganese- and iron-oxide surfaces (Fig. 34).

Conclusions

The chemical composition of pore water from holes drilled at Site 858 is similar to that of water that is discharging at 276°C from nearby hydrothermal vents. Hydrothermal fluids flow laterally through the upper 40 mbsf in Holes 858B and 858D.

ORGANIC GEOCHEMISTRY

The shipboard organic geochemical analyses of sediment samples from Holes 858A, 858B, 858C, 858D, and 858F included inorganic carbon; total carbon, hydrogen, nitrogen and sulfur; volatile hydrocarbon and nonhydrocarbon gases; organic matter fluorescence estimation; and total hexane-soluble lipid/bitumen analysis. In addition, a black fine-grained (carbonaceous) substance, which could be separated by density flotation or by squeezing from hydrothermally altered cores, was examined. Instrumentation, operating conditions, and procedures are summarized in the "Explanatory Notes" chapter (this volume).

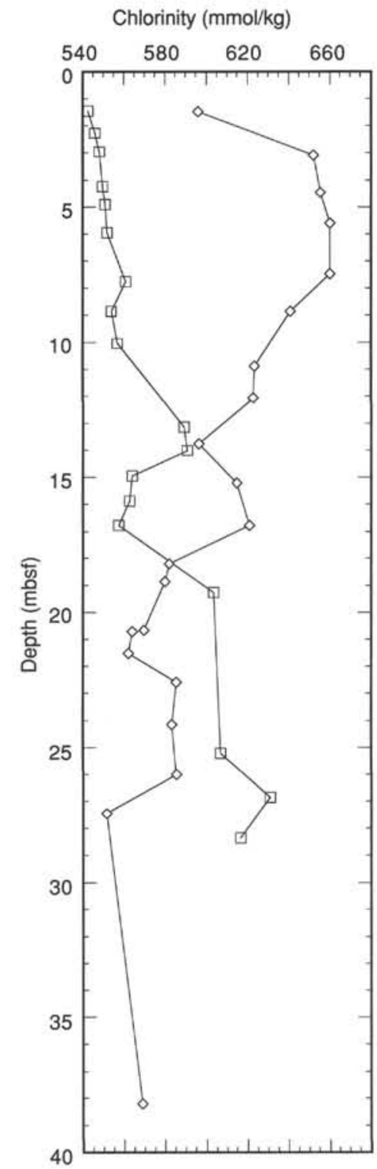

Figure 35. Profiles of chlorinity in pore water from sediment from Holes 858B and 858D. See Figure 32 caption for key to symbols. The chlorinity of waters squeezed from quarter-round pieces of core is corrected for evaporation during storage, which raised chlorinity by about 15 mmol/kg.

Volatile Gases

Volatile gases (C_1–C_3 hydrocarbons, CO_2, H_2S, and N_2) were continuously measured in the sediments at Site 858 as part of the shipboard safety and pollution monitoring program. Results are listed in Table 14. Methane concentrations in the headspace volumes range between 7 ppm (volume/volume) to 13% (or 130,000 ppm) of gas and generally increase with geothermal gradient (Figs. 37 through 41; approximate downhole temperatures are given on the left-hand methane plot in each figure; see "Heat Flow" section, this chapter). Low

Table 14. Composition of headspace gases for sediments from Holes 858A, 858B, 858C, 858D, and 858F.

Core, section, interval (cm)	Type[a]	Depth (mbsf)	Methane (ppm)	Ethane (ppm)	Propane (ppm)	Butane (ppm)	CO_2 (ppm)	H_2S (ppm)	Ethylene (ppm)	CS_{27} (ppm)	C_1/C_2
Lab air			0.0	0.0	0.0	0.0	542	0.0	0.0	0.0	—
139-858A-											
1H-2, 0–5	HS	1.50	24.0	0.0	0.0	0.0	3175	0.0	0.0	0.0	—
3H-6, 0–5	HS	19.40	10.0	0.0	0.0	0.0	3945	0.0	0.0	0.0	—
3H-6, 100	V	20.35	132	3.0	0.0	0.0	2820	0.0	0.0	47900	44
4H-2, 0–5	HS	22.90	7.0	0.0	0.0	0.0	6702	0.0	0.0	0.0	—
5H-5, 0–5	HS	36.90	10.0	0.0	0.0	0.0	1793	0.0	0.0	0.0	—
5H-5, 150	V	38.40	185	4.0	0.0	0.0	1304	0.0	0.0	3120	46
6H-3, 0–5	HS	43.40	23.0	0.0	0.0	0.0	8822	0.0	0.0	0.0	—
7H-2, 100–102	V	52.40	227	4.6	0.0	0.0	1479	0.0	0.0	0.0	49
7H-6, 0–5	HS	57.40	45.0	0.0	0.0	0.0	6993	0.0	0.0	0.0	—
9X-3, 148–150	HS	66.98	54.0	0.5	0.0	0.0	1916	0.0	0.0	0.0	108
11X-1, 0–1	HS	72.90	29.0	1.1	0.0	0.0	5260	0.0	0.0	0.0	26
14X-CC	HS	110.60	439	18.0	17.0	16.0	13949	0.0	51.2	0.0	24
15X-1, 81–84	HS	111.41	52.0	2.7	0.0	0.0	n.d.	0.0	0.0	0.0	19
16X-1, 0–3	HS	120.30	286	14.0	12.0	0.0	11049	0.0	0.0	0.0	20
17X-1, 0–2	HS	129.90	n.d.	5.0	5.0	0.0	3597	0.0	0.0	0.0	—
18X-3, 36–38	HS	142.96	601	8.0	10.0	0.0	n.d.	0.0	0.0	0.0	75
19X-1, 0–1	HS	149.30	757	10.0	11.0	18.0	8236	0.0	39.0	0.0	76
20X-4, 0–5	HS	163.50	660	11.0	4.0	0.0	7232	0.0	0.0	0.0	60
21X-1, 0–3	HS	168.60	2363	15.0	4.0	0.0	4767	0.0	0.0	0.0	158
22X-1, 0–1	HS	178.20	3541	16.0	0.5	0.0	11122	0.0	28.0	0.0	221
23X-1, 0–1	HS	187.90	2027	8.0	0.0	0.0	3062	0.0	0.0	0.0	253
24X-1, 0–3	HS	197.60	2331	5.0	0.0	0.0	10236	0.0	86.0	0.0	466
25X-CC	HS	216.90	8341	7.0	0.0	0.0	7882	0.0	37.0	0.0	1192
25X-CC	HS	216.90	6720	7.0	0.0	0.0	7105	0.0	135	0.0	960
26X-CC	HS	226.60	1642	2.4	0.0	0.0	2340	0.0	51.0	0.0	684
27X-CC	HS	236.20	16561	7.0	0.0	0.0	6918	0.0	0.0	0.0	2366
27X-CC	HS	236.20	22396	9.0	0.0	0.0	6239	0.0	23.0	0.0	2488
28X-CC	HS	245.90	41466	45.0	0.0	0.0	6796	0.0	122	0.0	921
29X-CC	HS	255.60	35705	252	40.0	0.0	5466	0.0, odor	30.0	0.0	142
30X-1, 90–102	IW	256.50	171912	619	23.0	0.0	n.d.	0.0	0.0	0.0	278
30X-CC	HS	265.30	40286	388	36.0	0.0	6164	0.0	290	0.0	104
31X-1, 0–3	HS	274.50	20759	110	12.0	36.0	6493	0.0	0.0	0.0	189
32X-1, 0–1	HS	281.70	5797	30.0	3.0	0.0	4765	0.0	11.0	0.0	193
34X-CC	HS	301.40	12521	1.0	0.0	0.0	5556	0.0	4.2	0.0	12521
35X-CC, 0–1	HS	311.20	4758	0.0	0.0	0.0	4583	0.0	39.0	—	0
36X-CC, 0–1	HS	315.20	23237	2.0	0.0	0.0	7046	0.0	0.0	0.0	11619
37X-1, 0–1	HS	315.20	12116	1.5	0.0	0.0	2982	0.0	31.0	0.0	8077
38X-CC	HS	332.40	22744	116	16.5	0.0	2263	0.0	15.0	0.0	196
39X-CC	HS	339.10	38096	288	27.0	0.0	1528	0.0	8.0	0.0	132
139-858B-											
1H-2, 0–5	HS	1.50	4.0	0.0	0.0	0.0	1396	0.0	34.0	0.0	—
2H-3, 0–5	HS	10.20	2350	23.0	13.0	0.0	3127	0.0	0.0	0.0	102
3H-1, 0–3	HS	16.70	35848	350	122	47	7570	0.0	12.0	0.0	102
4X-CC	HS	23.90	8430	140	28.0	0.0	4525	0.0	97.0	0.0	60
5H-4, 63	V, HP	29.03	136000	1167	410	0.0	5424	0.0	19.6	4200	117
5H-4, 63	V, Carle	29.03	59979	360	31.0	0.0	812	0.0	167	120.0	
5H-4, 134	V, HP	29.74	1736	60.0	0.0	0.0	1312	0.0	125	0.0	29
5H-CC	HS	31.50	84111	853	312	39.0	5398	0.0	0.0	0.0	99
139-858C-											
1H-2, 0	HS	1.50	4.3	0.0	0.0	0.0	1295	0.0	0.0	0.0	—
2H-2	V	5.00	n.d.	n.d.	n.d.	n.d.	1132	0.0	130	n.d.	—
2H-5, 0–5	HS	9.50	4.0	0.0	0.0	0.0	785	0.0	0.0	0.0	—
3H-2, 0–5	HS	14.50	11.5	1.1	0.0	0.0	7963	0.0	0.0		10
4P	Gas	22.50	3.3	0.0	0.0	0.0	953	0.0	0.0	0.0	—
5H-2, 0–5	HS	25.00	26.0	0.0	0.0	0.0	n.d.	0.0	0.0	0.0	—
6H-2	HS	34.50	6.0	0.0	0.0	0.0	8529	0.0	0.0	0.0	—
7H-2, 0–5	HS	43.00	6.6	0.0	0.0	0.0	n.d.	0.0	0.0	0.0	—
8H-CC	HS	47.50	37.0	4.5	5.8	0.0	7295	0.0	0.0	23.0	8
9H-CC, 15–20	IW	49.30	19.0	0.0	0.0	0.0	n.d.	0.0	0.0	0.0	—
10X-CC	HS	54.40	114	8.0	7.0	0.0	7130	3.2	0.4	0.0	14
11X-1, 0–5	HS	54.50	21.0	0.0	0.0	0.0	n.d.	0.0	0.0	0.0	—
11X-1, 0–5	HS	54.50	32.0	0.0	0.0	0.0	n.d.	0.0	0.0	0.0	—
11X-1, 0–5	IW (V)	54.50	7.0	0.0	0.0	0.0	n.d.	0.0	0.0	0.0	—
12X-CC	HS	73.70	39.0	1.3	0.0	0.0	7784	0.0	0.0	0.0	30
13X-CC	HS	83.40	197	15.0	11.0	0.0	1357	0.0	0.0	0.0	13
14X-1, 68–78	HS	84.08	69.0	3.6	0.0	0.0	3087	0.0	0.0	0.0	19

Table 14 (continued).

Core, section, interval (cm)	Type[a]	Depth (mbsf)	Methane (ppm)	Ethane (ppm)	Propane (ppm)	Butane (ppm)	CO_2 (ppm)	H_2S (ppm)	Ethylene (ppm)	CS_{27} (ppm)	C_1/C_2
139-858D-											
1H-6, 0–5	HS	7.50	938	14.0	0.0	0.0	1199	0.0	0.0	0.0	67
1H-6, 0–5	HS	7.50	4142	47.0	0.0	7553	0.0	0.0	0.0	0.0	88
1H-6, 100	V	8.50	129758	5723	1788	195	809	0.0	0.0	1520	23
2H-3, 0–5	HS	12.30	534	14.0	10.0	0.0	2197	0.0	0.0	0.0	38
2H-6, 0–5	V	16.80	n.d.	n.d.	n.d.	n.d.	5165	0.0	0.0	n.d.	—
2H-6	V	16.80	2227	17.0	6.0	0.0	4173	0.0	0.0	0.0	131
3P, bottle 1	Gas	19.80	6.2	0.0	0.0	0.0	405	0.0	0.0	0.0	—
3P, bottle 2	Gas	19.80	70000	3938	1622	133	6103	0.0	0.0	0.0	18
4H-3, 0–5	HS	22.80	1873	22.0	13.0	0.0	n.d.	0.0	0.0	0.0	85
4H-3, 0–5	HS	22.80	2447	32.0	18.0	0.0	n.d.	0.0	0.0	0.0	76
4H	V	20.00	14684	97.0	26.0	0.0	1210	0.0	0.0	0.0	151
6X-1, 104–105	HS	29.84	30332	219	28.0	0.0	3525	0.0	0.0	0.0	139
3P-1, 54–56	HS	19.34	4252	103	37.0	68.0	6279	0.0	0.0	0.0	41
139-858F-											
1W-3, 0–1	HS	1.50	523	19.0	18.0	0.0	3620	0.0	163	0.0	28
1W	V	0-27.80	n.d.	n.d.	n.d.	n.d.	8479	0.0	0.0	n.d.	—
2R-CC	HS	37.00	14421	144	22.0	0.0	2836	0.0	0.0	0.0	100
4R-CC	HS	56.00	37259	309	33.0	0.0	2461	0.0	101	0.0	121
9R-CC	IW(V)	103.90	9048	33.0	0.0	0.0	n.d.	0.0	0.0	0.0	274
13R-1, 0–3	IW	132.90	n.d.	n.d.	n.d.	n.d.	0.0	0.0	n.d.	n.d.	—
16R-CC, 0–1	HS	171.60	6097	27.0	4.0	0.0	1490	0.0	0.0	0.0	226
17R-CC, 0–1	HS	181.30	34328	339	75.0	0.0	2555	3.5	106	0.0	101
18R-CC, 0–1	HS	190.90	4044	61.0	30.0	0.0	1525	3.7	140	0.0	66
19R-CC, 0–1	HS	200.00	13408	178	29.0	0.0	2437	0.0	0.0	0.0	75
20R-CC, 0–1	HS	210.30	24351	192	30.0	0.0	1778	2.7	0.0	0.0	127
21R-CC, 0–1	HS	210.30	9533	198	22.0	0.0	1634	0.0	0.0	0.0	48
22R-CC, 0–1	HS	220.00	8735	113	0.0	0.0	772	3.0	0.0	0.0	77
23R-CC, 0–1	HS	229.60	2286	39.0	26.0	0.0	744	0.0	0.0	0.0	59
24R-CC, 0–1	HS	239.30	9822	132	9.5	0.0	1014	0.0	46.0	0.0	74
25R-1, 0–2	HS	248.90	26887	211	25.0	0.0	746	0.0	40.0	0.0	127
25R-1, 2–8	IW	248.90	92098	352	10.0	0.0	n.d.	0.0	0.0	0.0	262
LA-1	LA		54.0	1.0	0.0	0.0	5104	0.0	0.0	0.0	54
LA-1	LA		n.d.	n.d.	n.d.	n.d.	0.0	2.7	n.d.	n.d.	—

Note: n.d. = not determined.
[a]HS = headspace, V = vacutainer, IW = interstitial water gas, LA = borehole water sampler from Los Alamos National Lab.

concentrations comparable to those in Holes 857A, 856A, and 856B were found only in surface sections of the cooler Holes 858A and 858C. In all of the Site 858 holes, methane increases exponentially with increasing depth and temperature to reach maximum concentrations comparable to those found below 300 mbsf in Hole 857C.

Downhole profiles for headspace ethane and propane are also shown in Figures 37 through 41. In the cooler Holes 858A and 858C, both compounds were either absent or present in only trace amounts at depths shallower than 40 mbsf, or less than about 70° to 80°C. In Hole 858A (Fig. 37), both compounds then increase exponentially with depth, but with concentrations of about 100 to 1000 times lower than those observed for methane, as was the case for Hole 857C (see "Organic Geochemistry" section, "Site 857" chapter). In Holes 858B, 858D, and 858F, concentrations of ethane and propane increase steeply with increasing depth (Figs. 38, 40, and 41, respectively) consistent with the higher geothermal gradients in these three holes. The concentrations of both ethane and propane are relatively high at the surface in Hole 858F and show a further increase within the top 60 mbsf of the hole, followed by a slight decrease in ethane and a leveling off of propane in deeper intervals below 170 mbsf. Apparently, the limits of thermal stability for these two compounds, which are expected to crack to methane and graphite at high temperatures, have not been reached in these holes.

The C_1–C_3 concentrations follow the geothermal gradients remarkably well for all of the Site 858 holes (Figs. 37 to 41). The lowest thermal and methane gradients are observed for Holes 858A and 858C, which show roughly comparable methane trends (Figs. 37 and 39), even though the thermal gradient is higher in Hole 858C (about 2.5°C/m) than in Hole 858A (1.4°C/m; "Heat Flow" section, this chapter). Much steeper methane gradients are observed in Holes 858B and 858D (where the thermal gradient is near 9°C/m), where the concentrations of methane at less than 40 mbsf are comparable to those reached only at 235 mbsf in Hole 858A and at 300 mbsf in Hole 857A. Hole 858F is unique in showing relatively high methane concentrations at the sediment-water interface, a rapid exponential rise to about 60 mbsf followed by a small decrease in deeper sections (Fig. 41). The general shape of the profile is similar to that observed in Hole 857C. This suggests that some cooling mechanism may be provided by the sills (in the case of Site 857) or extrusives (in the case of Site 858) in deeper layers—possibly via fluid flow through the rocks themselves. Alternatively, the observed methane gradients in Holes 858A, 858B, 858C, and 858D are consistent with a source at depth followed by diffusion to the surface. This is not the case for either ethane or propane, whose profiles show a number of sharp discontinuities. Shore-based experiments will be needed to determine the relative contributions of *in-situ* generation vs. diffusion for the methane profiles.

The C_1/C_2 ratios are generally low for Site 858, in the range of 10 to 1000, consistent with a thermogenic methane source in these geothermally hot sediments (Fig. 42). In Holes 858A, 858D, and the upper sections of Hole 858F, the C_1/C_2 ratio increases with depth, contrary to the normal decreasing trend observed at numerous Deep Sea Drilling Program (DSDP) sites (Claypool, 1975), but consistent with conversion of sedimentary organic matter, including kerogen and bitumens, to methane and graphite at very high temperatures (Hunt, 1979). The "graphite" part of this reaction may be present as the fine-grained black substance which can be separated from many

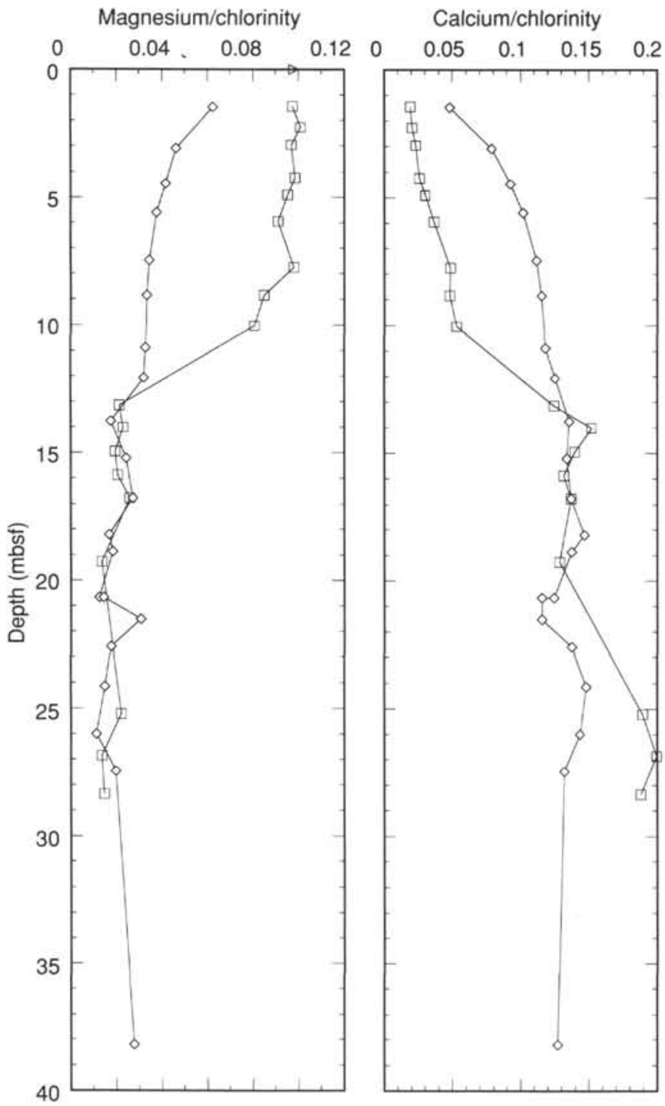

Figure 36. Profiles of the ratio of magnesium to chlorinity and calcium to chlorinity in pore water in sediment from Holes 858B and 858D. The triangle at 0 mbsf denotes bottom seawater. Squares = Hole 858B; diamonds = Hole 858D.

of the hydrothermally altered intervals, as discussed below. Elemental analysis shows that this "graphitic" material (the "black soot" from Hole 858A shown at the bottom of Table 15) is not pure carbon, although it is considerably richer in total organic carbon (TOC) than the parent sediment. The generally low or sporadic appearance of the higher molecular weight "wet" gases, propane (Fig. 37 to 41) and butane (Table 14) is consistent with a high-temperature source of methane. The petroleum source-rock potential of all sediments at Site 858 below the top 5 mbsf is poor, TOC = 0.1% to 0.4%, with values generally falling closer 0.1% (Figs. 37 through 41). Therefore, oil generation and migration is expected to be minimal via "normal" mechanisms for more organic-rich rocks (see "Organic Geochemistry" section, "Site 856" chapter). Any generated oil, along with residual kerogen, would be expected to remain dispersed in the rocks and undergo further cracking to gas and graphite as the sediments are subjected to higher temperatures. These gases would either remain close to their point of generation in these organic-lean sediments (via sorption onto the graphitic carbon or the sediments; Whelan et al., 1984), or could be swept out via hydrothermal flow.

Carbon dioxide is an ubiquitous constituent of the headspace gases of Site 858; it is present in concentrations of 1000 to 11,000 ppm (Figs. 37 through 41 and Table 14), comparable to those also found at other Leg 139 sites. For Hole 858A, the downhole profile for CO_2 is irregular, showing an overall increase to about 110 mbsf (about 150°C) followed by a decrease to the bottom of the hole at 340 mbsf. In both Holes 858B (Fig. 38) and 858D (Fig. 40), CO_2 increases steeply with depth (along with temperature and methane concentration) and then decreases somewhat with depth, as observed for Hole 858A. In Hole 858C (Fig. 39), CO_2 does not appear to be related to *in-situ* temperature, only an abrupt increase (starting at about 15 mbsf, or 50°C) is observed, followed by roughly constant concentrations to about 75 mbsf (corresponding to a temperature of about 190°C), and finally a decrease to low levels at about 83 mbsf (or temperatures above 200°C). In Hole 858F, CO_2 decreases with depth above 50 mbsf followed by a further small decrease in the interval from 170 to 250 mbsf.

The appearance of CO_2 in several intervals where only traces of inorganic carbonate are present, but where organic carbon is still significant (e.g., below 150 mbsf in Hole 858A, Fig. 37, and in sections of Hole 858C deeper than 35 mbsf, Fig. 39) suggests that the CO_2 is derived from organic carbon (i.e., kerogen) rather than carbonate in these intervals, and perhaps throughout the entire area. In addition, the steep increase of CO_2 in surface sections of Hole 858B is accompanied by a smooth decrease in TOC (Fig. 38), consistent with a thermal source from kerogen. Alternatively, a subsurface maximum also occurs in inorganic carbon in Hole 858B (Fig. 38), so that an inorganic source for gaseous CO_2 is also possible in surface sections of Hole 858B.

Other gases which were observed sporadically at this site included ethylene (1 to 300 ppm), hydrogen sulfide (2–4 ppm), and a compound identified on the basis of its retention time as carbon disulfide (Table 14; however, this identification needs to be confirmed with shore-based mass spectrometric studies). In Hole 858A, ethylene first appears in Sample 11X-1, 0–1 cm, at 110.6 mbsf, along with propane and butane, and relatively high concentrations of methane and CO_2. Ethylene is present in two shallower sediment samples, but only in trace amounts, and then goes through a maximum at about 200 to 250 mbsf, within a projected temperature range of 280°–350°C. The ethylene concentrations then drop to very low values at 300 mbsf within the same interval where ethane shows a minimum. Ethylene is also present in some intervals of the hot holes, 858B and 858F. However, temperature is not the only controlling parameter; ethylene is absent in both hot Hole 858D and cooler Hole 858C.

Hydrogen sulfide was not detected in any of the Leg 139 holes in more than trace amounts. It was present in small concentrations in headspace gases in one interval of Hole 858C (3 ppm at 60 mbsf) and a few intervals of Hole 858F from 180 to 220 mbsf (2.5 to 4 ppm).

An unknown compound, presumed to contain sulfur because of the similarity of its odor to H_2S, was also detected via the shipboard H_2S alarm systems in Core 139-858D-2H, as well as in some of the other Site 858 gas pockets which were sampled via vacutainer (Table 14). In Core 139-858D-2H, this compound was conclusively shown not to be H_2S both by the absence of a gas chromatograph (GC) response at the correct retention time and by the absence of a response to a titrimetric procedure which is sensitive at much lower levels (see "Fluid Geochemistry" section, this chapter). The compound could possibly have been sulfur dioxide (SO_2), which will set off the H_2S detectors at levels of 1000 ppm or more, or methyl mercaptan (CH_3SH). The faint pink color produced during the titrimetric procedure is consistent with the presence of SO_2. Further shore-based mass spectrometric (MS) studies will be carried out on gases collected from this interval to identify this compound definitively.

Pressure Coring System

The new pressure coring system (PCS) and manifold were successfully deployed in Hole 858D (Core 139-858D-3P in Table 14). The concentrations of the gases recovered are shown in Figure 43. A

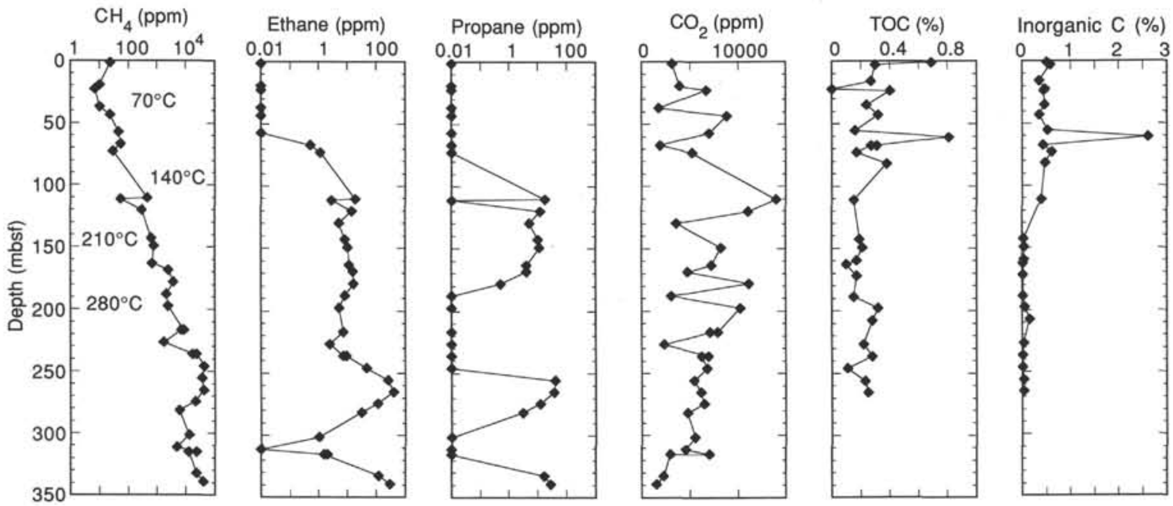

Figure 37. Concentrations of headspace gases, C_1–C_3 hydrocarbons, and CO_2; weight percentages of inorganic carbon and TOC vs. depth for Hole 858A.

description of the apparatus and manifold used for collecting the gases is described in the "Operations" section, "Explanatory Notes" chapter (this volume). The PCS is run using the APC/XCB bottom-hole assembly, thus allowing a pressurized core sample to be taken at any time from the mud line down to XCB refusal (even into basement).

The PCS Core 139-858D-3P (19.80 mbsf, estimated *in-situ* temperature about 180°C) was intended to collect sediment together with its associated fluids and gases. However, when the PCS is recovered, there is no way to verify the presence of core material; if the PCS is retrieved showing internal pressures greater than 1 atmosphere, it must be assumed to have successfully collected a sample, and treated carefully as described below if quantification of the gases present is to be achieved. The procedures by which PCS gases were collected and measured during Leg 139 are described below for Core 139-858D-3P. The same procedure was used on an earlier unsuccessful test (Core 139-858C-4P). In the earlier case, only water enriched in carbon dioxide relative to laboratory air was obtained (Fig. 43).

Following collection of Core 139-858D-3P, the PCS was brought to the rig floor, where a pressure of 800 to 1000 psi was measured. The pressurized chamber was taken into the laboratory and attached to the manifold, which was already under vacuum. An alumina trap immersed in a −60°C bath was used to protect the gas manifold collection part of the system from pump oil in the vacuum system. The evacuated manifold line to the first stainless steel gas collection bottle and the associated pressure gauge were isolated from the vacuum pump, and the line to the pressure core sampler was opened, so that gas from the PCS was transferred to the first bottle (volume 300 mL). During this initial gas collection process, the pressure at the core barrel and in front of the bottle dropped to just above atmospheric. The first bottle was then closed and isolated from rest of the manifold. The PCS was then put in line with a second bottle which also had been previously evacuated. After opening all valves between the second bottle and the PCS, a negative pressure reading was obtained. The line between the PCS and the second bottle was left open for about 20 min in order to bleed off any residual gas in the core. The pressure in the system increased slightly, but was still less than 1 bar at the end of this period. The valve between the PCS and the second gas bottle was then closed, the PCS was disconnected, and the entire system, except the two used bottles, was opened to the atmosphere. The two closed bottles were detached from the manifold

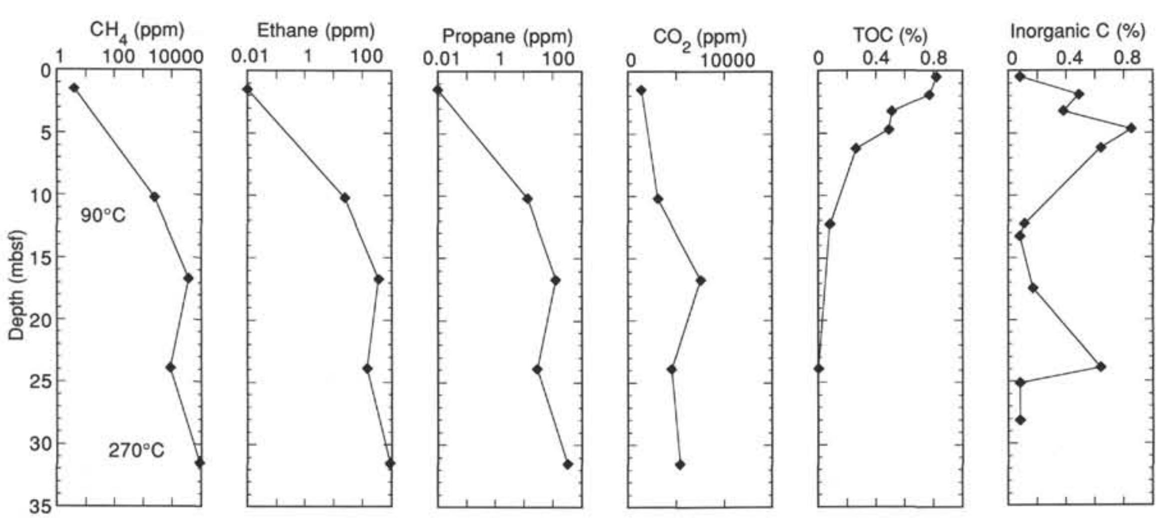

Figure 38. Concentrations of headspace gases, C_1–C_3 hydrocarbons, and CO_2; weight percentages of inorganic carbon and TOC vs. depth for Hole 858B.

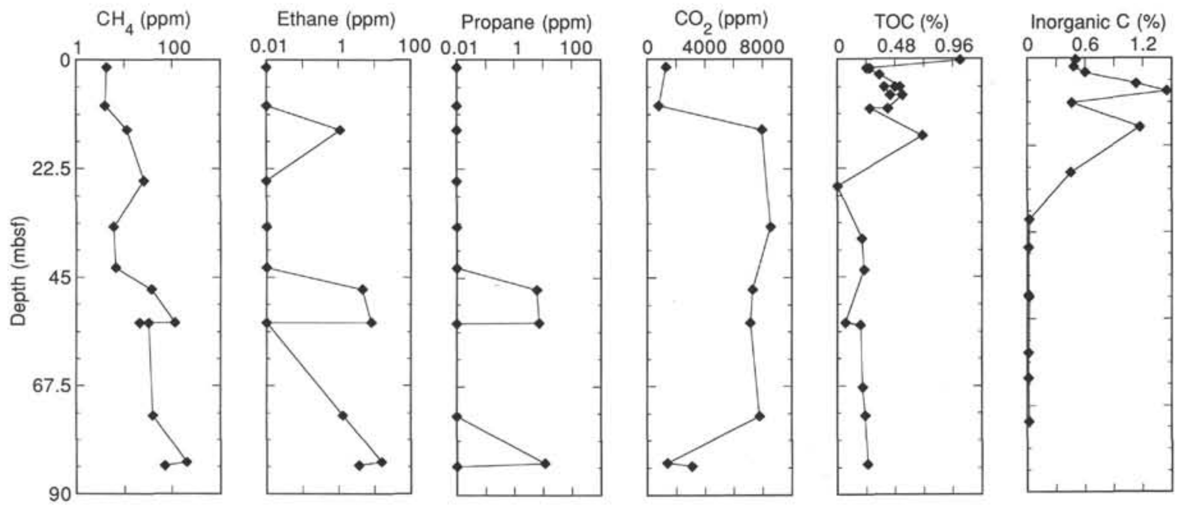

Figure 39. Concentrations of headspace gases, C_1–C_3 hydrocarbons, and CO_2; weight percentages of inorganic carbon and TOC vs. depth for Hole 858C.

and taken to the chemistry laboratory for preliminary analysis. Shore-based isotope studies and GC-MS analyses of gas compositions will also be conducted.

As a practical consideration to those deploying this apparatus on future legs, it is important to keep in mind that we did not know until the PCS was opened that an actual core had been obtained and, in fact, that the core barrel was completely filled with sediment. The sediment contained some gas, but not at high pressure; future legs drilling into sediments with higher gas pressures, such as those containing clathrates, may encounter problems very different from these described here.

The compositions of the gases recovered by the PCS along with the composition of headspace gases analyzed in the recovered core (Section 139-858D-3P-1) are shown in Figure 43. The first gas-collection bottle (labeled 3P, bottle 1) was still slightly pressurized but contained only air and a minor enrichment in CO_2. The second collection bottle (3P, bottle 2) contained relatively high concentrations of methane, ethane, propane, and carbon dioxide in approximately the same proportions as found in sediment headspace gases throughout the hole (Fig. 43) along with about 30% air which had been injected in order to bring the total pressure in the collection bottle to one bar. Evidently, considerable time was required for gases to bleed out of the sediment, which was packed tightly into the core tube. This slow bleed off must be taken into account during depressurization so that enough time is allowed for complete degassing before the PCS is opened. In hindsight, if we had realized that the core barrel was full of sediment, more time and additional collection bottles would have been used for degassing. If a quantitative estimation of gas in the PCS is desired, the bleeding off of core gas into sequential collection bottles should be continued until the gas levels in the collection bottles drop to background levels, as shown by GC.

Figure 43 also shows the composition of gas obtained from a previous (unsuccessful) deployment of the PCS, Sample 139-858C-4P, where only surface seawater (as shown from chlorinity, sulfate, etc.) slightly enriched in CO_2 was recovered. The analysis of laboratory air is also shown in Figure 43, for comparison to the various PCS samples. Slight enrichments in carbon dioxide are evident for all of the pressure core samples, including the unsuccessful 139-858C-4P sample. The C_1/C_2 ratio of the gas in the collection bottle 2 was 18. This value can be compared with values for headspace gas at Site 858

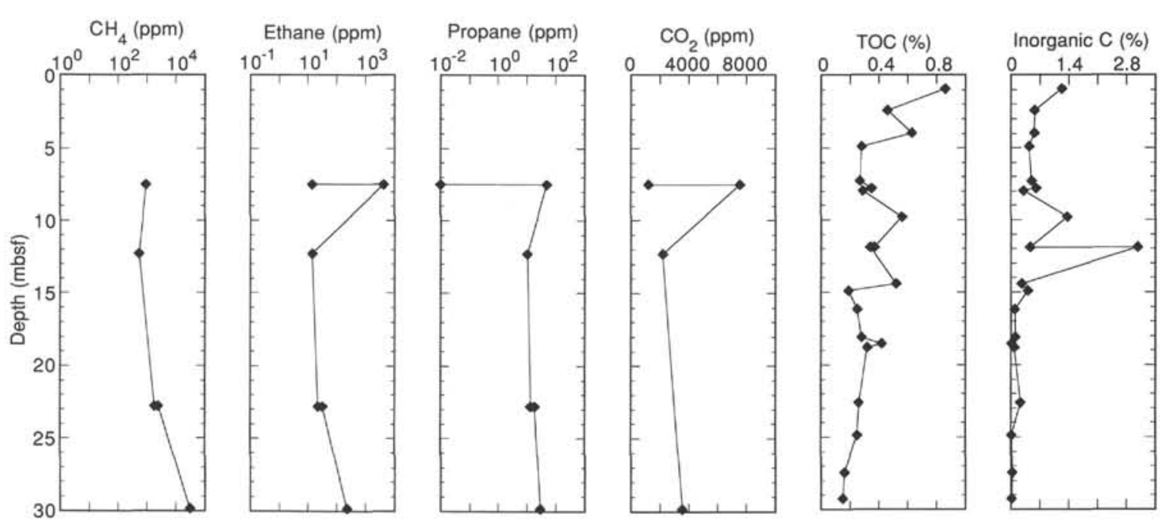

Figure 40. Concentrations of headspace gases, C_1–C_3 hydrocarbons, and CO_2; weight percentages of inorganic carbon and TOC vs. depth for Hole 858D.

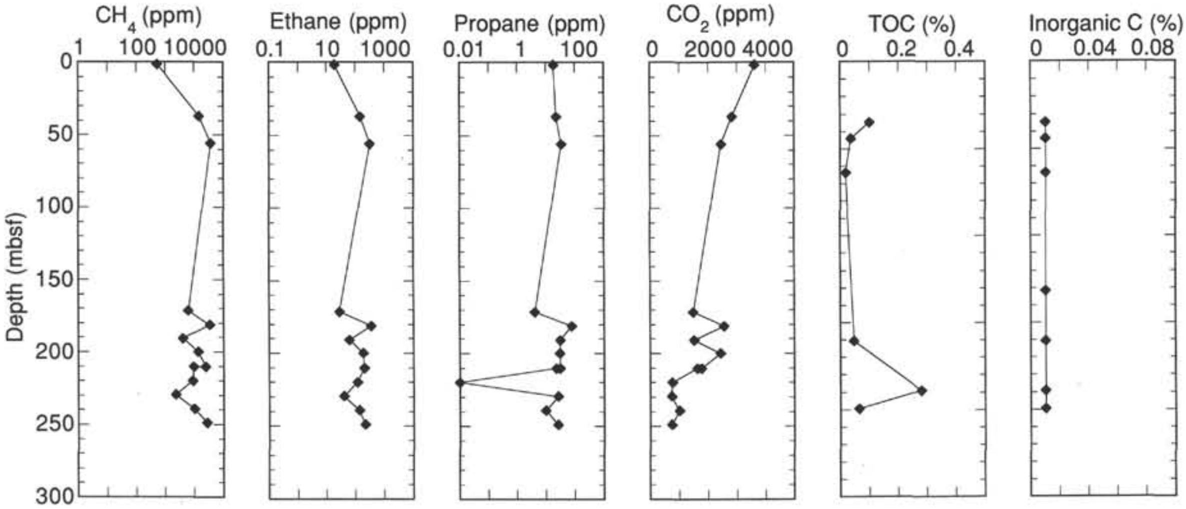

Figure 41. Concentrations of headspace gases, C_1–C_3 hydrocarbons and CO_2; weight percentages of inorganic carbon and TOC vs. depth for Hole 858F.

(Fig. 42). An attempt has been made below to calculate in-situ gas concentrations, represented by the gas bottle concentrations shown in Figure 43, by making the following assumptions: (1) the amount of gas collected in bottle 2, with a total volume of 300 mL, represents all of the gas in the core, (2) the porosity of the core is 64% (see "Physical Properties" section, this chapter), (3) the gas is dissolved in water, and (4) the total volume of sediment recovered was equal to the volume of the pressure core barrel, or 1191 mL. Then the in-situ concentration of gas (STP) in the core at depth can be calculated from the data in Table 14 as: $C_1 = 1.15$, $C_2 = 0.065$, $C_3 = 0.026$, $C_4 = 0.002$, and $CO_2 = 0.098$ mmol of gas at STP per liter of sediment (or $C_1 = 28$, $C_2 = 1.6$, $C_3 = 0.64$, $C_4 = 0.05$, and $CO_2 = 2.4$ mL of gas at STP per liter of sediment).

Fluorescence

Extracts from surficial sediments of Site 858 were yellow in discrete horizons (e.g., from Cores 139-858A-6H, -858C-3H, and -858D-3P) and from the remaining samples they were colorless. Hole 857C extracts were colorless. Yellow fluorescence was observed for surficial sediment from Holes 858A and 858D and strong white fluorescence was found at discrete horizons in Holes 858A (maximum at 50 mbsf), 858B (maxima at 0.5 and 2 mbsf), 858C (maxima at 4 and 13–15 mbsf), and 858D (maxima at 13 and 20 mbsf). The yellow fluorescence in the surficial sections is interpreted as thermal maturation of bitumen to the mature stage (i.e., bitumen generated from sediments exposed to temperatures of at least 50° to 90°C over geologic time or even higher temperatures for short times). The white fluorescence indicates horizons of overmature bitumen enriched in polynuclear aromatic hydrocarbons (PAH, i.e., organic matter heated to temperatures of at least 150°C over geologic time or even much higher for brief periods; Curray, Moore, et al., 1982). Probably both the white and yellow fluorescence, observed in discrete horizons, correspond to bitumen migrated by hydrothermal fluids (hydrothermal petroleum), with the former being generated at lower temperatures and the latter at higher temperatures in excess of approximately 200°C. In contrast, the yellow color, which appears to be diagnostic of lower maturities, is observed only in the cooler Site 858 holes, 858A and 858C. The concentrations of bitumen, based on the extract color and fluorescence intensities, are high and variable throughout the upper

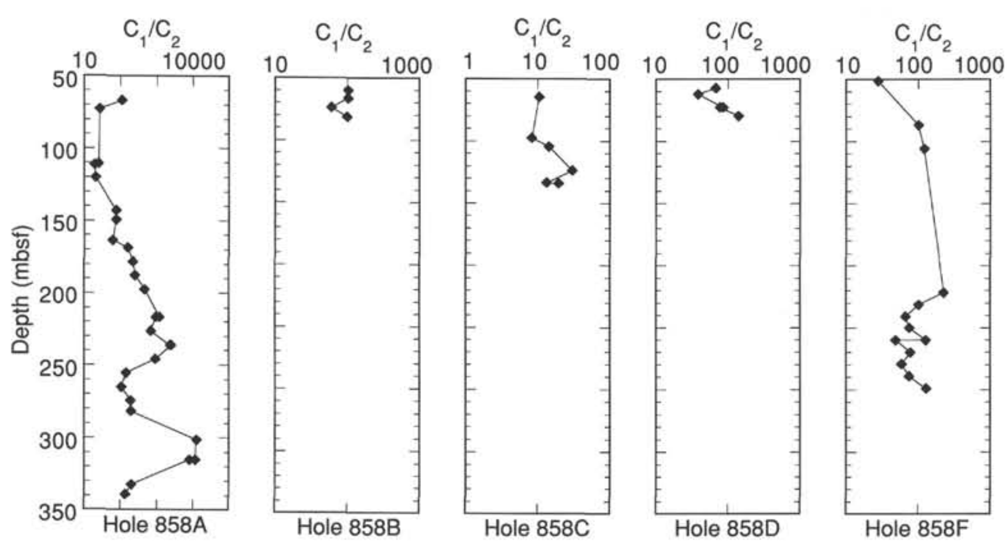

Figure 42. C_1/C_2 ratios in headspace gases for Holes 858A, 858B, 858C, 858D, and 858F.

Table 15. Weight percentages of C, H, N, S, inorganic C, and TOC, and ratios of C/H, C/N, and C/S for Holes 858A, 858B, 858C, 858D, and 85BF.

Sample (cm)	Depth (mbsf)	C (%)	H (%)	N (%)	S (%)	C/H[a]	C/N[a]	C/S[a]	Inorganic carbon (%)	TOC (%)
139-858A-										
1H-1, 81–83	0.81	1.20	0.59	0.053	0.00	2.03	23	—	0.51	0.69
1H-1, 81–83	0.81	1.20	0.49	0.030	0.00	2.45	40	—	0.51	0.69
2H-1, 34–36	2.74	0.88	0.44	0.032	0.32	2.00	28	2.8	0.58	0.30
3H-3, 81–85	15.71	0.62	0.38	0.032	0.30	1.63	19	2.1	0.35	0.27
4H-1, 90–94	22.30	0.43	0.37	0.016	0.00	1.16	27	—	0.47	0.00
4H-2, 79–83	23.60	0.84	0.43	0.058	0.72	1.95	14	1.2	0.44	0.40
5H-3, 100–105	34.90	0.70	0.36	0.038	0.30	1.94	18	2.3	0.46	0.24
6H-2, 94–96	42.84	0.67	0.38	0.036	1.30	1.76	19	0.5	0.35	0.32
7H-4, 93–97	55.33	0.68	0.39	0.039	0.00	1.74	17	—	0.52	0.16
8H-2, 39–41	60.79	3.42	0.28	0.023	0.00	12.21	149	—	2.61	0.81
9X-4, 47–57	67.47	0.74	0.47	0.045	0.21	1.57	16	3.5	0.43	0.31
9X-4, 47–57	67.47	0.70	0.49	0.037	0.00	1.43	19	—	0.43	0.27
11X-1, 2–7	72.92	0.78	0.34	0.017	0.32	2.29	46	2.4	0.61	0.17
12X-1, 18–20	81.78	0.85	0.47	0.032	0.28	1.81	27	3.0	0.47	0.38
15X-1, 60–62	111.20	0.54	0.35	0.024	0.13	1.54	23	4.2	0.39	0.15
18X-3, 16–20	142.76	0.21	0.52	0.020	0.34	0.40	11	0.6	0.02	0.19
19X-1, 15–19	149.45	0.25	0.60	0.037	0.40	0.42	7	0.6	0.04	0.21
20X-1, 58–61	159.58	0.20	0.52	0.026	0.80	0.38	8	0.3	0.03	0.17
20X-3, 67–70	162.67	0.11	0.35	0.010	0.67	0.31	11	0.2	0.01	0.10
21X-3, 48–51	172.08	0.18	0.30	0.014	1.28	0.60	13	0.1	0.01	0.17
23X-1, 90–92	188.80	0.16	0.38	0.0087	0.37	0.42	18	0.4	0.01	0.15
24X-1, 15–17	197.75	0.37	0.47	0.036	0.54	0.79	10	0.7	0.05	0.32
25X-1, 44–45	207.74	0.43	0.41	0.037	0.35	1.05	12	1.2	0.15	0.28
27X-l, 12–14	226.72	0.25	0.37	0.017	0.81	0.68	15	0.3	0.03	0.22
28X-CC, 26–28	236.49	0.29	0.49	0.029	0.56	0.59	10	0.5	0.01	0.28
29X-1, 20–23	246.10	0.12	0.31	0.008	1.77	0.39	15	0.1	0.01	0.11
30X-1, 64–67	256.24	0.26	0.43	0.014	1.60	0.60	19	0.2	0.03	0.23
31X-1, 18–20	265.48	0.28	0.46	0.025	1.94	0.61	11	0.1	0.03	0.25
139-858B-										
1H-1, 48–52	0.48	0.90	0.87	0.083	1.08	1.03	11	0.83	0.08	0.82
1H-2, 42–44	1.92	1.26	0.82	0.097	2.83	1.54	13	0.45	0.49	0.77
1H-3, 23–27	3.23	0.89	0.56	0.040	0.53	1.59	22	1.68	0.38	0.51
1H-4, 19–23	4.69	1.34	0.55	0.051	0.54	2.44	26	2.48	0.85	0.49
1H-5, 21–25	6.21	0.90	0.62	0.033	0.79	1.45	27	1.14	0.64	0.26
2H-2, 125–127	9.95	0.29	0.56	0.025	0.89	0.52	12	0.33	n.d.	—
2H-4, 57	12.27	0.19	0.83	0.013	18.20	0.23	15	0.01	0.11	0.08
2H-5, 11–13	13.31	0.19	0.39	0.020	1.74	0.49	9	0.11	0.08	0.11
3H-1, 76–78	17.46	0.18	0.74	0.00	1.18	0.24	—	0.15	n.d.	—
5H-1, 122–125	25.12	0.25	1.40	0.00	0.56	0.18	—	0.45	0.08	0.17
5H-3, 124–128	28.16	0.17	1.44	0.00	0.88	0.12	—	—	0.08	0.09
139-858C-										
1H-1, 22–26	0.22	1.52	0.60	0.100	0.73	2.53	15	2.08	0.50	1.02
1H-2, 42–46	1.92	0.75	0.50	0.026	0.24	1.50	27	3.13	0.48	0.27
1H-2, 42–44	1.92	0.74	0.52	0.033	0.26	1.42	22	2.85	0.48	0.26
1H-2, 42–44	1.92	0.72	0.47	0.013	0.00	1.53	55	—	0.48	0.24
1H-3, 21–25	3.21	0.95	0.52	0.026	0.35	1.83	37	2.71	0.60	0.35
2H-2, 77–79	5.77	1.65	0.47	0.043	0.35	3.51	38	4.71	1.13	0.52
2H-2, 77–79	5.77	1.61	0.43	0.039	0.28	3.74	41	5.75	1.13	0.48
2H-2, 77–79	5.77	1.52	0.45	0.026	0.00	3.38	58	—	1.13	0.39
2H-3, 98–100	7.48	1.89	0.47	0.053	0.41	4.02	36	4.61	1.45	0.44
2H-3, 98–100	7.48	1.99	0.50	0.055	0.36	3.98	36	5.53	1.45	0.54
2H-5, 71–73	10.21	0.88	0.45	0.041	1.71	1.96	21	0.51	0.46	0.42
3H-2, 133–135	15.83	1.88	0.23	0.028	6.55	8.17	67	0.29	1.17	0.71
5H-2, 121–123	26.21	0.44	0.35	0.004	1.23	1.26	110	0.36	0.45	0.00
6H-3, 104–106	37.04	0.22	0.49	0.003	1.36	0.45	73	0.16	0.02	0.20
7H-2, 53–55	43.53	0.23	0.49	0.013	1.95	0.47	18	0.12	0.01	0.22
10X-CC, 37–39	54.50	0.08	0.26	0.004	1.53	0.29	19	0.05	0.01	0.07
11X-1, 48–51	54.98	0.21	0.50	0.006	1.34	0.42	38	0.16	0.02	0.19
12X-3, 87–90	67.87	0.22	0.48	0.003	0.79	0.46	76	0.28	0.01	0.21
13X-1, 1–16	73.70	0.24	0.37	0.0064	0.39	0.65	38	0.62	0.01	0.23
13X-1, 1–16	73.70	0.24	0.39	0.013	0.51	0.62	18	0.47	0.01	0.23
14X-1, 34–36	83.74	0.27	0.39	0.016	0.50	0.69	17	0.54	0.02	0.25
139-858D-										
1H-1, 95–99	0.95	2.09	0.52	0.072	0.59	4.02	29	3.54	1.23	0.86
1H-2, 93–97	2.43	1.03	0.61	0.065	0.24	1.69	16	4.29	0.57	0.46
1H-3, 98–102	3.98	1.19	0.53	0.043	0.21	2.25	28	5.67	0.56	0.63
1H-4, 41–45	4.91	0.72	0.52	0.049	0.26	1.38	15	2.77	0.44	0.28
1H-5, 129–133	7.29	0.77	0.56	0.054	0.37	1.38	14	2.08	0.50	0.27
1H-6, 30–33	7.80	0.96	0.53	0.039	0.42	1.81	25	2.29	0.61	0.35

Table 15 (continued).

Sample (cm)	Depth (mbsf)	C (%)	H (%)	N (%)	S (%)	C/H[a]	C/N[a]	C/S[a]	Inorganic carbon (%)	TOC (%)
1H-6, 72–76	7.99	0.60	0.51	0.040	0.24	1.18	15	2.50	0.31	0.29
2H-1, 49–51	9.79	1.92	0.54	0.052	0.53	3.56	37	3.62	1.36	0.56
2H-2, 111–113	11.91	0.83	0.61	0.039	0.53	1.36	21	1.57	0.46	0.37
2H-3, 111–113	11.91	3.41	0.44	0.033	0.41	7.75	103	8.32	3.07	0.34
2H-4, 62–65	14.42	0.78	0.62	0.030	1.03	1.28	26	0.76	0.26	0.52
2H-4, 110–112	14.90	0.60	0.61	0.034	1.93	0.98	18	0.31	0.41	0.19
2H-5, 90–92	16.20	0.34	0.57	0.025	1.61	0.60	14	0.21	0.09	0.25
2H-6, 129–131	18.09	0.38	0.35	0.026	3.81	1.09	15	0.10	0.1	0.28
2H-7, 23–25	18.53	0.43	0.51	0.053	2.86	0.84	8	0.15	0.01	0.42
2H-CC, 37–40	18.80	0.40	0.53	0.053	2.32	0.75	8	0.17	0.08	0.32
4H-2, 133–135	22.63	0.49	0.53	0.070	0.98	0.92	7	0.50	0.23	0.26
4H-4, 59–63	24.89	0.26	0.47	0.039	0.3	0.55	7	0.87	0.01	0.25
4H-6, 16–20	27.46	0.19	0.41	0.019	2.09	0.46	10	0.09	0.03	0.16
4H-6, 100	28.30	0.34	0.51	0.044	0.81	0.67	8	0.42		
6X-1, 45–49	29.25	0.16	0.52	0.007	0.99	0.31	23	0.18	0.01	0.15
139-858F-										
7R-CC, 2–4	84.70	0.11	0.37	0.006	0.09	0.30	20	1.20	0.01	0.10
8R-CC, 7–9	94.20	0.05	0.47	0.004	0.10	0.10	13	0.48	0.01	0.04
9R-CC, 18–20	103.90	0.08	0.51	0.008	0.00	0.15	—	—	n.d.	—
10R-1, 23–24	104.13	0.09	0.39	0.008	0.11	0.22	11	0.78	n.d.	—
10R-1, 23–25	104.13	0.07	0.33	0.008	0.08	0.22	9	0.86	n.d.	—
10R-1, 35–37	104.25	0.05	0.29	0.000	0.08	0.16	—	—	n.d.	—
11R-1, 34–36	113.94	0.03	0.64	0.000	0.00	0.04	—	—	0.01	0.012
18R-1, 35–37	181.65	n.d.	n.d.	n.d.	n.d.	—	—	—	0.01	—
21R-1, 31–33	210.61	0.06	0.30	0.005	0.39	0.19	11	0.14	0.01	0.05
23R-CC, 11–13	239.30	0.29	0.52	0.010	0.16	0.56	30	1.8	0.01	0.28
25R-1, 40–42	249.30	0.24	0.58	0.004	0.00	0.41	50	—	n.d.	—
25R-1, 74–76	249.64	0.07	0.21	0.002	5.13	0.35	411	0.01	0.01	0.06
26R-1, 98	259.58	0.02	0.30	0.031	0.00	0.06	1	—	n.d.	—
27R-1, 39	268.19	0.02	0.20	0.000	0.00	0.10	—	—	n.d.	—
28R-1, 30	277.80	0.02	0.27	0.011	0.31	0.09	2	0.08	n.d.	—
29R-1, 9	287.29	0.14	1.54	0.038	1.38	0.09	4	0.1	n.d.	—
Miscellaneous:										
139-858A-										
6H (black soot)	43.00	2.01	0.68	0.042	0.79	2.96	48	2.5	n.d.	—
2H-5, 71 (nodule)	10.21	8.68	0.21	0.026	0.12	41.33	334	72.3	7.56	1.12
2H-5, 71 (sediment)	10.21	0.73	0.52	0.035	1.41	1.40	21	0.5	0.46	0.27

Notes: n.d. = not determined; — = not applicable.
[a]Calculated as percentage ratios.

sections of all four holes, suggesting considerable hydrocarbon redistribution, probably associated with complex fluid flow and heat distribution patterns in this active hydrothermal area.

Black Soot

Black soot (carbonaceous particulate matter) occurs in the deeper intervals of Holes 858A, 858B, 858C, and 858D. This type of carbonaceous soot, with higher TOC values, has been described in hydrothermally altered sediment drilled in Guaymas Basin (Curray, Moore, et al., 1982). The sample analyzed from this site has 2.01% carbon (Table 15) compared with much lower amounts in surrounding sediment (generally 0.1%–0.4%). This black soot occurs from the following depths to hole bottom: 858A—45 mbsf, 858B—5 mbsf, 858C—13 mbsf, and 858D—10 mbsf. These depths correspond to the intervals showing either yellow or white fluorescence (see above), suggesting this "soot" is a kerogen residue formed in zones exposed to hydrothermal flow, which also causes production and hydrothermally induced migration of bitumens.

Bitumen Analyses

Aliquots of the supernatants from hexane/methanol extracts of the samples from the fluorescence assessment or subsamples of freeze-dried sediments were concentrated under a stream of nitrogen to about 10–40 µL. Equal volumes of sediments (3 mL) and solvents were prepared for extraction so that the relative concentrations of the lipids/bitumen could be estimated vs. depth. The extract concentrates were analyzed by high-resolution gas chromatography and examples of GC traces are shown in Figures 44 and 45. Yields of extractable organic matter are high within discrete intervals in the upper sections of the holes and approach similar levels at the other depths as observed for the previous sites (Table 16, Figs. 46 to 49). These high yields, together with the elevated TOC values at shallow depths (see Figs. 37 to 40 and discussion below), indicate that migrated bitumens are probably important and the hydrocarbon signatures can be utilized as indicators for hydrothermal petroleum. Thus, samples with high bitumen yields (>50 × 10^6) and/or mature *n*-alkane signatures are defined here as hydrothermal petroleum intervals.

The bitumen parameters for maturation and organic matter sources which were measured aboard ship are listed in Table 16. The dominant compound series in the total extracts are hydrocarbons ranging from n-C_{14} to n-C_{35} (some of the hydrothermal petroleums have ranges from n-C_{10} to >n-C_{36}), with pristane ($C_{19}H_{40}$, Pr) and phytane ($C_{20}H_{42}$, Ph) as the major isoprenoid alkanes (e.g., Figs. 44A, 44B, 44D, and 45A–D). In the relatively unaltered sediments, the *n*-alkanes >C_{26} have a significant predominance of odd carbon numbers (carbon preference index, CPI, >1.0) and carbon number maximum (C_{max}) at

Table 16. Various parameters for the solvent soluble organic matter in sediments from Holes 858A, 858B, 858C, and 858D.

Core, section, interval (cm)	Depth (mbsf)	Relative yield ($\times 10^{-6}$)	Carbon maxima[a]	Carbon preference index (26–35)	Pr/Ph	Pr/n-C_{17}	Ph/n-C_{18}	U^K_{37}
139-858A-								
1H-1, 81–83	0.82	29.2	29, Pr	2.59	2.56	1.82	0.73	0.26
1H-1, 149–150	1.50	504.0	24	0.68	0.67	0.33	0.38	n.d.
1H-2, 12–14	1.63	29.8	29, Pr	2.07	3.40	2.07	0.74	0.24
2H-1, 34–36	2.75	9.0	29, 20	2.12	1.43	0.65	0.48	0.18
2H-2, 85–87	4.76	64.7	17, 29	3.64	0.95	0.35	0.79	0.34
2H-3, 45–49	5.87	12.3	29, 20	1.79	1.78	0.86	0.60	0.23
2H-5, 28–32	8.70	2.8	29, Pr	2.25	2.85	1.03	0.43	0.17
2H-CC	11.90	11.1	29, 20	1.69	0.71	0.50	0.53	0.32
3H-3, 81–85	15.73	7.8	29, 17	1.46	0.88	0.46	0.80	[b]0.34
3H-6, 0–1	19.41	10.7	29, Pr	3.10	1.11	2.86	4.15	n.d.
4H-2, 0–1	22.91	34.8	17, 27	0.98	4.57	0.64	0.17	n.d.
4H-4, 52–56	26.44	77.9	15, 27	1.11	4.44	0.98	0.28	n.d.
5H-5, 0–3	36.92	2.8	17, 27	1.05	1.04	0.27	0.50	n.d.
6H-3, 55–56	43.96	8.9	17, 27	1.04	0.63	0.05	0.24	n.d.
6H-CC	49.90	622.0	PAH	n.d.	n.d.	n.d.	n.d.	n.d.
7H-CC	58.90	1.9	17, 27	1.52	0.20	0.10	0.83	n.d.
11X-CC	81.60	9.2	27, 22	1.03	1.67	0.33	0.30	n.d.
139-858B-								
1H-1, 17–18	0.18	11.6	Pr, 27	1.22	2.50	2.00	0.65	0.32
1H-1, 48–52	0.50	741.3	17, 27	1.22	1.60	0.35	0.81	0.34
1H-2, 31–32	1.82	5.8	25, Pr	0.87	1.42	1.11	1.40	0.34
1H-2, 42–44	1.93	105.2	17, 20, 27	1.11	1.22	0.44	1.00	[b]0.39
1H-3, 23–27	3.25	26.3	17, 29	2.95	1.25	0.40	0.86	n.d.
1H-4, 19–23	4.71	24.4	17, 29	4.47	1.20	0.60	0.93	n.d.
1H-CC, 0–1	7.20	46.9	25, Pr	0.79	1.79	3.08	2.15	n.d.
2H-CC	16.70	37.1	17, 20, 27	0.83	0.42	0.29	1.33	n.d.
5H-2, 112–113	26.53	5.2	20, 29	0.91	0.29	0.21	0.57	n.d.
139-858C-								
1H-1, 22–26	0.24	26.2	Pr, 29	2.50	1.85	1.43	0.82	0.35
1H-2, 0–5	1.53	47.7	Pr, 29	2.36	2.18	1.42	0.77	0.26
1H-2, 42–46	1.94	20.4	17, 29	3.13	1.90	0.19	0.71	0.26
1H-3, 21–25	3.23	38.7	17, 29	4.09	1.05	0.20	1.19	[b]0.63
2H-1, 42–44	3.93	107.5	17, 29	3.26	1.08	0.27	0.66	0.39
2H-2, 77–79	5.78	25.1	17, 29	2.94	0.93	0.38	0.77	n.d.
2H-5, 71–73	10.22	63.2	17, 27	1.74	1.13	0.36	0.86	n.d.
2H-CC	13.00	572.3	Ph, 28	0.46	0.98	1.96	1.22	n.d.
3H-2, 53–54	15.04	848.0	Ph, 28	0.71	0.45	0.79	1.12	n.d.
3H-CC	22.50	14.7	Ph, 27	0.91	0.18	0.35	2.00	n.d.
5H-CC	33.00	7.1	26	0.85	n.d.	n.d.	n.d.	n.d.
7H-CC	46.50	21.2	20, 26	0.92	0.71	0.37	0.44	n.d.
10X-CC, 0–2	54.50	43.3	20, 26	0.96	0.84	0.51	0.46	n.d.
139-858D-								
1H-1, 0–1	0.00	7.1	29, 17	1.59	2.68	0.99	0.42	0.36
1H-1, 145–150	1.48	15.3	29, Pr	2.53	2.95	1.71	0.69	0.36
1H-3, 145–150	4.48	27.9	29, Pr	2.52	1.68	1.68	1.16	0.41
1H-4, 146–150	5.98	16.7	29, 17	1.85	1.95	0.96	0.81	n.d.
1H-5, 145–150	7.48	18.5	29, 17	2.07	2.00	0.74	0.68	n.d.
2H-3, 145–150	13.78	100.7	Pr, 28	0.71	1.92	2.44	1.13	n.d.
2H-5, 144–150	16.78	44.2	Pr, 28	0.78	2.22	2.08	0.88	n.d.
3P-1, 54–56	19.35	831.5	17	0.88	1.90	0.38	0.22	n.d.
4H-5, 144–150	27.28	28.4	24, Ph	0.90	0.30	0.43	1.43	n.d.
6X-1, 96–105	29.81	17.5	26, 17	0.87	0.40	0.27	0.69	n.d.

Note: n.d. = not determined because compounds not present.
[a]Major homologs are listed in decreasing order of intensity (C_{max}). Pr = pristane, PAH = polynuclear aromatic hydrocarbon, Ph = phytane.
[b]Trace.

C_{27} or C_{29} (e.g., Fig. 45C, Table 16; and see "Organic Geochemistry" sections of previous site chapters, this volume), typical for immature hydrocarbons with an origin from terrestrial higher plants (Simoneit, 1977, 1978). The n-alkane patterns $<C_{24}$ with the unresolved complex mixture (UCM) of branched and cyclic compounds and the C_{max} at C_{17} (e.g., Fig. 45B, Table 16, and see "Organic Geochemistry" sections of previous site chapters, this volume) are typical for autochthonous marine bitumen derived from alteration of microbial lipids (Simoneit, 1977, 1978).

Hydrothermal petroleums are products of rapid diagenesis/catagenesis and have alkane distributions analogous to those of conventional crude oils (Simoneit and Lonsdale, 1982; Simoneit, 1985, 1990a).

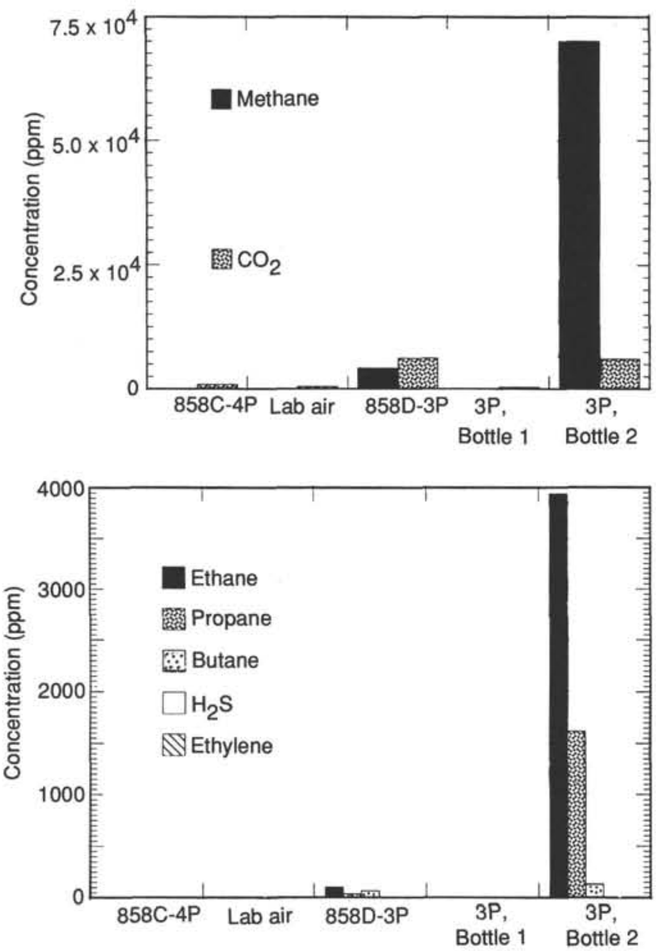

Figure 43. Relative concentrations of C_1–C_4 hydrocarbons, carbon dioxide, hydrogen sulfide, and ethylene in sediment headspace gas vs. gases collected with the pressure core-barrel manifold (Core 858C-4P).

The carbon number distributions and other geochemical parameters for hydrothermal petroleums generally reflect the source organic matter and the degree of thermal alteration or maturity (Kawka and Simoneit, 1987; Kvenvolden et al., 1986; Simoneit and Lonsdale, 1982; Simoneit, 1985, 1990a). The hydrothermal petroleum horizons in the cores drilled at Site 858 have diverse *n*-alkane distributions (e.g., Figs. 44A–D, 45A, 45B, and 45D) and also variable yields (cf. solid data points in the yield plots of Figs. 46 to 49).

Examples of immature hydrothermal petroleums are Samples 139-858A-1H-CC and 139-858C-3H-1, 44–45 cm, where the isoprenoids or n-C_{17} are predominant. Intermediate maturity is evident for Sample 139-858A-4H-4, 52–56 cm; full maturity is found for Samples 139-858A-1H-1, 149–150 cm, 139-858C-2H-CC, and 139-858D-2H-CC, 37–40 cm, where the former is partially biodegraded as inferred from the low amounts of hydrocarbons $<n$-C_{22} (Simoneit, 1990b). Overmaturity is indicated for Sample 139-858A-6H-CC, consisting primarily of aromatic hydrocarbons, typically generated at high temperatures (>200°C or more) (cf. Figs. 44 and 45). The hydrocarbon pattern of the latter sample is similar to that of the petroleum present in a barite chimney recovered with the *Alvin* submersible from this vent/mound system (Simoneit et al., in press).

The CPI (range C_{26}–C_{35}) is near one in the hydrothermal petroleum horizons of Holes 858A, 858B, 858C, and 858D (Figs. 46 to 49), indicative of full petroleum maturity caused by the high thermal stress. The CPI profiles for all holes remain at values near 1 below the oil horizons, consistent with full maturity vs. depth together with a source input of the even-predominance alkanes. The same pattern was observed at Site 857. The CPI <1 in various intervals of Holes 858A, 858B, and 858C, especially for the hydrothermal petroleum of Sample 139-858C-2H-CC, which has a strong even-carbon number predominance from n-C_{16} to n-C_{34} (Fig. 45A), should be emphasized. This low CPI seems to be a characteristic of these bitumens; although, this even carbon-number predominance of *n*-alkanes has also been described for immature sediments from DSDP Legs 5 and 18 in the northeast Pacific to the south of this region (Simoneit, 1977) and for sediments from other geographic areas (Grimalt and Albaiges, 1987). Thermal maturation generally does not produce CPI values of less than 1, so that the low CPI in these holes must be partially source-related and is transferred to the fully mature petroleums. Since thermal alteration in these sediments commences with immature organic matter that has not completed diagenetic alteration, the *n*-alkanols (also *n*-alkanoic acids) from terrestrial plant waxes (Simoneit, 1978) and other biopolymers may be the sources of the even-chain alkanes $>C_{24}$. For the *n*-alkanols this would require alteration by dehydration and double bond reduction, a facile process in hydrothermal systems (cf. earlier discussion in "Organic Geochemistry" section, "Site 856" chapter). The variability of the surficial CPI values in these holes probably reflects different source inputs of marine and terrestrial organic matter which are then overprinted by the degree of thermal stress (Figs. 46 to 49). For example, the two "cooler" holes, 858A and 858C, have higher surface CPI values than the two "hotter" holes, 858B and 858D.

Full maturation is not always evident in the isoprenoid to normal hydrocarbon ratios (Pr/n-C_{17} and Ph/n-C_{18}) for the hydrothermal petroleum zones in these holes, but in general these ratios are low below those horizons (Figs. 46 to 49). Low Pr/n-C_{17} and Ph/n-C_{18} values (<0.5) are characteristic of basin sediments which, at some time in their geologic history, have been heated to temperatures greater than 50°C, at the beginning of the oil thermal window ("Organic Geochemistry" section, "Site 855" chapter). This temperature correlation does not fit for these samples (see discussion below). The Pr/Ph ratio, which we believe to be influenced both by source and by maturation (cf. "Organic Geochemistry" section, "Site 856" chapter), generally shows fluctuating values in the range of 0.2 to 4.6 for all holes, both inside and outside intervals with hydrothermal petroleum (Figs. 46 to 49). This may reflect both the organic matter sources and lower temperature maturation.

The overall hydrocarbon signatures of the surficial intervals of these sediments with low thermal alteration are similar to those of Sites 856 and 857, and of shallow gravity cores taken near the Middle Valley hydrothermal vents (Simoneit et al., in press). The hydrocarbons in the surficial intervals with high extract yields reflect rapid maturation by hydrothermal processes, probably resulting from high-temperature fluid invasion of the deeper intervals and petroleum migration upward. The hydrothermal petroleum occurs at shallow depths in all holes (above 60 mbsf in 858A, and above 30 mbsf in 858B, 858C, and 858D). Often, there appears to be an accumulation of hydrocarbons, as indicated by an increase in relative yield, in association with zones of high carbonate concentration (e.g., at 50 mbsf in Hole 858A, Figs. 37 and 46; at 5 mbsf in Hole 858B, Figs. 38 and 47; at 14 mbsf in Hole 858C, Figs. 39 and 48; and the 13–19 mbsf interval of Hole 858D, Figs. 40 and 49). Rapid changes in CPI, Pr/n-C_{17}, Pr/n-C_{18}, and Pr/Ph are also commonly observed within the same intervals, suggesting that expulsion/migration aspects need to be studied further on shore by comparing bitumen maturation results with those of kerogens, which should not migrate.

If correct present-day subsurface temperatures can be extrapolated from the heat-flow and temperature data (see "Heat Flow" section, this chapter), then the approximate contemporary temperatures of the hydrothermal petroleum zones observed for Holes 858A, 858B, and 858C can be estimated (temperatures are indicated in Figs. 46 to 48). These temperatures range from 3° to more than 200°C. The lowest temperature commonly cited for the beginning of the conventional oil

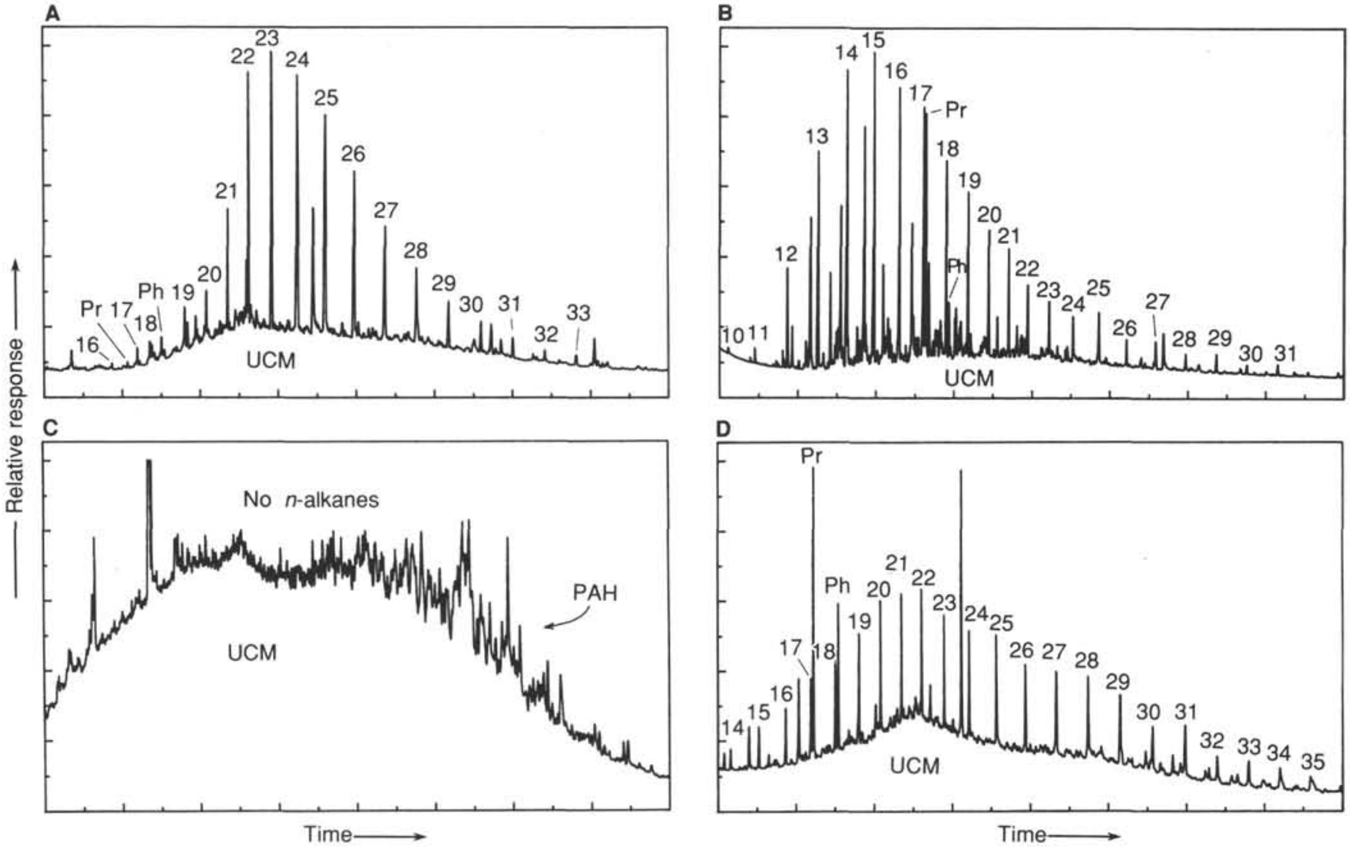

Figure 44. Representative gas chromatograms of the total extracts from samples. **A.** Sample 139-858A-1H-1, 149–150 cm, CPI = 0.68. **B.** Sample 139-858A-4H-4, 52–56 cm, CPI = 1.11. **C.** Sample 139-858A-6H-CC, CPI = not determined. **D.** Sample 139-858B-1H-CC, 14–15 cm, CPI = 0.93. Numbers refer to chain length of *n*-alkanes. Pr = pristane, Ph = phytane, PAH = polynuclear aromatic hydrocarbons, UCM = unresolved complex mixture.

generation window is 50°C, with peak generation occurring at about 80° to 100°C. The temperatures shown in Figures 46 to 48 include this range. Thus, the hydrothermal petroleum may have been generated *in situ*, although migration and deposition of oil into those intervals seems much more likely, particularly into zones where hydrothermal flow may have also caused capping by carbonate precipitation (see "Sediment Geochemistry and Alteration" section, this chapter). Bitumen concentrations in the intervals below the hydrothermal petroleum zones are low. This may indicate either that these zones were devoid of petroleum potential, or more likely, that the oil which had formed there has migrated both upward and laterally with hydrothermal fluids until it reached a zone where it could be trapped.

The measured temperature at 20.9 mbsf in Hole 858D was >208°C, which indicates a gradient of at least 9.9°C/m. The present-day temperatures in the zones with high relative yields of hydrothermal petroleum, from 14 to 28 mbsf, have experienced high temperatures, possibly as high as 280ÉC, based on nearby vent fluid and downhole temperature measurements ("Downhole Logging" section, this chapter). If the temperature window is truly this high, it seems unlikely that these bitumens could have survived for any length of time. Therefore, it is postulated that (1) these hydrocarbons have only recently migrated with hydrothermal fluids into this interval, (2) they are actively being generated and/or migrating, or (3) they were generated recently as the surrounding sediments were exposed to a pulse of hot fluid. Note that these hydrothermal petroleum zones with variable compositions in the sediments of Site 858 are very different from those described for Hole 857C. Only trace amounts of bitumen were encountered at depth in that hole, consistent with in-situ generation reflecting both the organic matter sources and the highest formation temperatures (see "Organic Geochemistry" section, "Site 857" chapter). Shore-based studies comparing bitumen compositions, which can be influenced by migration processes, with kerogen maturities, which record the highest time-temperature regimes experienced by the samples, should allow us to distinguish more clearly between migrational and *in-situ* generation processes at both Sites 857 and 858.

Molecular Stratigraphy

Molecular stratigraphy using the long-chain ketones (C_{37} and C_{38} alkenones) as markers for coccolithophorids was described earlier ("Organic Geochemistry" section, "Site 856" chapter). The alkenones were only detectable in the bitumen extracts of sediments from Holes 858A, 858B, 858C, and 858D to a maximum depth of 16 mbsf and generally only in the surficial sections (Table 16). Their presence in these holes parallels the occurrence of *Emiliania huxleyi* ("Biostratigraphy" section, this chapter), although the molecular fossils disappear before the fossil tests, due to decomposition with increasingly higher temperatures. The $C_{37:3}$ compound seems to degrade more rapidly than $C_{37:2}$. Since the alkenones are not stable under significant thermal stress their distribution is a good temperature indicator (subject to further definition by shore-based study), which is consistent with the current thermal regime (see "Site Geophysics and Geology" section, this chapter). The ketone unsaturation index (U^K_{37}; Marlowe et al., 1984; Brassell et al., 1986; Prahl and Wakeham, 1987) was calculated for sediments from this site as:

$$U^K_{37} = [C_{37:2}]/([C_{37:2}] + [C_{37:3}]).$$

The results show sea-surface temperature conditions (4°–9°C) in the upper sections as observed for the other sites of this leg (Fig. 50).

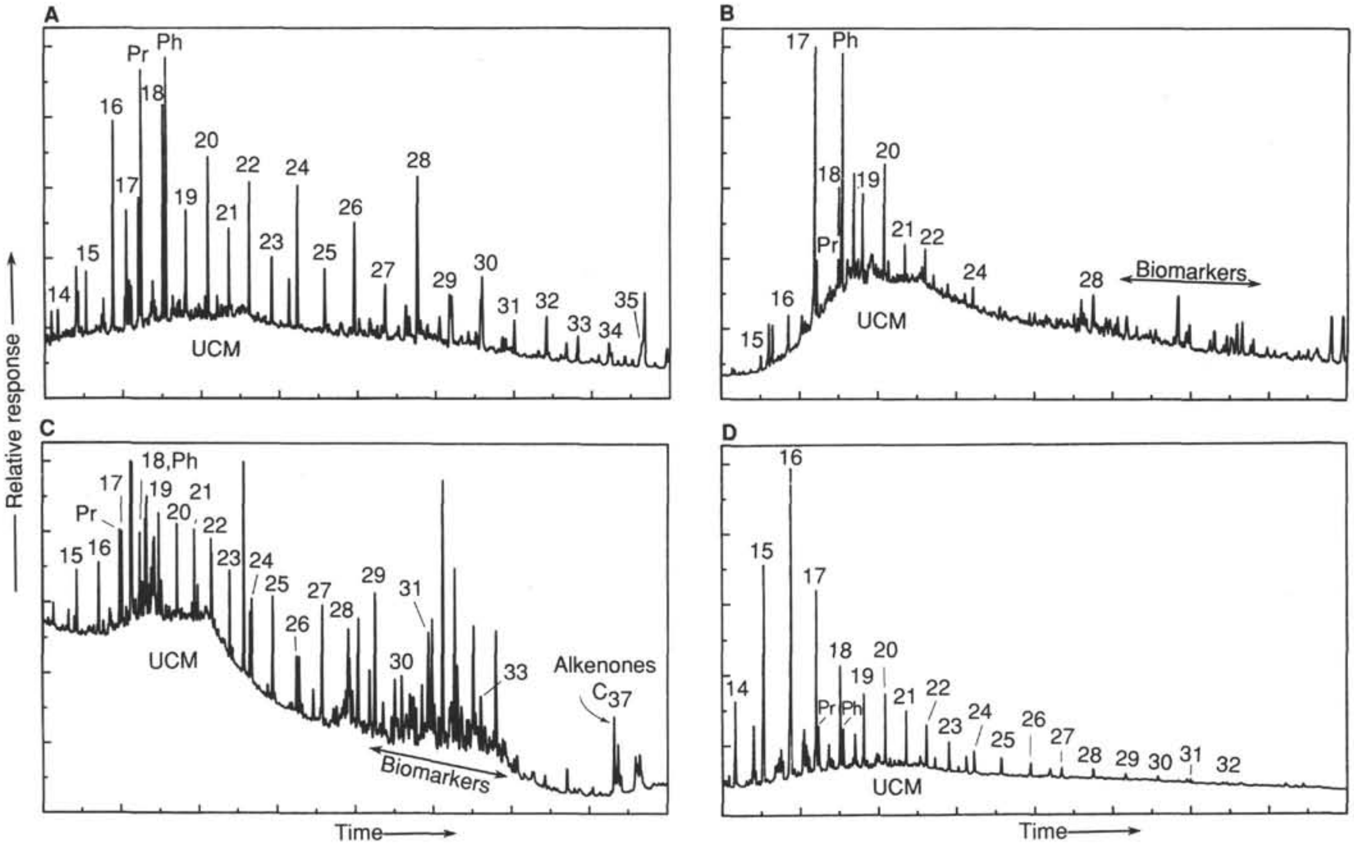

Figure 45. Representative gas chromatograms of the total extracts from samples. **A.** Sample 139-858C-2H-CC, CPI = 0.46. **B.** Sample 139-858C-3H-1, 44–45 cm, CPI = 0.75. **C.** Sample 139-858D-1H-1, 0 cm, CPI = 1.59. **D.** Sample 139-858D-2H-CC, 37–40 cm, CPI = 0.58. Numbers refer to chain length of *n*-alkanes. Pr = pristane, Ph = phytane, UCM = unresolved complex mixture.

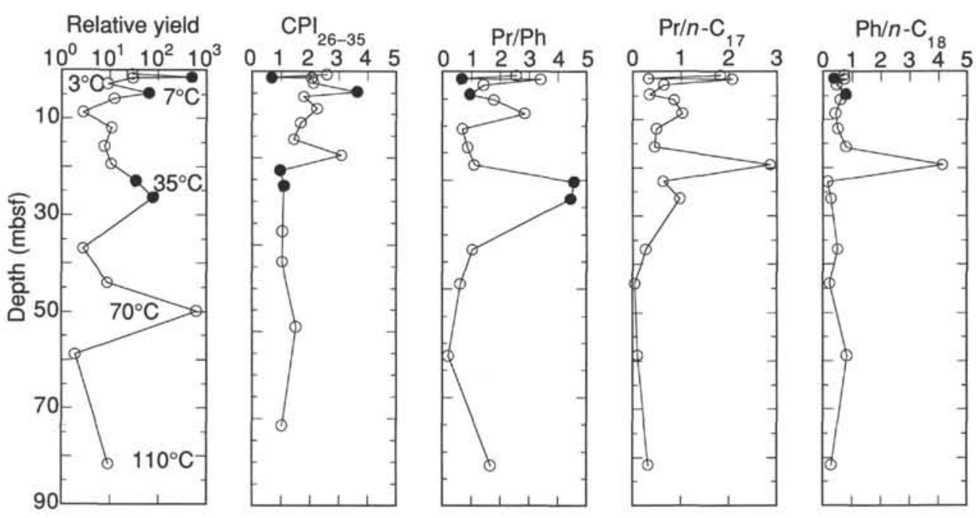

Figure 46. Selected parameters for bitumen extracts vs. depth for sediment from Hole 858A. Solid data points are for hydrothermal petroleum. The present *in-situ* temperatures are also given.

The U^K_{37} in the depth interval below 2 mbsf (below 8 mbsf in Hole 858A) is variable because of the low alkenone concentrations. Examples of this ratio with surface-seawater temperatures for alkenones in surficial sediment from the more tropical Site 658 on Walvis Ridge (Poynter et al., 1989) and Site 686 on the Peru Margin (Farrimond et al., 1990) are also shown.

Elemental Analyses

Downhole profiles for weight percentages of C, H, N, and S, as well as ratios of C/H, C/N, and C/S in all Site 858 holes, are shown in Table 15 and in Figures 51 through 55; profiles of inorganic and total organic carbon are shown in Figures 37 through 41.

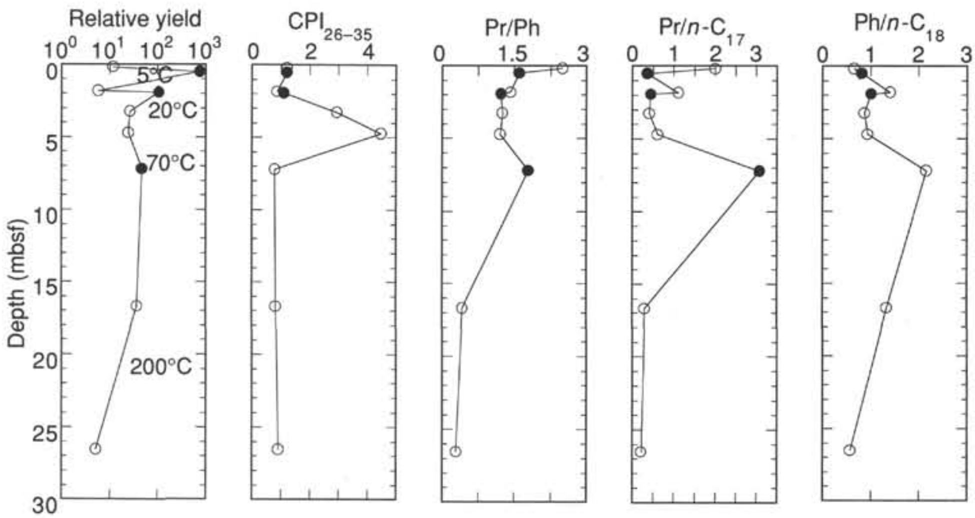

Figure 47. Selected parameters for bitumen extracts vs. depth for sediment from Hole 858B. Solid data points are for hydrothermal petroleum. The present *in-situ* temperatures are also given.

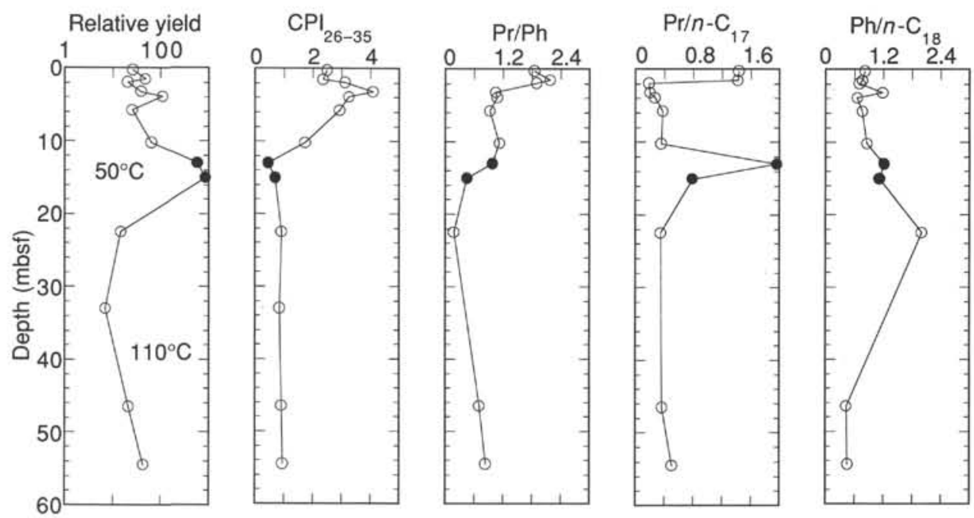

Figure 48. Selected parameters for bitumen extracts vs. depth for sediment from Hole 858C. Solid data points are for hydrothermal petroleum. The present *in-situ* temperatures are also given.

Total carbon varies from about 2.5% to 0.2% in Hole 858A and consists of about equal proportions of organic and inorganic carbon, as discussed above in detail under the section on gases. Concentrations of both total carbon and inorganic carbon decrease to very low levels below 120 mbsf, where the temperature is estimated to be at least 160°C (Fig. 37; see "Heat Flow" section, this chapter). Nitrogen occurs in low concentrations of 0.02% to 0.06% and decreases with depth in Hole 858A, comparable to concentrations observed in Hole 857A. The peaks and valleys in the profile are often inversely correlated with S, suggesting that the nitrogen is associated with clay and decreases during periods of sedimentary pyrite formation. However, these processes are not reflected in the hydrogen profile, where values remain fairly constant, in the range of 0.4% to 0.5% through the entire hole. This invariability of hydrogen with depth is also reflected in the C/H profile, which correlates closely with the C profile. Considerable variability in the C/S and, to a lesser extent, the C/N ratio occurs from 40 to 100 mbsf, probably reflecting changes in mineralogy within this zone.

In Hole 858B, total carbon undergoes a rapid decrease with depth and increasing temperature within the top 12 mbsf (Fig. 52). Nitrogen undergoes an exponential decrease within the same zone, from relatively high values of 0.1% to less than 0.02%. The corresponding decrease in TOC within the same interval (Fig. 38) suggests that the nitrogen is derived from organic matter in clays and minerals which is lost via thermal degradation and upward circulating hydrothermal fluids in this "hot" hole (geothermal gradient about 9°C/m, see "Heat Flow" section, this chapter). The increased influences of hydrothermal fluids and pyritization are also reflected in the relatively high hydrogen and sulfur percentages from 0 to 2 mbsf and at 12 mbsf (Fig. 52). However, there is also an interesting subsurface maximum in carbon at 5 mbsf (corresponding to a temperature of about 45°C), which is reflected in the C/H, C/N, and C/S profiles. A subsurface maximum in inorganic carbon, but not TOC, also occurs at this depth (Fig. 38). This maximum may be associated with a "cap" on the hydrothermal circulation system within this area (see "Sediment Geochemistry and Alteration" section, this chapter).

Hole 858C, which is one of the two coolest of the Site 858 holes has a geothermal gradient slightly higher than that of Hole 858A. There are some similarities between the C, H, N, and S profiles for the two holes (compare Fig. 53 with Fig. 51). Total carbon is high in

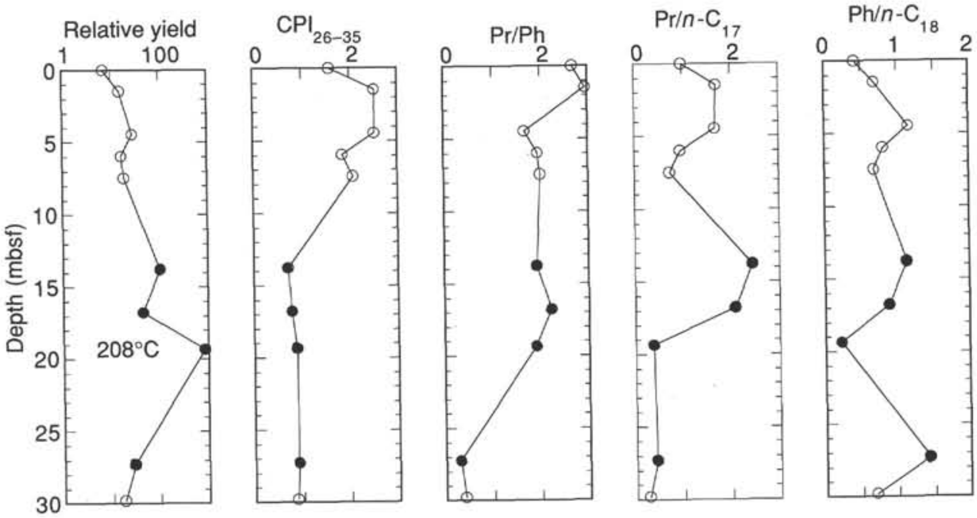

Figure 49. Selected parameters for bitumen extracts vs. depth for sediment from Hole 858D. Solid data points are for hydrothermal petroleum. The present measured temperature is also given.

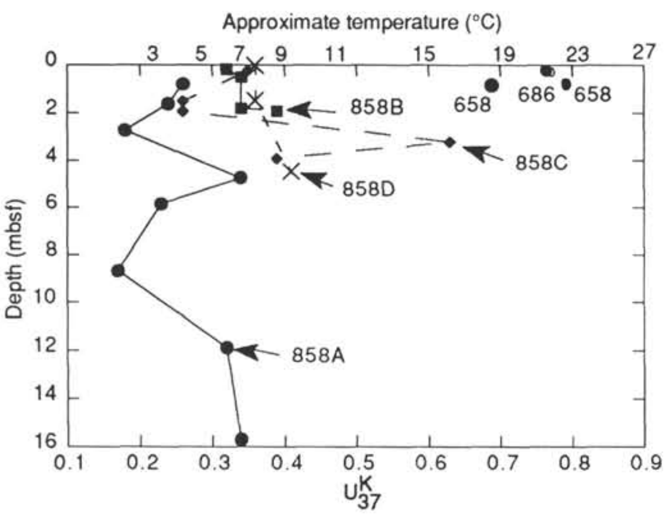

Figure 50. C_{37} alkenone parameter (U^{K}_{37}) and temperature estimate of the ocean surface water vs. sub-bottom depth in Holes 858A, 858B, 858C, and 858D. Other more tropical sites (Site 658 on Walvis Ridge and Site 686 on Peru Margin) are also shown for comparison.

surface sections and shows a subsurface maximum at 8 mbsf (Fig. 53). A large decrease then occurs below 50 mbsf, corresponding to a temperature of about 125°C, which correlates primarily with loss of inorganic carbon (Fig. 39). As is the case in Hole 858A, organic carbon remains in relatively constant low levels (about 0.2%) in all sections of the hole below 10 mbsf. Some interesting changes in both nitrogen and sulfur occur in surface sections above 10 mbsf—both north and south decrease along with C at 2 mbsf. However, as inorganic carbon and, to a lesser extent, organic carbon, reach a peak at 8 mbsf, N goes through a maximum. S has a major maximum at 2 mbsf, probably due to the presence of anhydrite, and then drops to low levels. Through all of these changes, hydrogen remains almost constant at 0.5%. The variations undoubtedly reflect mineralogic changes. However, it is not clear from shipboard studies whether these are primary depositional features or are caused by secondary alteration related to hydrothermal circulation. The latter seems more likely, because the overall primary character of all of the sediments before alteration of Leg 139 appears to be very similar (see "Sediment Geochemistry and Alteration" section, this chapter).

In sections of Hole 858C below 10 mbsf, sulfur increases steeply to concentrations of 1.4% to 1.8% at 10 mbsf, at the same point where carbon decreases. Although there is currently a gap in the data from 10 to 40 mbsf, sulfur appears to remain high until 45 mbsf (S = 2%) and then undergoes a gradual decrease to 0.5% at 75 mbsf. Hydrogen remains fairly constant throughout the hole, in the range of 0.4% to 0.5%. All of these changes, plus other more subtle features, are observed in profiles of the elemental ratios, including C/H (minimum at 55 mbsf), C/N (maximum at 68 mbsf, where N drops to its minimum value), and C/S (minimum at 55 mbsf).

Hole 858D has a geothermal gradient of about 9°C/m, similar to Hole 858B (see "Heat Flow" section, this chapter). As with Hole 858B, both nitrogen and total carbon decrease rapidly with depth within the top 5 mbsf (Fig. 54). In deeper intervals, two higher maxima in carbon at 10 and 14 mbsf consist of inorganic carbon (Fig. 40). Hydrogen stays fairly constant with depth, in the range of 0.4% to 0.6%. However, one minimum value of 0.35% at 18 mbsf corresponds to a minimum in N and a maximum in S, suggesting that pyrite formation is occurring at the expense of clay minerals. The depth profiles of C/H, C/N, and C/S in Figure 54 are dominated by the two carbonate peaks at 10 and 12 mbsf. Overall, the C, H, N, and S profiles differ markedly between Holes 858B and 858D, in spite of the similar geothermal gradients. These differences are probably related to the different mineralogies observed in the two holes as shown by shipboard XRD measurements (see "Lithostratigraphy and Sedimentology" section, this chapter).

The elemental profiles for C, H, N, and S for Hole 858F, which is adjacent to Hole 858D and therefore also has a high thermal gradient, are shown in Figure 55. Inorganic carbon is insignificant in all sections of this hole (Fig. 41); therefore, the decrease in total carbon from 80 to 110 mbsf is really a decrease in TOC, which is present only in low levels, generally less than 0.1%. Significant variations in C, H, N, S, and ratios of C/H, C/N, and C/S occur below 200 mbsf, in the vicinity of igneous basement. The highest total carbon values in the hole are found within this deeper zone: 0.29% and 0.24% for Samples 139-858F-23R-CC, 11–13 cm (239.30 mbsf), and 139-858F-25R-1, 40–42 (249.3 mbsf), respectively, and 0.14% for Sample 139-858F-29-1, 9–13 cm (290 mbsf), the deepest sample analyzed in this work.

SEDIMENT GEOCHEMISTRY AND ALTERATION

Site 858 comprises an 800-m-long by 400-m-wide area characterized by high acoustic backscatter and high heat flow. Within this area, 12 active vents and associated mounds have been observed (Davis and Villinger,

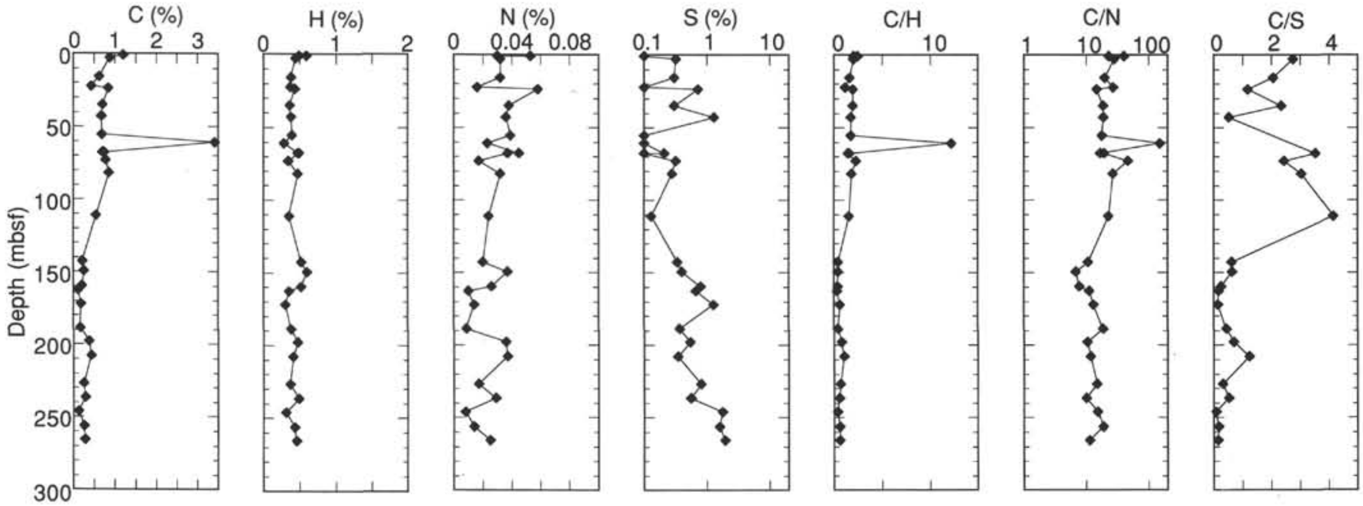

Figure 51. Percentages of C, H, N, and S and ratios of C/H, C/N, and C/S vs. depth, Hole 858A.

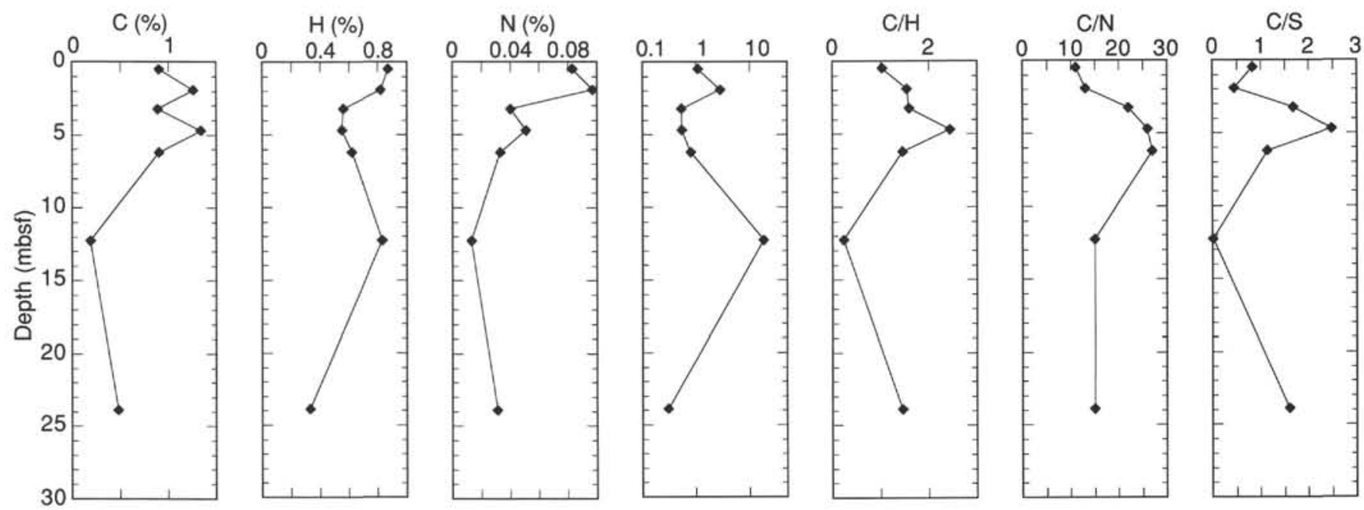

Figure 52. Percentages of C, H, N, and S and ratios of C/H, C/N, and C/S vs. depth, Hole 858B.

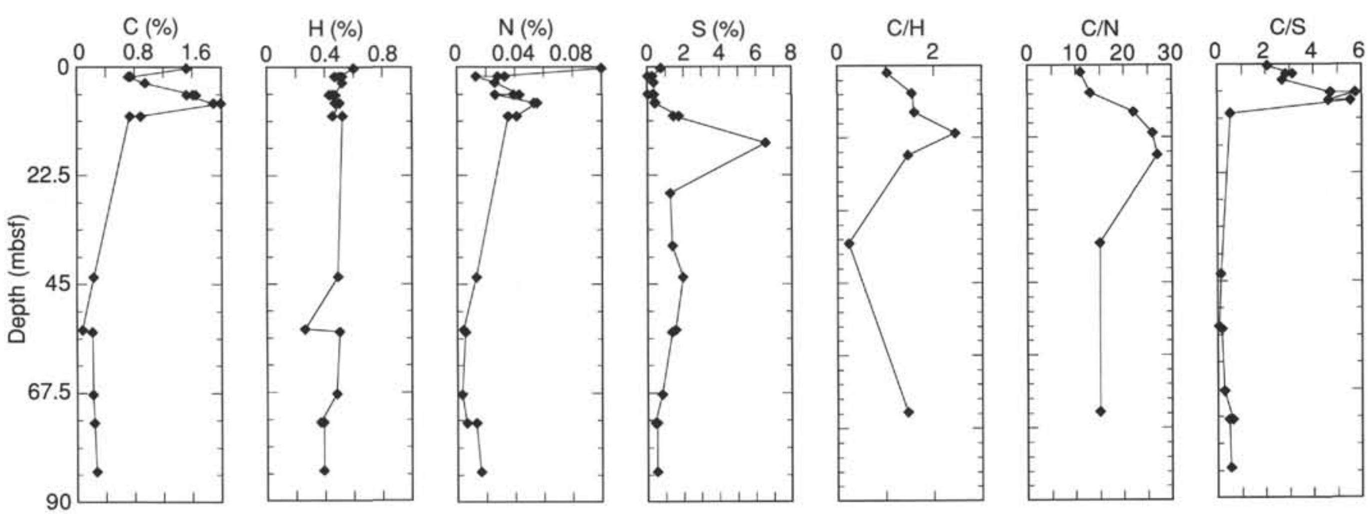

Figure 53. Percentages of C, H, N, and S and ratios of C/H, C/N, and C/S vs. depth, Hole 858C.

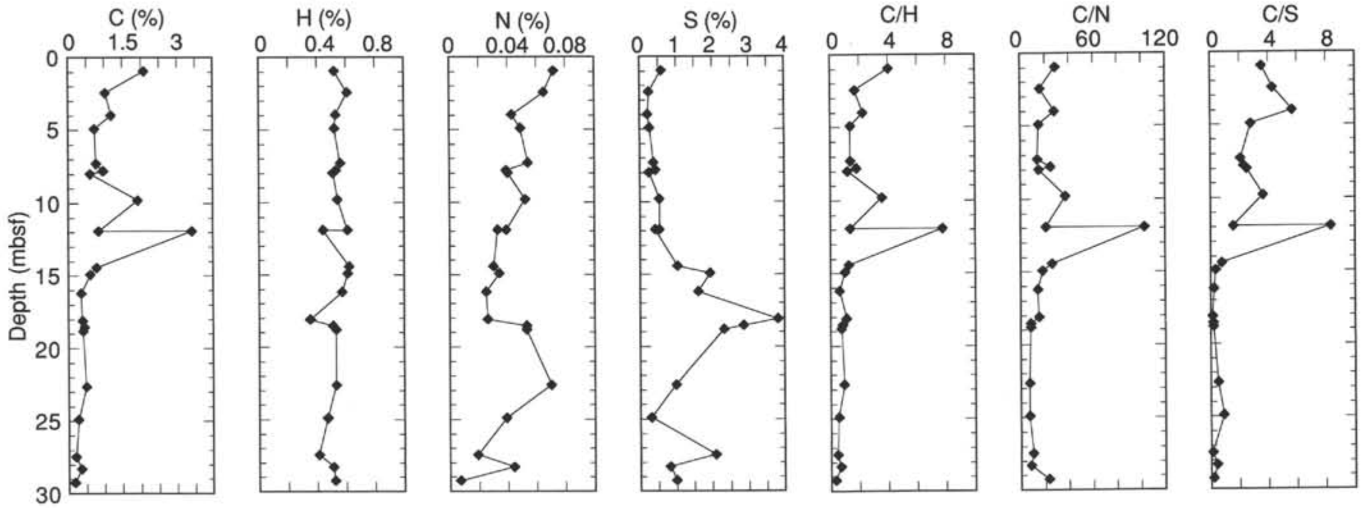

Figure 54. Percentages of C, H, N, and S and ratios of C/H, C/N, and C/S vs. depth, Hole 858D.

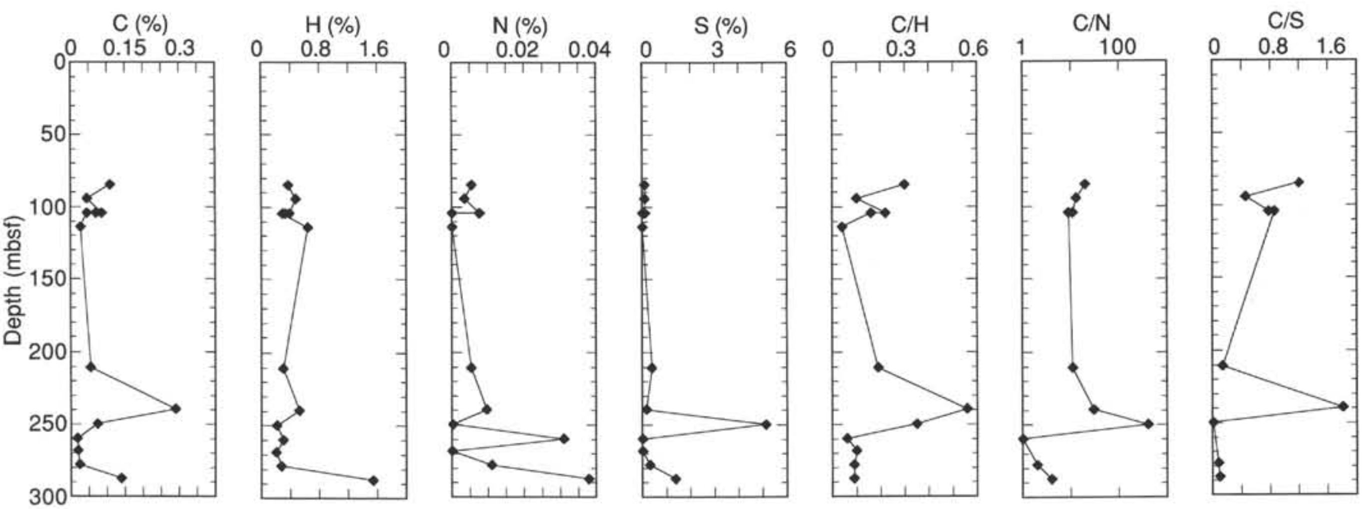

Figure 55. Percentages of C, H, N, and S and ratios of C/H, C/N, and C/S vs. depth, Hole 858F.

this volume). Of the six holes drilled at Site 858, five intersected hydrothermally altered sediment. Hole 858E was discontinued when it was realized that the drill had reentered Hole 858D. Hole 858A, the most distal from active vents at Site 858, is about 100 m west of the western margin of the acoustically rough area and about 250 m northwest of an active vent site observed in 1990 during an *Alvin* submersible dive (J. Franklin, pers. comm., 1991). This reflective area corresponds to heat flow values greater than 1 W/m^2 (Davis and Villinger, this volume). Hole 858B was drilled approximately 20 m from an active vent site containing chimneys growing on top of a 15-m-high mound. Hole 858C penetrated sediment 150 m west of Hole 858B and is within the area of high acoustic roughness, Holes 858D and 858F are situated about 75 m north of Hole 858B in the center of the heat flow anomaly, but in an area devoid of mounds or chimneys (Fig. 56). Surface sediment cores from this area contain hydrothermal pore fluids (J. Lydon, pers. comm., 1991).

Three important objectives of drilling at this site are to understand the generation of hydrothermal fluids in reaction zones, to map the pathways of fluid discharge to the seafloor, and to understand better the chemical evolution of these fluids, including mineral depositional processes within the upflow zone and at the seafloor.

This chapter describes hydrothermal structures and textures, mineralogy, and the bulk chemical composition of fluid-sediment reaction products within the fluid discharge conduit and at the seafloor.

Alteration

All of the holes cored at Site 858 recovered hydrothermally altered sediment. The alteration assemblages and the spatial distribution of these assemblages vary with depth and lateral distance from centers of hydrothermal fluid discharge.

Hole 858A

The hydrothermal alteration minerals are zoned vertically within Hole 858A, although many of the zones overlap. Between 0 and 20 mbsf, fine-grained hemipelagic sediment has a distinct green color due to the presence of authigenic clay (see "Lithostratigraphy and Sedimentology" section, this chapter). The greenish coloration occurs in clumps of more indurated hemipelagic sediment and within turbiditic layers. Studies of similar sediment recovered in shallow cores from this area have shown that this clay consists of Mg-rich smectite that

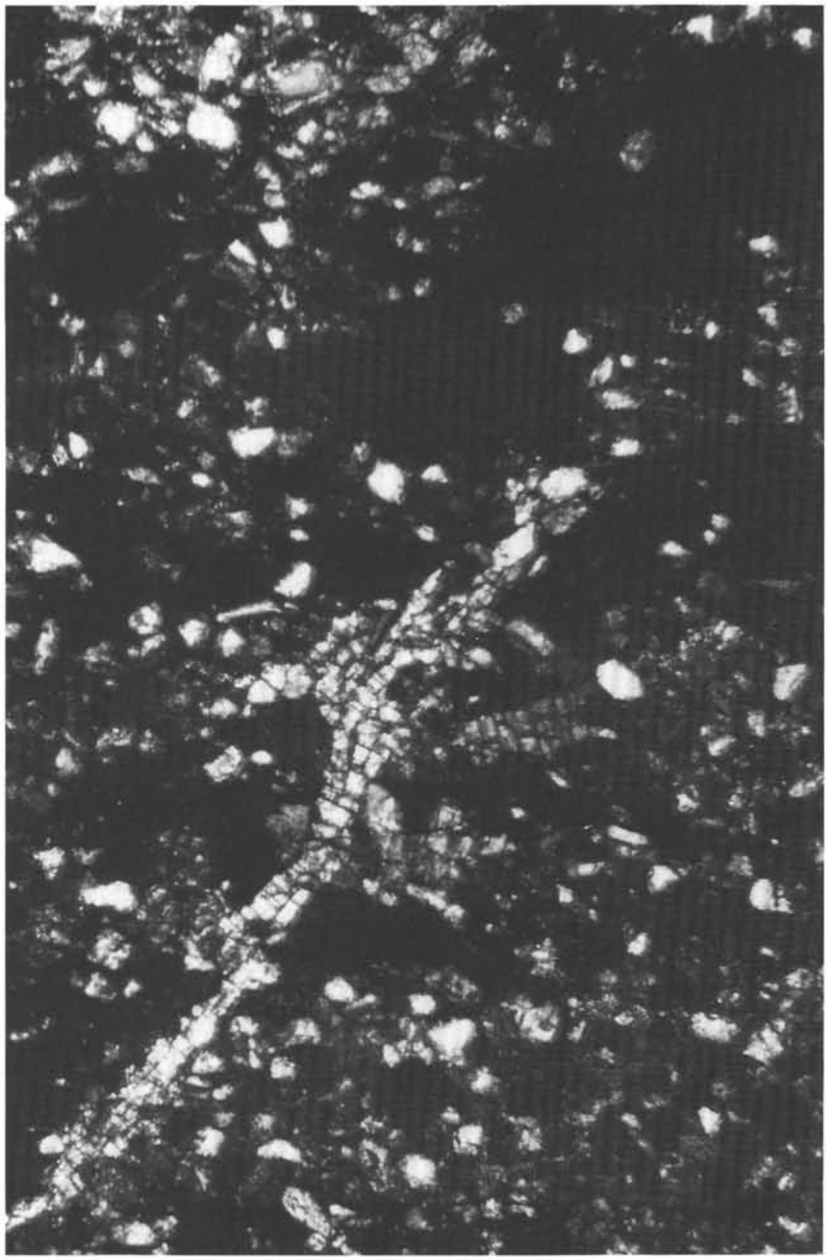

Figure 56. Photomicrograph showing euhedral crystals of anhydrite growing in hydrothermally altered hemipelagic sediment, Hole 858A (thin-section Sample 139-858A-17X-1, 13–16 cm) (plane light, 2.5× objective).

forms interstitially (W. Goodfellow, pers. comm., 1991). Carbonate concretions, disseminated pyrite, and pyrite concretions occur at depths below 20 mbsf; carbonate concretions become rare below 62 mbsf. Disseminated pyrite persists to the bottom of Hole 858A (338 mbsf), whereas pyrite concretions were not observed below 270 mbsf. Unlike disseminated pyrite, pyrite concretions occur discontinuously between 20 and 270 mbsf. Pyritized burrows are restricted to a narrow interval between 140 and 150 mbsf.

The carbonate concretions are similar to those described in Hole 856A (see "Sediment Geochemistry and Alteration" section, "Site 856" chapter). Most concretions are oblate or spherical, although they can have very irregular shapes. Some concretions have a branching morphology presumably due to infilling of burrows (e.g., Samples 139-858A-2H-CC, 3–7 cm, and 139-858A-2H-7, 41–43 cm). Their size is also highly variable; they can range from 1 cm to the width of the core liner. They extend up to 10 cm (interval 139-858A-5H-6, 45–55 cm) along the direction of the core axis. The contact with the surrounding soft or weakly indurated sediment is typically sharp. Cut specimens can be either massive or concentrically zoned, and some contain concentric bands of finely disseminated pyrite. Foraminifers are incorporated into the outside margins of some nodules (e.g., at interval 139-858A-5H-6, 40–50 cm). Pyrite is finely disseminated in most carbonate concretions. Carbonate concretions occur preferentially in clay immediately underlying sandy layers. Previous studies of concretions in this area show that barite and authigenic Mg-rich clay are commonly associated with concretions (Goodfellow and Blaise, 1988). Small bladed crystals observed in a nodule at interval 139-858A-2H-7, 32–36 cm, may be barite. Calcite also forms cement in the more permeable turbiditic silt and sand beds in the zone where carbonate concretions are common.

Pyrite occurs in many forms and grain sizes in Hole 858A. Fine-grained euhedral pyrite occurs disseminated in hemipelagic clay or turbiditic sand and silt throughout the entire hole. Because pyrite forms in the interstices of coarser grained turbidites, it commonly displays a laminated texture. Pyrite also forms concretions, where it is typically fine-grained. Between 230 and 280 mbsf pyrite infills molds of what was probably anhydrite and coats anhydrite in veins. Near the bottom of the hole, it occurs with quartz in veins cutting silicified sediment.

White anhydrite concretions, several millimeters to 1 cm across and composed of radiating crystals, occur between 62 and 100 mbsf. These concretions are followed at depth by rhombic crystals of white anhydrite that appear to form preferentially in moderately indurated hemipelagic clay. The anhydrite crystals range in size from 2 mm to 1 cm, are randomly distributed and vary significantly in abundance. In Section 139-858A-18X-2, anhydrite crystals comprise up to 50% of the sediment over 5-cm intervals. The form and distribution of the anhydrite crystals are very similar to the molds described in Hole 856B (see "Sediment Geochemistry and Alteration" section, "Site 856" chapter). Anhydrite molds also occur in Hole 858A at 125 mbsf and between 150 and 160 mbsf, but they are typically less abundant than in Section 139-858A-18X-2.

Anhydrite veins with pyrite growing on crystal surfaces occur along microfaults cutting silty claystone in interval 139-858A-27X-1, 36–44 cm. Pyrite is more concentrated along faults and fractures but also forms concretions and occurs disseminated with anhydrite in dark gray claystone in Core 139-858A-30X.

Quartz veins oriented at different directions and cutting massive gray silicified claystone first appear in Core 139-858A-39X, the last core recovered in Hole 858A. The veins are typically 1 cm thick and contain fine-grained (<1 mm) pyrite but rarely sphalerite. One of the small pieces in Core 139-858A-39X is a quartz-cemented microbreccia composed of clasts up to 0.5 cm across.

Hole 858B

Hole 858B was drilled to a depth of 38.6 mbsf. Sections 139-856B-1H-1 and -2 consist of layers of gelatinous green clay interbedded with hemipelagic sediment. Included in the hydrothermal clay beds are nontronite black patches and specks of sulfide. Studies of previous cores from this area have shown that the green clay is a Mg-rich smectite and the black sulfide is mostly Cu-Fe-sulfide with the composition of isocubanite (W. Goodfellow, pers. comm., 1991). Bands of blue-green clay alteration occur between 4 and 8 mbsf, and between 24 and about 38 mbsf. Fine pyrite cubes occur in the interstices of silt beds in Section 139-858B-1H-5.

Massive sulfide with anhydrite and botryoidal silica occur between 21 and 51 cm in Section 139-858B-2H-3. Below this massive sulfide interval to a depth of 14 mbsf, pyrite and anhydrite infill and partly replace strata, and form nodules and veins cutting gray hemipelagic clay. Coarser grained euhedral and finer grained pyrite occur throughout this interval. Below about 15 mbsf, anhydrite forms veins cutting interbedded silty clay and turbiditic silt containing disseminated pyrite.

In Section 139-858B-3H-1, the sediment consists of more indurated gray silty claystone that is cut by a network of 1- to 3-mm-wide fractures. The fractures are filled with quartz, minor pyrite, euhedral pyrrhotite, and trace amounts of chalcopyrite. Below Section 139-858B-5H-1 to the bottom of the hole (38.6 mbsf), the sediment is pale gray, moderately indurated, brecciated, and hydrothermally altered to Mg-rich mixed-layer chlorite/smectite, chlorite, and euhedral pyrite (Table 17).

Hole 858C

Hole 858C was drilled to a depth of 93.6 mbsf. This hole consists of interbedded hemipelagic and turbiditic sediments that contain a zoned sequence of hydrothermal products including carbonate concretions and carbonate cemented burrows, disseminated and concretionary pyrite, sparry calcite veins, and anhydrite nodules, molds, and veins.

Calcite-cemented worm burrows first appear in Section 139-858C-1H-3, 10 cm. Calcite concretions occur in Section 139-858C-2H-1 and become increasingly abundant to a depth of 15 mbsf where a massive carbonate breccia was recovered. The carbonate concretions are similar in shape and size to those recovered in Hole 858A. Within Section 139-858C-3H-1, the carbonate concretions have hollow cores and are vuggy, presumably due to postdepositional leaching. Within Section 139-858C-3H-2, carbonate concretions and vuggy sparry calcite patches with a sediment matrix grade into a massive carbonate layer that has been partly brecciated by coring. The massive carbonate is composed of subrounded carbonate-altered and variably replaced claystone breccia clasts that are cemented by carbonate. This massive carbonate unit is underlain by sparry calcite patches and veins, and by carbonate concretions. In interval 139-858C-3H-3, 40–42 cm, a calcite concretion is zoned from pyrite in the interior to an outer carbonate shell. A large (8 cm across) dolomite (?) concretion at interval 139-858C-6H-4, 42–50 cm, contains radial anhydrite overgrowths and is surrounded by calcite-cemented silty sandstone.

The massive carbonate layer is underlain by intensely brecciated and fractured sediment that persists to about 46 mbsf. This breccia consists of subrounded clasts (up to several centimeters across) of medium gray, moderately indurated clay containing euhedral and nodular pyrite disseminated throughout. The pyrite is highly variable in grain size, ranging from <1 mm to 4 mm. This breccia displays textures that are similar to those observed in Hole 856B (see "Sediment Geochemistry and Alteration" section, "Site 856" chapter). Pyrite replaces hexagonal pyrrhotite between Section 139-858C-5H-1 and -4. Calcite crystals growing in hemipelagic sediment occur between 23 and 28 mbsf. Horizontal and vertical calcite veins cut the sediment in Section 139-858C-5H-5. Turbiditic siltstone and sandstone layers are infilled with fine-grained euhedral pyrite and have been locally dismembered by coring. Unlike the hemipelagic clay, the siltstone and sandstone beds appear to retain their original horizonal position and have not been significantly brecciated.

Anhydrite concretions become prominent in Section 139-858C-6H-1 and continue to a depth of 40 mbsf. Vertical and horizontal anhydrite veins first appear in Section 139-858C-6H-2 and they persist to a depth of 40 mbsf except for isolated veins in Sections 139-858C-12X-CC and 139-858C-14X-CC. The anhydrite concretions range up to 1 cm across and commonly display radiating textures. A few anhydrite concretions have rims of gypsum interpreted to have formed by the hydration of anhydrite. Anhydrite molds occur at 67 and 74 mbsf.

Hole 858D

Hole 856D is composed mostly of hemipelagic clay with laminae and thin beds of turbiditic silt (see "Lithostratigraphy and Sedimentology" section, this chapter). Carbonate concretions first appear near the seafloor and continue to 30 mbsf. The hemipelagic sediment containing carbonate concretions is also calcareous and many of the turbiditic silt beds are cemented by calcite. The dominant carbonate mineral between Sections 139-858D-2H-3, 3 cm, and -2H-4, 84 cm, is probably dolomite.

Fine-grained euhedral pyrite is disseminated throughout the hemipelagic clay and partly fills the interstices of turbiditic silt layers. Concretions and burrows consisting of fine-grained pyrite are common between 10 and 30 mbsf. Sphalerite fills some burrows in Section 139-858D-6X-1 and a sphalerite-zeolite vein occurs in intervals 139-858D-6X-1, 61–64 cm, and 139-858D-6X-CC, 0–5 cm. The 1- to 3-mm-wide zeolite veins consist of equant zeolite growing in open space with euhedral sphalerite and minor chalcopyrite.

Anhydrite concretions consisting of radiating crystals first appear in Section 139-858D-4H-3 and continue to the bottom of Section

Table 17. X-ray diffraction mineralogy for bulk samples from Hole 858A.

Core, section, interval (cm)	Quartz	Feldspar	Hornblende	Chlorite	Mica	Calcite	Anhydrite
139-858A-							
1H-1, 81–83	***	*	*	*	*	*	
2H-1, 34–36	***	*	*	*	*	*	
3H-3, 77–81	***	***	*	***	***	*	
3H-3, 81–85	******	***	*	***	***	*	
4H-1, 90–94	***	*		*	*	*	
4H-2, 79–83	******	*		***	***	*	
5H-3, 100–105	******	*		***	*	***	
6H-2, 94–96	******	***		***	*	*	
7H-4, 93–97	******	***		*	*	***	
8H-2, 39–41	******	***		*	*	******	
9X-4, 47–51	******	*		*	*	*	
11X-1, 2–7	******	***		*	*	***	
12X-1, 18–20	******	***		***	*	***	
15X-1, 60–62	******	******		***	*	***	
15X-1, 77–79	******	***		***	*		
18X-3, 16–20	******	******		******	*		
19X-1, 15–19	******	******		******	*		
20X-1, 58–61	******	******		***	*		***
21X-1, 13–17	******	******		***	*		******
21X-3, 48–51	******	***		***	*		******
23X-1, 93–95	***	******		***	*		
24X-1, 15–17	******	******		******	******		
25X-1, 44–45	***	******		******	*		
27X-1, 12–14	******	******		******	*		
28X-CC, 27–28	***	******		******	*		
29X-1, 20–23	******	********		******	*		
30X-1, 54–57	***	******		******	*		
30X-CC, 15–18	***	******		******	*		
31X-1, 18–20	***	******		******	*		
31X-1, 24–26	***	******		***	*		
32X-CC	***	******		******	*		
34X-CC	***	******		******	*		

Notes: Relative mineral abundances were determined by peak heights and are indicated as follows: * = trace; *** = minor; ****** = major; ******** = dominant. Because peak heights are determined by mineral morphology in addition to mineral abundance, this table cannot be used to quantitatively determine the relative abundances of different minerals. See "Sediment Geochemistry and Alteration" section, "Explanatory Notes" chapter (this volume), for a description of X-ray diffraction methods.

139-858D-4H-4. Associated with the anhydrite concretions are banded, coarsely crystalline anhydrite veins that are commonly dismembered.

Hole 858F

Hole 858F was rotary drilled within meters of Hole 858D and penetrated 249 m of hemipelagic and turbiditic sediment before intersecting basalt. Because the recovery was very poor (2.74%), and because it is unlikely that the sediment recovered is representative of the entire core, the type and depth distribution of alteration assemblages probably give a biased view of what actually exists at depth. From the FMS logs (see "Downhole Logging" section, this chapter), it is clear that Hole 858F intersected a very heterogeneous zone consisting of highly fractured, brecciated, and veined sediment with irregular areas that probably represent hydrothermal mineralization. The recovered core confirms that the sediment is indurated and hydrothermally altered.

Cores between 30 and 60 mbsf consist of gray siltstone with white spots formed by hydrothermal alteration. Between 60 and about 160 mbsf, siltstone, sandstone, and claystone are cut by fractures and small faults that are partly filled by zeolite and quartz veins with subordinate epidote, pyrite, and sphalerite. Siltstone and claystone also contain vugs that are lined with zeolite and quartz crystals. Coarse-grained sandstone displays quartz overgrowths and is cemented by zeolite and fine-grained euhedral epidote. Euhedral quartz crystals typically grow from the margins to the center of fractures and commonly have penecoidal terminations. In Core 139-858F-10R, fractures are partly filled with zeolite crystals up to 2 mm across, doubly terminated quartz crystals, and sphalerite up to 3 mm across. Between 110 to 170 mbsf, the minerals filling fractures and vugs are dominantly quartz and anhydrite with minor pyrite and chalcopyrite. In Core 139-858F-11R, an anhydrite vein with minor pyrite and chalcopyrite cuts sandstone that has quartz and zeolite growing in the matrix. Anhydrite forms concretions with coarse-grained (up to 1 mm) euhedral pyrite in Core 139-858F-13R. Anhydrite also lines veins filled with zeolite in Core 139-858F-15R.

Between 170 and about 200 mbsf, star-shaped anhydrite concretions up to a few centimeters across occur in spotted claystone that is highly altered to clay minerals. Vugs lined with anhydrite crystals are also common at these depths. Euhedral pyrite is disseminated throughout claystone within the interstices of coarser grained turbidites. From about 230 mbsf to the basalt contact, sandstone and claystone are cut by fine veinlets of quartz and zeolite. The claystone displays a spotted texture and the sandstone is greener than normal due to hydrothermal alteration. Detrital quartz in sandstone has a granular texture presumably due to quartz recrystallization or the overgrowth of clastic minerals by quartz.

Mineralogy

Thin sections of sediment were difficult to make with the facilities aboard ship and were commonly very thick. This, combined with the fine-grained matrix of hemipelagic sediment, made precise identification of minerals difficult using conventional optical microscopy. Despite these difficulties, it was possible to identify the type and form of coarser grained authigenic minerals that infill and replace sediment in some of the more highly altered cores.

In Section 139-858A-17X-1, 13–16 cm, clear euhedral anhydrite displaying a distinctive cleavage and high relief forms a 0.2-mm-wide vein cutting hemipelagic sediment. The sediment is partly infilled and cemented by an olive green clay mineral, probably smectite. Tabular anhydrite crystals, 0.5 to 1 mm long, also form authigenically in hemipelagic sediment that is altered to a green smectite (Fig. 56; Section 139-858A-17X-1, 15–16 cm). Detrital quartz, feldspar, and magnetite grains in these sections have ragged margins, presumably the result of postsedimentary partial dissolution, and magnetite is partly replaced by pyrite.

In thin section from Sample 139-858D-6X-1, 1–3 cm, sediment is variably infilled and replaced by euhedral analcime(?) crystals that are overgrown by a green clay mineral. In Hole 858F, zeolite, including analcime and wairakite, occur in veins cutting moderately indurated hemipelagic and turbiditic sediment. The analcime forms clear, euhedral grains up 1 mm in length that display a distinctive cubic cleavage. Prismatic quartz growing outward from the margins is intergrown with analcime in fractures and vugs (Fig. 57). Analcime and quartz also form interstitially within siltstone and sandstone. Detrital quartz grains appear recrystallized and overgrown by quartz. Yellowish green euhedral epidote crystals with a pseudohexagonal outline and a high birefringence form authigenically in Cores 139-858F-9R and -10R (thin-section samples 139-858F-9R-CC, 12–14 cm, and -10R-CC, 1–2 cm). The epidote is intergrown with quartz crystals, some of which are doubly terminated and must therefore have nucleated in open space.

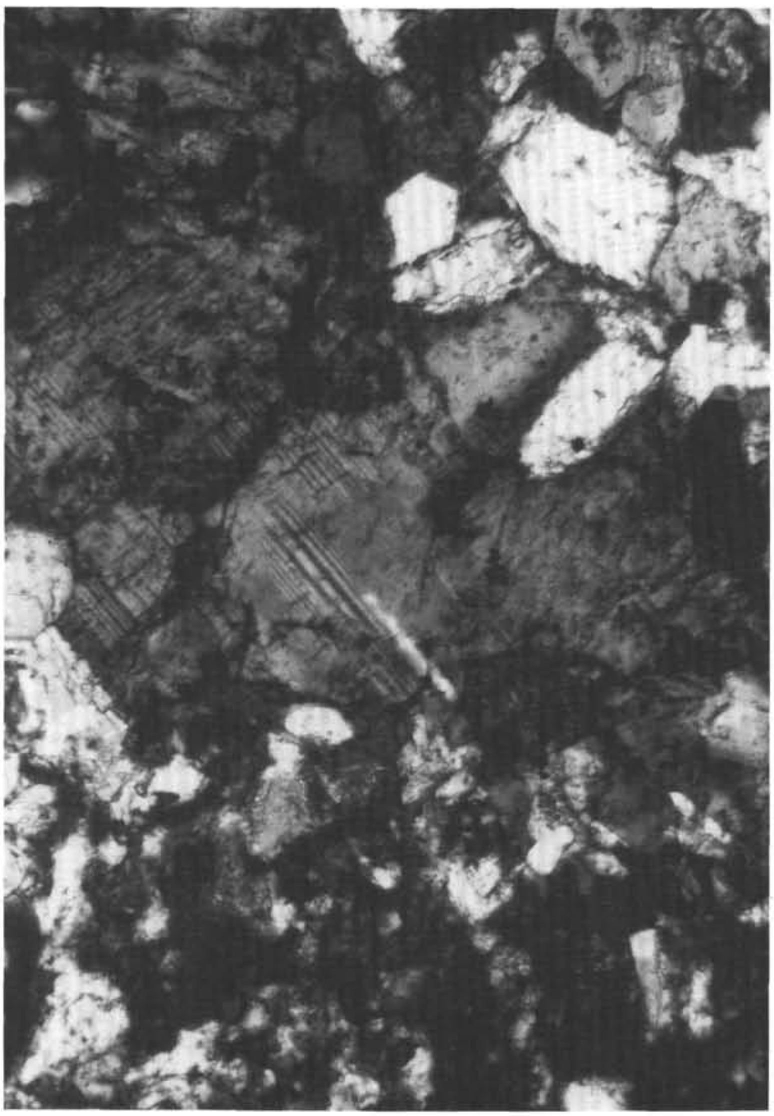

Figure 57. Photomicrograph showing euhedral analcime with a well-developed twinning intergrown with prismatic quartz crystals in fractures cutting hydrothermal altered sediment, Hole 858F (thin-section Sample 139-858F-18R-1, 12–14 cm) (crossed polars, 10× objective).

The X-ray diffraction mineralogy is presented for Holes 858A, 858B, 858C, 858D and 858F in Tables 18 through 21, respectively. X-ray diffraction results for hemipelagic sediment from Hole 858A (Table 17) show that hornblende disappears below Section 139-858A-4H-1, whereas feldspar and chlorite peak intensities increase with depth. Figures 58 and 59 show bulk XRD patterns for Samples 139-858A-1H-1, 81–83 cm, and 139-858A-28X-CC, 26–28 cm, respectively. Feldspar and chlorite peak intensities are higher in Sample 139-858A-28X-CC than in unaltered sediment (Sample 139-858A-1H-1, 81–83 cm).

Comparison of XRD patterns for the clay fractions from Samples 139-858A-9X-2, 52–54 cm, and 139-858A-31X-1, 24–26 cm (Figs. 60 and 61), show that chlorite and mica peaks for Sample 139-858A-31X-1, 24–26 cm, are sharper and higher than for Sample 139-858A-9X-2, 52–54 cm. This indicates that the crystallinity of clay minerals increases with depth. Furthermore, chlorite (002)/(001) and (003)/(001) basal peak intensity ratios for Sample 139-858A-31X-1, 24–26 cm, are higher than for Sample 139-858A-9X-2, 52–54 cm. These chlorite peak intensity ratios show that the Al and/or Fe content of chlorite increases with depth.

In Holes 858A, calcite occurs to the depth of Core 139-858A-15X, below which it is not detectable by XRD. The disappearance of calcite on the diffractogram is followed by the appearance of anhydrite as a major phase in Cores 139-858A-20X and -21X. Quartz contents reach a maximum between Cores 139-858A-4H and -21X, whereas plagioclase and chlorite are major phases below Core 139-858A-12X (about 100 mbsf). Although the type of plagioclase cannot be readily determined from XRD patterns for bulk sediment, the petrography and bulk chemistry (see "Geochemistry" subsection below) indicate that albite is the dominant feldspar.

The mineralogy in Hole 858B (Table 18) consists of Mg-rich smectite in green hydrothermal sediment in Sections 139-858B-1H-1, -1H-2, and -2H-3, and a mixed-layer chlorite/smectite below Section 139-858B-2H-3. Quartz becomes a major phase near the bottom of Hole 858B, whereas chlorite appears as minor phase. The disappearance of mica below about 15 mbsf is consistent with the systematic decrease of K_2O with depth (see "Geochemistry" subsection below).

XRD patterns for Samples 139-858B-2H-3, 94–96 cm (Fig. 62), and -5H-1, 122–125 cm (Fig. 63), show that the sediment is highly altered to clay minerals. These samples are characterized by almost pure smectite (Sample 139-858B-2H-3, 94–96 cm) and a chlorite/saponite mixed-layer mineral (Sample 139-858B-5H-1, 122–125 cm). The (060) peak for these clay minerals occurs at about 1.542 Å, indicating that their octahedral sites are occupied mainly by Mg and/or ferrous Fe. The high Mg content of these clay minerals is confirmed by X-ray fluorescence analytical data on a bulk sediment sample from Section 139-858B-5H-1 that contains more than 30% MgO.

The swelling-layer component in the chlorite/saponite mixed-layer minerals also changes with depth. Figures 64 and 65 show XRD patterns of clay fractions. The XRD pattern for untreated Sample 139-858B-3H-CC (Fig. 64) is similar to Mg-chlorite with almost the same high intensities of (001) and (002) basal reflections. The ethylene glycol–treated specimen shows, however, broad basal reflection peaks around (001), (002), and (003) (Fig. 64), indicating the existence of a saponite swelling layer. Sample 139-858B-5H-CC has a typical XRD pattern for regular chlorite/saponite mixed-layer minerals with a 30-Å reflection.

In Hole 858C, calcite appears discontinuously to a depth of 30 mbsf and is a major phase between about 8 and 30 mbsf (Table 19). Between Section 139-858B-3H-1 and the bottom of the hole, quartz becomes a major phase and the abundance of both plagioclase and chlorite increase downhole. Mica disappears with depth in Section 139-858C-6H-6, and gypsum (probably after anhydrite) is present in trace amounts between Sections 139-858C-7H-1 and -10X-CC.

The downhole XRD mineralogy for Hole 858D shows the disappearance of hornblende and calcite at about 10 mbsf, the appearance

Table 18. X-ray diffraction mineralogy for bulk samples from Hole 858B.

Core, section, interval (cm)	Quartz	Feldspar	Chlorite	Mica	Mixed layered chlorite/smectite	Calcite	Dolomite	Smectite
139-858B-								
1H-1, 48–52								********
1H-2, 3–7								********
1H-2, 42–47								********
1H-3, 23–27	***	*	*	*		*		
1H-4, 19–23	***	*	*	*		*		
1H-5, 21–25	***	*	*	*				
2H-1, 9–11	***	*	*	*				
2H-1, 78–80	***	*	*	*				
2H-3, 13–15				*	******			
2H-3, 35–37							********	
2H-3, 94–96								********
2H-4, 57–59					******			
2H-5, 11–13	******	***	*	*				
2H-CC	***		***	*				
3H-1, 76–78	***				********			
3H-CC	***				********			
4H-CC					********			
5H-1, 122–125					********			
5H-3, 124–128	*				********			
5H-4, 23–26	***				********			
5H-4, 131–134					********			
5H-CC	******				******			
6H-CC	********		***					
9H-CC	********				***			

Note: See notes to Table 17.

Table 19. X-ray diffraction mineralogy for bulk samples from Hole 858C.

Core, section, interval (cm)	Quartz	Feldspar	Chlorite	Mica	Calcite	Dolomite	Anhydrite	Gypsum
139-858C-								
1H-1, 22–26	***	*	*	*	*			
1H-2, 42–46	***	*	*	*	*			
1H-3, 21–25	***	*	*	*	*			
2H-1, 42–44	***	*	*	*	*			
2H-3, 25–27	***	*	*	*		***		
2H-3, 98–100	***	*	*	*	******			
2H-4, 97–99	***	*	*	*	******			
2H-5, 71–73	***	*	*	*	*			
2H-6, 12–14	***	*	*	*	*			
3H-1, 123–125	******	*	*	*	******			
3H-3, 103–105	******	*	*	*	******			
3H-4, 42–44	******	***	*	*				
5H-2, 111–112	******	***	***	***				
5H-3, 15–17	******	***	***	***				
5H-4, 96–98	******	***	*	*	*			
5H-5, 90–92	******	*	*	*	******			
6H-1, 41–43	******	***	***	*				
6H-3, 104–106	******	***	***	*				
6H-6, 36–38	******	***	***					
7H-1, 10–11	******	***	*					
7H-2, 49–51	***	***	*					*
10X-CC, 20–25	******	******	***					*
10X-CC, 30–35	******	******	***					*
10X-CC, 37–39	******	******	*				*	*
12X-1, 80–82	******	******	***					
12X-3, 20–23	******	******	*					
12X-3, 87–90	******	******	***					
13X-1, 10–16	******	******	***					
14X-1, 34–36	******	******	******	*				

Notes: See notes to Table 17.

Table 20. X-ray diffraction mineralogy for bulk samples from Hole 858D.

Core, section, interval (cm)	Quartz	Feldspar	Hornblende	Chlorite	Mica	Calcite	Dolomite	Anhydrite	Analcime
139-858D-									
1H-1, 95–99	***	*	*	*	*	***			
1H-1, 109–112	***	*	*	*	*	***			
1H-2, 93–97	***	*	*	*	*	*			
1H-3, 98–102	***	*	*	*	*	*			
1H-4, 41–45	***	*	*	*	*	*			
1H-5, 129–133	***	*	*	*	*	*			
1H-6, 30–33	***	*		*	*	*			
1H-6, 72–76	***	*	*	*	*				
2H-1, 49–51	***	*		*	*	*	*		
2H-2, 106–108	***	*		*	*				
2H-2, 111–113	***	*		*	*				
2H-3, 106–108	***	*		*	*		***		
2H-3, 111–113	***	*		*	*				
2H-4, 62–65	***	*		*	*				
2H-4, 110–112	******	*		*	*				
2H-5, 41–43	***	*		*	*				
2H-5, 57–59	***	*		*	*				
2H-5, 90–92	***	*		*	*				
2H-6, 89–92	***	*		*	*				
2H-6, 129–131	******	*		***	***				
2H-7, 10–13	***	*		*	*				
2H-7, 23–25	***	*		*	*				
2H-CC, 37–40	***	*		*	*				
4H-2, 133–135	***	*		*	*				
4H-3, 132–135	******	*		***	*			******	
4H-4, 49–53	******			*	*			******	
4H-4, 59–63	******	*		*	*				
4H-4, 144–148	******			******	******				
4H-5, 128–131	******			*	*				
4H-6, 16–20	******			*	*				
6X-1, 45–49	******			*	*				***
6X-1, 57–60	******			*	*				***

Note: See notes to Table 17.

Table 21. X-ray diffraction mineralogy for bulk samples from Hole 858F.

Core, section, interval (cm)	Quartz	Feldspar	Chlorite	Mica	Analcime	Wairakite
139-858F-						
7R-CC, 2–4	******	***	***			
8R-CC, 4–5	***	***	******			
8R-CC, 7–9	******				******	********
9R-CC, 18–20	******				******	********
11R-1, 11–12	******		*		******	******
11R-1, 24–25	***	***	*			
11R-1, 34–36	******				******	***
18R-1, 23–24	******	******	***			
18R-1, 35–37	******	******	***			
21R-1, 26–28	***	******	******	*		
21R-1, 31–33	******	********	***			
23R-CC, 11–13	***	******	******	*		
23R-CC, 14–16	******	********	******			
24R-CC, 10–12	******	********	******			
25R-1, 32–33	***	******	***	*		
25R-1, 40–42	***	******	******	*		
25R-1, 74–76	******	********	***	*		

Note: See notes to Table 17.

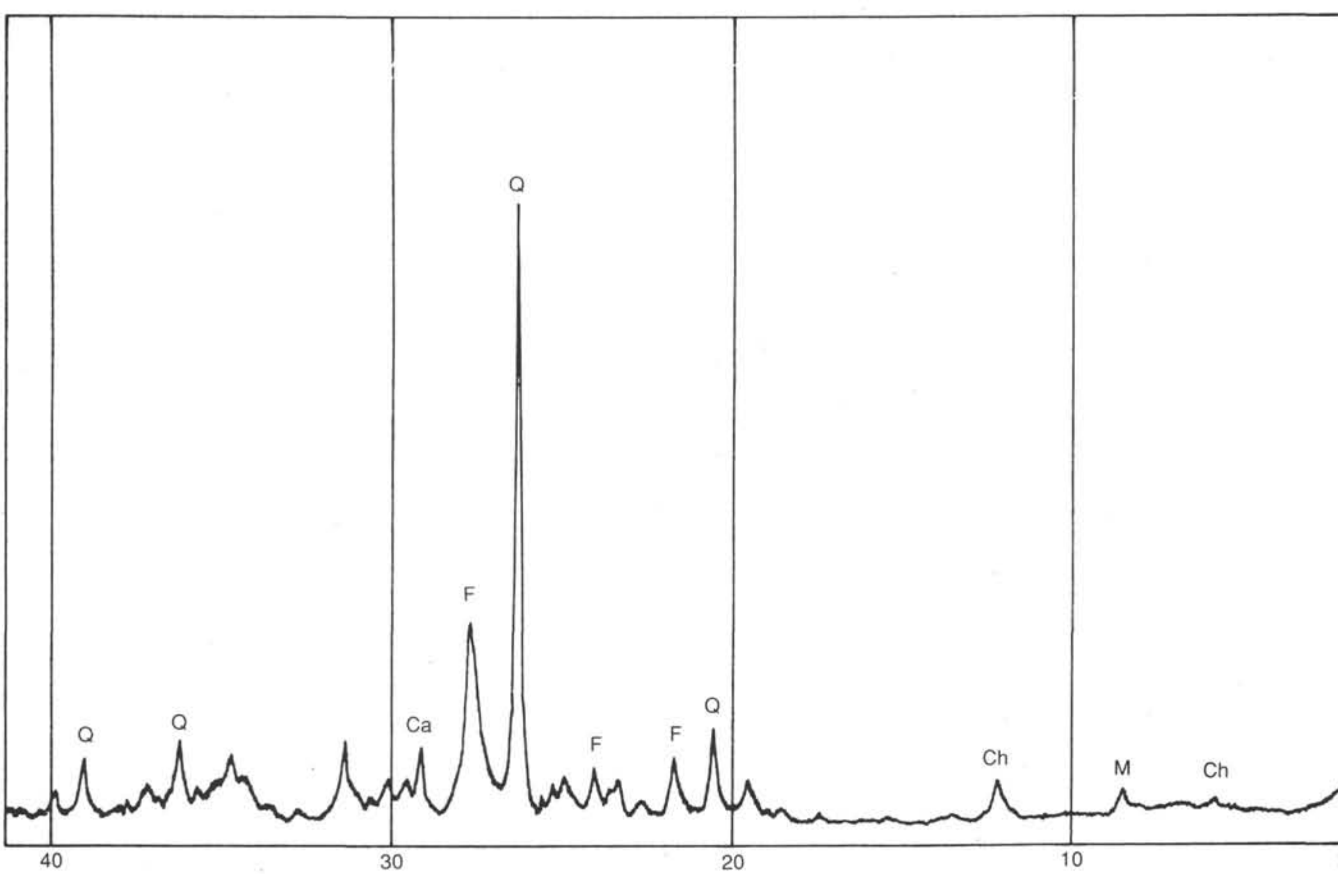

Figure 58. X-ray diffractogram of bulk sediment from Hole 858A (Sample 139-858A-1H-1, 81–83 cm) (Q = quartz, F = feldspar, Ch = chlorite, M = mica, Ca = calcite).

of dolomite or ankerite in Sections 139-858D-2H-1 and -2H-3, and the occurrence of anhydrite in Sections 139-858D-4H-3 and -4H-4 (Table 20). Quartz is commonly a major phase below Section 139-858D-4H-3, and analcime appears as a minor phase in Section 139-858D-6X-1. Between Sections 139-858F-8R-CC and -11R-1, both analcime and wairakite occur as major phases. The XRD pattern for Sample 139-858F-8R-CC, 7–9 cm (Fig. 66), shows that the zeolite minerals are a mixture of wairakite and analcime. The absence of feldspar in zeolite-bearing samples indicates that zeolite minerals replaced feldspars. The disappearance of zeolite minerals below Core 139-858F-11R is followed by marked increases in albite(?) and chlorite, which persist to the bottom of the hole.

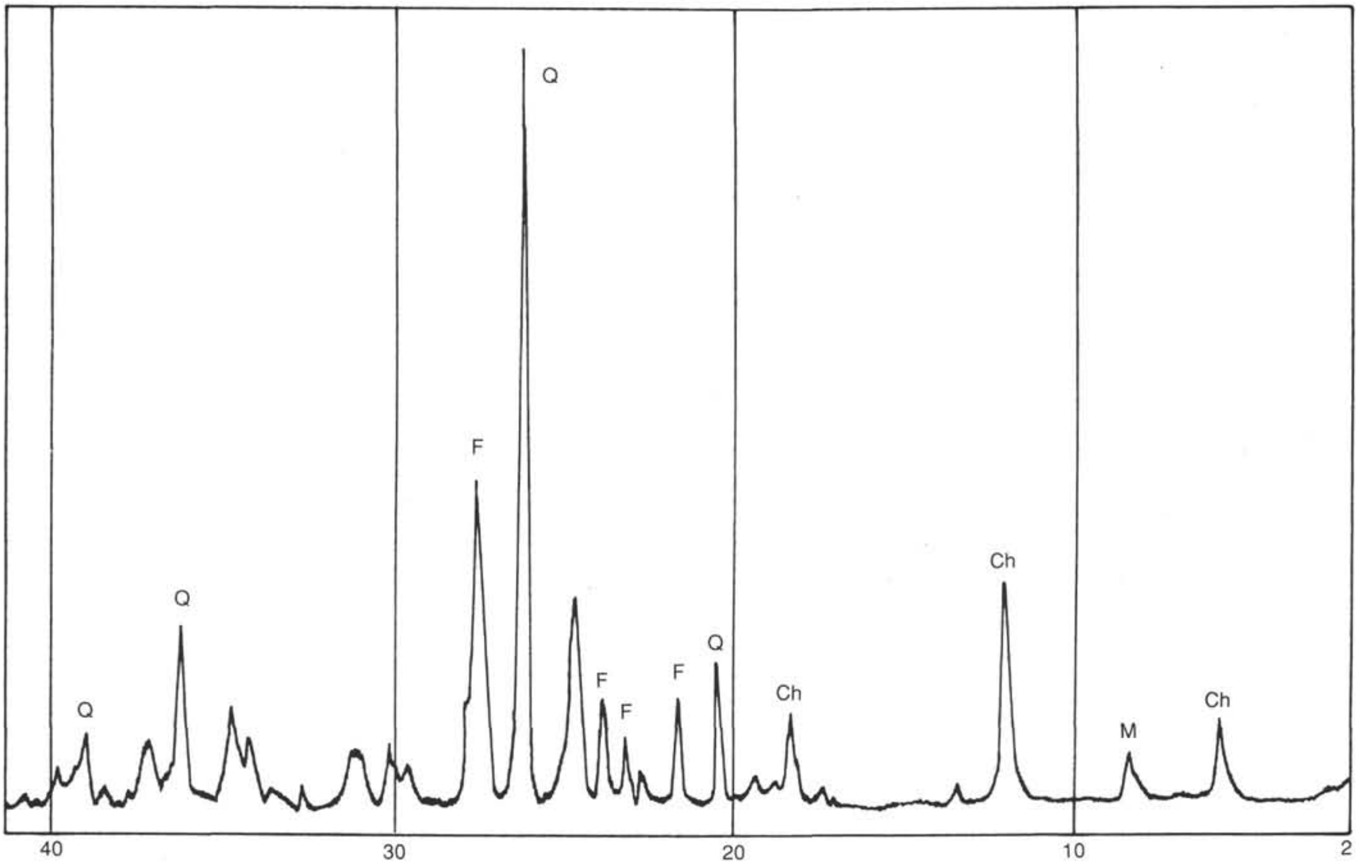

Figure 59. X-ray diffractogram of bulk sediment, Sample 139-858A-28X-CC, 26–28 cm (Q = quartz, F = feldspar, Ch = chlorite, M = mica).

Geochemistry

The major element and volatile content of sediment is presented in Table 22. The data have been normalized to 100% on the basis of loss on ignition (LOI) and the total weight percentage of all elements measured by X-ray fluorescence (XRF) on the fused disks. The trace element content is tabulated in Table 23. Depth profiles for the major elements and element oxides are presented for Holes 858A, 858B, 858C, and 858D plus 858F in Figures 67, 68, 69, and 70, respectively. Much of the downhole variability in elemental abundances is controlled by the detrital mineralogy of the sediment, similar to Sites 855 and 856. Turbiditic sediment is coarse-grained and consists predominantly of detrital quartz, feldspar (mostly plagioclase), mica (muscovite and biotite), chlorite, magnetite, and dense and resistant minerals such as zircon. Hemipelagic clay, by contrast, is composed of detrital and authigenic clay with variable but generally minor amounts of detrital quartz, feldspar, chlorite, and mica. Biogenic components consist of foraminifers, diatoms, radiolarians, and nannofossils, and they are most abundant in shallow hemipelagic sediment where the sedimentation rates are slower and the effects of hydrothermal alteration are less severe.

Because the sedimentary sequence in Middle Valley consists of interbedded hemipelagic and turbiditic sediments, profiles for the major oxides are highly variable with depth and reflect the relative proportions of the different detrital minerals. This can be seen in Hole 858A, where SiO_2 varies inversely with elements bound predominantly in clay minerals (e.g., Al_2O_3, TiO_2, Fe_2O_3, and MgO). Although Na_2O covaries with SiO_2 in unaltered sediment from Sites 855 and 856, it generally increases with depth in Hole 858A, reaching a value of 8% at about 142 mbsf, whereas K_2O decreases (Fig. 67). This marked increase in sodium is accompanied by a high MgO value at the same depth and corresponds to higher chlorite and feldspar abundances as measured by X-ray diffraction (Table 18). The correlation of high Na_2O with increased plagioclase peak heights on XRD traces suggest that authigenic albite has formed in the sediment. Inorganic carbon is high in the zone of carbonate concretions above 120 mbsf, but decreases to values of less than 0.2% below this depth. Because much of the calcium is bound in carbonate minerals, CaO generally covaries with inorganic carbon. Sulfur content is erratic, but generally enriched to a depth of 50 mbsf, decreases to values less than 0.4% between 50 and about 130 mbsf, and is generally elevated at depths greater than 130 mbsf, reaching values of 2% near the bottom of the Hole. The high S abundance between 130 and 270 mbsf corresponds to the zone of higher chlorite and feldspar as measured by X-ray diffraction.

In Hole 858B, SiO_2, TiO_2, Al_2O_3, Na_2O, K_2O, and P_2O_5 all generally decrease and covary with depth (Fig. 68). Contents of MgO and MnO increase with depth and reach values of 34% and 0.26%, respectively, at 25 mbsf. The zone with high magnesium has been shown by X-ray diffraction correlate with the occurrence of mixed-layer smectite/chlorite that infills and replaces quartz-and feldspar-altered siltstone and claystone. If we assume that titanium behaved conservatively during hydrothermal alteration, the small decrease in TiO_2 below 25 mbsf suggests that sediment detritus has been diluted by addition of hydrothermal clay. CaO and TOC show a steady decrease with depth, whereas inorganic carbon exceeds values of 0.8% at 5 mbsf and decreases with depth between 5 and 13 mbsf. Total S generally decreases downhole, except for a zone of massive sulfide at 10.8 mbsf, where values are greater than 4%.

At about 2 mbsf, the content of MgO exceeds 20% in a hydrothermal sediment layer characterized by abundant smectite with dark specks and patches of sulfide. A skeletal network of voids within the

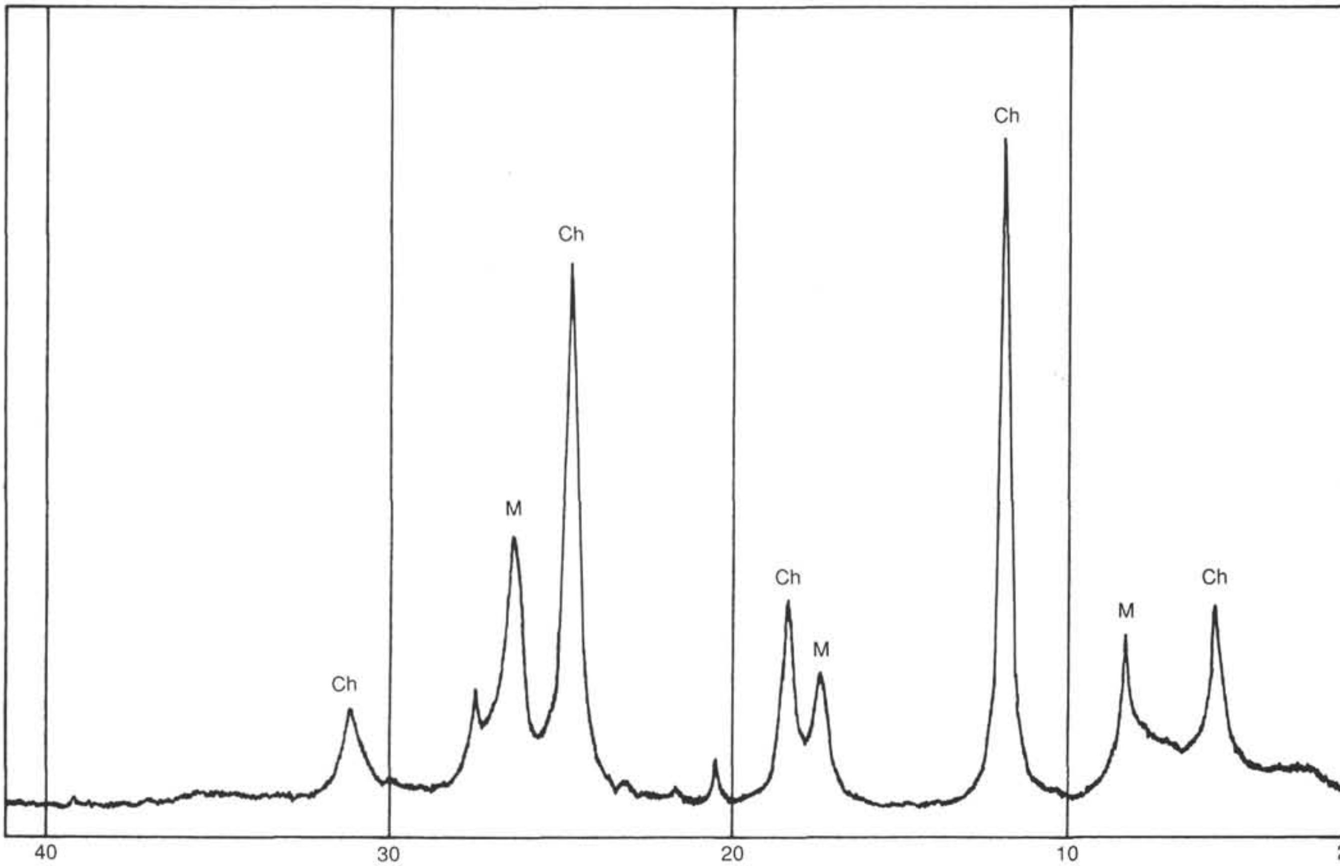

Figure 60. X-ray diffractogram of bulk sediment, Sample 139-858A-9X-2, 52–54 cm (Ch = chlorite; M = mica).

clay has a texture similar to skeletal intergrowths of anhydrite in nearby chimneys and suggests that this sediment represents resedimented chimney material from which anhydrite has been dissolved. A marked drop in TiO_2 and other element oxides to values less than 25% of their content in the surrounding hemipelagic and turbiditic sediment indicates a high rate of hydrothermal sedimentation.

In Hole 858C, there is a general inverse correlation with depth between SiO_2 and TiO_2. CaO decreases downhole after reaching a maximum concentration of 1.5% at about 7 mbsf (Fig. 69). The CaO depth profile is different from that for inorganic C, and is characterized by a broad zone of enrichment in the top 20 mbsf, and an isolated spike at 55 mbsf. In the former case, the high CaO at 16 mbsf is associated with Fe_2O_3 values greater than 13%, and suggests that most of the calcium is tied up in a ferroan carbonate, possibly ankerite. Because inorganic C was determined by leaching the sample with 16% HCl, it represents a partial extraction of soluble carbonates only (see "Organic Geochemistry" section, "Explanatory Notes" chapter, this volume). Minerals such as ankerite, dolomite, and siderite will not be totally dissolved by this method.

Profiles for MgO and Na_2O generally increase and covary with depth, whereas K_2O displays an inverse trend. The correlation of sodium with magnesium suggests formation of hydrothermal albite and chlorite at depths greater than about 20 mbsf (Table 19), coupled with hydrothermal alteration of potassium-bearing phases, particularly illitic clay. The depth profile for MgO behaves inversely to Mg in pore water (see "Fluid Geochemistry" section, this chapter).

Total S increases sharply at about 11 mbsf and remains above 1% to 60 mbsf, below which it decreases to values around 0.5% to a depth of 85 mbsf. Most of this S occurs as coarse-grained euhedral pyrite that is disseminated throughout brecciated sediment below a massive carbonate layer at 15 mbsf.

Because Holes 858D and 858F are separated by only a few meters, they will be treated as one hole for the purposes of discussing downhole geochemical patterns. In Holes 858D and 858F, SiO_2 values show a steady increase to values greater than 75% at a depth of 94 mbsf, before steadily decreasing to 55% at 250 mbsf (Fig. 70). MgO also generally increases with depth, to values exceeding 6% at 18.5 mbsf, then decreases to less than 0.5% at 94 mbsf, and increases to over 9% at 250 mbsf. TiO_2, Al_2O_3, and CaO all decrease with depth in Hole 858D, but increase in Hole 858F. Sulfur, for which a larger number of samples have been analyzed, increases systematically downhole, reaching a maximum value of 3.8% at about 18 mbsf, before decreasing downhole. In Hole 858F, S values are generally less than 0.1% except at 250 mbsf, where one sample contains more than 5% S. Inorganic carbon values decrease downhole except for an interval between 9 and 13 mbsf, where values exceed 1%. Below about 16 mbsf, inorganic carbon contents rarely exceed 0.2% and are commonly less than 0.1% in Hole 858F.

Discussion

Four distinct hydrothermal alteration zones, from the core to the margins of the hydrothermal upflow zone, are recognized at Site 858 (Fig. 71).

Zone 1 is characterized by a chlorite-albite-quartz-pyrite assemblage and occurs in the higher temperature core of the upflow zone. Quartz-albite veins with variable pyrite contents cut indurated, chloritized, and fractured hemipelagic and turbiditic sediment. The pyrite is typically euhedral and occurs both in veins and disseminated within indurated sediment.

Zone 2 consists of a quartz-zeolite-sulfide assemblage and is recognized only in Hole 858F, where it occurs vertically above Zone 1.

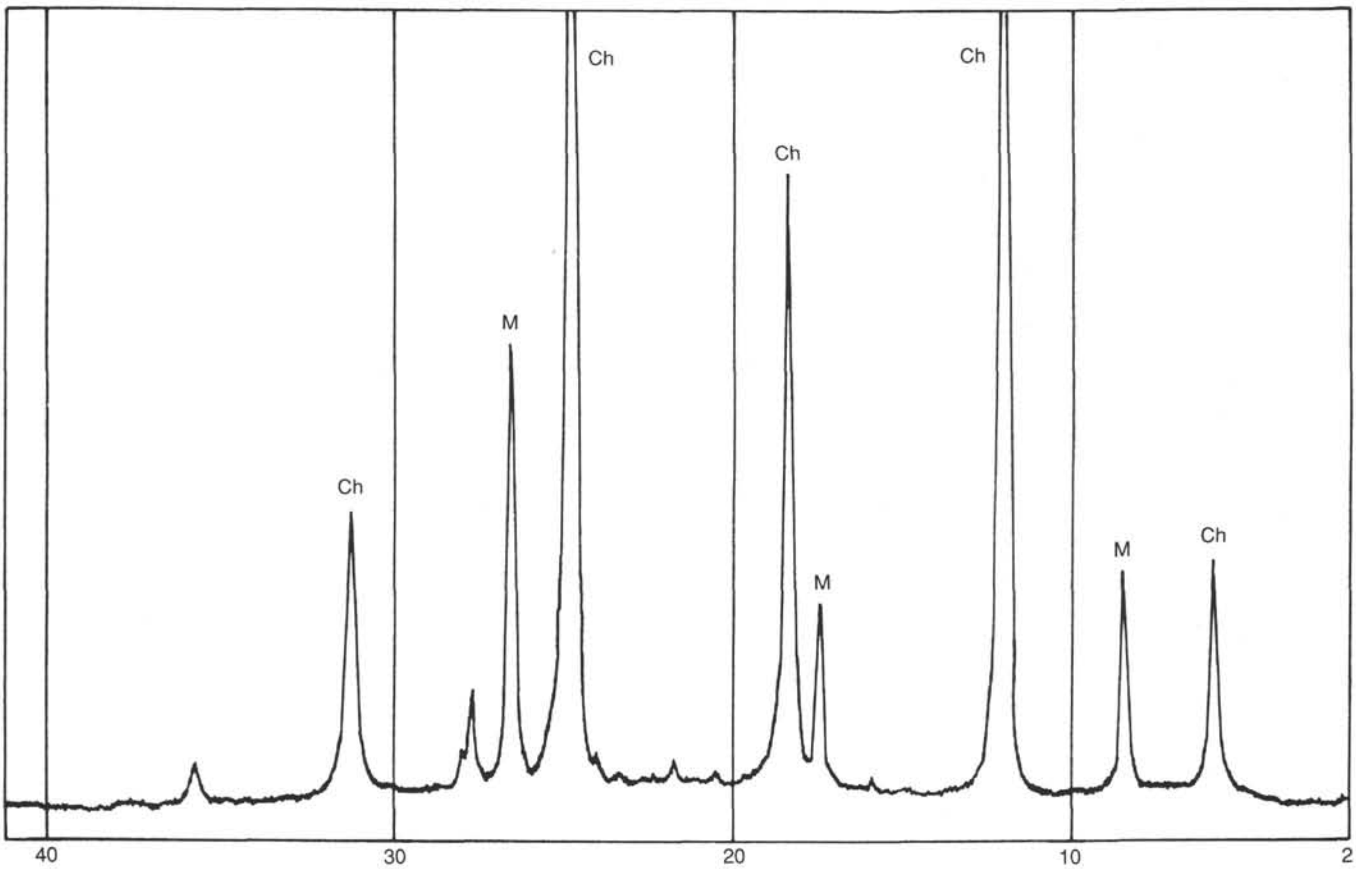

Figure 61. X-ray diffractogram of clay fraction, Sample 139-858A-31X-1, 24–26 cm (Ch = chlorite, M = mica).

Quartz and zeolite minerals infill fractures cutting indurated sediment, line vugs, and occur within the sediment matrix. The zeolite minerals identified by XRD are wairakite and analcime. Sulfide minerals consist of euhedral pyrite with minor sphalerite.

Zone 3 is characterized by an anhydrite-pyrite assemblage and forms above Zone 1 in Holes 858A and 858C, and above Zone 2 in Hole 858F. Anhydrite forms veins and occurs as euhedral crystals or subrounded concretions growing in weakly to moderately indurated claystone. The sediment in Zone 3 is not brecciated except in Hole 858C. Veins are more common near the base of this zone, whereas anhydrite concretions are generally restricted to the top of the zone. Euhedral pyrite occurs finely disseminated throughout this zone.

Zone 4 is represented by a carbonate-pyrite assemblage that forms at different depth ranges depending on the distance from hydrothermal fluid discharge conduits. In Hole 858A, Zone 4 spans about 70 m, whereas in Holes 858C and 858D, it spans approximately 15 m. The carbonate consists mostly of calcite concretions, veins, and cement, with variable amounts of fine-grained euhedral pyrite. In Hole 858C, the base of this zone is marked by a massive carbonate interval that formed by the infilling and complete cementation of brecciated sediment.

The zonal distribution of hydrothermal minerals is interpreted to reflect a gradient from high-temperature conditions near vent sites to lower temperature conditions at the margins of the vent field. This temperature gradient is consistent with heat flow values in this area that show a systematic decrease from typically 5–10 W/m^2 within the vent field to less than 2 W/m^2 in Hole 858A (Davis and Villinger, this volume; "Heat Flow" section, this chapter). Furthermore, the zonal distribution of alteration minerals is similar to the pattern of hydrothermal alteration observed in shallow (<12 m) piston cores (W. Goodfellow, pers. comm., 1991). Alteration minerals in these cores are zoned from chlorite-pyrite near vent sites to anhydrite-barite followed by carbonate concretions further out. Mg-rich authigenic clay associated with the sulfate and carbonate minerals.

Major changes in the bulk chemical composition of the sediment show that the hydrothermal minerals in the alteration zones were precipitated from fluids that migrated through the sedimentary sequence. Major chemical changes include a buildup of Mg and S and a corresponding decrease in Ca in Zone 1, an increase of Mg and S in Zone 2, a buildup of Ca and S in Zone 3, and an enrichment of Ca, CO_2 and S in Zone 4. None of these changes in the bulk composition can be accounted for by *in-situ* reactions of sediment with conductively heated pore fluids. The magnitude of chemical change indicates high water/rock ratios and therefore fluid convection. Because the hydrothermal fluids in Middle Valley are depleted in Mg and SO_4^{2-} (J. Lydon, pers. comm., 1991), the magnesium and sulfate in chlorite and anhydrite must be derived from pore water or downward-diffusing seawater. The origin of Ca is more difficult to determine since it has high concentrations in both hydrothermal fluid and seawater. The most likely source of most of the reduced sulfur bound in pyrite and sphalerite is hydrothermal H_2S. Although seawater contains sufficient sulfur in the form of sulfate (about 28 mmol/kg), it is unlikely to be reduced inorganically below 150°C (Kiyosu, 1980), and the S/C mole ratios are too high (>0.12) to account for all the sulfur by bacterial sulfate reduction. The S/C atomic ratio of typical of modern sediment (0.12) is controlled by the stoichiometry of reduction of sulfate by oxidation of organic carbon by sulfate-reducing bacteria in sediment under open conditions (Goldhaber and Kaplan, 1974). Open conditions assumes an unlimited supply of sulfate diffusing in from the overlying water column, and sufficient Fe to precipitate all the sulfide generated by bacterial sulfate reduction.

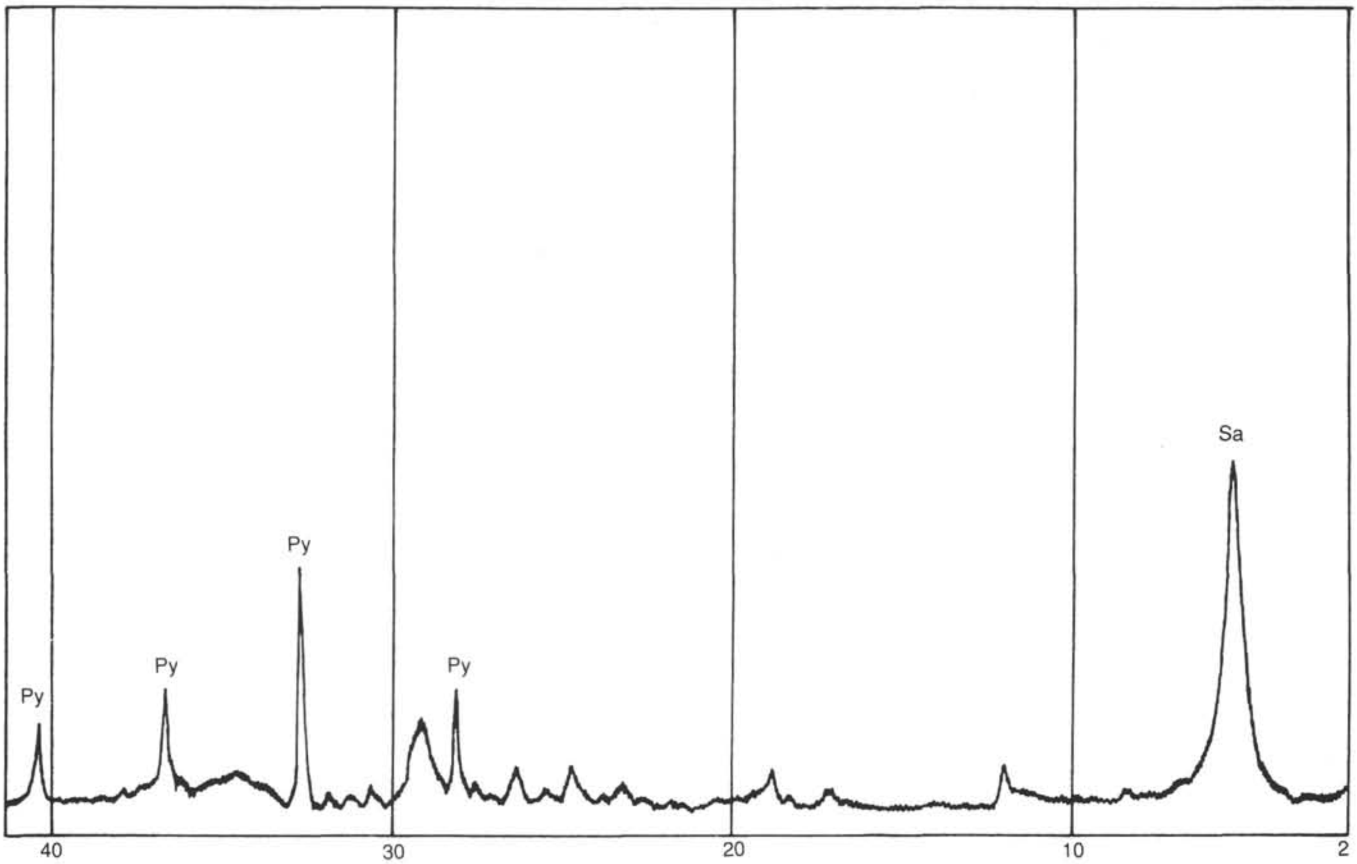

Figure 62. X-ray diffractogram of bulk sediment, Sample 139-858A-2H-3, 94–96 cm (Sa = saponite, Py = pyrite).

The most likely model to account for mineralogical and chemical changes to the sediment is outward migration of hydrothermal fluid which mixes with pore water and downward-diffusing seawater. The zone of mixing between pore fluid and hydrothermal fluid probably moves outward from the center of fluid discharge with time as the sediment becomes hydrothermally indurated. According to this model, the sequence of alteration minerals is expected to prograde from lower to higher temperature assemblages. As the higher temperature front moves outward from the core of the fluid discharge conduit, minerals that are unstable are either dissolved (e.g., anhydrite, carbonate) or replaced by more stable phases (e.g., Mg-smectite and mixed-layer clay minerals by chlorite). Furthermore, elements carried upward and laterally by the hydrothermal plume are precipitated as concretions and within open space near the margins where the chemical gradients are large. The cementation of the sediment may generate an impervious cap that seals the hydrothermal system and influences the lateral migration of hydrothermal fluids.

Flow of hydrothermal fluid through the sediment in Zones 1 and 2 is consistent with the presence of fractured and brecciated sediment. Initial $^{87}Sr/^{86}Sr$ ratios in carbonate, barite, and anhydrite from these zones are considerably less than those for seawater or sediment and approach values for oceanic basalt (W. Goodfellow, pers. comm., 1991). Delta^{13}C values for carbonate concretions are –30 to –40 per mil and considerably lighter than values for seawater carbonate, indicating a contribution from sedimentary organic matter (W. Goodfellow, pers. comm., 1991). Widespread dispersion halos for elements that are enriched in hydrothermal fluids but depleted in seawater (e.g., As, Sb, Se, Hg, and Ba) occur in surface sediment and require a hydrothermal component to the sediment (W. Goodfellow, pers. comm., 1991).

The occurrence of a massive carbonate layer underlain by brecciated sediment in Hole 858C suggests that carbonate precipitation near the margins of a sub-seafloor zone of hydrothermal fluid flow may have generated an impervious cap that diverted fluid to flow laterally away from the initial discharge sites. An increase in the content of hydrocarbons below this cap (see "Organic Geochemistry" section, this chapter) is consistent with restricted vertical discharge of hydrothermal fluid to the seafloor. Pore-water profiles near the top of Hole 858D are also most readily explained by lateral flow of fluid from active vents near Hole 858B (see "Fluid Geochemistry" section, this chapter).

Hole 858B is near the summit of a mound from which hydrothermal fluid is venting. The MgO content of sediment at depths between 16 mbsf and the bottom of the hole (38.6 mbsf) typically exceeds 25 wt%. Mg was probably concentrated in the sediment by the local drawdown of seawater and the subsurface precipitation of Mg-rich mixed-layer clays around vent sites. Local seawater recharge into the vent complex is consisted with heat flow measurements taken by the *Alvin* submersible that show the active vents to be surrounded by a local zone of relatively low heat flow compared to measurements more remote from the mounds (J. Franklin, pers. comm., 1991). Sediment is being heated by hydrothermal fluids that have migrated outward from discharge conduits, but is being cooled in the immediate vicinity of the vents by local recharge of seawater.

The green hydrothermal smectite near the surface of the mound in Hole 858D probably represents hydrothermal sediment. Textures preserved as void space in Mg-smectite rich sediment are similar to those observed in anhydrite chimneys from this area, and indicate that this sediment formed by the collapse and resedimentation of anhydrite chimneys. The anhydrite chimneys also contain Mg-rich clay and

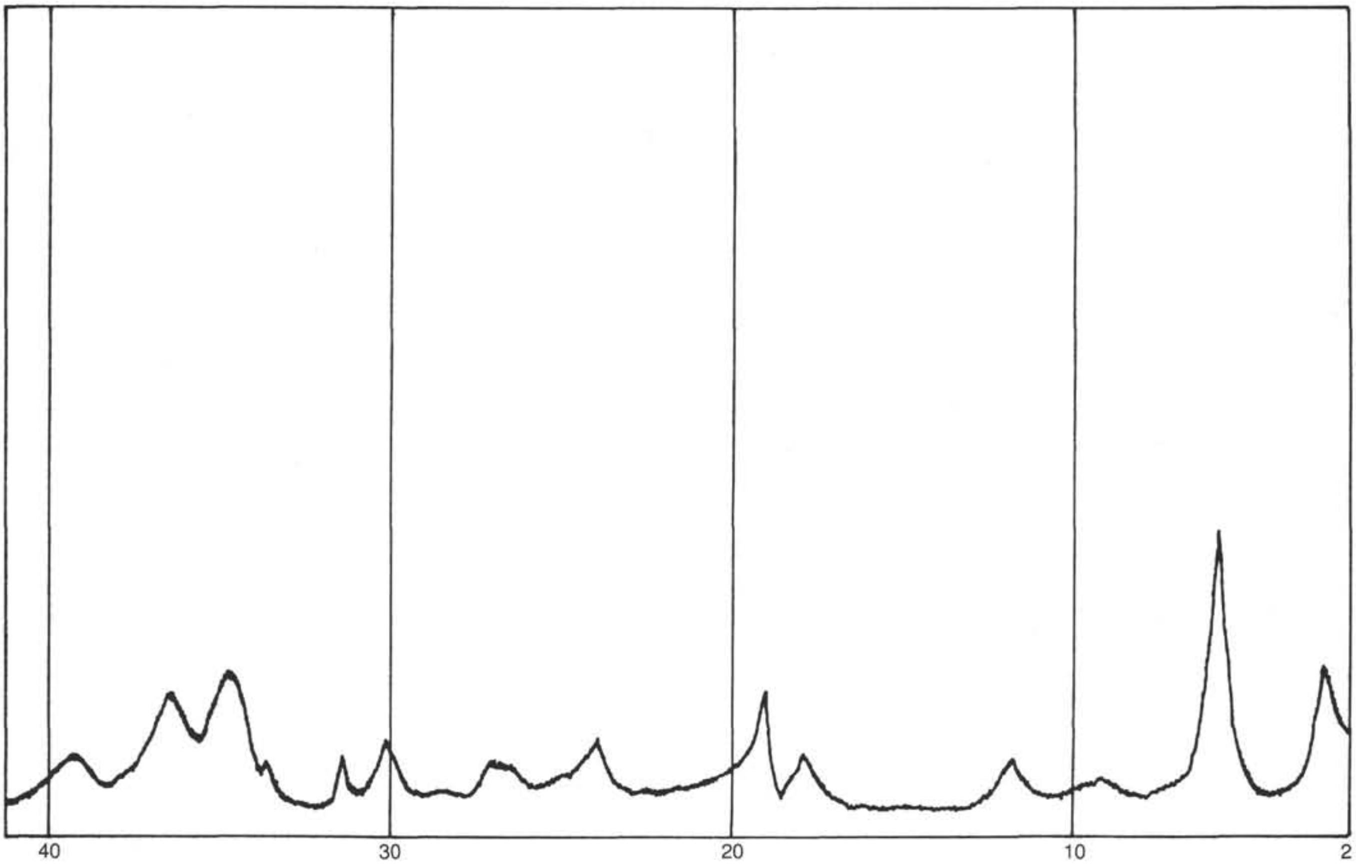

Figure 63. X-ray diffractogram of bulk sediment, Sample 139-858B-5H-1, 122–125 cm.

Cu-Fe-sulfide (W. Goodfellow, pers. comm., 1991). The Mg-clays and associated Cu-Fe-sulfides were probably concentrated in the surface sediment of the mounds by the preferential dissolution of anhydrite after resedimentation. These conclusions are consistent with the low content of detrital components (e.g., TiO_2, Al_2O_3) and with textural and mineralogical studies conducted previously on similar hydrothermal products collected from Site 858 (W. Goodfellow, pers. comm., 1991).

IGNEOUS PETROLOGY AND GEOCHEMISTRY

Igneous rocks were recovered in the lower 48 m of Hole 858F (248.9–296.9 mbsf) and throughout the entire cored length of Hole 858G (276.5–432.6 mbsf). The purpose of drilling at Site 858 was to penetrate into a zone of high heat flow and active hydrothermal discharge. The specific goal of the igneous petrology effort was to characterize the petrogenesis and amount of metamorphism of the igneous rocks within the upflow zone. The site is centered over what appeared to be, in the seismic data, a shallow hard reflector that might represent igneous basement. This was inferred to focus hydrothermal discharge in this area. Volcanic rocks were intersected at a relatively shallow depth at Site 858, in comparison with the position of the sills in Site 857, nearby. Taken together, drilling in Holes 858F and 858G provided 184 m of volcanic rocks, which form a paleotopographic (basement?) high associated with high heat flow values. Average recovery of igneous rock was only 5%.

Lithology and Units

Core recovery from Holes 858F and 858G is presented schematically in Figure 72. Lithologic unit designations are provided in Table 24. Poor recovery of igneous rocks provided only limited information upon which to base these divisions. All igneous rock recovered excluding the last core taken in Hole 858G (Section 139-858G-16R-1, 37–90 cm, is a very coarse-grained spherulitic diabase) is a variety of aphyric to sparsely phyric, fine-grained basalt. The average basalt from both holes is relatively homogenous in composition and there are few phyric units. Every core recovered fragments of basalt with chilled, altered margins and groundmass crystals with skeletal morphology. Most of these exhibited spectacular variolitic textures which gave the rocks a mottled appearance with dark grey aphanitic zones and light colored devitrified zones. In only a few instances could complete cooling units be confidently identified. In contrast to the sills drilled previously, the grain size did not coarsen between quench margins beyond a slightly holocrystalline basalt (except for the basal diabase in which drilling was terminated). The repetition of chilled margins, in addition, suggests numerous sequential eruptive units, possibly as a series of thin massive flows. Many of the basalt pieces are blocky, not pie-shaped, and only one piece of a pillow-shaped fragment was recovered. One to two quench intervals occur per core, suggesting cooling units no more than 5–10 m thick. Lithologic units in general encompass more than one cooling unit. Unit designations are based upon phenocryst populations or the inference of a single large cooling unit from the systematic association of chilled margins and coarse interiors. Broad characterization of the unit subdivisions is given here for each hole.

Hole 858F

Igneous rock was first intersected at a contact with sediments in Section 139-858F-25R-1, 90 cm. The rock near the contact is chilled, metamorphosed, and cut by large sulfide-bearing veins (Fig. 73). Of

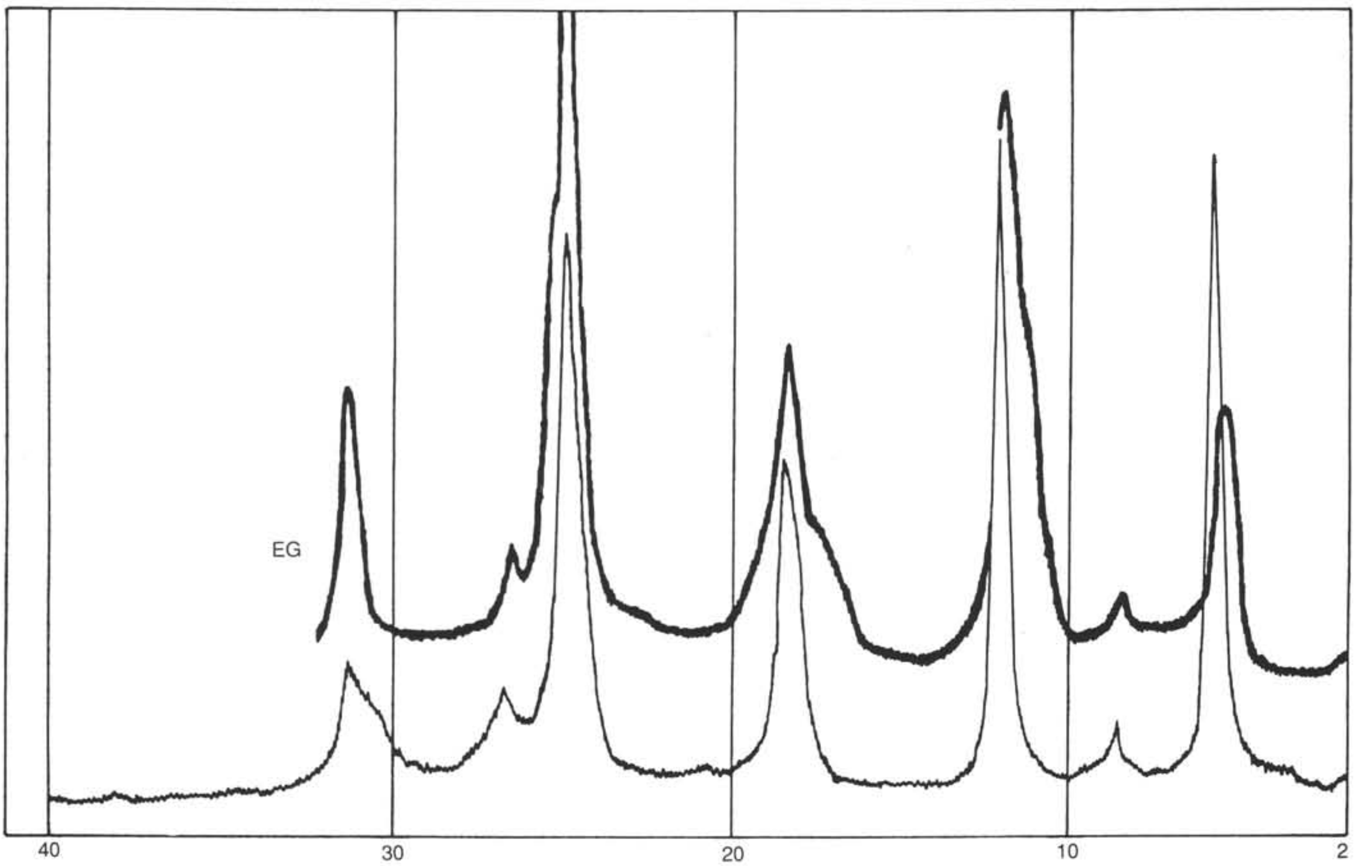

Figure 64. X-ray diffractogram of oriented preparation of clay fractions, Sample 139-858B-3H-CC. Trace labeled EG is from the sample after treatment with ethylene glycol.

the 48 m drilled into basement below this contact, the most abundant rock type is aphyric to sparsely plagioclase-phyric variolitic basalt. The groundmass for these variolitic rocks is typically aphanitic to microcrystalline in the devitrified zones. Plagioclase microlites are ubiquitous and cross the boundaries of the varioles. There are local vesicle-rich horizons, typically adjacent to fine-grained chills. Several of the chills are bleached to a pinkish white color due to hydrothermal alteration. The vesicles are frequently filled with the same secondary minerals as those which pseudomorphically replaced the phenocrysts, making the latter difficult to identify. Phenocrysts of plagioclase, pseudomorphed olivine, and chromian spinel rarely exceed 1%–2% in abundance. The morphology and association with Cr-rich spinel led us to infer olivine as the original mineral for the common ovoid pseudomorphs. The amount of apparent homogeneity led us to include all of Hole 858F into Unit 1, with four subunits based on inferred boundaries between cooling units (Table 24).

Subunit 1A includes the sediment contact zone and the interval of variolitic basalt that is crosscut by epidote-chlorite-quartz-pyrite veins (Fig. 73). The rocks are vesicular, including some elongate pipe vesicles; the vesicles are all filled with chlorite. Core 139-858-26R was designated Subunit 1B based on a chilled contact at the top, and a slight increase in grain size with depth. Subunit 1B also contains basalt that is on average less phyric than Subunit 1A.

Subunit 1C is bounded on the top by a well-developed contact with several pieces exhibiting chilled margins. The basalts in this interval are all fine-grained and variolitic with varying proportions of 1- to 3-mm sized phenocrysts. Plagioclase is the dominant phenocryst, however numerous ovoid chlorite pseudomorphs are suggestive of olivine appearing as a second phenocryst phase. A single piece of holocrystalline basalt with microlitic plagioclase and clinopyroxene may represent the center of a larger flow unit.

Subunit 1D is separated from Subunit 1C by the presence of a small pebble of metamorphosed sandstone. This small fragment could have been imported from farther up the hole. However, the rocks immediately beneath the sandstone are a fine-grained chilled margin suggesting that it is an artifact as a thin interflow sediment horizon. Several pieces within this horizon are reminiscent of pillowed shapes. Vesicles are present up to 5% and are filled with chlorite or epidote. Plagioclase is the only conspicuous phenocryst and it is only present up to 3%.

Hole 858G

Hole 858G was cored too late in the leg to obtain shipboard chemical or petrographic data, although petrographic data was subsequently obtained for this volume. The units and subunits are thus designated solely on hand sample descriptions. The top of Hole 858G and the bottom of Hole 858F cored the same 20-m interval, thus they are given the same subunit designations.

A chilled margin and vesicular variolitic basalt are taken as the boundary to Subunit 2A. This unit is either aphyric or sparsely phyric with less than 1% plagioclase. The subunit contains slightly coarser samples in Core 139-858G-5R, with fine-grained holocrystalline intervals separated by pieces with chilled textures. It is likely that this interval samples at least one distinct cooling unit per core. The boundary to Subunit 2B occurs in Core 139-858G-6R with the appearance of successive chilled margins separating lithologically indistinguishable pieces. Unit 3 similarly contains several pieces of distinct chilled margins, but includes intervals that have greater abundances of macroscopically conspicuous plagioclase phenocrysts. A distinct silicified chilled margin with celadonite on one surface is taken as the boundary to Unit 5, which includes multiple, presumably

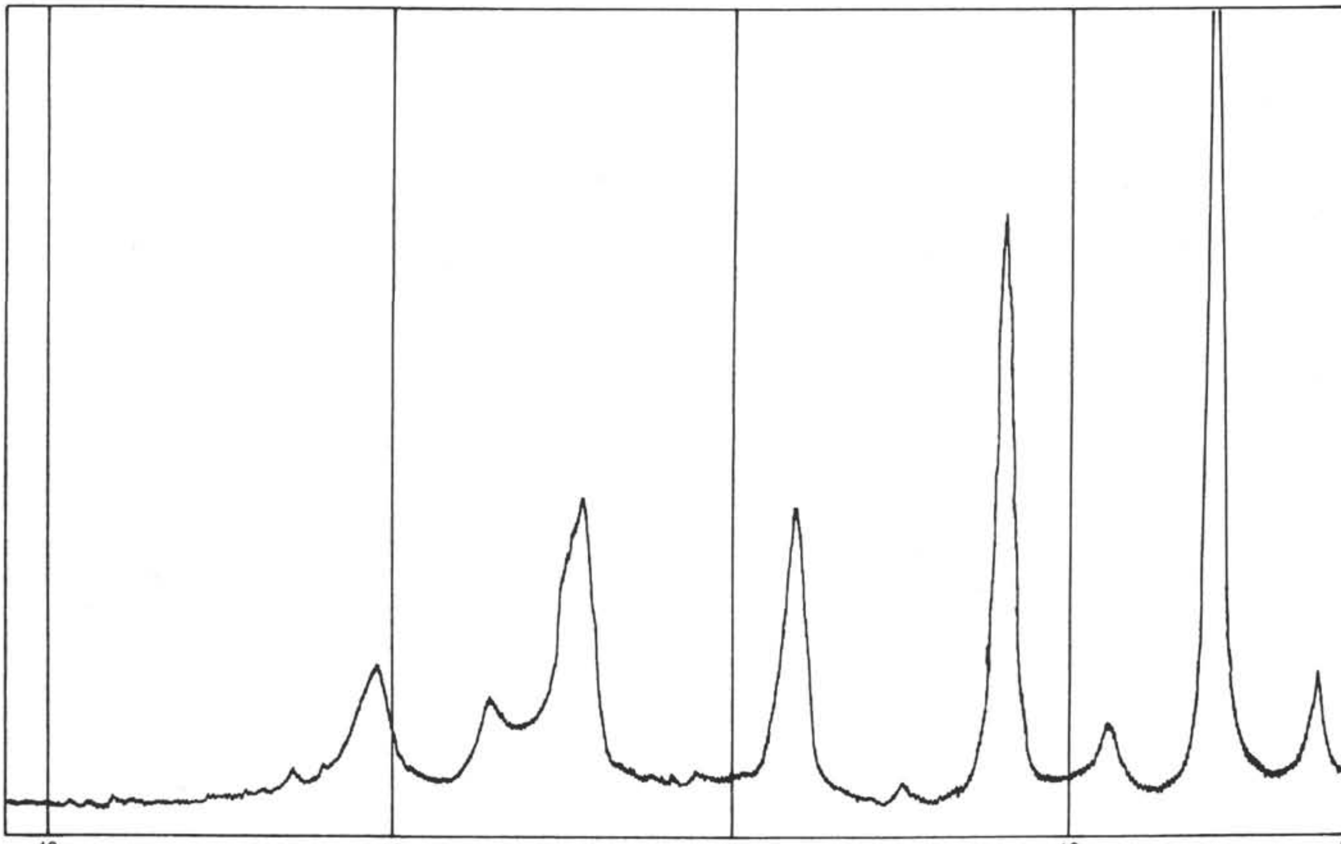

Figure 65. X-ray diffractogram of clay oriented preparation of fractions, Sample 139-858B-4H-CC.

thin cooling units. Plagioclase phenocrysts are present only in trace amounts but the groundmass contains abundant relatively large (0.5 mm) plagioclase microlites. Of interest is the presence of a 1-cm fragment of silicified gray mudstone mixed with basalt fragments in Section 139-858G-12R-1. Such enigmatic, dark, cherty fragments appeared twice in the lower part of the hole. Also in Core 139-858G-13R, one piece is interpreted as a highly leached pillow or pillow bud fragment. In this pillowed fragment, a 2-mm-long plagioclase phenocryst exhibits well-developed swallow-tail quench structure.

The boundary to Unit 6 is at the top of Core 139-858G-14R, where chips of silicified siltstone or chert were intermixed with basalt fragments with bleached chilled margin. This unit extends through the contact with the coarse-grained rock in Core 139-858G-16R, and includes some highly vesicular fragments as well as holocrystalline fragments. Some of the pieces have a distinctive blocky appearance as if from a massive unit rather than pillowed. Unit 7 includes the lower half of Core 139-858G-16R (Section 139-858G-16R-1, 37–90 cm). This is a very coarse-grained diabase to microgabbro (average grain size is >2.0 mm) with well-developed spherulitic morphology developed in pale brown clinopyroxene crystals. The plagioclase and mesostasis material are extensively replaced by chlorite.

Petrography

Hole 858G was drilled in the final 1.5 weeks of the cruise, which prevented any shipboard petrographic examinations of these rocks. The shipboard descriptions here are from eight samples from Hole 858F. These results are discussed here and summarized in Table 25. Petrographic data for 15 samples from Hole 858G, obtained soon after the end of the cruise, supplement the shipboard data. In general, the samples from all except Unit 7 show quench textures with sparse phenocrysts. The secondary alteration mimics the texture of the rock and is only clearly visible in replacement of phenocrysts and void-filling minerals. Minerals replacing groundmass are frequently too fine-grained to identify petrographically with certainty. This preservation of the original rock texture and fine-grained character of the replacement phases gives the rocks a fresh appearance if only examined in a cursory manner. The presence of low-temperature phases, including carbonate and celadonite, also obscure the presence of high-temperature metamorphic minerals.

Texture and Mineralogy

Of the eight basalt samples examined petrographically from Hole 858F, only two are adequately crystalline to include clinopyroxene as a groundmass phase. The groundmass in the others is composed of plagioclase (An_{40-60}) with a variety of quenched, skeletal shapes in a matrix of aphanitic glass to crypto- or microcrystalline matrix. Basalts from Hole 858G, the deeper portion of the section, contain a more crystalline groundmass with all but two samples out of the 15 studied containing groundmass clinopyroxene. The quench morphology of plagioclase includes needle-like microlites, feathery microlites, blocky microphenocrysts with swallowtail structures, and hollow, lantern shapes (Fig. 74). The more crystalline samples include groundmass clinopyroxene in either prismatic microlitic, granular intergrown with plagioclase or spherulitic morphology. Ilmenite is present as small opaque grains or occasional skeletal crystals. All of the studied samples include a significant proportion of glass devitrified in the groundmass—none were holocrystalline. Varioles of more crystalline material are rounded to ovoid. These are frequently preferentially altered to spherical aggregates of secondary minerals. One of the most crystalline samples from Hole 858F was studied (Sample

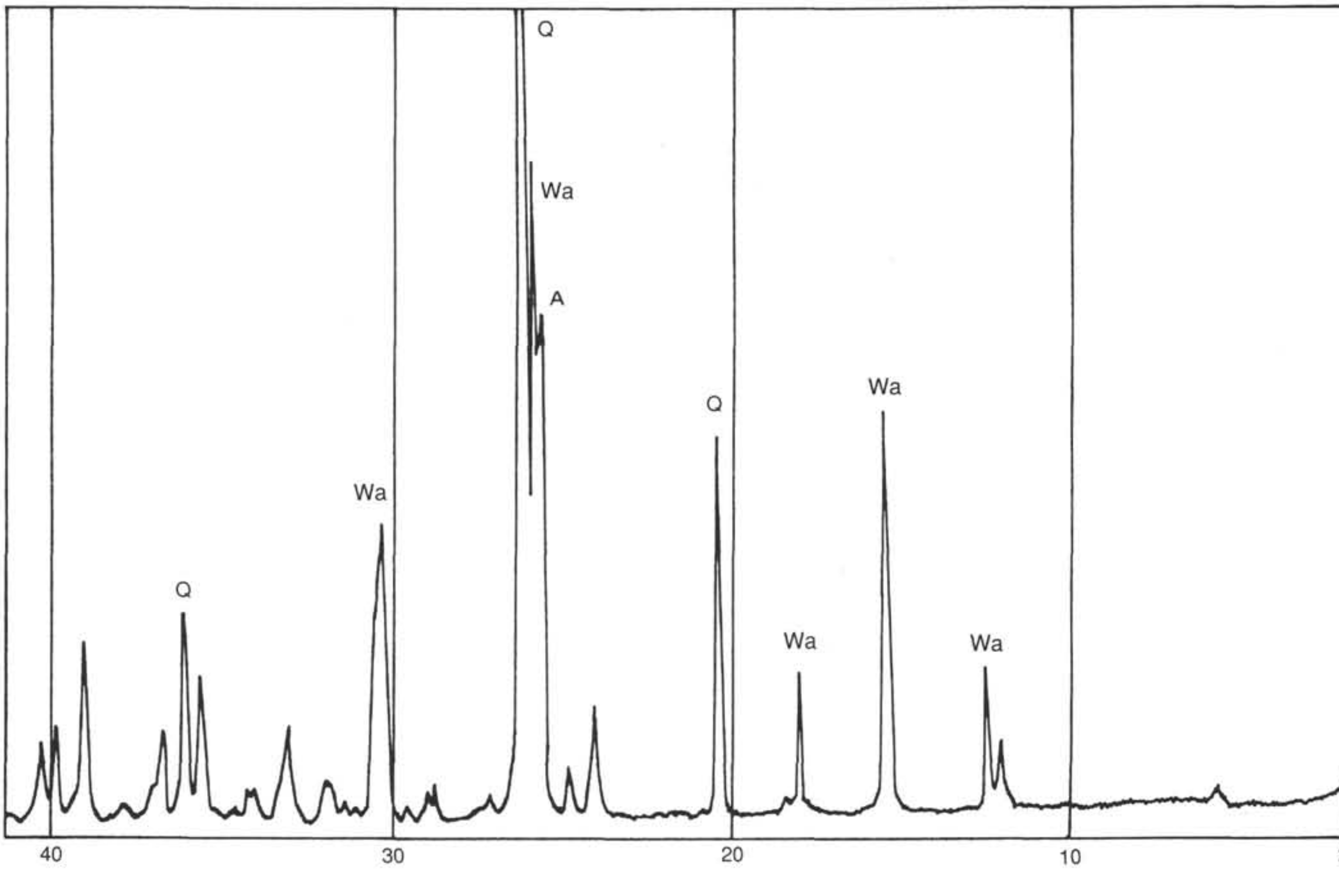

Figure 66. X-ray diffractogram of bulk sediment, Sample 139-858F-8R-CC, 7–9 cm (Wa = wairakite; Q = quartz; A = analcime).

139-858F-27R-1, Piece 9, 41–42 cm) and contains mesostasis with microcrystalline pyroxene barely discernible in a cryptocrystalline matrix. These characteristics document that most of the igneous rocks from this hole cooled very quickly in relatively thin units near the surface. Samples from Hole 858G are typically more crystalline, with microlitic to granular clinopyroxene visible in most of the studied samples. Skeletal plagioclase is the dominant phase and is always a larger grain size than the coexisting clinopyroxene, forming an intersertal texture. The low recovery at this site precludes drawing any conclusions from this difference in crystallinity regarding relative flow thickness. The ubiquitous groundmass plagioclase with quench, skeletal textures, however, supports the assumption that Hole 858G is composed of relatively thin flows that quenched rapidly. Unit 7 is composed of coarsely crystalline spherulitic diabase. Sparse euhedral plagioclase phenocrysts exhibit concentric zonation. More than 75% of the groundmass is an intersertal intergrowth of lathlike plagioclase and bladed to spherulitic clinopyroxene. Skeletal and granular oxides fill intergranular spaces. The texture and grain size could originate either in the center of a thick flow or in a sill.

All the samples except one contain a small proportion of plagioclase phenocrysts (1%–5%). They are columnar or tabular and vary in size from 0.5 to 3.0 mm and have an average composition of An_{65-75}. The plagioclase phenocrysts are broken, embayed, partially replaced, and show concentric zonation from calcic cores (An_{70-75}) to sodic rims (An_{40-50}). Five of the samples studied also contain 1%–2% mafic phenocrysts, typically completely replaced by chlorite, or chlorite/smectite. Their small (1 mm or less) size and ovoid shapes are similar to olivine. In one sample, <0.5-mm granular clinopyroxene formed similar ovoid pseudomorphs, so this association may not be diagnostic. However, all the samples that contain the large mafic pseudomorphs also contain sparse, euhedral chromian spinel. The spinel is dark red, chemically zoned, and contains devitrified glass inclusions. As spinel and olivine are phases that form in concert early in the fractionation of mid-ocean ridge basalt (MORB), it is likely that these samples are olivine-bearing basalts. There is no apparent stratigraphic relationship between the appearance of the olivine-spinel and depth within the core, so it is taken as a general characteristic of the magma type for the entire Unit 1. Mafic phenocrysts and chromian spinel were also observed near the bottom of Hole 858G (Sample 139-858G-15R-1, Piece 6, 30–32 cm), suggesting that this is characteristic of all the units.

Alteration

As previously mentioned, the basalt from this hole has been statically metamorphosed with a high preservation of the original texture. Alteration minerals were identified principally in pseudomorphs, veins, and vesicle filling. The petrographic summaries in Table 25 include a large proportion of unaltered mesostasis. The minerals within these phases are too fine-grained to distinguish any secondary phases, and the most conservative estimates were used consistently. Samples from Hole 858G contain exceptionally fresh mesostasis.

The fine-grained basalt at the contact with sediment (Sample 139-858-25R-1, Piece 3, 107–108 cm) is pervasively replaced by pale (magnesian?) chlorite in spherulitic bundles, mixed with quartz. Plagioclase phenocrysts in this rock are replaced by epidote, albite quartz, and prehnite. Epidote and prehnite also fill veins with euhedral sulfide. Quartz and sphene also locally replaces mesostasis.

The most conspicuous replacement texture occurs as ovoid mafic pseudomorphs. These are replaced by Fe-rich chlorite/smectite with some chlorite in the shallow portion of the hole (Sample 139-858F-26R-1, Piece 11, 98–100 cm) or by what appears to be a mixture of chlorite and actinolite (e.g., Sample 858F-26R-1, Piece 7, 66–67 cm). This same mineral (coarsely crystalline chlorite/smectite) fills veins and vesicles in the rock. Deeper in the section (e.g., Sample 139-858F-29R-1, Piece 14, 84–85 cm) the pseudomorphs are a fibrous to bladed mineral with strong yellow to green pleochroism, identified as an Fe-rich chlorite (Fig. 75). Mafic phenocrysts in Hole 858B are also replaced by this strongly pleochroic(?) chlorite. Filled vesicles, veins, and altered mesostasis typically contain the same minerals. Epidote and prehnite are most abundant as vesicle and vein fillings. Epidote is, in addition, frequently associated with sulfides in veins. The phyllosilicate minerals are extremely variable in optical properties. Pale acicular magnesian chlorite is associated with a dark brown chlorite-smectite in vesicles and replaced mesostasis. The chlorite-smectite occurs as dark radiating masses or as vesicle linings.

The presence of saponite or smectite/chlorite in the mafic pseudomorphs suggests lower temperature alteration. Although the limited information provided by eight thin sections is not conclusive, it is noted that the appearance of smectite clay minerals in pseudomorphs, veins, and vesicles is associated with other low-temperature minerals: the appearance of celadonite replacing mesostasis and trace amounts of carbonate replacing plagioclase. This mineral association suggests either a low-temperature overprint or possibly the lower temperature portion of a hydrothermal aureole.

The plagioclase pseudomorphs have a mottled, patchy extinction or are conspicuously replaced. Prehnite or albite is present in six of eight sections and epidote is present in seven of eight sections from Hole 858F. These are the most common minerals to replace plagioclase in association with chlorite. In the deeper part of the hole (Samples 139-858F-29R-1, Piece 3, 10–12 cm, and Piece 17, 98–105 cm) wairakite (or another zeolite) joins albite, prehnite, and epidote in replacing plagioclase giving the pseudomorphs a mottled extinction (Fig. 76). Prehnite, chlorite, and epidote are closely associated and appear to be in equilibrium. Some samples contain block pseudomorphs rimmed by quartz and filled with a pale Mg-rich chlorite. These are inferred to be replaced plagioclase phenocrysts.

Sulfide Minerals

Sulfide minerals are ubiquitous in the igneous rocks from Site 858 in quantities of 1%–5%. In general they are less abundant than in the sills observed in Site 857, but their mode of occurrence is very similar to that observed in the sills at the latter site (see "Site 857" chapter). They occur in two types of veins, one with chlorite and pyrite, the other with chalcopyrite, sphalerite quartz, zeolite, and epidote. Pyrite forms ovoid "porphyroblasts" within the rock, apparently indiscriminately replacing minerals and mesostasis. Such "porphyroblasts" apparently nucleate in cryptocrystalline or interstitial regions and grow outward in a spherical morphology. The formation of the original pyrite porphyroblasts is independent of any hydrous alteration, including the formation of chlorite. Plagioclase phenocrysts are even occasionally preferentially replaced. A later hydrous overprint typically alters the pyrite to a mixture of pyrite-chalcopyrite-pyrrhotite-sphalerite. The ovoid porphyroblasts must grow by some type of dissolution-reprecipitation mechanism that occasionally preserves the quench morphology of the replaced basalt.

Geochemistry

The volcanic rocks obtained for chemical analyses from Hole 858F are remarkably homogeneous in composition (Table 26). One of the six analyzed samples, Sample 139-858F-25R-1, 111 cm, has very high LOI (5.13%) and correspondingly high MgO. This sample is clearly altered, and will be discussed separately from the others. The remainder of the samples have compositions that vary only slightly more than analytical error. For example, TiO_2 has a range of only 0.06%. Na_2O, CaO, and MgO have the greatest variability; this may be the result of alteration also, as these rocks are very fine-grained, and hydrous alteration is clearly visible in thin section.

Immobile element compositions reflect this homogeneity, as they form tight clusters in Figures 77 and 78. They contain an average of 160 ppm Zr, much higher than most basalt compositions from the Juan de Fuca Ridge (typically 75–130 ppm, Karsten et al., 1990). Their compositions lie on the boundary between calc-alkaline and ocean-floor tholeiite fields (Fig. 77), and they are just outside the ocean-floor tholeiite field in Figure 78. Their TiO_2 contents are typical of ocean-floor basalts, and most of the abnormality in their composition is a result of their high Zr content.

In comparison with other Juan de Fuca compositions (Fig. 79) they have unusually low CaO/Al_2O_3 ratios. In the latter figure, the compositions lie on a near-vertical line, suggestive of plagioclase fractionation. However, as phenocrysts are not abundant in these rocks, plagioclase must have been removed in a subvolcanic magma chamber. The normative composition of feldspar for these samples (Table 27, An_{58} average) indicates that they are relatively albite-rich compared with samples from other sites. This possibly results from the pervasive albitization of the plagioclase phenocrysts.

Most of the Site 858 and Site 857 major element compositions (Fig. 79 and 80) are in coincident fields. Site 857 has both more evolved and more primitive compositions than Site 858 (Fig. 80). In Figure 79, the Site 858 compositions are offset to slightly higher values of Mg number at the same value of CaO/Al_2O_3, suggesting parallel fractionation series. The lower normative plagioclase composition and distinctly higher incompatible element composition of the Site 858 samples suggest that they are a late phase of a major magmatic event. The presence of plagioclase-olivine-spinel phenocrysts, however, precludes extensive crustal fractionation (Fig. 78), Site 858 basalts fall on the same fractionation path as the Site 855 basalts, and could represent increased amount of crystal fractionation to high concentrations of Ti and Zr. This is contradicted, however, by the high values of Mg number for Site 858 compared to Site 855 which precludes these magmas being related by crystal fractionation.

The single altered sample (from Section 139-858F-25R-1) has high LOI, high Al_2O_3, TiO_2, Na_2O, and MgO content, and very low CaO content (5.5% vs. 11.97% for unaltered samples). It has undergone both albitization and chloritization of feldspar. The high content of both alumina and titania, considered to be immobile elements, was probably generated by loss of volume from the sample. The lower zinc content of the altered sample indicates leaching of sulfide.

Conclusions

All of the igneous rocks sampled from Site 858 except for a single basal unit of spherulitic diabase, can be characterized as fine-grained basalts. The well-developed quench textures, local vesicularity, and presence of low-temperature alteration minerals (carbonate, celadonite, smectite) suggest that these rocks formed as extrusive massive flows. The small quantity of metasiltstone or chert was probably representative of very thin, discontinuous interflow sediment. Petrographic examination has revealed that they contain sparse amounts of phenocrysts or microphenocrysts of plagioclase, olivine, and spinel.

The metamorphic assemblages observed in Hole 858F are characteristic of upper zeolite (wairakite-chlorite-prehnite) to greenschist (albite-epidote-chlorite-actinolite) facies. Zeolite facies metamorphism can take place over a temperature range of 100°–300°C. The stability range of prehnite in natural rocks is not well known, but experimental studies (Bird and Helgeson, 1981; Liou et al., 1983) suggest that it has an upper limit of 400°C. Analcime, observed in a single sample, has an upper stability limit of 200°C, where it is replaced by albite. A temperature range of 200°–300°C is suggested for metamorphism at this site.

The general similarity in composition of the basalt from Site 858 with the sills from Site 857 indicate that these two mafic sequences

Table 22. Weight percentage of SiO_2, TiO_2, Al_2O_3, Fe_2O_3, MnO, MgO, CaO, Na_2O, K_2O, P_2O_5, CO_2, H_2O, S, and organic C in sedimentary rocks from Holes 858A, 858B, 858C, 858D, and 858F.

Core, section, interval (cm)	Depth (mbsf)	Na_2O	MgO	MnO	TiO_2	K_2O	SiO_2	CaO	Fe_2O_3	Al_2O_3	P_2O_5	Total	LOI
139-858A-													
1H-1, 81–83	0.81	2.34	3.79	0.12	0.94	2.25	60.61	4.44	7.99	16.77	0.211	99.461	5.66
1H-1, 81–83	0.81	2.29	3.81	0.12	0.93	2.24	59.9	4.42	7.99	16.63	0.2	98.53	5.66
2H-1, 34–36	2.74	1.82	2.02	0.16	1.02	3.36	63.81	8.01	5.99	14.39	0.24	100.82	6.91
2H-1, 34–36	2.74	1.92	2.1	0.17	1.01	3.38	64.19	8	6.03	14.5	0.23	101.53	6.91
3H-3, 81–85	15.48	2.25	3.66	0.1	0.86	2.74	61.95	3.67	7.48	17.48	0.19	100.38	3.9
3H-3, 81–85	15.48	2.23	3.6	0.1	0.85	2.71	61.54	3.65	7.33	17.44	0.18	99.63	3.9
4H-2, 79–83	23.69	1.65	3.49	0.09	0.88	3.72	63.32	3.39	6.94	17.41	0.2	101.09	5.03
4H-2, 79–83	23.69	1.71	3.55	0.09	0.89	3.71	62.67	3.36	6.94	17.59	0.2	100.71	5.03
5H-3, 100–105	34.9	1.93	3.17	0.09	0.92	4.26	64.38	3.37	6.7	16.14	0.32	101.28	4.16
5H-3, 100–105	34.9	1.89	3.1	0.1	0.92	4.28	64.71	3.38	6.84	16.32	0.32	101.86	4.16
6H-2, 94–96	42.84	1.44	4.65	0.1	0.99	4.39	59.59	2.33	8.68	17.71	0.23	100.11	5.14
6H-2, 94–96	42.84	1.44	4.7	0.1	0.99	4.39	59.95	2.32	8.56	17.7	0.23	100.38	5.14
7H-4, 93–97	55.33	1.61	3.05	0.08	0.86	3.7	66.53	3.49	6.35	15.11	0.2	100.98	4.5
7H-4, 93–97	55.33	1.62	3.02	0.08	0.84	3.66	65.81	3.45	6.27	14.92	0.19	99.86	4.5
8H-2, 39–41	60.72	2.61	4.38	0.14	1.11	2.04	60.1	6.08	8.54	16.47	0.26	101.73	5.49
8H-2, 39–41	60.72	2.53	4.37	0.14	1.11	2	59.5	6.05	8.6	16.33	0.26	100.89	5.49
9X-4, 47–51	67.47	1.38	5.11	0.1	0.97	4.13	61.42	2.68	8.36	17.54	0.26	101.95	5.93
9X-4, 47–51	67.47	1.49	5.07	0.09	0.96	4.12	60.95	2.65	8.04	17.45	0.25	101.07	5.93
11X-1, 2–7	72.92	1.87	1.83	0.16	0.79	2.9	64.27	10.27	5.06	12.93	0.19	100.27	7.9
11X-1, 2–7	72.92	1.75	1.78	0.16	0.78	2.87	63.61	10.06	4.92	12.77	0.19	98.89	7.9
12X-1, 18–20	81.78	1.57	4.45	0.09	0.94	3.09	61.93	3.09	7.57	16.66	0.19	99.58	5.4
12X-1, 18–20	81.78	1.67	4.6	0.26	0.74	3.11	62.35	3.11	7.63	16.61	0.19	100.27	5.4
15X-1, 60–62	111.2	2.74	2.9	0.12	0.78	2.36	67.95	3.21	4.94	15.11	0.18	100.29	3.81
15X-1, 60–62	111.2	2.72	2.8	0.12	0.77	2.39	68.08	3.22	5	15.13	0.18	100.41	3.81
18X-3, 16–20	142.76	2.74	7.87	0.13	0.96	1.46	60.1	1.09	8.49	16.74	0.22	99.8	4.36
18X-3, 16–20	142.76	2.81	7.9	0.13	0.97	1.46	60.76	1.09	8.56	16.88	0.22	100.78	4.36
139-858B-													
1H-2, 42–44	1.92	1.47	22.39	0.15	0.27	0.69	54.81	2.64	9.22	6.27	0.09	98	8.75
1H-2, 42–44	1.92	1.55	21.97	0.14	0.26	0.69	54.01	2.6	8.86	6.2	0.08	96.36	8.75
1H-3, 23–27	3.23	1.8	3.78	0.11	1.13	3.28	61.23	3.65	7.8	17.79	0.24	100.81	5.21
1H-3, 23–27	3.23	1.87	3.71	0.11	1.1	3.22	60.51	3.61	7.65	17.55	0.24	99.57	5.21
1H-5, 21–25	6.21	1.99	6.55	0.12	0.95	2.97	60.04	2.26	8.48	18.16	0.22	101.74	5.66
1H-5, 21–25	6.21	1.97	6.49	0.12	0.95	2.95	59.68	2.25	8.47	18.03	0.22	101.13	5.66
2H-2, 125–127	9.95	1.82	8.91	0.1	0.83	2.49	59.49	1.2	8.94	17.29	0.18	101.25	4.21
2H-2, 125–127	9.95	1.97	8.85	0.1	0.83	2.47	59.16	1.2	8.92	17.11	0.18	100.79	4.21
2H-5, 11–13	13.31	1.49	5.14	0.09	0.71	1.58	69.48	0.78	7.85	13.77	0.15	101.04	3.81
2H-5, 11–13	13.31	1.45	5.12	0.08	0.71	1.6	69.68	0.78	7.77	13.88	0.15	101.22	3.81
5H-1, 122–125	25.12	0	34.37	0.3	0.87	0.02	43.4	1.59	5.04	15.51	0.02	101.12	10.47
5H-1, 122–125	25.12	0.01	34.18	0.3	0.84	0.01	42.97	1.57	4.99	15.32	0.01	100.2	10.47
5H-3, 124–128	28.14	0	34.15	0.26	0.73	0.02	43.36	1.66	5.65	13.72	0.02	99.57	9.81
5H-3, 124–128	28.14	0.13	34.08	0.26	0.74	0.03	43.51	1.66	5.64	13.75	0.02	99.82	9.81
139-858C-													
1H-2, 42–46	1.92	1.9	3.44	0.1	1.12	3.27	61.35	3.78	8.03	15.43	0.23	98.65	5.76
1H-2, 42–46	1.92	1.8	3.46	0.1	1.12	3.28	61.32	3.76	7.96	17.7	0.24	100.74	5.76
2H-2, 77–79	5.77	2.65	3.98	0.13	0.87	2.45	56.83	7.86	8.23	16.94	0.2	100.14	8.06
2H-2, 77–79	5.77	2.47	3.86	0.13	0.85	2.44	56.48	7.84	8.21	16.66	0.2	99.14	8.06
3H-2, 133–135	15.83	1.12	0.92	0.16	0.87	5.75	49.49	8.14	13.96	15.36	0.24	96.01	7.87
3H-2, 133–135	15.83	1.15	0.89	0.16	0.84	5.94	48.38	7.94	13.66	15.08	0.24	94.28	7.87
5H-2, 121–123	26.21	1.95	3.65	0.07	0.92	4.3	63.17	1.52	6.1	18.85	0.2	100.73	4.12
5H-2, 122–123	26.22	1.93	3.63	0.07	0.91	4.27	62.8	1.51	6.09	18.76	0.2	100.17	4.12
6H-3, 104–106	37.04	2.36	6.79	0.13	0.93	2.16	61.99	0.75	8.44	16.34	0.22	100.11	4.13
6H-3, 104–106	37.04	2.36	6.67	0.13	0.91	2.15	61.41	0.74	8.4	16.23	0.21	99.21	4.13
7H-2, 53–55	43.53	2.81	7.5	0.13	0.92	0.81	62.61	0.65	7.95	15.99	0.23	99.6	4.91
7H-2, 53–55	43.53	2.9	7.59	0.14	0.93	0.83	62.72	0.66	8.01	15.99	0.24	100.01	4.91
10X-CC, 37–39	49.87	2.09	3.48	0.86	0.86	1.35	69.32	1.57	5.07	12.17	0.18	96.95	2.62
10X-CC, 37–39	49.87	2.95	3.49	0.87	0.87	1.41	71.31	1.61	5.08	12.69	0.18	100.46	2.62
11X-1, 48–51	54.98	2.96	4.24	0.24	0.91	2.26	56.63	6.61	8.17	17.06	0.23	99.31	4.39
11X-1, 48–51	54.98	2.93	4.24	0.24	0.93	2.25	56.94	6.64	8.24	17.16	0.23	99.8	4.39
12X-3, 87–90	67.87	3.63	7.29	0.15	0.98	0.08	62.3	1.27	7.25	15.9	0.23	99.08	4.03
12X-3, 87–90	67.87	3.6	7.46	0.14	0.98	0.09	63.09	1.29	7.38	16.19	0.24	100.46	4.03
13X-1, 1–16	73.71	3.75	6.39	0.15	0.95	0.05	61.84	2.73	7.71	15.96	0.31	99.84	3.4
13X-1, 1–16	73.71	3.68	6.51	0.15	0.96	0.05	61.25	2.74	7.7	16.05	0.32	99.41	3.4
14X-1, 34–36	83.74	3.49	5.7	0.14	0.96	0.69	61.72	2.39	8.42	17.25	0.02	100.78	3.64
14X-1, 34–36	83.74	3.63	5.7	0.14	0.97	0.7	61.73	2.4	8.38	17.22	0.2	101.07	3.64

Table 22 (continued).

Core, section, interval (cm)	Depth (mbsf)	Na_2O	MgO	MnO	TiO_2	K_2O	SiO_2	CaO	Fe_2O_3	Al_2O_3	P_2O_5	Total	LOI
139-858D-													
1H-3, 98–102	3.98	1.71	3.26	0.08	1	3.05	59.31	4.59	8.17	17.47	0.22	98.86	6.46
1H-3, 98–102	3.98	1.66	3.34	0.09	1.01	3.04	59.71	4.6	8.28	17.44	0.22	99.39	6.46
1H-6, 30–33	7.8	2.58	4.03	0.12	0.91	2.83	58.74	5.3	8.25	17.97	0.23	100.96	5.77
1H-6, 30–33	7.8	2.67	3.99	0.12	0.9	2.83	58.72	5.29	8.26	17.97	0.23	100.98	5.77
2H-2, 111–113	11.91	1.67	4.82	0.09	0.9	3.09	59.31	2.63	9.48	16.99	0.19	99.17	5.23
2H-2, 111–113	11.91	1.8	4.91	0.09	0.91	3.09	59.48	2.66	9.46	17.03	0.19	99.62	5.23
2H-7, 23–25	18.53	1.16	7.17	0.11	0.82	3.64	61.21	0.58	9.57	16.05	0.16	100.47	6.76
2H-7, 23–25	18.53	1.16	7.05	0.11	0.82	3.61	60.81	0.58	9.39	15.96	0.16	99.65	6.76
4H-4, 59–63	23.63	0.47	5.56	0.05	0.8	3.3	69.78	0.45	4.68	16.04	0.21	101.34	28.8
4H-4, 59–63	23.63	0.29	5.51	0.06	0.81	3.27	69.32	0.44	4.55	15.94	0.21	100.4	28.8
139-858F-													
9R-CC, 18–20	94.38	0	0.29	0.03	0.38	0	76.53	7.15	1.59	13.36	0.08	99.41	
9R-CC, 18–20	94.38	0	0.32	0.03	0.37	0	75.81	7.08	1.59	13.3	0.08	98.58	
13R-CC, 7–9	132.97	3.23	5.06	0.08	0.8	0.05	66.83	2.95	5.48	14.15	0.18	98.81	3.03
13R-CC, 7–9	132.97	3.18	4.97	0.08	0.82	0.05	66.62	2.96	5.44	14.08	0.18	98.38	3.03
25R-1, 40–42	249.3	4.42	9.34	0.17	1.1	0.53	54.87	1.88	8.21	15.29	0.17	95.98	
25R-1, 40–42	249.3	4.45	9.38	0.17	1.1	0.54	55.37	1.9	8.29	18.53	0.26	99.99	

Notes: All element oxides and elements were normalized to 100 wt% but multiplying all values by (100 – LOI)/Total, where "total" is the total weight of all elements and element oxides determined by X-ray fluorescence on the fused disk. Values for loss on ignition (LOI) and totals on the fused disk are given so that the measured values can be recalculated. See "Sediment Geochemistry and Alteration" section, "Explanatory Notes" chapter (this volume), for analytical methods.

are possibly cogenetic. However, the melt that produced the 858 flows was higher in Zr than the parent to most of the Site 857 sills, indicating that these flows formed either as the latest part of a major magmatic event or from a different magma source region. Differentiation of the parent magma was pronounced, which indicates efficient removal of heat from a subvolcanic magma chamber. Such heat removal would necessitate a moderate level of water circulation in the overlying strata, and might be effective in forming a high-temperature hydrothermal fluid.

PHYSICAL PROPERTIES

Site 858 is located over an active hydrothermal vent field north of Site 857 and comprises six holes. Hole 858A is located about 200 m northwest of currently active hydrothermal vents and is the coldest hole drilled at this site, with an estimated heat flow of 1.9 W/m^2 (see "Heat Flow" section, this chapter). Hole 858C, with a heat flow of 3.3 W/m^2, is intermediately hot. Holes 858B, 858D, 858F, and 858G, drilled in the immediate vicinity of active hydrothermal vents, have a heat flow of about 10 W/m^2 and are the hottest holes drilled during Leg 139.

High temperatures encountered at very shallow depths in Holes 858B and 858D required the use of aluminum liners. The aluminum liners posed severe problems for some of the MST measurements. Volume magnetic susceptibility measurements on whole-round cores in aluminum liners were not reliable as the presence of a highly conductive liner material resulted in unrealistically high negative volume magnetic susceptibility in the order of about −0.02. These values may be due to electromagnetic induction within the liner caused by the alternating electromagnetic field of the measuring loop. Aluminum does not have such a high negative (diamagnetic) volume magnetic susceptibility.

P-wave logger (PWL) measurements on cores in aluminum liners suffered also as the signal strength was always too low to be detected by the receiver. Sediments from these high heat flow areas also tended to have a high gas content that caused the core to fracture on a visible (centimeter) to almost invisible (submillimeter) scale. This effect was also evident during the measurement of the compressional wave velocity with the digital sound velocimeter (DSV) on split cores. Gamma-ray attenuation porosity evaluator (GRAPE) measurements were made on all cores in aluminum liners after recalibrating the system using an aluminum liner as a sleeve around the aluminum standard.

Apart from problems related to the aluminum liners, all cores were subjected to routine physical properties measurements. Index properties samples were taken at or adjacent to other measurement locations whenever possible and at a frequency of two to three per core. In the case of Hole 858F the sampling frequency was sometimes lower due to very poor core recovery. Volume magnetic susceptibility data for samples from Hole 858F are not shown as the values were used only as a qualitative indicator of the sudden appearance of material with high volume magnetic susceptibility in a sequence of otherwise low volume magnetic susceptibility (see "Physical Properties" section, "Site 857" chapter). GRAPE and PWL measurements could not be made on material recovered from Hole 858F.

Volume magnetic susceptibility data are given in SI units and have not been corrected for either the core-to-inner coil diameter ratio of 0.825 or the effects of partially filled liners. None of the physical properties data has been corrected for *in-situ* temperature, *in-situ* pressure, or rebound effects. A detailed description of the lithological units, referred to in the following discussion of the physical properties results, can be found in "Lithostratigraphy and Sedimentology" section (this chapter).

Volume Magnetic Susceptibility

Hole 858A was cored continuously with APC to 62.5 mbsf with very good recovery and continued with XCB to a final depth of 339.0 mbsf. Unit I, from 0 to 21.4 mbsf, consisting of fine-grained hemipelagic clay with minor turbidites, is characterized by volume magnetic susceptibility of 0.002 to 0.003 with interspersed sections of volume magnetic susceptibility of an order of magnitude less (Fig. 81A). A similar signature in the shallow volume magnetic susceptibility was observed at previous sites; causes of the signal and of the magnitude are discussed there (see "Physical Properties" section, "Site 856" chapter). The low volume magnetic susceptibility of 0.0002 to 0.0003 between 23.0 and 36.0 mbsf falls entirely in Unit IIA, which consists of interbedded hemipelagic turbidites of Pleistocene age. In this depth interval carbonate concretions become abundant (see "Sediment Geochemistry and Alteration" section, this chapter) which might indicate increased diagenetic and hydrothermal

Table 23. Trace element data for sedimentary rocks from Holes 858A, 858B, 858C, 858D, and 858F.

Core, section, interval (cm)	Depth (mbsf)	Ba	Ce	Cr	Cu	Nb	Ni	Rb	Sr	V	Y	Zn	Zr
139-858A-													
3H-3, 81–85	15.48	705	22	101	51	12	48	98	303	160	23	117	173
4H-2, 79–83	23.69	743	22	107	51	14	67	133	212	146	22	114	154
139-858B-													
1H-2, 42–44	1.92	194	0	26	4249	3	27	22	141	87	0	1813	47
139-858C-													
6H-3, 104–106	37.04	790	9	102	55	11	57	35	113	165	23	102	143
12X-3, 87–90	67.87	661	25	107	87	10	52	2	206	166	18	151	165
14X-1, 34–36	83.74	141	16	98	57	10	49	15	228	180	24	124	164
139-858D-													
2H-7, 23–25	18.53	954	13	101	63	11	60	109	90	180	19	144	130
4H-4, 59–63	23.63	491	15	114	38	13	37	108	53	153	19	103	150
139-858F-													
9R-CC, 18–20	94.38	122	109	15	166	9	0	1	54	60	9	12	63
13R-CC, 7–9	132.97	131	80	66	15	11	11	0	196	112	19	39	119
25R-1, 40–42	249.3	229	53	85	19	14	41	12	155	205	19	122	103

Note: See "Sediment Geochemistry and Alteration" section, "Explanatory Notes" chapter (this volume), for analytical methods.

activity. These processes in turn may have altered the magnetite to iron sulfide which would explain the complete lack of a volume magnetic susceptibility signal normally associated with turbidites within this depth interval. The moderately to well-indurated hemipelagic turbiditic strata (Unit IIIC) from 38.4 mbsf to 74.0 mbsf show highly variable values of 0.01 to 0.0004. These variations correlate well with visually identified turbidite sequences (see "Physical Properties" section, "Site 856" chapter). Below 74.0 mbsf the core recovery becomes very sparse. However, the volume magnetic susceptibility measurements show a very distinct decrease of an order of magnitude below 80 mbsf (Fig. 81B) that is comparable to the volume magnetic susceptibility profile of Hole 857C (Fig. 83A).

The top of Hole 858B (Fig. 82A) consists of oxidized, metalliferous sediments (Unit III) with low volume magnetic susceptibility in the range of 0.00005 to 0.0003. The sharp increase in volume magnetic susceptibility at 1.97 mbsf marks the Holocene/Pleistocene boundary and the transition to Unit I. The sharp decrease at 4.9 mbsf may correlate to a similar decrease seen at 5.2 mbsf in Hole 858A (see Fig. 81A). Below 7.0 mbsf volume magnetic susceptibility data logging was discontinued due to the use of aluminum liners.

Cores from the upper 8.5 m of Hole 858C (Unit I) are characterized by volume magnetic susceptibility of 0.001 to 0.003, which decreases sharply by an order of magnitude below this depth (Fig. 83A). A similar decrease in volume magnetic susceptibility at this depth was apparent in Hole 858A and 858B. At 13.0 mbsf the volume magnetic susceptibility drops again by an order of magnitude to values of 2×10^{-6} to 6×10^{-6}, the lowest values measured on Leg 139. Cores recovered from this depth interval are described as part of a massive and concretion-rich carbonate layer (Section 139-858C-3H-2; see

Table 24. Extent of igneous units actually recovered from Site 858.

Unit	Top (cm)	Bottom (cm)	Thickness (cm)
	139-858F-		
1A	25R-1, 90	25R-1, 126	36
1B	26R-1, 0	26R-1, 122	122
1C	27R-1, 0	29R-1, 16	119
1D	29R-1, 23	29R-1, 124	101
	139-858G-		
1C	1R-1, 0	1R-1, 65	65
1D	2R-1, 0	3R-1, 5	81
2A	3R-1, 5	6R-1, 7	162
2B	6R-1, 7	7R-1, 69	110
3	8R-1, 0	9R-1, 5	47
4	9R-1, 5	9R-1, 35	30
5	10R-1, 0	13R-1, 47	246
6	14R-1, 0	16R-1, 37	123
7	16R-1, 37	16R-1, 90	53
		Total	12.95 m

Table 25. Estimated modal proportions of representative thin sections from Hole 858F.

Core, section:	25R-1	26R-1	27R-1	28R-1	29R-1	29R-1
Interval (cm):	107–108	66–67	41–42	30–32	10–12	84–85
Piece number:	3	7	9	5	3	14
Primary minerals (%)						
Plagioclase	o.p.	19	26	9	16	11
Olivine	o.p.	o.p.		o.p.		o.p.
Clinopyroxene	o.p.	20	10			
Spinel	tr	1		tr		1
[a]Mesostasis	o.p.	49	54	68	66	
Secondary minerals (%)						
Smectite			tr	3		
Carbonate		tr		tr	1	
Chlorite	50	5	5	10	5	10
Albite	2	5	1	2	1	5
Actinolite		1		4		
Epidote	15	5	3	2	5	10
Prehnite	8		1		5	
Sulfides	10		1	2		
Quartz	15	tr	tr			

Notes: o.p. = phase was originally present, now totally replaced; tr = trace. Some of the plagioclase and all the olivine and spinel occur as phenocrysts.
[a]Interstitial or matrix glass.

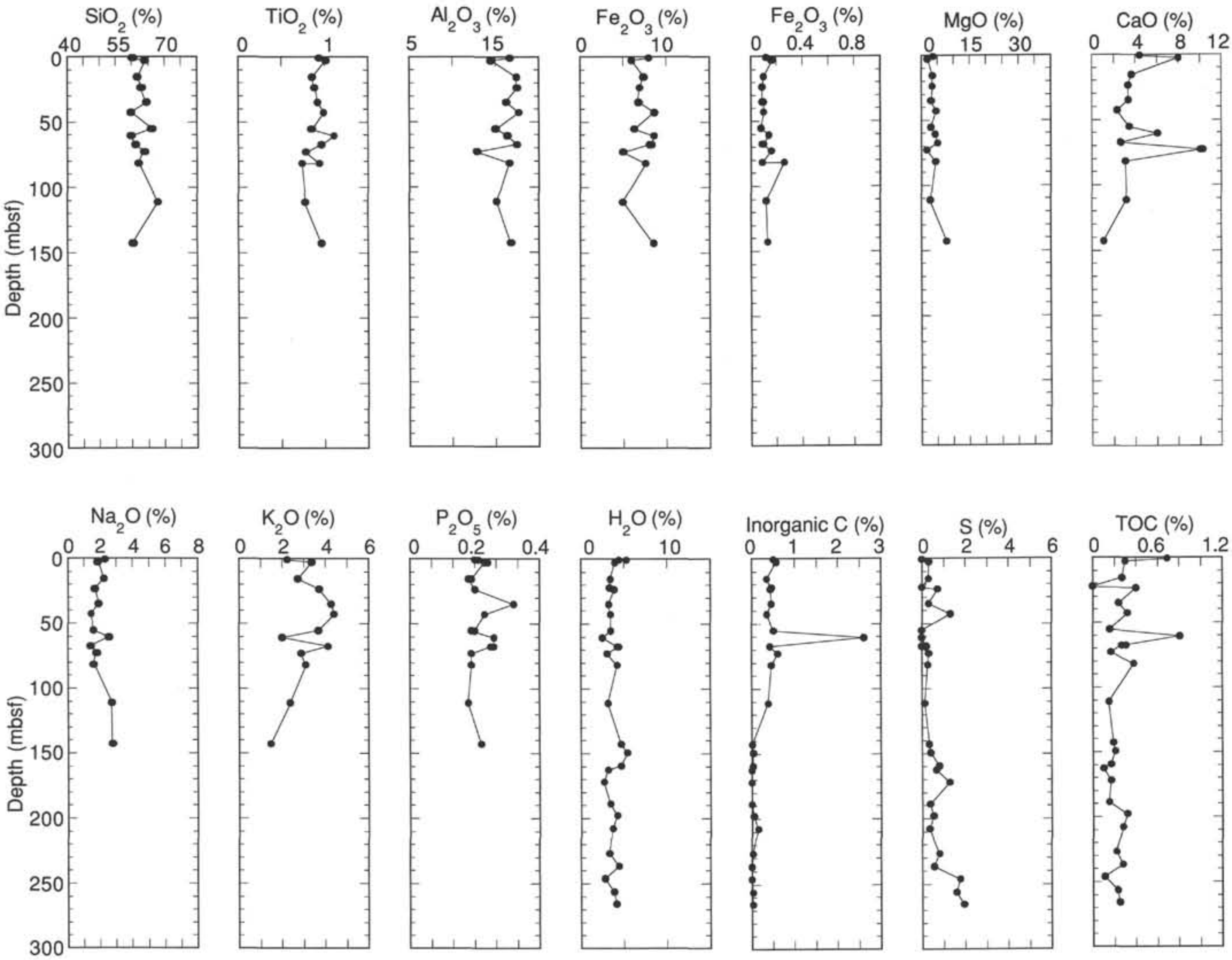

Figure 67. Depth profiles of SiO_2, TiO_2, Al_2O_3, Fe_2O_3, MnO, MgO, CaO, Na_2O, K_2O, P_2O_5, H_2O, inorganic C, S, and organic carbon (TOC) in sediment from Hole 858A. The content of all element oxides and elements is expressed as weight percentage.

"Sediment Geochemistry and Alteration" section, this chapter) that continues to 23.0 mbsf. The high peak in volume magnetic susceptibility at 23.5 mbsf (interval 139-858C-5H-1, 0–42 cm) is probably caused by volcanic debris. This depth interval is described as "drilling fragments" which indicates that this material may have fallen down the hole ("Lithostratigraphy and Sedimentology" section, this chapter). However, the high volume magnetic susceptibility values and the accompanying high wet-bulk densities (see discussion of GRAPE results of Hole 858C, this section) cannot be found anywhere higher in the section. The interval from 23.5 to 23.9 mbsf, therefore, may represent an autochthonous layer of as yet unknown origin and composition. Unit IIB (14.85 to 48.90 mbsf) is characterized by low volume magnetic susceptibility and the complete absence of a marked volume magnetic susceptibility signal from turbidites compared to the signature seen from Hole 858A (see Fig. 81A). The presence of numerous anhydrite concretions at 33.0 mbsf is indicated by a distinct low in volume magnetic susceptibility. The concretion zone ends at 40.0 mbsf, which roughly coincides with an increase of volume magnetic susceptibility by a factor of two to three. The low values of volume magnetic susceptibility in general, the almost complete absence of turbidite volume magnetic susceptibility signals and the sediment geochemistry suggest that the sediments in Hole 858C have experienced major geochemical changes due to diffuse fluid flow.

Hole 858D, although drilled farther from an active vent site, had higher temperatures at comparable depths than Hole 858B. Volume magnetic susceptibility in Hole 858D drops from background level of 0.002 at 8.95 mbsf, to low values of 0.0002 to 0.0004 below this depth (as in Hole 858C) then increases again to a background level at 15.0 mbsf. Part of this increase may be an artifact of rust embedded in partially melted plastic liners (see "Paleomagnetism" section, this chapter). Volume magnetic susceptibility measurements had to be discontinued below 19.8 mbsf since aluminum liners were used.

As the recovery in Holes 858F and 858G was only 2% to 5%, only occasional check measurements were made as discussed previously.

GRAPE Wet-Bulk Density

Raw GRAPE wet-bulk density data have been filtered for outliers and smoothed with a 50-cm-wide running average to clarify trends and larger scale features. The rather coarse and unsophisticated preliminary processing can cause offsets between unsmoothed and smoothed wet-bulk densities and suppresses high-frequency signals. These effects will not be discussed here. Detailed processing, including a careful adjustment of GRAPE values to wet-bulk densities from index properties measurements, will be done post-cruise. The wet-

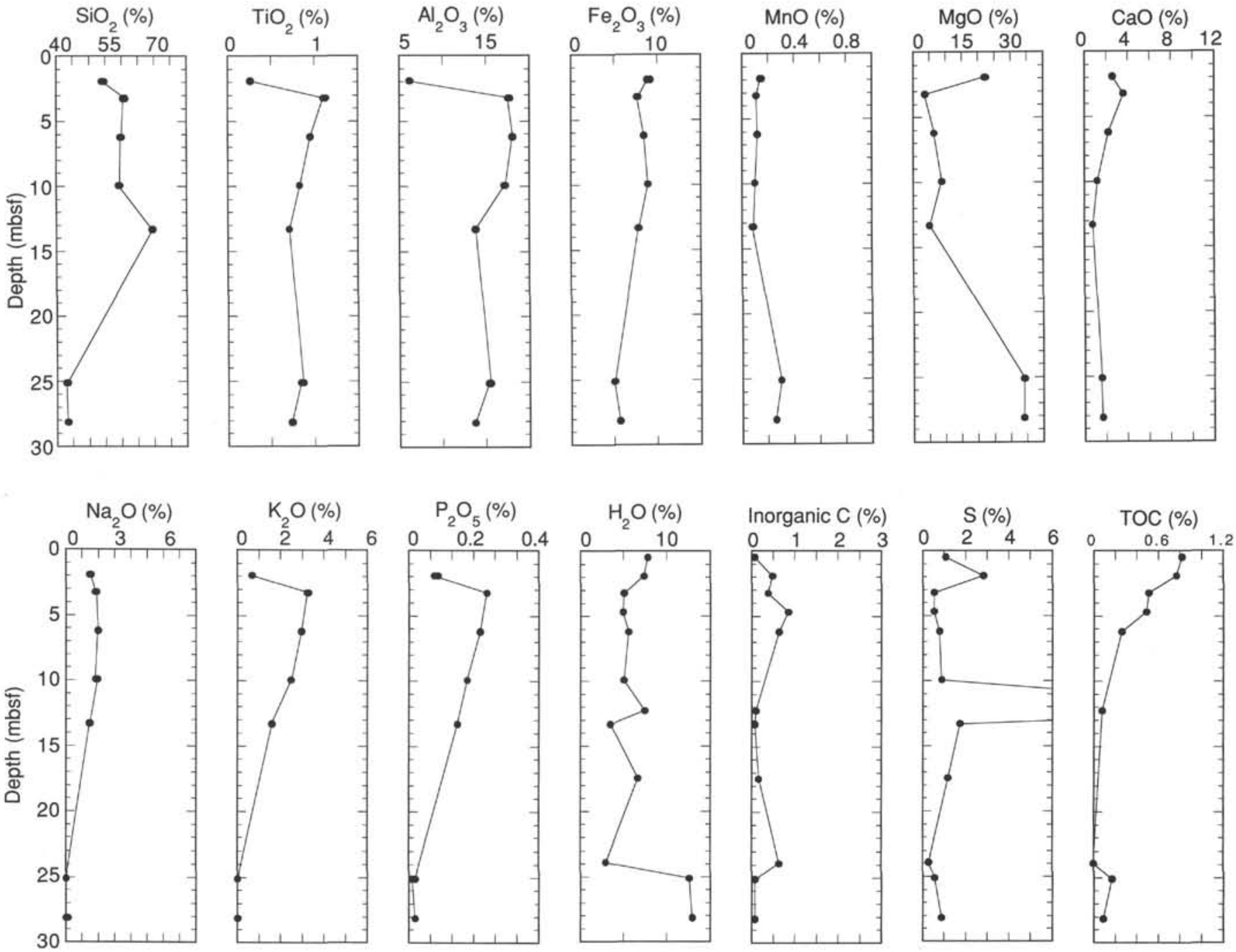

Figure 68. Depth profiles of SiO_2, TiO_2, Al_2O_3, Fe_2O_3, MnO, MgO, CaO, Na_2O, K_2O, P_2O_5, H_2O, inorganic C, S, and organic carbon (TOC) in sediment from Hole 858B. The content of all element oxides and elements is expressed as weight percentage.

bulk density from GRAPE measurements quoted in the following discussion should be regarded as qualitative.

At Hole 858A (Fig. 81C) wet-bulk density increases steadily from very low values around 1.4 g/cm^3 at the very unconsolidated and probably disturbed top of Section 139-858A-1H-1 to high values in the range of 1.9 g/cm^3 at 44.2 mbsf. No core was recovered between 44.2 mbsf and 49.9 mbsf; at 49.9 mbsf wet-bulk density drops to around 1.6 g/cm^3. The volume magnetic susceptibility record shows a rapid decrease at 44.2 mbsf that may be indicative of a substantial change in lithology between 44.2 and 49.9 mbsf. Below that depth the wet-bulk density increases with depth again to values around 1.9 g/cm^3. Superimposed on this general trend are sawtooth-like signals with periods of several meters and an amplitude of 0.05 to 0.1 g/cm^3 (Fig. 81C, 6.0–11.1 mbsf, 24.8–29.2 mbsf, and 50.5–55.5 mbsf). Within these depth intervals small-scale variations over 10 to 50 cm are also visible. This is especially interesting in the interval from 31.0 to 36.0 mbsf where the volume magnetic susceptibility data do not reflect the presence of turbidites; in contrast GRAPE wet-bulk density data do reflect these fining-upward sequences. Between 50.5 and 55.5 mbsf both volume magnetic susceptibility record and GRAPE wet-bulk density data show the turbidite sequence very clearly. We have no explanation yet for the very prominent large peaks in the record at 30.0, 59.2, and 60.8 mbsf.

GRAPE measurements on cores from Hole 858B (Fig. 82B) are the only whole-core physical properties data available for sediments contained in aluminum liners. The wet-bulk density of 1.25 to 1.3 g/cm^3 in Unit III (0 to 1.97 mbsf; highly unconsolidated oxidized metalliferous sediments) increases sharply at the top of Unit I (1.92 mbsf) and remains between 1.5 and 1.6 g/cm^3 to 10.4 mbsf. The occurrence of a semimassive sulfide layer in Section 139-858B-2H-3 (10.41–12.70 mbsf) increases the wet-bulk density to very high values of 2.3 g/cm^3. Below this depth the cores are increasingly disturbed (drilling breccia) so that a detailed discussion of the GRAPE wet-bulk density is not appropriate.

Wet-bulk density in Hole 858C (Fig. 83B) shows a steady increase from 1.4 g/cm^3 at the seafloor to 1.8–2.0 g/cm^3 at 15.0 mbsf. A sharp peak in wet-bulk density to 2.0 g/cm^3 occurs within the massive carbonate layer at 14.5–17.0 mbsf (see "Sediment Geochemistry and Alteration" section, this chapter). Below 17.0 mbsf wet-bulk density varies between 1.8 and 2.0 g/cm^3 with a peak of 2.25 g/cm^3 that coincides with a volume magnetic susceptibility peak (Fig. 83A).

Figure 84B shows the wet-bulk density profile of Hole 858D; density increases from 1.3 g/cm^3 at the seafloor to 1.85 g/cm^3 at 29 mbsf. Superimposed on this overall increase with depth are long-wavelength variations with periods from 5 to 10 m. It is unclear how

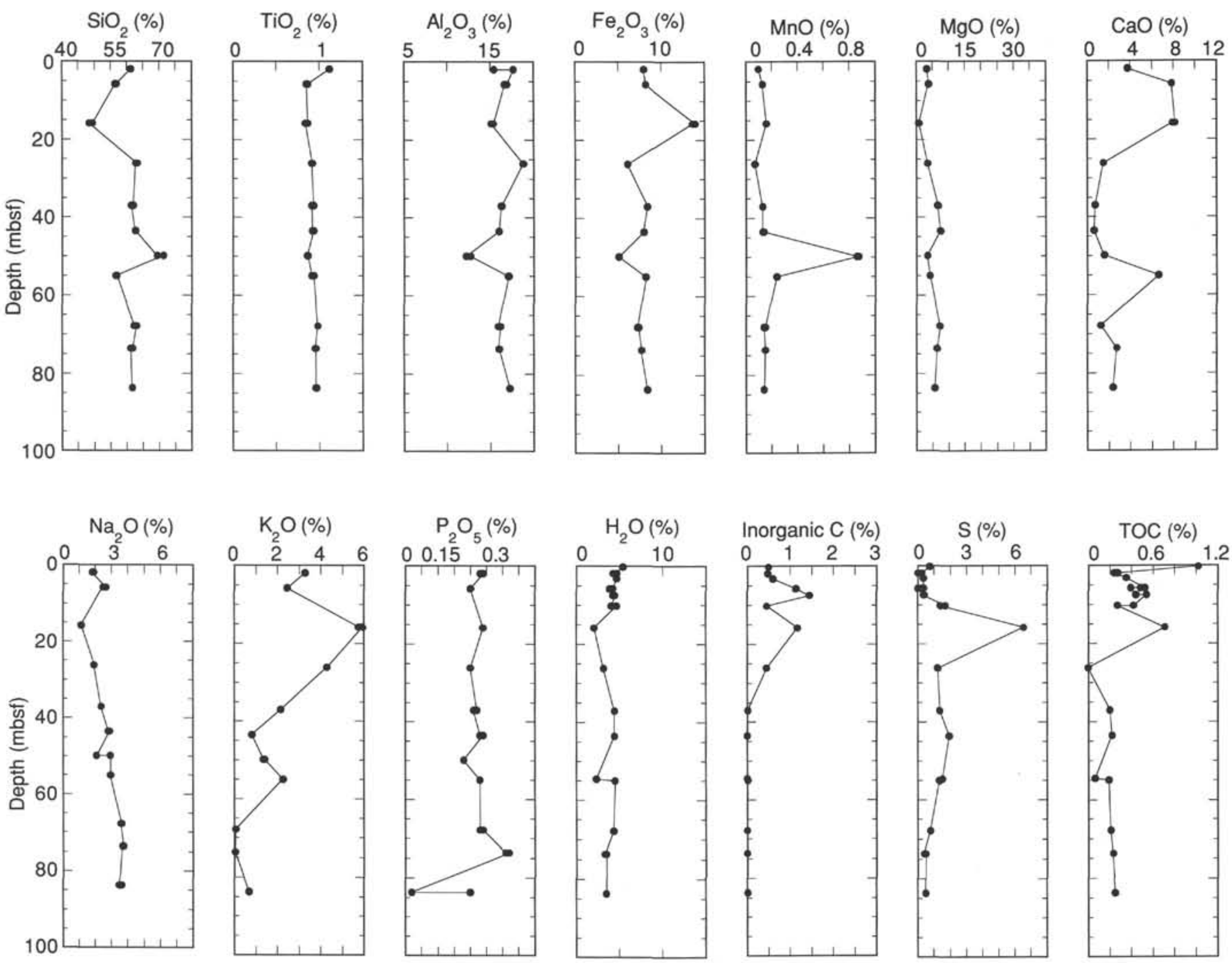

Figure 69. Depth profiles of SiO_2, TiO_2, Al_2O_3, Fe_2O_3, MnO, MgO, CaO, Na_2O, K_2O, P_2O_5, H_2O, inorganic C, S, and organic carbon (TOC) in sediment from Hole 858C. The content of all element oxides and elements is expressed as weight percentage.

the density variations are expressed in the lithology. A distinct minimum in wet-bulk density at 9.4–9.8 mbsf correlates with a soupy layer at the top of Section 139-858D-2H-1. The wet-bulk density increases from the bottom of section 139-858D-1H-6, suggesting that the decreasing wet-bulk density 9–10 mbsf is part of a larger trend.

PWL Compressional Wave Velocity

Measurement of compressional wave velocity with the PWL is hampered on APC cores due to variable coupling between core and liner and the problems associated with the automatic detection of the first break. In the high heat flow areas of Site 858, almost all cores contained variable amounts of gas. Even small amounts of gas in the sediment will attenuate the acoustic signal dramatically. Additional problems arise since the degassing of the sediment leads to severe fracturing of the cores. Thus the data quality of the PWL measurements on cores from Site 858 is generally lower when compared to other sites. However, the compressional wave velocities provide a good indication of the change of physical properties with depth in general. The raw PWL data have been filtered to remove outliers and smoothed with a running average of 50-cm width. The data still look very noisy and will need further processing post-cruise. No PWL measurements are available from Hole 858D.

Compressional wave velocities in Hole 858A (Fig. 81D) reflect the different lithological units. Unit I (0–21.4 mbsf) is characterized by velocities varying from 1460 to 1540 m/s with a small steady increase in the background level from 1470 m/s at seafloor to 1490 m/s at 21.4 mbsf. A sharp jump in compressional wave velocity at 12.7 mbsf from 1450 to 1540 m/s corresponds to a substantial increase in wet-bulk density but core descriptions at this depth do not indicate a major lithologic change. Within Unit IIA (21.4–38.4 mbsf) velocity increases from 1490 to 1530 m/s. As the sediment became more indurated in Unit IIC the measurement of compressional wave velocity with the PWL became more difficult; measurements were finally discontinued at 46.6 mbsf.

In Hole 858B (Fig. 82C) continuous compressional wave velocity data are available only for the uppermost 6.5 m of the hole as for reasons discussed earlier. The highly unconsolidated oxidized metalliferous mud (Unit III, 0–1.98 mbsf) has a high compressional wave velocity of 1530 to 1540 m/s. This value drops to 1480 and 1500 m/s in Unit I, the fine-grained hemipelagic sediment.

The compressional wave velocity in Hole 858C (Fig. 83C) at the mudline of 1460 m/s is comparable to the values in Hole 858A and rises to 1480 m/s at the bottom of Unit I at 14.85 mbsf. The massive carbonate layer (14.5–17.0 mbsf) at the top of Unit IIB, is seen in the compressional wave velocity record as a peak of 1620 m/s at 16.2

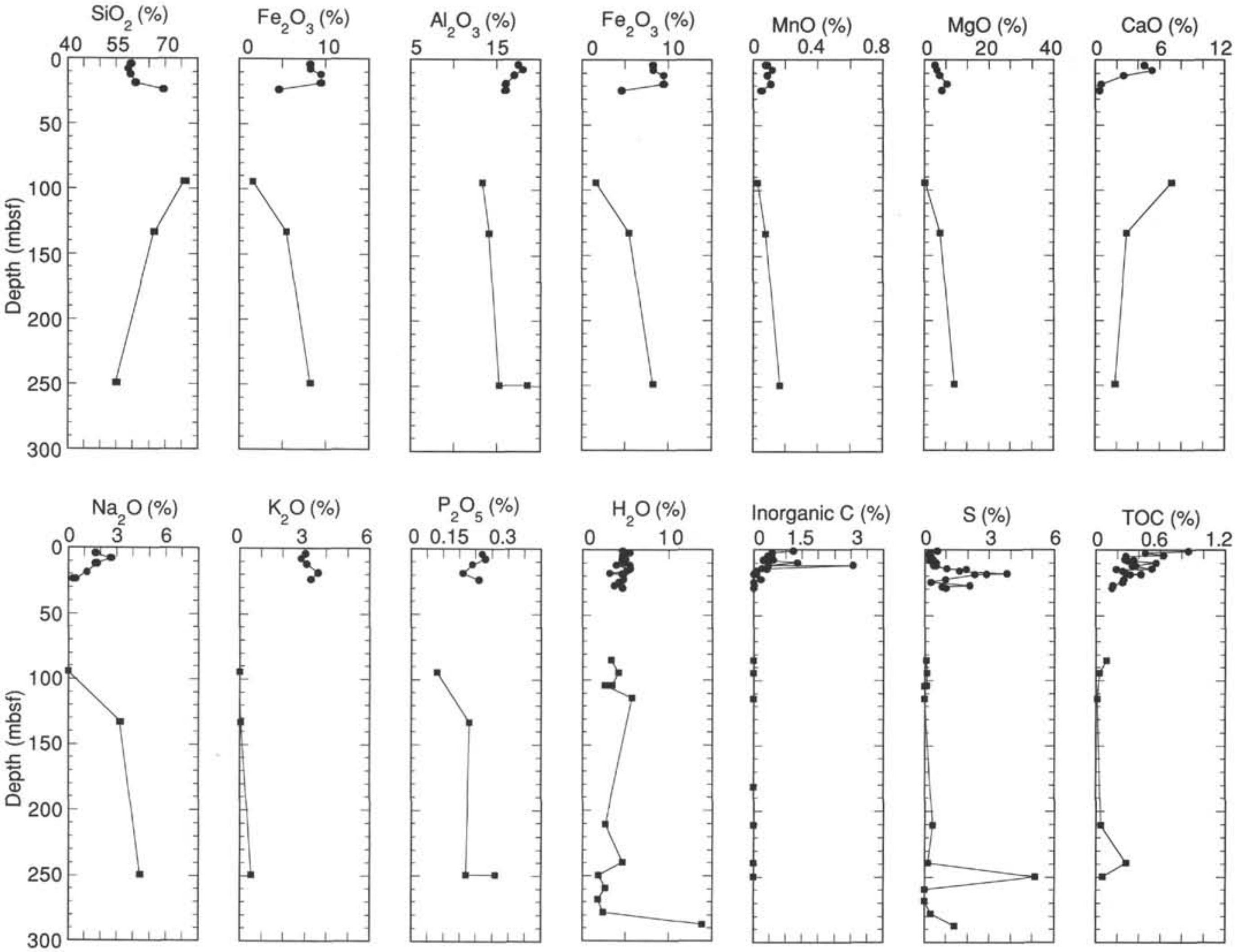

Figure 70. Depth profiles of SiO_2, TiO_2, Al_2O_3, Fe_2O_3, MnO, MgO, CaO, Na_2O, K_2O, P_2O_5, H_2O, inorganic C, S, and total organic carbon (TOC) in sediment from Hole 858D (circles) and 858F (squares). The content of all element oxides and elements is expressed as weight percentage.

mbsf. This correlates with high GRAPE wet-bulk densities at the same depth (Fig. 83B). Below the carbonate cap the compressional wave velocity decreases to 1520 m/s but rises rapidly to 1650 m/s at 37.9 mbsf as the sediment becomes more indurated.

Figure 85 shows a comparison of the compressional wave velocities of Holes 858A, 858B, and 858C. Down to 15 mbsf, the Hole 858A and 858C profiles have similar trends. At this depth, however, the massive carbonates in Hole 858C increase the compressional wave velocity substantially. The jump in the compressional wave velocity seen in Hole 858A at 17.2 mbsf could be related to an increase of carbonates in the sediments not described up to now by the sedimentologists. Below 15 mbsf the compressional wave velocity in Hole 858C is consistently about 90 m/s higher than that in Hole 858A, most likely as a result of the higher temperatures and, therefore, higher degree of indura-tion in Hole 858C. Compressional wave velocity in Hole 858B is everywhere higher than in Holes 858A and 858C, perhaps reflecting the high temperatures at shallow depth.

Index Properties

Index properties data for Site 858 samples are given in Tables 28 through 48 and Figures 86 to 90. No samples were taken from Holes 858E and 858G.

Wet-bulk density in Hole 858A (Fig. 86B) increases from 1.45 g/cm^3 at the seafloor to 2.05 g/cm^3 at 81.85 mbsf. The two high values at 55.23 and 60.64 mbsf are samples taken from the bases of turbidites. Wet-bulk density increases gradually below 82 mbsf, reaching 2.22 g/cm^3 at 265.51 mbsf and 2.31 g/cm^3 at the bottom of the hole. A change in gradient at around 80–100 mbsf coincides with an abrupt reduction in core recovery. Grain densities are in the range of 2.65 to 2.85 g/cm^3 and show a small increase by 0.05 to 0.1 g/cm^3 at 80 mbsf; the average is 2.75 g/cm^3. Porosity and water content follow the trend described above for the wet-bulk density . Porosity decreases rapidly within Unit I from 76.8% to 62.2% at 23.66 mbsf and then decreases slowly to 45% at 81.85 mbsf. Values decrease more gently to 30.4% at 315.34 mbsf.

Hole 858B wet-bulk densities (Fig. 87B) are very similar to those in Hole 858A, increasing from 1.42 g/cm^3 at 2.48 mbsf to 1.72 g/cm^3 at 28.67 mbsf. The grain density is fairly uniform and averages 2.70 g/cm^3. The porosity decrease from 77.6% at 2.48 mbsf to 59.6% at 28.67 mbsf is larger than that in Hole 858A.

Wet-bulk densities in Hole 858C (Fig. 88B) increase within the first 20 mbsf from 1.52 g/cm^3 to 1.97 g/cm^3, then between 1.7 and 2.05 g/cm^3 without a significant depth trend. Average grain density of 2.71 g/cm^3 is identical to that in Hole 858B, given the experimental uncertainty. Porosity decreases with depth from 70% to 40% at 66.91 mbsf, with a

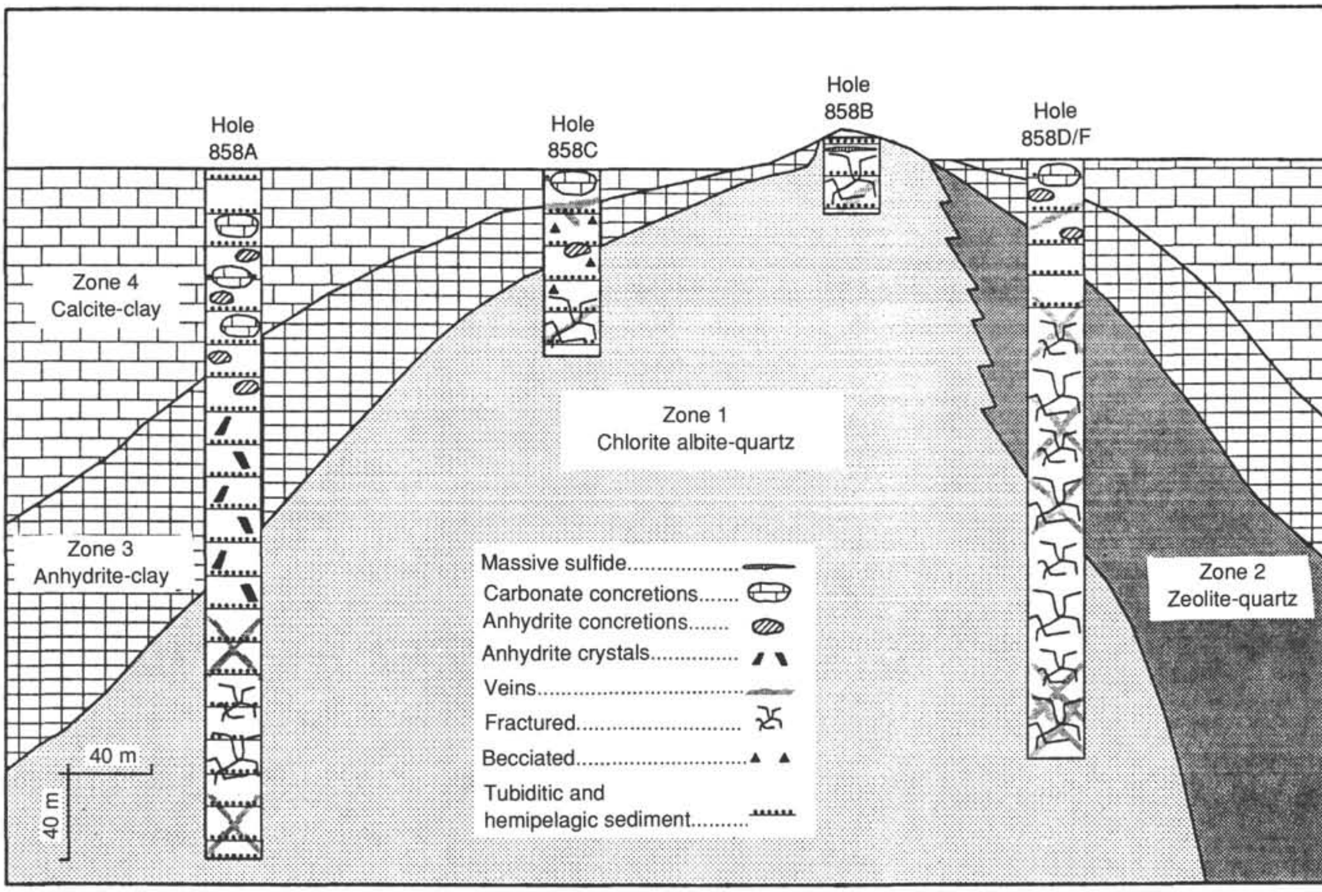

Figure 71. Interpretative cross section of Site 858 showing the distribution of hydrothermal alteration minerals, massive sulfide, breccias, and fractured sediment in Holes 858A, 858B, 858C, 858D, and 858F.

Table 26. Major and trace element compositions of igneous rocks from Hole 858F.

Core, section: Interval (cm):	25R-1 111–113	26R-1 63–65	26R-1 98–100	27R-1 39–41	28R-1 30–32	29R-1 9–11	29R-1 81–83
(wt%)							
SiO_2	50.85	50.44	50.33	51.02	49.97	51.76	50.01
TiO_2	2.04	1.65	1.62	1.65	1.66	1.65	1.66
Al_2O_3	19.12	15.90	16.00	15.85	16.20	15.68	15.86
Fe_2O_3	7.81	9.27	9.89	9.08	9.80	8.78	9.46
MnO	0.21	0.15	0.17	0.16	0.15	0.16	0.16
MgO	11.23	7.51	8.46	7.77	8.09	8.20	8.21
CaO	5.46	12.86	12.13	12.57	12.40	11.45	11.19
Na_2O	3.19	2.09	2.43	2.57	2.45	3.06	3.07
P_2O_5	0.23	0.18	0.18	0.18	0.19	0.18	0.19
Total	100.18	100.07	101.24	101.05	101.12	101.12	99.83
LOI (%)	5.12	2.13	2.08	2.16	2.71	2.2	2.37
(ppm)							
Rb	1	1	1	1	0	0	0
Sr	202	194	194	208	195	212	199
Y	36	31	31	32	31	31	31
Zr	183	159	157	161	160	160	162
NB	6	5	5	5	5	5	5
Ni	100	82	84	82	87	76	80
Cr	463	345	382	373	373	388	356
V	308	272	284	275	287	283	272
Cu	33	101	82	77	82	73	115
Zn	101	49	58	52	60	44	57
Ba	70	36	37	32	42	43	37

minimum of about 50% at 21 mbsf. This porosity low correlates with the base of the zone of frequent carbonate concretions.

In Hole 858D the wet-bulk density increases steadily within Units I and IIA, from 1.44 g/cm^3 at 1.07 mbsf to 1.8 g/cm^3 at 26.3 mbsf (Fig. 89B). The hole terminates in Unit IIC (moderately to well-indurated sediments) characterized by a wet-bulk density of 2.1 g/cm^3. Grain density varies between 2.6 and 2.8 g/cm^3 with an average of 2.69 g/cm^3. Porosity decreases from 77.5% at the seafloor to 56.6% at 26.3 mbsf and is about 37% at 29.5 mbsf at the top of Unit IIC, substantially lower than estimated from a linear extrapolation of the porosity decrease in Unit IIA.

Wet-bulk densities in Hole 858F vary between 2.05 g/cm^3 and 2.45 g/cm^3 in the upper 250 mbsf without showing any distinctive trend (Fig. 90B). Wet-bulk density increases substantially to 2.9 g/cm^3 in igneous rock. Sediment grain density averages 2.75 g/cm^3, whereas that of the igneous rock is, at 2.87 g/cm^3, significantly higher. Porosities in the sediments are very variable (20%–45%) and drop to 5%–10% in the igneous rock.

Figure 91 shows a comparison of the porosity data from Holes 858A, 858B, 858C, and 858D. The porosity data for Hole 858A are fitted with a least-squares third-order polynomial in order to clarify the change of porosity with depth in a "cold" hole. The porosities in Holes 858B and 858D do not differ significantly from the Hole 858A trend. This suggests that the much higher temperatures in Hole 858B or Hole 858D have not significantly reduced the porosity in these sediments.

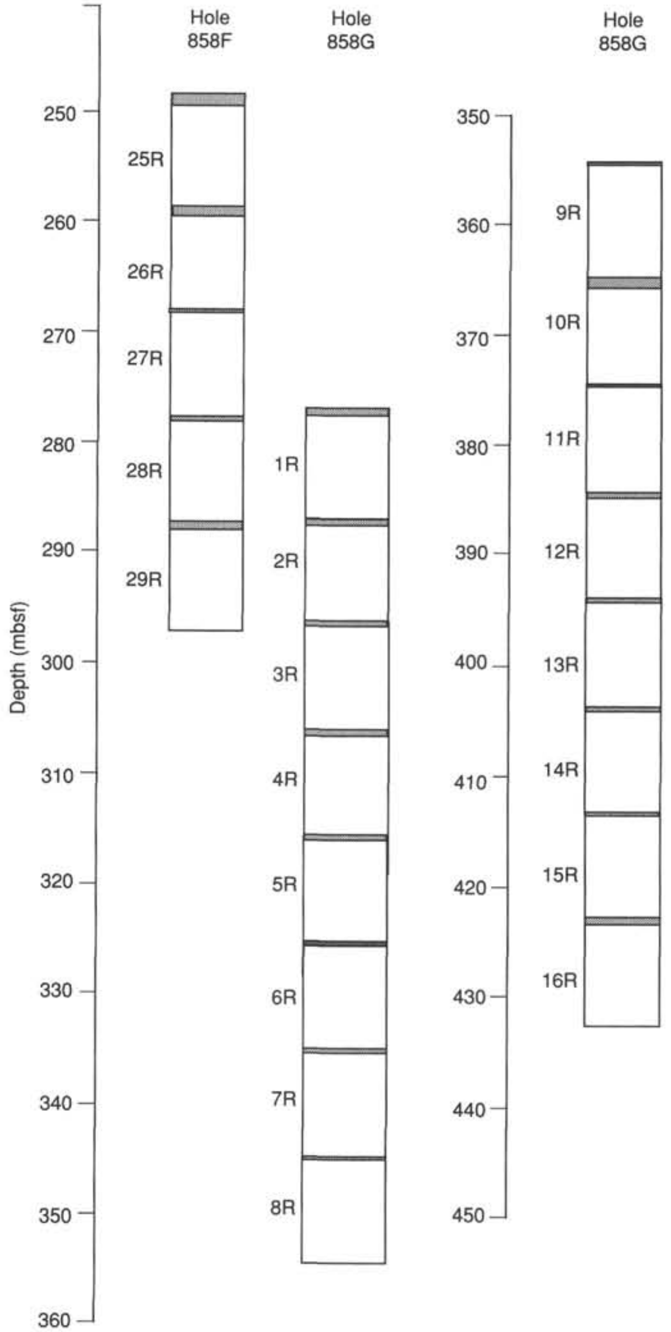

Figure 72. Stratigraphic column of igneous units recovered at Site 858. The columns show the thickness actually cored compared to the recovery of igneous rock. The average recovery for igneous rocks from the two holes at this site was 5%.

Thermal Conductivity

The thermal conductivities of the Holes 858A, 858B, 858C, and 858D are shown in the Figures 86E to 89E. Because of instrument problems, thermal conductivity measurements on samples from Hole 858F are not usable. The thermal conductivity in all holes generally increases with depth in the unconsolidated sediments from 0.9 W/(m·K) at the seafloor to 1.5 W/(m·K) at a depth where the sediment was too consolidated to use a needle probe. No strong correlation with lithology is apparent, except in Hole 858C. There the thermal conductivity increases only slightly from a seafloor value of 0.9 W/(m·K) to 1.12 W/(m·K) at 13.75 mbsf, then jumps to 1.44 W/(m·K) at 15.26 mbsf, at the top of the massive carbonate layer (see "Sediment Geochemistry and Alteration" section, this chapter). Below that horizon the thermal conductivity of semi-indurated sediments varies between 1.5 and 2.0 W/(m·K) up to 44 mbsf but does not significantly increase with depth.

Table 27. Normative mineral compositions of unaltered rocks from Hole 858F.

Core, section: Interval (cm):	26R-1 63–65	26R-1 98–100	27R-1 39–41	28R-1 30–32	29R-1 9–11	29R-1 81–83
Apatite	0.40	0.39	0.42	0.41	0.39	0.42
Ilmenite	3.16	3.07	3.12	3.15	3.13	3.19
Orthoclase	0.12	0.18	0.12	0.12	0.06	0.12
Albite	17.80	20.47	21.57	20.70	25.83	26.21
Anorthite	34.17	32.51	31.90	33.09	28.95	29.71
Corundum	0.00	0.00	0.00	0.00	0.00	0.00
Magnetite	1.23	1.30	1.19	1.29	1.16	1.26
Hematite	0.00	0.00	0.00	0.00	0.00	0.00
Diopside	23.63	21.45	23.57	22.17	21.63	20.49
Hypersthene	18.29	16.07	17.23	14.04	15.64	9.73
Quartz	1.21	0.00	0.00	0.00	0.00	0.00
Forsterite	0.00	2.84	0.56	3.08	2.09	5.56
Fayalite	0.00	1.74	0.33	1.94	1.13	3.31
Total	100.00	100.00	100.00	100.00	100.00	100.00

Table 28. Index properties, Hole 858A.

Core, section, interval (cm)	Depth (mbsf)	Wet-bulk density (g/cm^3)	Grain density (g/cm^3)	Wet porosity (%)	Wet water content (%)	Void ratio
139-858A-						
1H-1, 76–78	0.76	1.45	2.71	76.8	54.4	3.31
1H-2, 32–34	1.82	1.53	2.73	71.2	47.6	2.47
2H-3, 49–52	5.89	1.44	2.66	74.3	52.7	2.89
2H-5, 93–96	9.33	1.61	2.71	69.2	43.9	2.25
3H-3, 85–87	15.52	1.71	2.74	61.7	36.9	1.65
3H-6, 87–90	20.04	1.62	2.70	68.7	43.4	2.19
4H-2, 76–80	23.66	1.73	2.71	62.2	36.9	1.65
4H-4, 46–50	26.36	1.49	2.68	54.2	37.2	1.18
4H-6, 48–50	29.38	1.77	2.76	57.9	33.6	1.38
4H-6, 87–89	29.77	1.80	2.71	56.8	32.3	1.31
5H-3, 98–102	34.88	1.73	2.71	59.9	35.6	1.49
5H-6, 76–80	39.16	1.70	2.72	60.0	36.1	1.50
6H-1, 110–117	41.54	1.70	2.69	61.6	37.1	1.60
6H-3, 88–91	44.28	1.77	2.74	58.3	33.7	1.40
7H-4, 83–86	55.23	2.00	2.66	44.7	23.0	0.81
7H-5, 54–57	56.44	1.77	2.71	59.6	34.5	1.48
8H-2, 31–33	60.64	1.99	2.72	47.3	24.3	0.90
9X-2, 38–40	64.38	1.88	2.75	51.9	28.3	1.08
9X-6, 129–133	71.29	1.77	2.73	59.0	34.2	1.44
11X-CC, 17–21	73.64	1.95	2.75	47.9	25.2	0.92
12X-CC, 5–7	81.85	2.06	2.75	45.0	22.4	0.82
15X-1, 35–37	110.95	2.10	2.81	43.2	21.0	0.76
16X-1, 38–40	120.68	1.90	2.78	51.9	28.0	1.08
17X-1, 24–26	130.14	2.14	2.73	38.6	18.5	0.63
18X-1, 17–19	139.77	2.12	2.73	36.6	17.6	0.58
18X-3, 14–16	142.74	2.09	2.86	52.3	25.6	1.10
19X-1, 28–30	149.58	1.95	2.79	50.2	26.3	1.01
20X-1, 62–64	159.62	2.04	2.81	46.0	23.0	0.85
20X-3, 65–67	162.58	2.16	2.76	40.1	19.0	0.67
21X-1, 21–23	168.81	2.14	2.77	40.2	19.3	0.67
21X-2, 128–130	171.38	2.05	2.79	46.0	23.0	0.85
22X-1, 12–14	178.32	2.06	2.86	52.1	25.9	1.09
23X-1, 113–115	189.03	2.02	2.72	45.9	23.3	0.85
24X-1, 72–74	198.32	2.14	2.83	37.0	17.8	0.59
25X-1, 46–48	207.76	2.15	2.78	42.0	20.0	0.72
30X-1, 36–38	255.96	2.20	2.79	37.5	17.5	0.60
31X-1, 21–23	265.51	2.22	2.83	36.6	16.9	0.58
35X-CC, 5–6	301.45	2.28	2.73	37.4	16.8	0.60
37X-CC, 14–16	315.34	2.31	2.71	30.4	13.5	0.44

Table 29. Compressional wave velocity (HFV), Hole 858A.

Core, section, interval (cm)	Depth (mbsf)	Direction (a, b, c)	HFV velocity (m/s)
139-858A-			
7H-2, 49–51	51.89	c	1557
7H-3, 73–75	53.63	c	1577
7H-4, 59–61	54.99	c	1564
7H-5, 57–59	56.47	c	1683
7H-6, 54–56	57.94	c	1638
8H-3, 13–15	61.91	c	1613
9X-3, 18–20	65.68	c	1834
9X-4, 56–58	67.56	c	1972
9X-5, 117–119	69.67	c	1715
9X-6, 132–134	71.32	c	1746
11X-CC, 19–21	73.66	c	2013
12X-CC, 3–5	81.83	c	2291
12X-CC, 5–7	81.85	a	2196
12X-CC, 5–7	81.85	b	2258
12X-CC, 5–7	81.85	c	2244
15X-1, 30–32	110.90	c	2241
15X-1, 35–37	110.95	a	2063
15X-1, 35–37	110.95	b	2240
15X-1, 35–37	110.95	c	2202
15X-1, 72–74	111.32	c	1972
15X-CC, 8–10	111.66	c	1951
15X-CC, 13–15	111.71	c	1970
16X-1, 11–13	120.41	c	2075
16X-1, 30–32	120.60	c	1985
16X-1, 38–40	120.68	a	1727
16X-1, 38–40	120.68	b	2006
16X-1, 38–40	120.68	c	1980
16X-1, 44–46	120.74	c	2016
17X-1, 24–26	130.14	a	2611
17X-1, 24–26	130.14	b	2817
17X-1, 24–26	130.14	c	2800
17X-1, 24–26	130.14	c	2801
17X-1, 25–27	130.15	c	2688
18X-1, 17–19	139.77	a	2368
18X-1, 17–19	139.77	b	2674
18X-1, 17–19	139.77	c	2730
18X-1, 18–20	139.78	c	2683
18X-1, 34–36	139.94	c	2127
18X-1, 101–103	140.61	c	2766
18X-2, 17–20	141.27	c	2100
18X-2, 87–89	141.97	c	2261
18X-3, 14–16	142.74	a	1789
18X-3, 14–16	142.74	b	2229
18X-3, 14–16	142.74	c	2284
18X-3, 14–16	142.74	c	2242
19X-1, 10–12	149.40	c	2123
19X-1, 28–30	149.58	a	1853
19X-1, 28–30	149.58	b	2155
19X-1, 28–30	149.58	c	2176
19X-1, 31–33	149.61	c	2065
20X-1, 25–27	159.25	c	2277
20X-1, 62–64	159.62	a	1895
20X-1, 62–64	159.62	b	2338
20X-1, 62–64	159.62	c	2363
20X-1, 62–64	159.62	c	2365
20X-1, 125–127	160.25	c	2231
20X-2, 29–31	160.72	c	2271
20X-2, 100–102	161.43	c	2235
20X-2, 123–125	161.66	c	2374
20X-3, 15–17	162.08	c	2488
20X-3, 64–66	162.57	c	2737
20X-3, 65–67	162.58	a	2337
20X-3, 65–67	162.58	b	2640
20X-3, 65–67	162.58	c	2669
20X-3, 130–132	163.23	c	2272
20X-4, 22–24	163.66	c	2267
20X-4, 69–71	164.13	c	2676
20X-4, 75–77	164.19	c	2310
20X-4, 127–129	164.71	c	2200

Table 29 (continued).

Core, section, interval (cm)	Depth (mbsf)	Direction (a, b, c)	HFV velocity (m/s)
21X-1, 20–22	168.80	c	2700
21X-1, 21–23	168.81	a	2605
21X-1, 21–23	168.81	b	2778
21X-1, 21–23	168.81	c	2785
21X-1, 50–52	169.10	c	2169
21X-1, 119–121	169.79	c	2157
21X-1, 128–130	169.88	a	1967
21X-1, 128–130	169.88	b	2287
21X-1, 128–130	169.88	c	2273
21X-2, 59–61	170.69	c	2178
21X-2, 64–66	170.74	c	2271
21X-2, 129–131	171.39	c	2238
21X-3, 20–22	171.61	c	2328
21X-3, 72–74	172.13	c	2262
22X-1, 12–14	178.32	a	1883
22X-1, 12–14	178.32	b	2304
22X-1, 12–14	178.32	c	2190
22X-1, 15–17	178.35	c	2344
23X-1, 111–113	189.01	c	2344
23X-1, 113–115	189.03	a	1751
23X-1, 113–115	189.03	b	2280
23X-1, 113–115	189.03	c	2267
23X-CC, 4–6	189.18	c	2279
24X-1, 11–13	197.71	c	2263
24X-1, 72–74	198.32	a	2085
24X-1, 72–74	198.32	b	2443
24X-1, 72–74	198.32	c	2242
24X-1, 72–74	198.32	c	2384
25X-1, 45–47	207.75	c	2190
25X-1, 46–48	207.76	a	2054
25X-1, 46–48	207.76	b	2317
25X-1, 46–48	207.76	c	2334
25X-1, 62–64	207.92	c	2350
27X-1, 56–58	227.16	c	2481
29X-1, 11–13	246.01	c	2796
29X-1, 42–44	246.32	c	2826
30X-1, 34–36	255.94	c	2724
30X-1, 36–38	255.96	a	2104
30X-1, 36–38	255.96	b	2828
30X-1, 36–38	255.96	c	2671
30X-1, 69–71	256.29	c	2799
31X-1, 19–22	265.49	c	2819
31X-1, 21–23	265.51	a	2035
31X-1, 21–23	265.51	b	2795
31X-1, 21–23	265.51	c	2766
37X-CC, 15–18	315.35	c	2916

A correlation of thermal conductivity with porosity is shown in Figure 92. Using the same assumptions for the correlation as described in the "Site 857" chapter ("Physical Properties" section, "Site 857" chapter) the calculated best-fitting grain thermal conductivity is 3.9 W/ (m·K). This value is even higher than that calculated for Sites 857 and 856.

Compressional Wave Velocity

Compressional wave velocity measurements were made with the DSV in unconsolidated sediments. When the sediments became too lithified for the DSV blades to penetrate, measurements on cubes and on half-core pieces were made with the Hamilton frame velocimeter. All compressional wave velocity measurements made at Site 858 are shown in Figure 86A through 90A. Most of the measurements were made on samples from Hole 858A due to the good recovery. Only the vertical component of the compressional wave velocity vector (abbreviated with compressional wave velocity) will be discussed here unless otherwise noted.

Table 30. Compressional wave velocity (DSV), Hole 858A.

Sample (cm)	Depth (mbsf)	Longitudinal/ transverse (L/T)	DSV velocity (m/s)
139-858A-			
1H-1, 77	0.77	L	1492
1H-1, 77	0.77	T	1529
1H-1, 120	1.20	L	1492
1H-1, 120	1.20	T	1543
1H-2, 13	1.63	L	1497
1H-2, 13	1.63	T	1517
1H-2, 34	1.84	L	1494
1H-2, 34	1.84	T	1543
2H-1, 55	2.95	L	1520
2H-1, 55	2.95	T	1568
2H-1, 110	3.50	L	1492
2H-1, 110	3.50	T	1523
2H-2, 25	4.15	L	1520
2H-2, 25	4.15	T	1446
2H-2, 85	4.75	L	1507
2H-2, 85	4.75	T	1538
2H-3, 98	6.38	L	1497
2H-3, 98	6.38	T	1532
2H-3, 50	5.90	L	1495
2H-3, 50	5.90	T	1538
2H-4, 40	7.30	L	1510
2H-4, 40	7.30	T	1583
2H-4, 100	7.90	L	1505
2H-4, 100	7.90	T	1574
2H-5, 30	8.70	L	1494
2H-5, 30	8.70	T	1543
2H-5, 95	9.35	L	1500
2H-5, 95	9.35	T	1546
2H-6, 50	10.40	L	1515
2H-6, 50	10.40	T	1574
2H-6, 124	11.14	L	1555
2H-6, 124	11.14	T	1564
3H-2, 75	13.92	L	1487
3H-2, 75	13.92	T	1574
3H-3, 85	15.52	L	1515
3H-3, 85	15.52	T	1599
3H-4, 76	16.93	L	1500
3H-4, 76	16.93	T	1589
3H-6, 87	20.04	L	1515
3H-6, 87	20.04	T	1638
3H-7, 36	21.03	L	1531
3H-7, 36	21.03	T	1611
4H-1, 90	22.30	L	1524
4H-1, 90	22.30	T	1618
4H-2, 78	23.68	L	1510
4H-2, 78	23.68	T	1595
4H-3, 80	25.20	L	1531
4H-3, 80	25.20	T	1608
4H-4, 48	26.38	L	1536
4H-4, 48	26.38	T	1618
4H-5, 64	28.04	L	1540
4H-5, 64	28.04	T	1661
4H-6, 90	29.80	L	1557
4H-6, 90	29.80	T	1729
4H-6, 50	29.40	L	1538
4H-6, 50	29.40	T	1611
4H-7, 32	30.72	L	1548
4H-7, 32	30.72	T	1682
5H-1, 67	31.57	L	1580
5H-1, 67	31.57	T	1628
5H-2, 95	33.35	L	1558
5H-2, 95	33.35	T	1644
5H-3, 99	34.89	L	1524
5H-3, 99	34.89	T	1641
5H-4, 60	36.00	L	1543
5H-4, 60	36.00	T	1763
5H-5, 110	38.00	L	1538
5H-5, 110	38.00	T	1628
5H-6, 78	39.18	L	1528
5H-6, 78	39.18	T	1775
5H-7, 36	40.26	L	1583
5H-7, 36	40.26	T	1654
6H-1, 115	41.55	L	1590
6H-1, 115	41.55	T	1618
6H-2, 90	42.80	L	1533
6H-2, 90	42.80	T	1634
6H-3, 90	44.30	L	1576
6H-3, 90	44.30	T	1668
7H-1, 60	50.50	L	1515
7H-1, 60	50.50	T	1586
9X-1, 100	63.50	L	1825
9X-1, 100	63.50	T	1775
9X-1, 5	62.55	L	1624
9X-1, 5	62.55	T	1733
9X-2, 58	64.58	T	1700

Compressional wave velocities at the seafloor are slightly higher than 1500 m/s. In Hole 858A (see also Fig. 93) compressional wave velocity increases steadily to 1600 m/s at 60 mbsf and reaches 2200 m/s at 80 mbsf. Compressional wave velocity remains in the range of 1800 to 2200 m/s with two major maxima of 2600 m/s at 130 and 170 mbsf. These high velocities were measured on fine- to medium-grained sandstone samples that probably originate from the base of thick turbidites. Figure 94 shows the velocity anisotropy measured on cube samples and with the DSV. The anisotropy increases from 1% at the seafloor to about 5% at 15 mbsf. This value does not change noticeably down to 70 mbsf from whereon it increases slowly to 30% at 270 mbsf. Superimposed on this general trend are intervals consisting of claystone with anisotropy values up to 30%. The anisotropies of sandstone samples are generally lower than those of claystone samples.

The compressional wave velocity in Hole 858C (Fig. 88A) increases from 1500 m/s at the seafloor to around 2000 to 2200 m/s at 65 mbsf where it suddenly rises to 2500–3000 m/s in well-indurated claystone. Anisotropy is noticeable but was not calculated due to the limited number of available data. The compressional wave velocity profile in Hole 858D strongly resembles that from 858C with the exception that the high velocities in claystone are already present at a shallow depth of 29.3 mbsf.

Hole 858F penetrated 41 m of highly altered igneous rock, with the latter first appearing at 256 mbsf. Sediment compressional wave velocity in Hole 858F varies between 2000 and 3000 m/s and increases to 5000 m/s in the igneous rock. A detailed discussion of the compressional wave velocity is not warranted due to the very low recovery. Velocity anisotropy is 5% to 10% in the sediments at 50 mbsf. Values just above and below the sediment-basalt contact are highly variable between −7% and +5%.

Discussion

Intuitively, one would expect that the temperature structure and the presence of hydrothermal alteration profoundly effect the sediment porosity structure; that is, sediments that are deposited in high-temperature environments or heated postdepositionally are expected to lose their porosity faster than those at comparatively cooler sites. Figure 95 shows a comparison of the porosities of Holes 855A, 856A, 857A,

Table 31. Thermal conductivity, Hole 858A.

Core, section, interval (cm)	Depth (mbsf)	Full-space/ half-space (F/H)	Thermal conductivity (W/[m·K])
139-858A-			
1H-1, 76	0.76	F	0.99
1H-2, 30	1.80	F	0.98
2H-1, 75	3.15	F	1.00
2H-2, 70	4.60	F	0.97
2H-3, 70	6.10	F	1.03
2H-4, 75	7.65	F	1.01
2H-5, 70	9.10	F	1.08
2H-7, 20	11.60	F	1.14
3H-1, 60	12.50	F	1.04
3H-2, 75	13.92	F	1.04
3H-4, 70	16.87	F	1.07
3H-5, 70	18.37	F	1.10
3H-6, 75	19.92	F	1.30
3H-7, 30	20.97	F	1.20
4H-1, 90	22.30	F	1.20
4H-2, 78	23.68	F	1.19
4H-3, 80	25.20	F	1.20
4H-4, 50	26.40	F	1.14
4H-5, 60	28.00	F	1.19
4H-6, 50	29.40	F	1.18
4H-6, 90	29.80	F	1.42
4H-7, 25	30.65	F	1.40
5H-1, 65	31.55	F	1.22
5H-2, 95	33.35	F	1.14
5H-3, 95	34.85	F	1.25
5H-4, 60	36.00	F	1.53
5H-5, 110	38.00	F	1.20
5H-6, 40	38.80	F	1.18
5H-6, 50	38.90	F	1.26
5H-6, 60	39.00	F	1.38
5H-6, 63	39.03	F	1.18
5H-6, 70	39.10	F	1.19
5H-6, 78	39.18	F	1.15
5H-7, 40	40.30	F	1.08
6H-1, 118	41.58	F	1.28
6H-2, 75	42.65	F	1.26
6H-3, 90	44.30	F	1.35
7H-1, 65	50.55	F	1.27
7H-2, 50	51.90	F	1.07
7H-3, 75	53.65	F	1.21
7H-4, 60	55.00	F	0.94
7H-5, 55	56.45	F	1.33
7H-6, 60	58.00	F	1.47
8H-1, 30	59.20	F	1.84
8H-1, 75	59.65	F	1.25
8H-2, 30	60.63	F	1.56
8H-2, 80	61.13	F	1.17
9X-1, 73	63.23	F	1.06
9X-2, 87	64.87	F	1.18
9X-3, 87	66.37	F	1.11
9X-4, 82	67.82	F	1.79
9X-5, 60	69.10	F	1.68
9X-5, 83	69.33	F	1.21
9X-6, 70	70.70	F	1.68
9X-6, 90	70.90	F	1.19
11X-1, 28	73.18	F	1.36
11X-CC, 28	73.75	F	1.40
12X-CC, 22	82.02	F	1.41
14X-CC, 10	101.10	F	1.20
15X-CC, 23–43	110.83	H	1.54
15X-CC, 1–11	111.59	H	1.73
16X-1, 4–19	120.34	H	1.64
16X-1, 23–37	120.53	H	1.66
16X-1, 36–50	120.66	H	1.56
17X-1, 15–23	130.05	H	2.01
18X-1, 5–28	139.65	H	1.90
18X-1, 30–40	139.90	H	1.80
18X-1, 97–106	140.57	H	2.14

Table 31 (continued).

Core, section, interval (cm)	Depth (mbsf)	Full-space/ half-space (F/H)	Thermal conductivity (W/[m·K])
18X-2, 9–20	141.19	H	1.72
18X-2, 74–91	141.84	H	2.01
18X-2, 129–144	142.39	H	1.78
19X-1, 8–17	149.38	H	1.76
19X-1, 27–45	149.57	H	1.63
20X-1, 20–29	159.20	H	1.69
20X-1, 59–66	159.59	H	1.73
20X-1, 122–131	160.22	H	1.70
20X-2, 19–34	160.62	H	1.63
20X-2, 90–115	161.33	H	1.66
20X-2, 115–127	161.58	H	1.86
20X-3, 12–22	162.05	H	1.91
20X-3, 59–70	162.52	H	1.99
20X-3, 124–135	163.17	H	1.82
20X-4, 15–26	163.59	H	1.79
20X-4, 69–71	164.13	H	1.75
20X-4, 75–77	164.19	H	1.93
20X-4, 125–133	164.68	H	1.55
21X-1, 17–38	168.77	H	2.22
21X-1, 39–57	168.99	H	1.74
21X-1, 117–129	169.77	H	1.60
21X-2, 59–61	170.69	H	1.65
21X-2, 64–66	170.74	H	1.83
21X-2, 114–116	171.24	H	1.89
21X-2, 129–131	171.39	H	2.00
21X-3, 7–23	171.48	H	1.96
21X-3, 67–80	172.08	H	1.73
23X-CC, 1–8	189.15	H	1.59
24X-1, 10–22	197.70	H	1.73
25X-1, 40–54	207.70	H	1.61
25X-1, 61–68	207.91	H	1.86
27X-1, 55–60	227.15	H	1.93
29X-1, 1–15	245.91	H	1.99
30X-1, 33–41	255.93	H	1.71
30X-1, 80–88	256.40	H	1.91
31X-1, 18–25	265.48	H	1.90
37X-CC, 1–7	315.21	H	2.21
37X-CC, 12–19	315.32	H	2.58

and 858A for the top 100 m of the holes. Despite the fact that Hole 858A has the lowest heat flow of the suite of holes at Site 858, it was chosen for this comparison because its porosity structure is representative for this site (see Fig. 91). In Figure 95 the porosities of Hole 858A have been fitted with a third-order polynomial curve to clarify the porosity profile. The comparison of porosities from other holes to this curve is complicated by the bimodal distribution due to the sampling of low-porosity sandy turbidites and high-porosity clay, especially in Hole 856A. After comparing the upper bounds of the porosity profiles, it is apparent that only the porosities from Hole 855A stand out as being distinctly higher. Of the holes shown in this comparison, Hole 856A has most likely experienced the highest temperatures in the past and shows the largest degree of alteration; even there a major reduction of its pore space is not indicated. The other holes show similar behavior. Careful editing of the data sets in order to compare porosities measured on comparable lithologies may reveal more about the influence of alteration and temperature on porosity reduction. However, compaction is obviously the dominant mechanism by which the pore space is reduced.

DOWNHOLE LOGGING

Logging at Site 858 was carried out in several stages. Open-hole temperatures were logged in Holes 858A, 858B, and 858F, and two

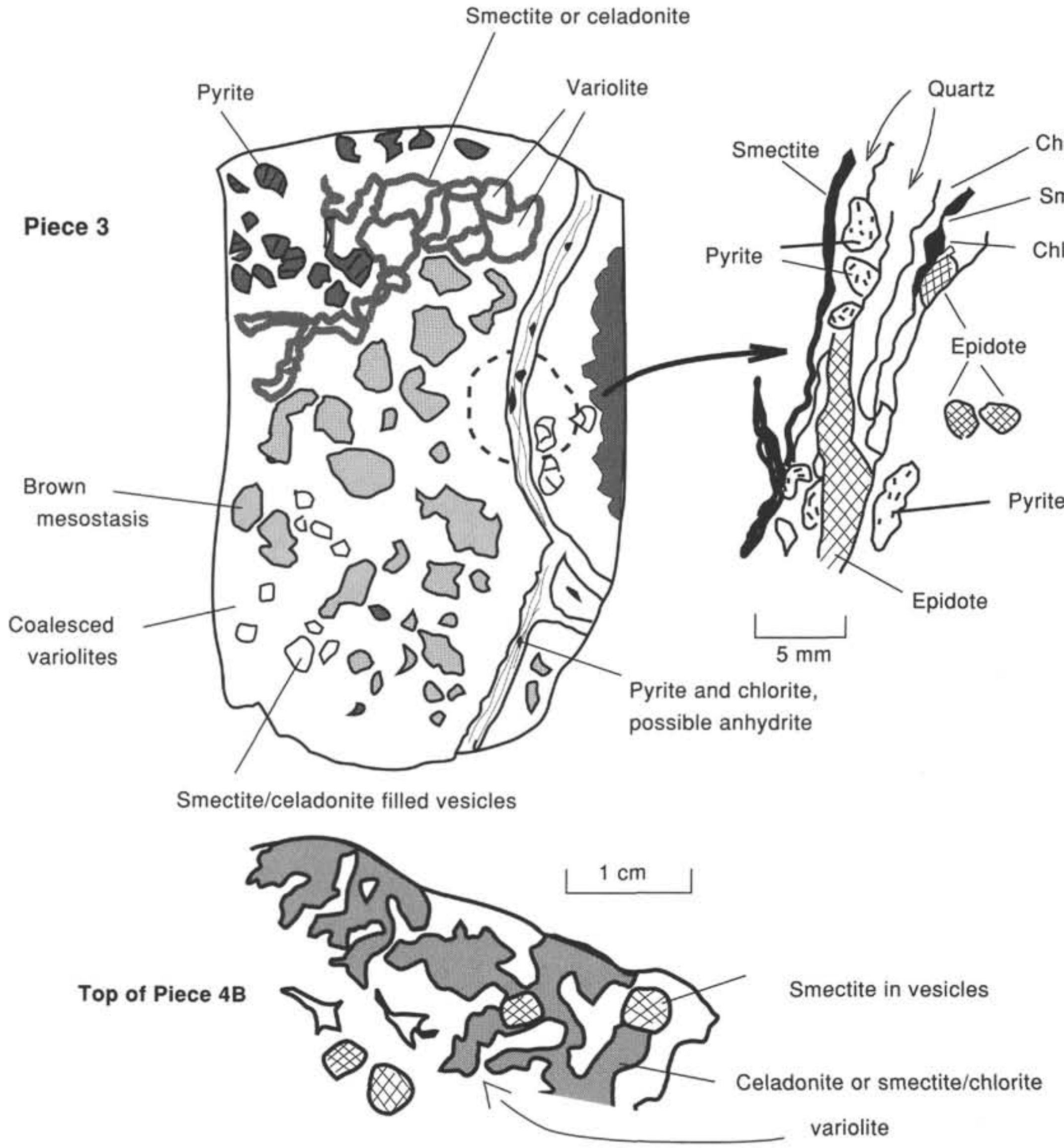

Figure 73. Sketch of Sample 139-858F-25R-1, Pieces 3 and 4B, illustrating the well-developed variolitic texture and cross-cutting sulfide-bearing veins.

Schlumberger logging runs were made in Hole 858F between 12 August and 20 August. The Schlumberger runs included the seismic stratigraphy string and the formation microscanner string (Table 49). The logs obtained in Hole 858F are generally of good to excellent quality, and appear at the end of this chapter.

The next stage in the logging program began 3 September when the *JOIDES Resolution* returned to the reentry hole at Site 858, Hole 858G. A temperature run was made in the casing in the reentry hole which was still cemented at its lower end and had been left undisturbed for 11 days. After the hole was deepened to 432 mbsf we made two additional temperature runs and logged with a combination of the dual induction, lithodensity, and spectral natural gamma tools.

Temperature Measurements

We made seven deployments of temperature logging tools at four holes at Site 858 (see Table 49). Hole 858A is located about 100 m west of the vent area. Sediment temperature measurements using the APC tool and WSTP yielded a heat flow of 1.9 W/m^2 ("Heat Flow" section, this chapter). The gradient of the open-hole temperature profile between 60 and 264 mbsf, measured with the GRC high-temperature tool (Fig. 96), is everywhere much lower than would be predicted by a heat flow of 1.9 W/m^2, probably because the hole was still strongly affected by the circulation of cold water during drilling.

Hole 858B was drilled about 10–20 m away from an active vent. We measured temperatures at 37 mbsf in loose debris at the bottom of the 42 m deep hole. The temperature rose rapidly to 150°C after penetration of the probe into the fill (Fig. 97). This measurement was made primarily to see if high temperature water was flowing up this hole where a seafloor gradient of about 10°C/m was measured in the upper 20 m of the section with the WSTP ("Heat Flow" section, this chapter). Although the observed temperature (150°C) is very high, it is considerably less than that suggested by the high temperature gradient in the upper 20 m (above 350°C at 37 m) and less than that observed at the nearby vent (275°C). Thus, this result indicated that water was not flowing from the formation into Hole 858B.

Figure 74. Photomicrograph illustrating quench texture of groundmass plagioclase characteristic of the basalt from this site. Sample 139-858F-25R-1, Piece 1, 85–87 cm, transmitted polarized light, ×5.

Hole 858F is one of three closely spaced holes that were drilled on the vent field just north of an active area (858D, 858F, and 858G). The GRC high temperature tool was accidentally "deployed" for a 19-hr temperature measurement at the bottom of Hole 858F (Fig. 98A; see "Operations" section, this chapter). The connection between the instrument and the cable broke just after the tool was put into the pipe and it fell from the top of the pipe to the bottom of the hole. The tool was retrieved by fishing and it was still operating normally when the pressure vessel was opened. An extrapolation of the temperature history using the relation for cooling of a drill hole at long times after circulation (Lachenbruch and Brewer, 1959) leads to an estimated equilibrium temperature of 250° to 260°C (Fig. 98B). This temperature is comparable to that of water flowing from the nearby vents.

In the interval between the time that the GRC high-temperature tool fell to the bottom and was retrieved, we logged temperatures in Hole 858F with the JAPEX wireline high-temperature tool. The resulting profile is shown in Figure 99. The temperatures and gradients that we measured are much lower than the equilibrium conductive curve inferred from the nearly sediment temperature measurements. Hole 858F was in the early phases of recovery from the circulation which stopped about 14 hr before logging. Curiously, the temperature measured when the JAPEX tool was at the bottom of the hole was 65°C colder than that recorded by the GRC tool, which at that time was buried in the fill a meter or so below. This may have resulted because the fill in the bottom of the hole equilibrated more rapidly with the surrounding rock than water in the open hole, or if there was drawdown of seawater to the level of the deepest measurement made with the JAPEX temperature tool. Similar results were obtained from borehole temperature measurements in Hole 857C ("Downhole Logging" section, "Site 857" chapter).

Three temperature profiles were measured in Hole 858G with the GRC high-temperature tool. The first was made when we returned to reenter Hole 858G, which had been equilibrating for 11 days, but before the cement shoe at the base of the casing was drilled. The drill bit was lowered 10 m into the top of the casing without circulation so as not to disturb the thermal regime of the cased hole, and the GRC tool was run through the bit to a depth of 160 mbsf. Although the casing had been set to 276 mbsf the tool was stopped by an obstruction at 160 mbsf (probably a cement ledge) and could not be lowered to the bottom.

The temperatures at the top of the casing were very high; the maximum temperature was 268°C at only 25 m below the seafloor (Fig. 100). There was a zone of much colder water (minimum value of 100°C) at 55 to 75 mbsf. Temperatures below 55 mbsf increased rapidly with depth to 250°C at 150 mbsf.

The temperature measurements in Holes 858F and 858G suggest that the undisturbed formation temperatures deep in the drilled section may not reach temperatures higher than 300°C. For this to be true the gradients of 10°C/m observed at shallow depths in Holes 858B, 858D, and 858G cannot continue much below 25 to 30 m; the temperature gradient must decrease greatly as illustrated in Figure 100. Such a large decrease in gradient requires that the heat transfer at depths below 25 m be strongly dominated by vigorous mixing of fluids beneath the vents of the field.

Ideas about how the temperature minimum observed in the casing at Hole 858G was produced are speculative. The possibility we think

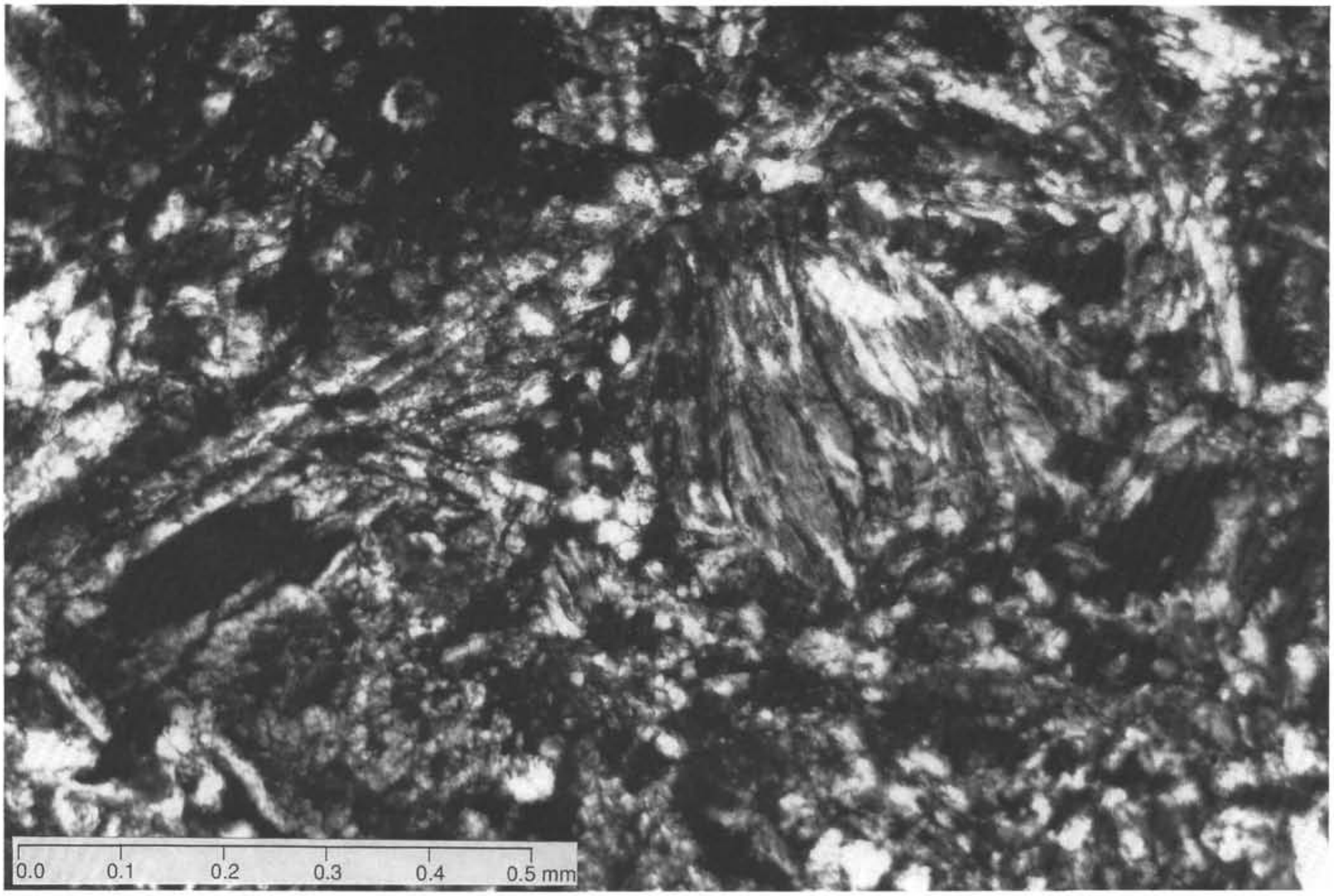

Figure 75. Photomicrograph of highly pleochroic Fe-rich chlorite replacing a mafic phenocryst. Morphology and frequent association with Cr-rich spinel suggests that original minerals is olivine. Sample 139-858F-29R-1, Piece 14, 84–85 cm. Transmitted polarized light, ×10.

most likely is that cold water flowed down nearby Hole 858F, and spread out laterally along a permeable zone at 50–60 mbsf. If this cold flow is a naturally occurring feature of the hydrogeologic regime, it would imply that a tongue of cold water sinks around the perimeter of the vent field and flows back below the plume of high-temperature water that feeds the vents. Given the central position of this hole in the vent field, the latter explanation is unlikely. Initial observations made after Hole 858 was sealed confirm that cold seawater is flowing down Hole 858F (Davis et al., this volume).

The second run in Hole 858G (6 September) was made after the hole had been deepened to 432 mbsf. The third and last profile was measured after completion of the first set of packer tests (see "Special Downhole Experiments" section, this chapter). This 7 September profile shows that opening the hole into basement initiated a flow of cold water down the hole. The gradient to a depth of 330 mbsf is only 0.15°C/m, compared to over 10°C/m measured before drilling out the casing. Flowmeter tests confirmed the downward flow of water in the hole and showed that it enters the formation at about 320 mbsf, which is the same level as the break in gradient in the 7 September profile (Fig. 100; see "Special Downhole Experiments" section, this chapter).

Results of Schlumberger Logs

A summary plot of the parameters measured by the Schlumberger logging programs in Holes 858F and 858G are shown in Figures 101 and 102.

Formation Microscanner

The formation microscanner provided nearly continuous and clear images of the walls of Hole 858F. Two passes were made with the string, but on the second pass the pads ran in nearly the same tracks as the first. Consequently, the results are largely redundant. The microscanner image provides a complete stratigraphic record of layers that are thicker than about 5 mm in the sedimentary section above the basalt units in Hole 858F. A brief summary of the features seen in the images processed on board is presented below. The processed FMS images can be found in back-pocket microfiche at the end of this volume.

The FMS image from 60 to 112 mbsf has a medium dark background indicating low electrical resistivity typical of high porosity clays. There are numerous rhythmically distributed lighter gray, higher resistivity bands (.5 to 5 cm thick) that are believed to be layers of turbiditic silt and sand. These layers often appear as closely spaced sets of 2 or 3 bands; each set may have been produced by a single depositional event.

The zone from 112 to 214 mbsf is characterized by thin higher resistivity layers as in the zone above, but also includes several thick layers of higher resistivity material (2 to 5 m) that are probably composed of thick turbidite sand. These thick silt and sand layers produce the prominent peaks seen in the resistivity logs in this hole and in Hole 857C. A few large, open vertical fractures are discernible in the microscanner image in the lower part of this zone, which may have been produced by thermal stresses induced by drilling.

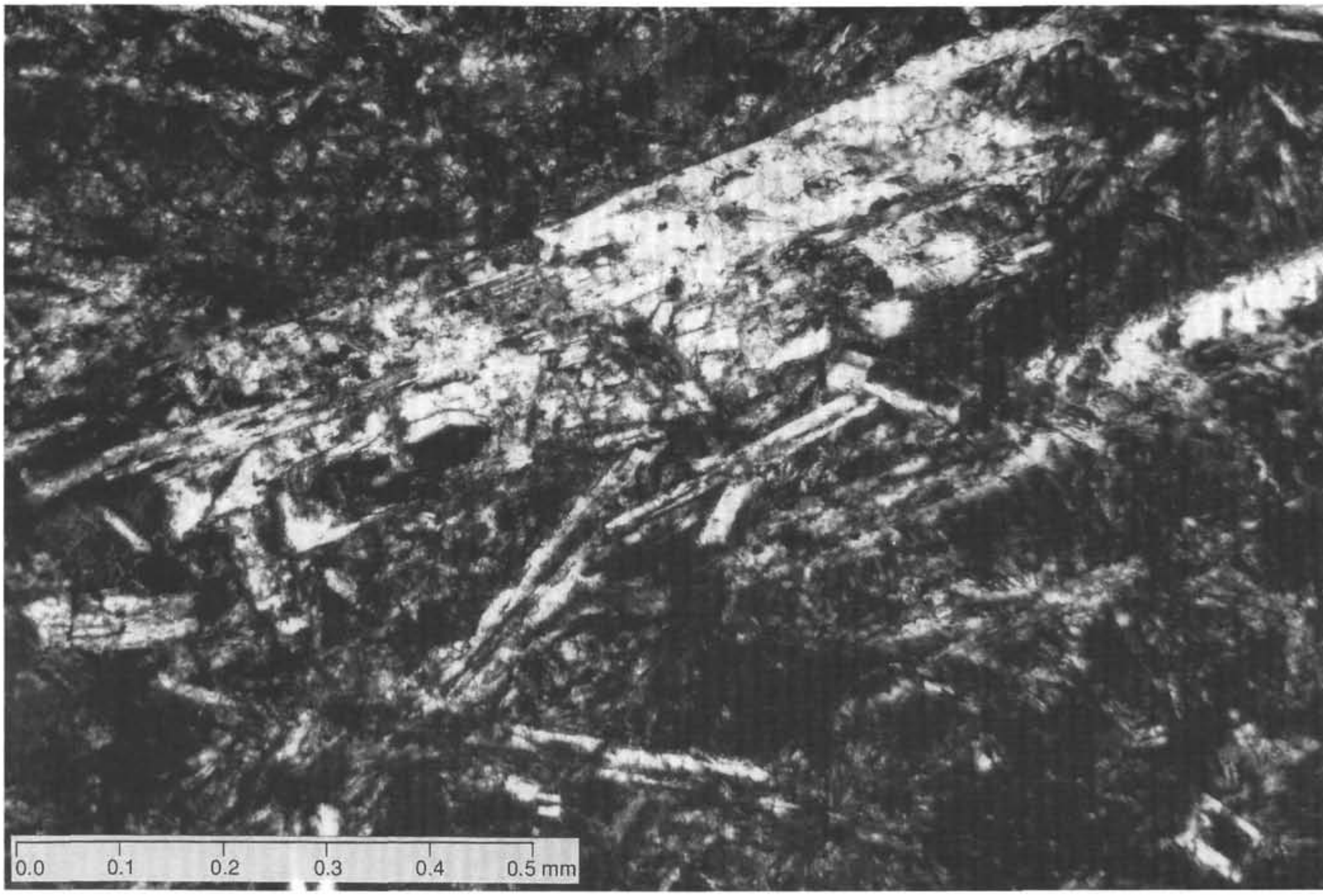

Figure 76. Photomicrograph of replacement of a plagioclase phenocrysts by albite, chlorite, and prehnite. Note mottled extinction. Sample 139-858F-29R-1, Piece 5, 30–32 cm. Transmitted polarized light, ×10.

The zone from 214 to 257 mbsf produced an image that is generally lighter gray with numerous thin, horizontal bands; however, the contrast between the thin bands of higher resistivity material (turbidites) and background lower resistivity material (clay layers) is much less than in the upper 214 m of the section.

The zone from 256.4 mbsf to the bottom of the logged interval at 264.2 mbsf is mainly basalt. Because of its relatively high resistivity the microscanner image of the solid basalt is lighter gray. Interfaces between blocks and pillows are seen as darker lines (Fig. 103). The microscanner imaged two basaltic units separated by a 0.6- to 0.7-m band of low resistivity material that may be sediment. The volcanic units are made up of blocks with irregular and rounded margins similar to basalt pillows. Most of the individual blocks have a network of fine fractures and wide vertical fractures that probably were produced by thermal stresses that resulted from the cold circulating water in contact with the high-temperature wall rock (see also "Downhole Logging" section, "Site 857" chapter).

Resistivity

Results from the dual induction resistivity log, together with the caliper measurements from the formation microscanner log, are shown in Figure 101. The resistivity profile in Hole 858F is very similar to that recorded in Hole 857C. The two profiles are compared in Figure 104. The profiles shown in the figure have been matched by eye and centered on a thick high-resistivity peak at 115 mbsf in Hole 858F and 165 mbsf in Hole 857C. The correlation between the profiles is good only within the zones 100–210 mbsf in Hole 858F and 155–275 mbsf in Hole 857C. Above and below these zones the profiles are poorly correlated.

Correlation of the two profiles provides a record of the different depositional histories of the two sites. During the time interval represented by the zones that are correlatable, both sites were receiving sediments via frequent turbidity flows at about the same rate. This suggests that the seafloor at both sites was at about the same elevation during this interval. The section in Hole 858F is slightly compressed compared to that in Hole 857C, indicating a slightly lower sedimentation rate (slightly higher elevation?) or anomalous consolidation in the vent area.

The resistivity log in Hole 858F between 210 mbsf and basement at 259 mbsf shows little variation, whereas the same section at Hole 857C shows large-amplitude variations of short spatial wavelength, which are probably associated with thin interbedded turbidites that are absent in this interval in Hole 858F. This suggests that basement at Site 858 was a topographic high during that interval of time represented by the sedimentary section between 210 and 259 mbsf, so that it was receiving mainly fine-grained hemipelagic deposits, whereas the seafloor at Site 857 was at a lower elevation and received turbidites at a high rate. Shore-based studies should confirm these tentative interpretations.

The sedimentary section above the correlatable sequence at Site 857 is 50 m thicker than at Site 858, indicating a significantly higher rate

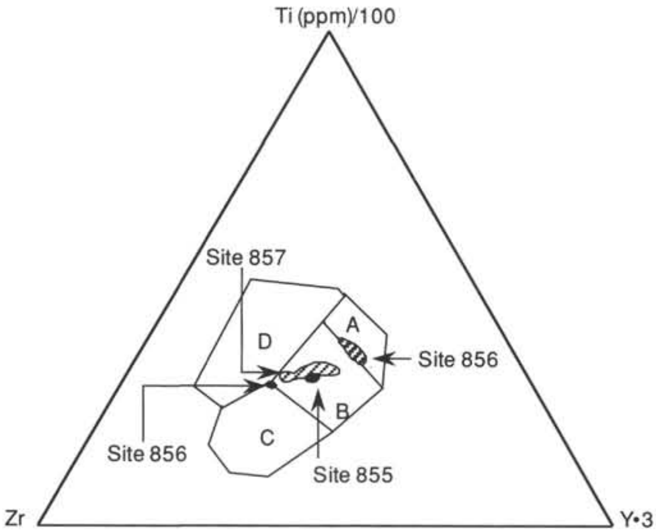

Figure 77. Plot of Ti-Y-Zr, showing major fields for basaltic rocks (after Pearce and Cann, 1973).

of sedimentation at Site 857 in recent times. This could have been the result of an increase in elevation of Site 858 relative to Site 857 at the time corresponding to the loss of correlation (100 mbsf at Site 858 and 150 mbsf at Site 857). The tilting of the block into which Sites 858 and 857 were drilled may have occurred at this time.

The results from the resistivity, density, and natural gamma logs in the deepened part of Hole 858G are shown in Figure 102. They show several resistivity and density values that are relatively high, and low natural gamma-ray intensity over most of the interval. This indicates that most of the drilled section is composed of basalt. There are two sections near the bottom of the logged interval at 318–326 mbsf and 334–338 mbsf where the density and resistivity values are lower and gamma-ray counts are higher. Water flow into the formation is inferred to have occurred at roughly this depth (see Fig. 100; "Special Downhole Experiments" section, this chapter).

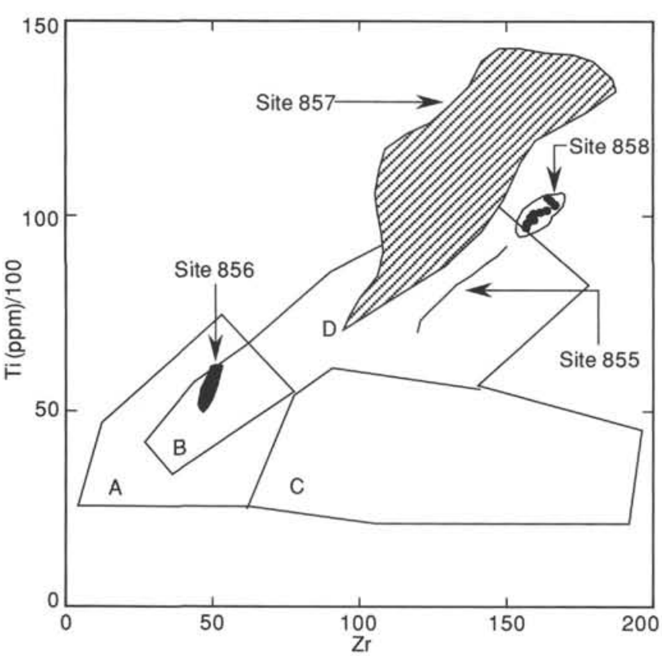

Figure 78. Plot of Ti vs. Zr. Fields from Pearce and Cann (1973).

Table 32. Electrical resistivity, Hole 858A.

Sample (cm)	Depth (mbsf)	Electrical resistivity, seawater readings	Electrical resistivity, sample readings	Formation factor
139-858A-				
1H-1, 100	1.00	0.019	0.030	1.60
1H-2, 30	1.80	0.020	0.030	1.50
2H-1, 100	3.40	0.018	0.029	1.59
2H-2, 75	4.65	0.018	0.023	1.29
2H-3, 80	6.20	0.017	0.028	1.65
2H-4, 110	8.00	0.017	0.028	1.70
2H-5, 110	9.50	0.018	0.029	1.66
2H-6, 58	10.48	0.017	0.034	2.00
3H-1, 66	12.33	0.017	0.046	2.74
3H-2, 75	13.92	0.017	0.032	1.94
3H-3, 85	15.52	0.018	0.035	1.96
3H-4, 76	16.93	0.018	0.033	1.79
3H-5, 78	18.45	0.017	0.039	2.24
3H-6, 87	20.04	0.018	0.033	1.85
3H-7, 36	21.03	0.022	0.041	1.83
4H-1, 90	22.30	0.019	0.047	2.42
4H-2, 78	23.68	0.018	0.042	2.27
4H-3, 80	25.20	0.016	0.045	2.74
4H-4, 48	26.38	0.020	0.049	2.51
4H-5, 64	28.04	0.020	0.050	2.56
4H-6, 50	29.40	0.019	0.050	2.56
4H-6, 90	29.80	0.021	0.052	2.42
4H-7, 32	30.72	0.021	0.046	2.17
5H-1, 67	31.57	0.018	0.045	2.42
5H-2, 95	33.35	0.018	0.045	2.54
5H-3, 99	34.89	0.017	0.085	4.86
5H-4, 43	35.83	0.018	0.057	3.26
5H-5, 110	38.00	0.017	0.049	2.85
5H-6, 78	39.18	0.017	0.042	2.44
5H-7, 36	40.26	0.017	0.046	2.66
6H-1, 115	41.55	0.017	0.043	2.50
6H-2, 90	42.80	0.017	0.049	2.85
6H-3, 90	44.30	0.018	0.053	3.00
7H-1, 60	50.50	0.017	0.044	2.62
7H-2, 50	51.90	0.018	0.068	3.76
7H-3, 74	53.64	0.019	0.048	2.49
7H-4, 60	55.00	0.020	0.052	2.65
7H-5, 58	56.48	0.029	0.059	2.05
7H-6, 55	57.95	0.020	0.069	3.38
8H-1, 30	59.13	0.018	0.090	5.00
8H-2, 30	60.63	0.021	0.079	3.77
8H-3, 35	62.18	0.029	0.057	1.95
9X-1, 75	63.25	0.024	0.075	3.13
9X-2, 50	64.50	0.023	0.075	3.26
11X-CC, 30	70.70	0.022	0.054	2.45

Other Logs

The sonic log was run in Hole 858F but the results are poor because of excessive noise in the hole. The spontaneous potential profiles vary greatly between passes in the same hole, indicating that fluctuations in the ship's potential produced much of the variation we recorded.

HEAT FLOW

Site 858 encompasses an area of extremely high and locally variable heat flow, ranging from background values of about 1 W/m^2 to as much as 10–20 W/m^2 in the vicinity of active hydrothermal vents (Davis and Villinger, this volume). An intensive program of *in-situ* sediment temperature measurements was planned in each of the five holes cored before finalizing the location for the reentry hole at this site. This program was quite successful, but was limited in Holes 858B and 858D by the extreme temperatures encountered downhole, which quickly exceeded the operating ranges of the tools. In addition, logs of borehole temperatures were made in Holes 858F and 858G; these results are discussed in the "Downhole Logging" section (this chapter).

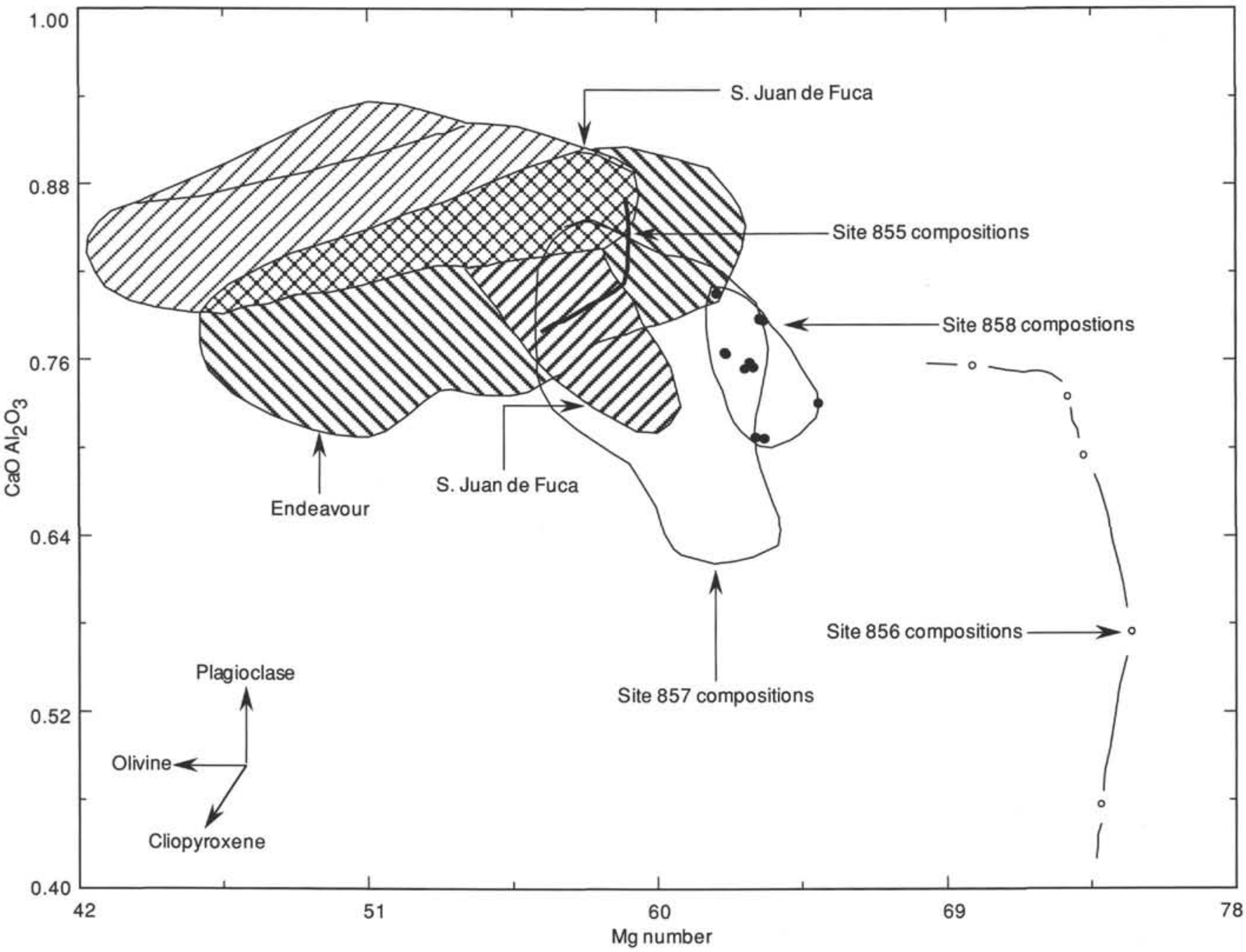

Figure 79. Plot of CaO/Al_2O_3 vs. Mg number. Fields taken from Karsten et al. (1990).

Table 33. Index properties, Hole 858B.

Core, section, interval (cm)	Depth (mbsf)	Wet-bulk density (g/cm^3)	Grain density (g/cm^3)	Wet porosity (%)	Wet water content (%)	Void ratio
139-858B-						
1H-2, 98–102	2.48	1.42	2.70	77.6	55.8	3.46
1H-3, 74–77	3.74	1.45	2.69	75.5	53.3	3.08
1H-4, 79–82	5.29	1.58	2.76	70.9	46.0	2.44
1H-5, 58–61	6.58	1.55	2.70	73.8	48.8	2.81
2H-1, 73–76	7.93	1.63	2.72	67.9	42.7	2.11
2H-2, 121–124	9.91	1.54	2.71	72.3	48.1	2.61
2H-5, 16–18	13.36	1.50	2.72	53.2	36.4	1.14
2H-6, 75–77	15.45	1.66	2.70	65.1	40.1	1.87
5H-1, 117–121	25.07	1.60	2.67	69.5	44.4	2.28
5H-3, 118–121	28.08	1.69	2.67	62.7	38.0	1.68
5H-4, 27–31	28.67	1.72	2.65	59.6	35.5	1.48

Table 34. Compressional wave velocity (DSV), Hole 858B.

Sample (cm)	Depth (mbsf)	Longitudinal/ transverse (L/T)	DSV velocity (m/s)
139-858B-			
1H-1, 74	0.74	L	1550
1H-1, 74	0.74	T	1654
1H-1, 130	1.30	L	1528
1H-1, 130	1.30	T	1675
1H-2, 51	2.01	L	1528
1H-2, 51	2.01	T	1631
1H-2, 100	2.50	L	1525
1H-2, 100	2.50	T	1624
1H-3, 75	3.75	L	1528
1H-3, 75	3.75	T	1665
1H-4, 10	4.60	L	1528
1H-4, 10	4.60	T	1634
1H-4, 80	5.30	L	1531
1H-4, 80	5.30	T	1634
1H-5, 26	6.26	L	1543
1H-5, 26	6.26	T	1634
1H-5, 60	6.60	L	1560
1H-5, 60	6.60	T	1654

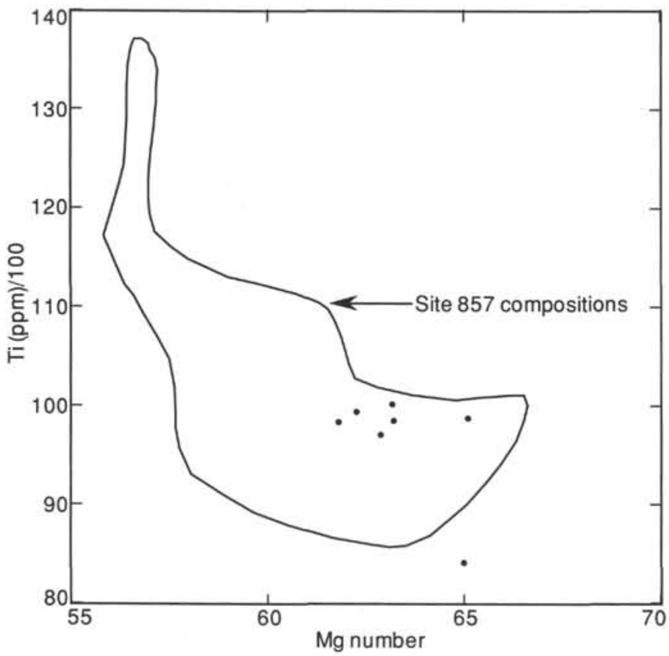

Figure 80. Plot of Ti vs. Mg number. Note that the samples from Site 858 lie in a similar area to the bulk of the samples from Site 857.

Table 50 summarizes the results of the 18 measurements of sediment temperatures in Holes 858A through 858E. These measurements included 10 deployments of the APC temperature tool and eight deployments of the WSTP, and were highlighted by the highest sediment temperatures ever measured *in situ* during the DSDP or ODP.

The temperature records for the 18 tool deployments at Site 858 are shown in Figures 105 through 107. Hole 858A was cored farthest from the high heat flow anomaly, and the less extreme gradient there allowed nine successful tool deployments. Hole 858C was cored closer to the peak of the heat flow anomaly, and five successful measurements were made before temperatures exceeded the operating ranges of the tools.

Holes 858B, 858D, and 858E were located in the heart of the high heat flow anomaly, and the extreme gradients meant that the tool operating ranges were exceeded at depths of only about 20 mbsf. As a result of the extreme temperatures and the poor mechanical strength of such shallow sediments, only one of the five measurements attempted at these three holes was completely successful (Table 50).

To estimate *in-situ* temperatures, the APC temperature data were fit to the theoretical decay function of Horai and Von Herzen (1985), and the WSTP temperatures were fit to the theoretical decay function of Bullard (1954), using procedures described in the "*In-situ* Temperatures" section, "Explanatory Notes" chapter (this volume). Figures 108 through 111 demonstrate that the data for the 14 successful measurements closely fit the theoretical curves using an average thermal conductivity value of 1.2 W/(m·K) ("Physical Properties" section, this chapter). In particular, the single station taken with the WSTP at 19.5 mbsf in Hole 858B shows a remarkably good fit to the theoretical decay function (Fig. 109A), validating the accuracy of the extremely high temperature of 196.6°C measured there. The disturbed measurements in Holes 858D and 858E suggest similarly high temperatures at such shallow depths.

Table 35. Thermal conductivity, Hole 858B.

Sample (cm)	Depth (mbsf)	Thermal conductivity (W/[m·K])
139-858B-		
1H-1, 120	1.20	0.77
1H-2, 50	2.00	0.89
1H-2, 100	2.50	0.92
1H-3, 75	3.75	1.01
1H-4, 10	4.60	0.99
1H-4, 75	5.25	0.98
1H-5, 30	6.30	1.05
1H-5, 60	6.60	0.99
2H-1, 75	7.95	1.01
2H-1, 110	8.30	0.94
2H-2, 75	9.45	1.02
2H-2, 110	9.80	1.04
2H-3, 30	10.50	0.96
2H-5, 80	14.00	1.16
2H-6, 40	15.10	1.22
2H-6, 110	15.80	1.23
5H-1, 30	24.20	1.10
5H-1, 90	24.80	1.16
5H-2, 35	25.75	1.26
5H-3, 30	27.20	1.16
5H-4, 30	28.70	1.13
5H-4, 90	29.30	1.37
5H-4, 120	29.60	1.37

Note: All measurements were made in the full-space configuration.

Table 36. Electrical resistivity, Hole 858B.

Sample (cm)	Depth (mbsf)	Electrical resistivity, seawater readings	Electrical resistivity, sample readings	Formation factor
139-858B-				
2H-1, 75	7.95	0.021	0.132	6.29
2H-1, 110	8.30	0.027	0.045	1.67

Table 37. Index properties, Hole 858C.

Core, section, interval (cm)	Depth (mbsf)	Wet-bulk density (g/cm^3)	Grain density (g/cm^3)	Wet porosity (%)	Wet water content (%)	Void ratio
139-858C-						
1H-2, 38–42	1.88	1.52	2.68	70.0	50.2	2.89
1H-3, 17–21	3.17	1.52	2.72	69.5	46.7	2.28
2H-1, 88–91	4.38	1.57	2.73	70.4	45.8	2.38
2H-4, 72–75	8.72	1.45	2.69	80.8	57.0	4.20
2H-6, 78–81	11.78	1.70	2.70	63.5	38.2	1.74
3H-1, 13–16	13.13	1.78	2.76	59.7	34.4	1.48
3H-2, 136–139	15.86	1.84	2.71	54.0	30.1	1.17
3H-3, 107–109	17.07	1.80	2.70	56.9	32.4	1.32
3H-4, 77–80	18.27	1.82	2.68	54.5	30.6	1.20
3H-5, 58–60	19.58	1.91	2.70	50.8	27.2	1.03
3H-6, 86–89	21.36	1.97	2.71	47.2	24.5	0.89
5H-1, 72–75	24.22	1.93	2.70	50.0	26.6	1.00
5H-2, 106–108	26.06	1.75	2.73	60.0	35.2	1.50
5H-3, 19–21	26.69	1.70	2.71	62.7	37.8	1.68
5H-4, 93–95	28.93	1.83	2.71	55.6	31.1	1.25
5H-5, 88–90	30.38	1.81	2.68	56.0	31.6	1.27
6H-1, 80–82	33.80	1.96	2.69	47.9	25.0	0.92
6H-3, 108–110	37.08	1.78	2.73	57.5	33.2	1.35
7H-1, 11–12	41.61	1.83	2.71	56.1	31.4	1.28
7H-2, 55–58	43.55	1.83	2.69	55.1	30.8	1.23
7H-2, 143–146	44.43	1.82	2.71	55.3	31.0	1.23
11X-1, 22–24	54.72	1.95	2.73	50.9	26.8	1.04
11X-1, 22–24	54.72	2.04	2.68	52.7	26.5	1.11
12X-2, 53–55	66.03	1.86	2.72	56.7	31.3	1.31
12X-2, 141–143	66.91	2.13	2.70	39.7	19.1	0.66

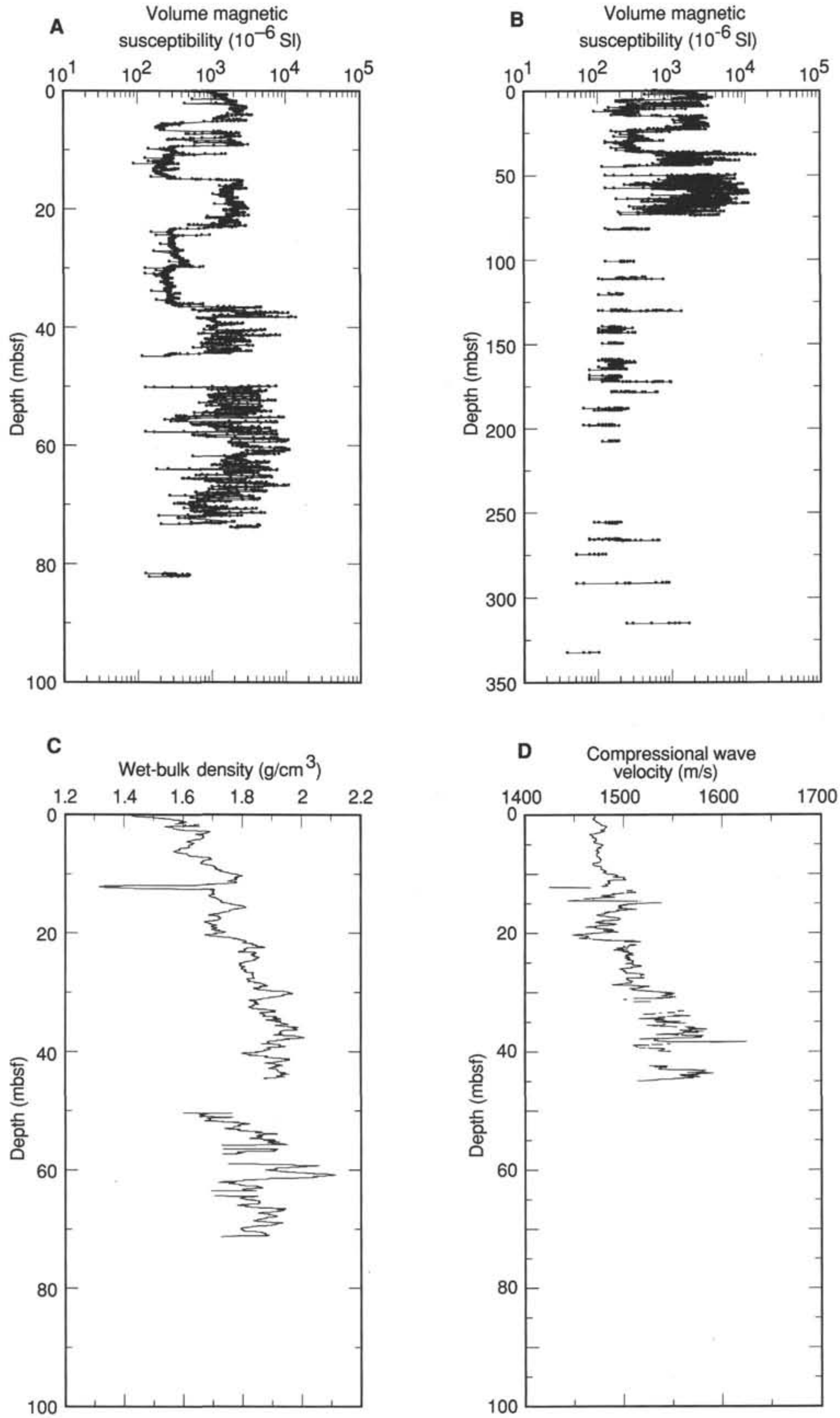

Figure 81. Volume magnetic susceptibility, 0 to 100 mbsf (**A**), volume magnetic susceptibility, 0 to 350 mbsf (**B**), GRAPE wet-bulk density (**C**), and PWL compressional wave velocity (**D**) in Hole 858A. Data gaps reflect low core recovery.

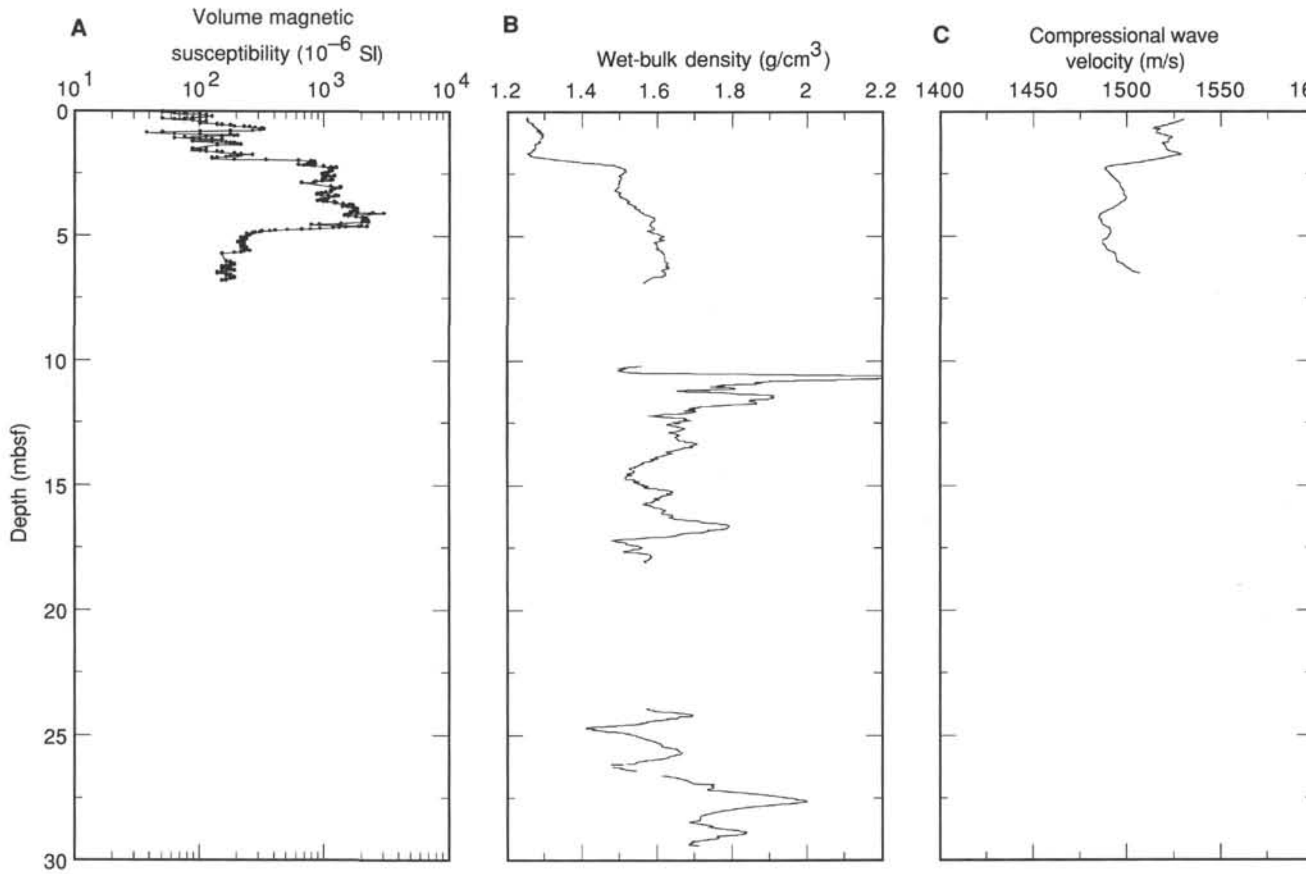

Figure 82. Volume magnetic susceptibility (**A**), GRAPE wet-bulk density (**B**), and PWL compressional wave velocity (**C**) in Hole 858B. Data gaps reflect low core recovery.

Estimated *in-situ* temperatures vs. depth and cumulative thermal resistance (Bullard, 1939) for Holes 858A through 858D are shown in Figure 111. The WSTP measurements in Hole 858A at 74.0 and 92.4 mbsf are interpreted to have been made in fill, as the extrapolated temperatures fall off the main trend defined by the other measurements. For the first of these measurements, this interpretation is supported by the chemistry of the fluid sample collected during this run, which indicates significant borehole contamination ("Fluid Geochemistry" section, this chapter), even though the sampling valve opened well after the probe was pressed into the mud. The temperature estimate of 111.7 mbsf also falls off the main trend and probably was also made in cold fill, but no fluid sample was available to confirm this explanation.

In a steady-state, one-dimensional, purely conductive system, a plot of temperature vs. thermal resistance will be linear (Bullard, 1939), with the mean heat flow at any depth given by the slope of the curve which best fits the data. The measurements in shallow sediments from Hole 858A are consistent with heat flow of about 1.9 W/m^2, although there is enough structure in the Bullard plot to suggest the possibility of transient, non-one-dimensional or nonconductive heat transfer (Fig. 111B). The distribution of thermal conductivity measurements is spotty and the data are not corrected for pressure and temperature effects ("Physical Properties" section, this chapter). These factors could contribute to the nonlinearity described above.

Even more structure is apparent in the Bullard plot for Hole 858C, where heat flow is about 3.3 W/m^2. The data form a consistently nonlinear curve with a projected seafloor intercept of about 10°C, significantly higher than the measured bottom-water temperature of 1.7° C. This pattern could result from some combination of lateral and vertical fluid flow through shallow sediments ("Fluid Geochemistry" section, this chapter), although there is no direct evidence for the presence of a conduit through which fluid could be flowing (see "Physical Properties" section, this chapter).

The highest heat flow measured during Leg 139 was about 10.6 W/m^2 at both Holes 858B and 858D. The apparent colinearity of temperatures measured in the two holes (and thus heat flow in Figure 111B) is probably fortuitous, as the holes are separated by about 80 m. It was expected that the heat flow would be high in Hole 858B, as this hole was sited a few meters from active hydrothermal vents which discharge fluids with temperatures >280° C. Finding similarly high heat flow in Hole 858D was surprising, however, as this hole was spudded about 60 m from the nearest known vents; our expectation was that Hole 858D would have a heat flow value intermediate between that measured in Holes 858B and 858C.

SPECIAL DOWNHOLE EXPERIMENTS

An extensive program of logging and downhole experiments was conducted in Hole 858G after it had been cased to 270 mbsf and deepened to 432.6 mbsf. This program was very much like that conducted in Hole 857D and included temperature and Schlumberger logging described in the "Downhole Logging" section (this chapter), as well as several special experiments designed to assess the hydrogeological and thermal state of the section penetrated in Hole 858G. The latter included packer experiments to determine bulk permeability and average formation fluid pressure, a flowmeter log conducted in conjunction with the packer to assess the fine-scale distribution of permeability, and the emplacement of a long-term instrumented borehole seal or "CORK." Methods for the packer and flowmeter experiments are summarized in the "Spe-

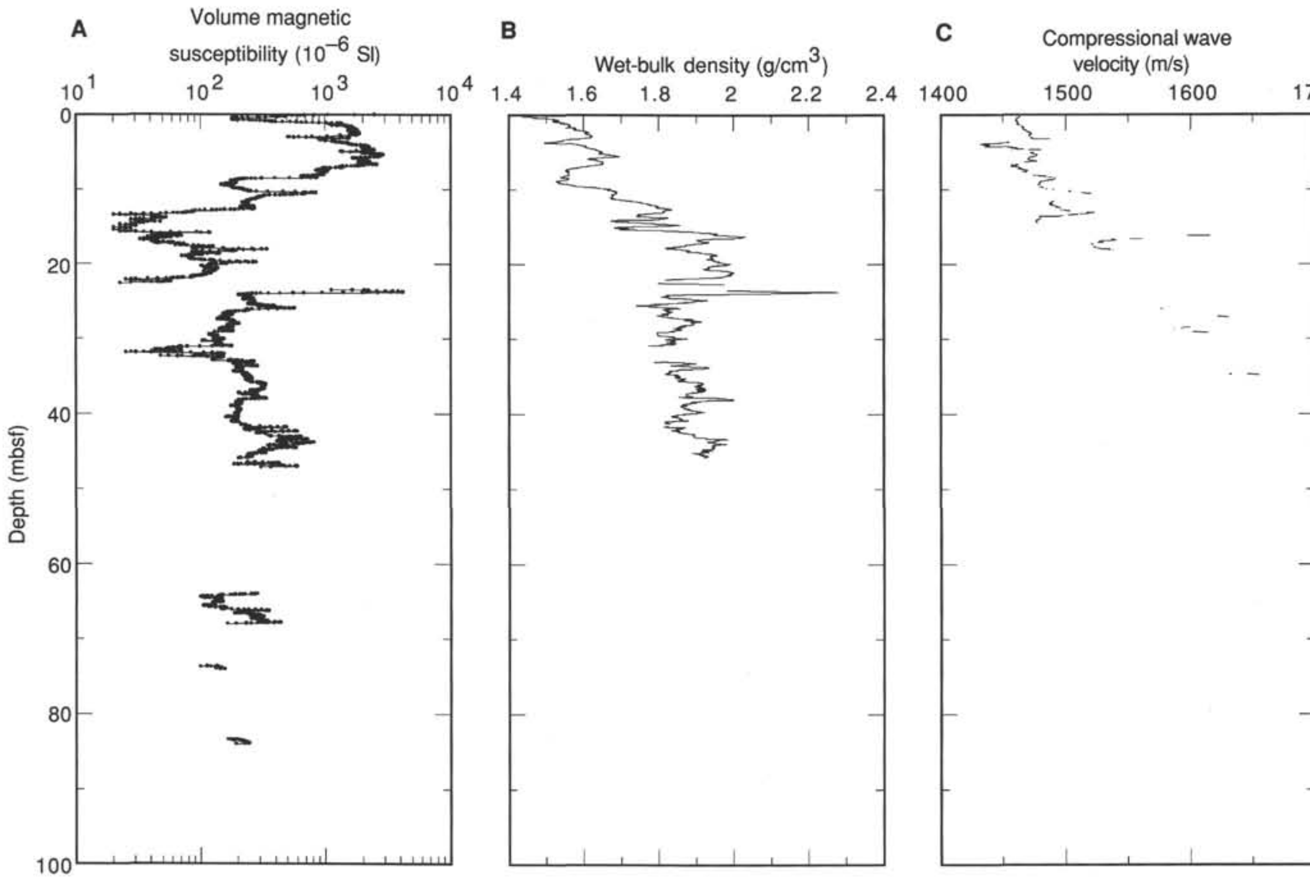

Figure 83. Volume magnetic susceptibility (**A**), GRAPE wet-bulk density (**B**), and PWL compressional wave velocity (**C**) in Hole 858C. Data gaps reflect low core recovery.

cial Downhole Experiments" section, "Explanatory Notes" chapter (this volume), and the CORK is described in Davis et al. (this volume). The data from the packer and flowmeter experiments require analyses that could not be completed in the brief time remaining during Leg 139, and the CORK will provide no data or samples until revisited with the *Alvin* submersible shortly after Leg 139. Therefore, this section comprises a summary of operations during these experiments and a qualitative assessment of the results of the packer and flowmeter experiments.

Packer and Flowmeter Experiments

The packer and flowmeter experiments were conducted as described in the "Special Downhole Experiments" section, "Explanatory Notes" chapter (this volume) with the same modification as in Hole 857D: the packer was deployed with two inflation elements instead of one, in order to double its mechanical and hydraulic holding power when inflated in casing. The two elements were separated by only about 0.5 m, so the packer acted essentially as a double-seal single packer that isolated the zone between the entire packer assembly and the bottom of the hole. Three go-devils were deployed, and the packer was inflated three times within casing during a sequence of standard permeability tests and the flowmeter experiment.

First Go-devil (Packer at 104 Mbsf)

After reentry, the packer assembly was positioned at 104 mbsf in order to test the permeability of the section between the casing shoe at 270 mbsf and the bottom of Hole 858G at 436.2 mbsf. The go-devil was deployed with one mechanical Kuster K-3 pressure recorder and one electronic GRC ERPG-300 recorder; the pressure record from the latter is shown in Figure 112. After the go-devil landed, the packer was inflated at 1500 psi and two slug tests were conducted, including the slug test that occurs on inflation. These gave indications of only moderate permeability, apparently consistent with the first two temperature logs in the hole ("Downhole Logging" section, this chapter), which showed no indication of strong downhole flow as had occurred in Hole 857D.

Two injection tests were then attempted at low pumping rates. Pressure gauges connected to the rig floor plumbing yielded disturbed records, suggesting that flow through the go-devil might have been restricted, among other possibilities. Indeed, when the go-devil was retrieved, it was found to be partially plugged with rust and grease, and the downhole gauges also yielded disturbed records (Fig. 112). It was unclear when the blockage of the go-devil occurred, or whether it might have affected the results of the earlier slug tests, which otherwise appeared reasonable. Therefore, it was decided to repeat the packer experiment, after a third temperature log that was run when the first packer go-devil was retrieved. Despite the blockage of the go-devil, the downhole pressure record does show clear evidence of an underpressure (relative to cold hydrostatic) of about 0.5 MPa in the isolated zone once it was sealed by the packer.

Second Go-devil (Packer at 96 Mbsf)

The go-devil was modified to ensure the largest possible flow passages, and the packer experiment was repeated at the same inflation depth. The modified go-devil was deployed with redressed Kuster and GRC pressure recorders, and the packer was again inflated

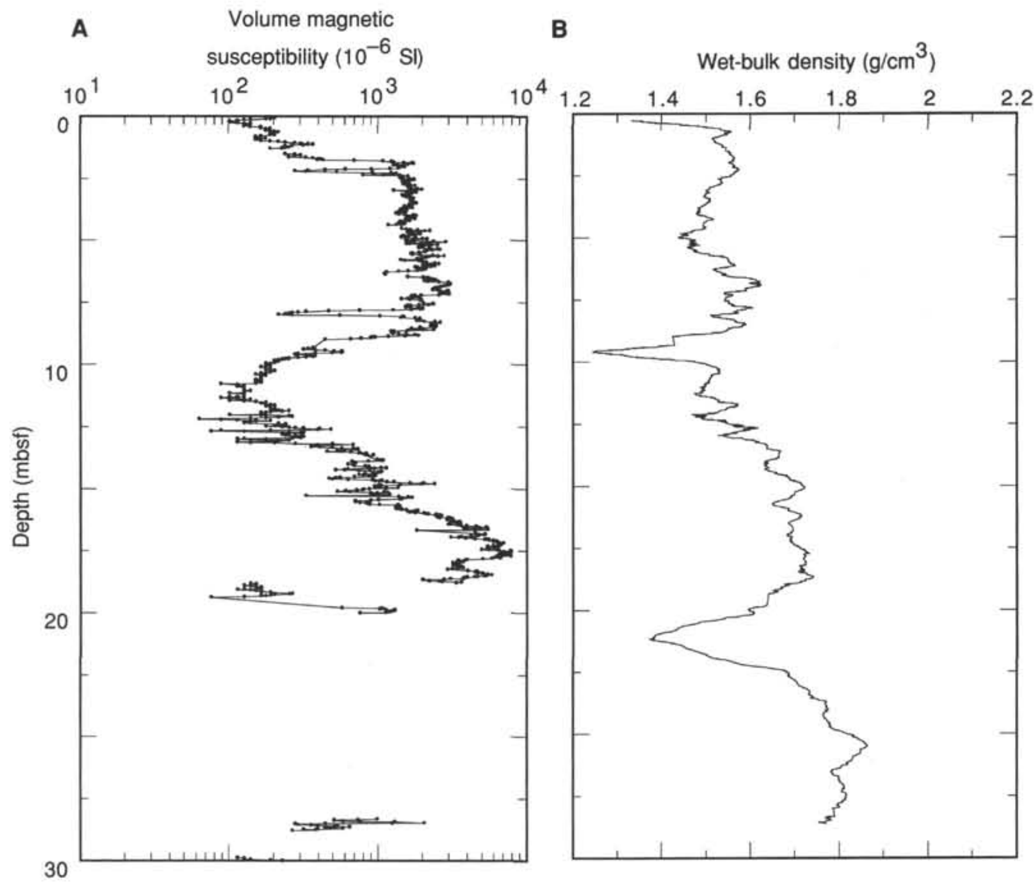

Figure 84. Volume magnetic susceptibility (**A**) and GRAPE wet-bulk density (**B**) in Hole 858D. Data gaps reflect low core recovery.

at 1500 psi. The temperature log conducted between the two packer experiments had shown evidence for slow flow of ocean bottom water down the hole, indicating significant permeability in the formation, and the test sequence was conducted accordingly.

Figure 113 shows the pressure record collected with the GRC recorder during this test sequence. First, two slug tests were conducted, producing moderate decay curves like the first slug test during the first packer inflation. This supported the hypothesis that the blockage of the go-devil during the first packer experiment occurred during pumping after packer inflation.

Four injection tests were then conducted, at significantly higher pumping rates than had been possible during the first packer inflation at this depth. The pressure records from these injection tests are of good quality, although the uncorrected data at first glance appear to deviate somewhat from the ideal record, as follows: in a proper injection test, pressure will increase continuously with the log of time (Horner, 1951; Matthews and Russell, 1967), but these records show slight decreases of pressure at long injection times before the smooth decays when pumping was stopped (Fig. 113). This appears to be an effect of the superposed residual pressure decays from previous slug and injection tests, for which careful corrections are required before the average permeability of the formation can be calculated.

Third Go-devil and Flowmeter Experiment (Packer at 96 Mbsf)

The moderate permeability of the formation provided a good test of the resolution of the flowmeter/injection experiment, which had been run under conditions of exceptionally vigorous downhole flow in Hole 857D. The packer was left uninflated in position in the casing, logging sheaves were rigged, and the flowmeter logging tool, sinker bar, and logging cable go-devil were run into the hole. After a pressure calibration stop above mudline at 2388.9 mbsf, the go-devil was run to the packer and the packer was successfully inflated. Pump pressure was then increased to shear the release pins in the go-devil and free the logging cable so that the flowmeter tool could be run into the section of hole isolated by the packer.

The flowmeter tool was lowered to near the bottom of casing, and the ship's pumps were used to calibrate the spinner reading at known flow rates. At given pumping rates, pressures rose much more than in Hole 857D because the formation is less permeable in Hole 858G. At the higher injection rates there was significant leakage of the pumped fluids at the gland on the top drive that sealed the logging line. Because of this effect, injection rates had to be kept lower than in Hole 857D, and the resolution of the flowmeter was limited.

The flowmeter tool was then run into the hole for stationary measurements at 10-m intervals. At the first measurement depth, an injection rate of 100 strokes per minute (spm) was attempted, but fluid leakage at the seal on the logging line was significant, and the experiment was conducted at 50 spm. Within 80 m below the bottom of the casing, the flowmeter readings dropped so low relative to the noise introduced by heave that no reliable information would have been collected by continuing any deeper. The tool was then raised back into the casing, where it was recalibrated at a pumping rate of 50 spm, and the packer was deflated. After deflation, the flowmeter reading indicated that there was no detectable downhole flow, in contrast to the vigorous downhole flow observed in Hole 857D, and the experiment was ended.

At each station, flow, pressure, and caliper were logged. These three parameters are necessary to convert the variation in flow rates to a permeability "log" of the formation. Calculating the variation of

Table 38. Compressional wave velocity (DSV), Hole 858C.

Sample (cm)	Depth (mbsf)	Longitudinal/ transverse (L/T)	DSV velocity (m/s)
139-858C-			
1H-1, 32	0.32	L	1492
1H-1, 32	0.32	T	1671
1H-1, 115	1.15	L	1498
1H-1, 115	1.15	T	1574
1H-2, 40	1.90	L	1498
1H-2, 40	1.90	T	1605
1H-2, 67	2.17	L	1490
1H-2, 67	2.17	T	1561
1H-2, 120	2.70	L	1500
1H-2, 120	2.70	T	1446
1H-3, 18	3.18	L	1490
1H-3, 18	3.18	T	1549
2H-1, 90	4.40	L	1507
2H-1, 90	4.40	T	1574
2H-2, 65	5.65	L	1510
2H-2, 65	5.65	T	1564
2H-3, 68	7.18	L	1502
2H-3, 68	7.18	T	1564
2H-4, 75	8.75	L	1500
2H-4, 75	8.75	T	1583
2H-5, 100	10.50	L	1524
2H-5, 100	10.50	T	1602
2H-6, 80	11.80	L	1524
2H-6, 80	11.80	T	1608
2H-7, 24	12.74	L	1548
2H-7, 24	12.74	T	1624
3H-1, 16	13.16	L	1564
3H-1, 16	13.16	T	1571
3H-1, 104	14.04	L	1500
3H-1, 104	14.04	T	1583

Table 39. Compressional wave velocity (HFV), Hole 858C.

Core, section, interval (cm)	Depth (mbsf)	Direction (a, b, c)	HFV velocity (m/s)
139-858C-			
3H-3, 79–81	16.79	c	1713
3H-3, 128–130	17.28	c	1606
3H-4, 79–81	18.29	c	1540
3H-5, 82–84	19.82	c	1862
3H-6, 85–87	21.35	c	1634
5H-1, 87–88	24.37	c	1673
5H-2, 108–110	26.08	c	1549
5H-3, 83–85	27.33	c	1675
5H-4, 61–63	28.61	c	1708
5H-5, 20–22	29.70	c	1692
5H-5, 72–74	30.22	c	1645
5H-5, 124–126	30.74	c	2021
7H-2, 55–57	43.55	c	1847
7H-2, 144–146	44.44	c	1831
11X-1, 46–48	54.96	c	2487
12X-1, 28–30	64.28	c	2368
12X-1, 83–85	64.83	c	2252
12X-1, 97–99	64.97	c	2329
12X-2, 14–16	65.64	c	2717
12X-2, 42–44	65.92	c	2158
12X-2, 83–85	66.33	c	2238
12X-2, 118–120	66.68	c	2567
12X-2, 53–55	66.03	a	2000
12X-2, 53–55	66.03	b	2262
12X-2, 53–55	66.03	c	2152
12X-2, 141–143	66.91	a	2666
12X-2, 141–143	66.91	b	2889
12X-2, 141–143	66.91	c	2668
13X-CC, 7–8	74.23	c	1843
14X-1, 6–8	83.46	c	1823

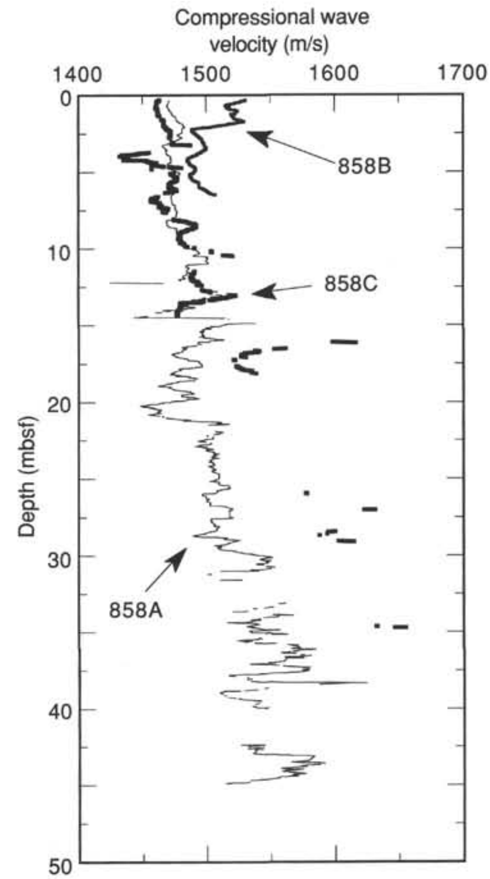

Figure 85. Comparison of the compressional wave velocity, measured with the PWL on whole-round cores from Holes 858A, 858B and 858C.

permeability with depth will require considerable post-cruise analysis, but comparing the variation in flow readings allows a qualitative interpretation (Fig. 114). Note that, at the injection rate of 50 spm, some of the variations in the raw flowmeter readings may be due simply to changes in hole diameter. Nevertheless, the variation in flowmeter readings indicates that the most permeable zone in Hole 858G lies between 340 and 350 mbsf. The temperature log measured between the first and second packer inflations shows a change in slope at this depth, with a steep gradient below and a more nearly isothermal gradient above ("Downhole Logging" section, this chapter). Thus it appears that the permeable zone at 340–350 mbsf was drawing ocean bottom water down Hole 858G, although at a rate much lower than that at which bottom water was flowing down Hole 857D.

Instrumented Borehole Seal or CORK

At the end of operations at Site 858, Hole 858G was sealed with the CORK and instrumented with a thermistor string, pressure sensor, fluid sampling tubing, and long-term data logger. Figure 115 shows the configuration of the instrumentation deployed. It had been planned to install a 400-m-long high-temperature thermistor cable, but a ledge or obstruction had stopped logging tools and impeded the drill bit at a depth of 393–399 mbsf. To ensure a successful deployment, the cable was shortened by doubling its lower 15 m back up towards the top, and the sinker bar was hung off the cable loop created at the new end of the cable at 385 m. This changed only the position of the lowermost thermistor, which was raised from 400 m to 370 mbsf, 10 m deeper than the next thermistor.

On the basis of experience gained during the deployment in Hole 857D, the fluid sampling tubing was attached to the thermistor

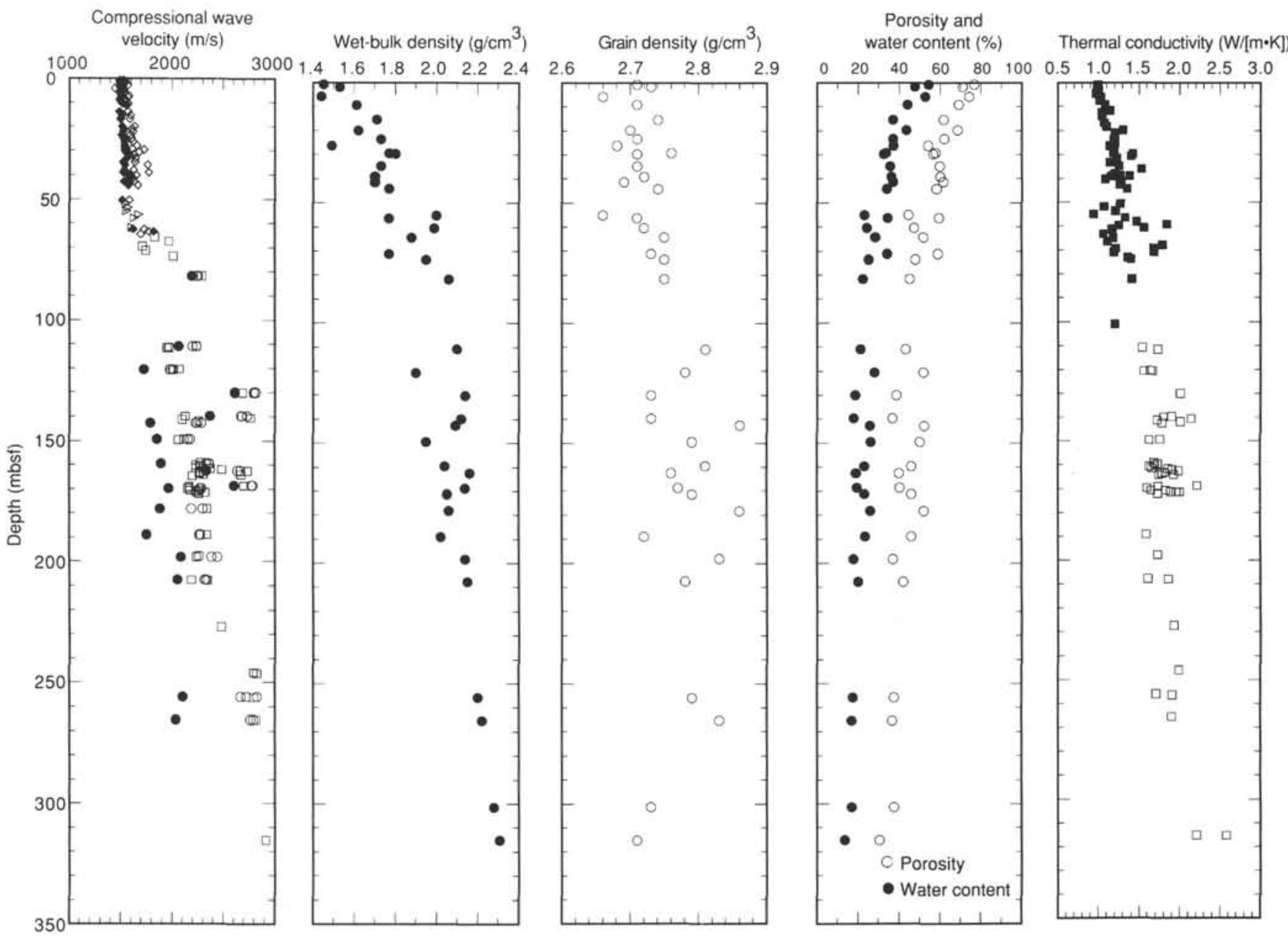

Figure 86. Compressional wave velocity, wet-bulk density, grain density, porosity and water content, and thermal conductivity vs. depth in Hole 858A. Open (transverse velocity) and solid (longitudinal velocity) diamonds in the plot of compressional wave velocity are data measured by the digital sound velocimeter (DSV); open squares and open triangles are data from the Hamilton frame velocimeter (HFV) either measured on half-core pieces or taken as in-liner measurements in the c-direction (transverse); open and solid circles are measurements on cubes in b- or c-directions and in a-direction, respectively. In thermal conductivity plot, open squares are half-space configuration and solid squares are full-space configuration.

cable as it was run into the hole. Deployment operations proceeded even more smoothly than in Hole 857D and required several hours less than budgeted. Data and samples from the CORK were scheduled to be collected from the *Alvin* submersible about 10 days after the end of Leg 139, approximately 2 weeks after the deployment of the instrumentation.

SUMMARY AND CONCLUSIONS

Site 858 is located at an active hydrothermal vent field in Middle Valley. Its structural setting is similar to that at Site 857 1.6 km to the south: both are situated about 5 km west of the eastern rift-bounding scarp of Middle Valley and about 6 km east of the valley axis, over an uplifted but fully buried basement fault block. Sediment thickness in the vicinity of Site 858 ranges from 400 to 700 m, but the vent field itself lies above a local basement high that rises to within 250 m of the seafloor. The vent field is defined by a region of high acoustic backscatter that extends about 800 m along and 400 m across the strike of Middle Valley. Within this area there are several discrete sites where hot water is venting at temperatures as high as 276°C, but generally in the range 255° to 265°C. Heat flow surrounding the region of high backscatter is typically 1.0 to 1.5 mW/m^2, but it increases to between 4 and 25 W/m^2 within the vent field itself.

Holes 858A through 858D were drilled with the APC/XCB system in an array about 250 m across from just off the edge to the center of the vent field. These four holes were drilled to document the local fluid flow and thermal regimes and the associated sediment alteration. Hole 858F was an exploratory RCB hole for deep-reentry of Hole 858G. Both were drilled in the center of the vent field to characterize the deeper hydrothermal and geologic structure of the upflow zone.

Hole 858A was drilled 100 m west of the area of high acoustic backscatter, 170 m northwest of the nearest high-temperature vent. It penetrated 339 m of sediment and has a conductive thermal gradient of 1.7°C/m over the upper 110 mbsf. Hole 858C was drilled on the western edge of the area of high backscatter, 70 m west of the nearest known vent. It penetrated 93 m of hydrothermally altered sediment and has a temperature gradient of 3°C/m. Hole 858D was drilled at the center of the vent field, 70 m northeast of the nearest vent at Hole 858B. It penetrated 41 m of sediment and yielded a measured temperature of 208°C at 18.5 mbsf. Hole 858B was drilled within 5 to 20 m of a vent that was discharging water at 276°C. It penetrated 39 m of sediment and yielded a temperature of 197°C at 19.5 mbsf. Visits to this hole by the manned submersible *Alvin* within two months of its drilling revealed that it was vigorously venting hot water and black smoke. Penetration in each of these three shallow APC/XCB holes at Site 858 stopped when highly silicified sediment was encountered.

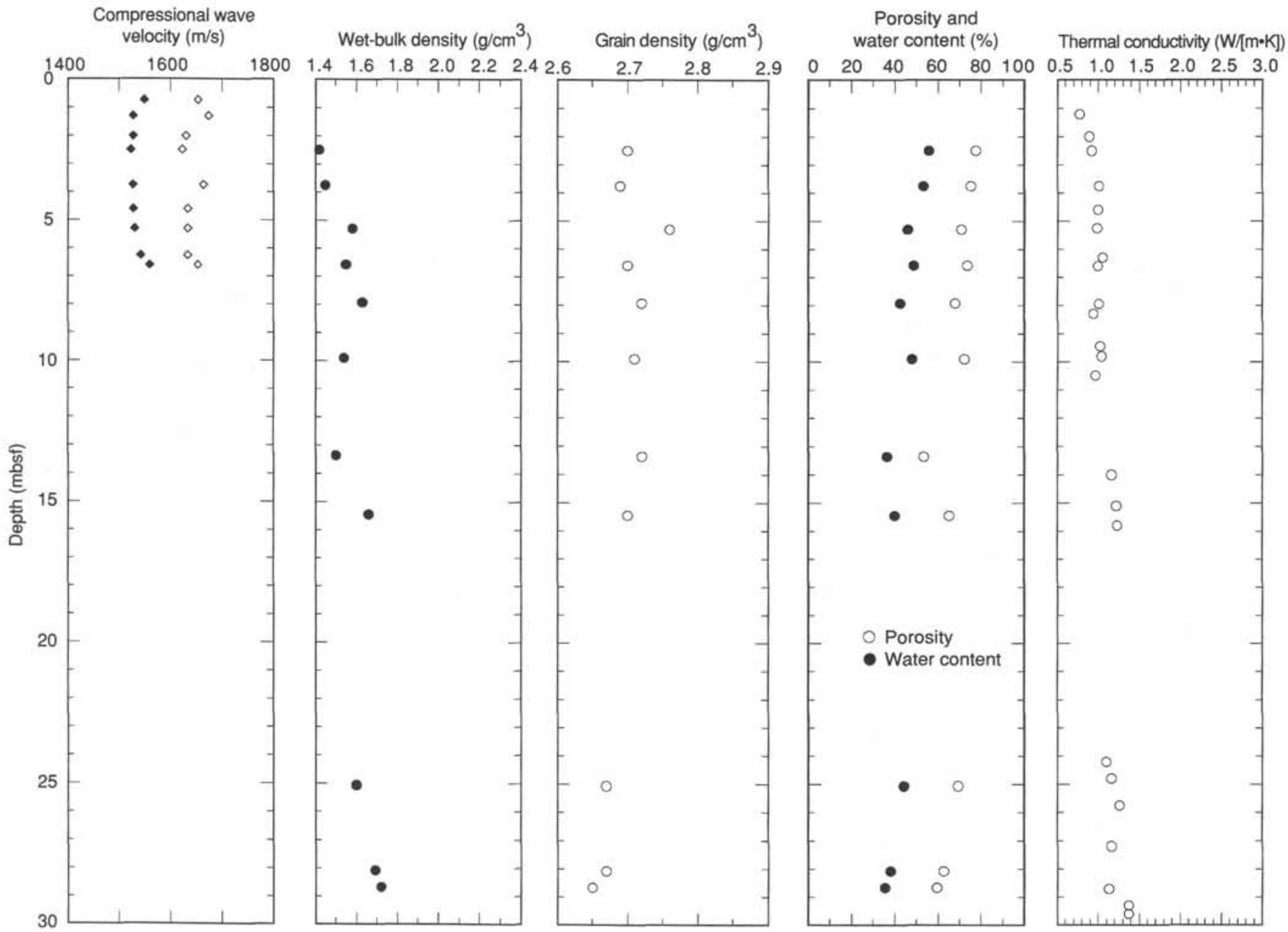

Figure 87. Compressional wave velocity, wet-bulk density, grain density, porosity and water content, and thermal conductivity vs. depth in Hole 858B. Open (transverse velocity) and solid (longitudinal velocity) diamonds in plot of compressional wave velocity are data measured by the digital sound velocimeter (DSV); open squares and open triangles are data from the Hamilton frame velocimeter (HFV) either measured on half-core pieces or taken as in-liner measurements in the c-direction (transverse); open and solid circles are measurements on cubes in b- or c-directions and in a-direction, respectively.

RCB Holes 858F and 858G were drilled adjacent to Hole 858D at the center of the vent field. Hole 858F penetrated 258 m of sediment and into extrusive basalt. That this hole is only 240 m southeast of Hole 858A, which penetrated 339 m of sediment without encountering basement, indicates that the basement high beneath the vent field slopes at more than 17°. Reentry Hole 858G was cased throughout the sediment section and drilled to 433 mbsf in basalt flows, then sealed with an instrumented CORK for long-term monitoring of temperature and pressure and for water sampling. Recovery was very poor in both of these holes, averaging only 3% in sediment and 5% in basalt.

Observations at Site 858 indicate that the lateral boundary of the upflow system is very sharp. Upward flow of pore water at a rate that can be detected thermally is limited to the area beneath the vent field itself. Below about 30 mbsf, the section is inferred to be nearly isothermal and dominated by convection, while nearby shallow thermal gradients are conductive. Lateral flow appears to be significant at various levels in all of the holes drilled at this site.

The strata recovered at Site 858 are similar to those recovered at the other sites: alternating hemipelagic and turbiditic sediment that is increasingly indurated and decreasingly calcareous with depth. Four sedimentary units were defined on the basis of the proportion of turbidites present, the degree of alteration, and the presence of sulfide. Unit I is fine-grained hemipelagic silty clay with only minor turbidites, up to 25% carbonate, and small carbonate nodules. It ranges in age from Holocene to late Pleistocene and occupies most of the uppermost 15 to 20 mbsf in APC Holes 858A to 858D. Dolomite and fine-grained disseminated pyrite are present in this unit in Holes 858B and 858D. Unit II comprises alternating hemipelagic and turbiditic sequences and is correlative to Unit II at all other Leg 139 sites. As at Site 856, it can be divided into four subunits, three of which are based on degree of induration, hydrothermal alteration, and presence of brecciation. The most altered of the three is completely silicified, commonly fractured, and contains abundant authigenic silicate and sulfide minerals. The fourth subunit, IIB, is a brecciated, anhydrite- and carbonate-rich sequence that contains semimassive sulfide deposited by nearby hydrothermal vents. It occurs only between about 15 and 50 mbsf in Holes 858B and 858C. Although the interpretation is controversial and coring artifacts cannot be ruled out, the geometry of the breccias, the associated mineralization, and the presence of a carbonate-cemented "cap" all suggest that fluids have flowed laterally along bedding planes and other permeable horizons, probably at local lithostatic pressure. Unit III consists of metalliferous surficial sediment that overlies strata containing semimassive sulfide. It probably formed by reaction of hydrothermal solutions with sediment. Unit IV consists of strata-bound semimassive sulfide in the coarse portion of turbidites. Units III and IV were found only in Hole 858B, the hole nearest a high-temperature vent.

Sediment from all five holes is hydrothermally altered and metasomatized, but the alteration assemblages and their distribution vary with depth and lateral distance from vent sites in response to the thermal

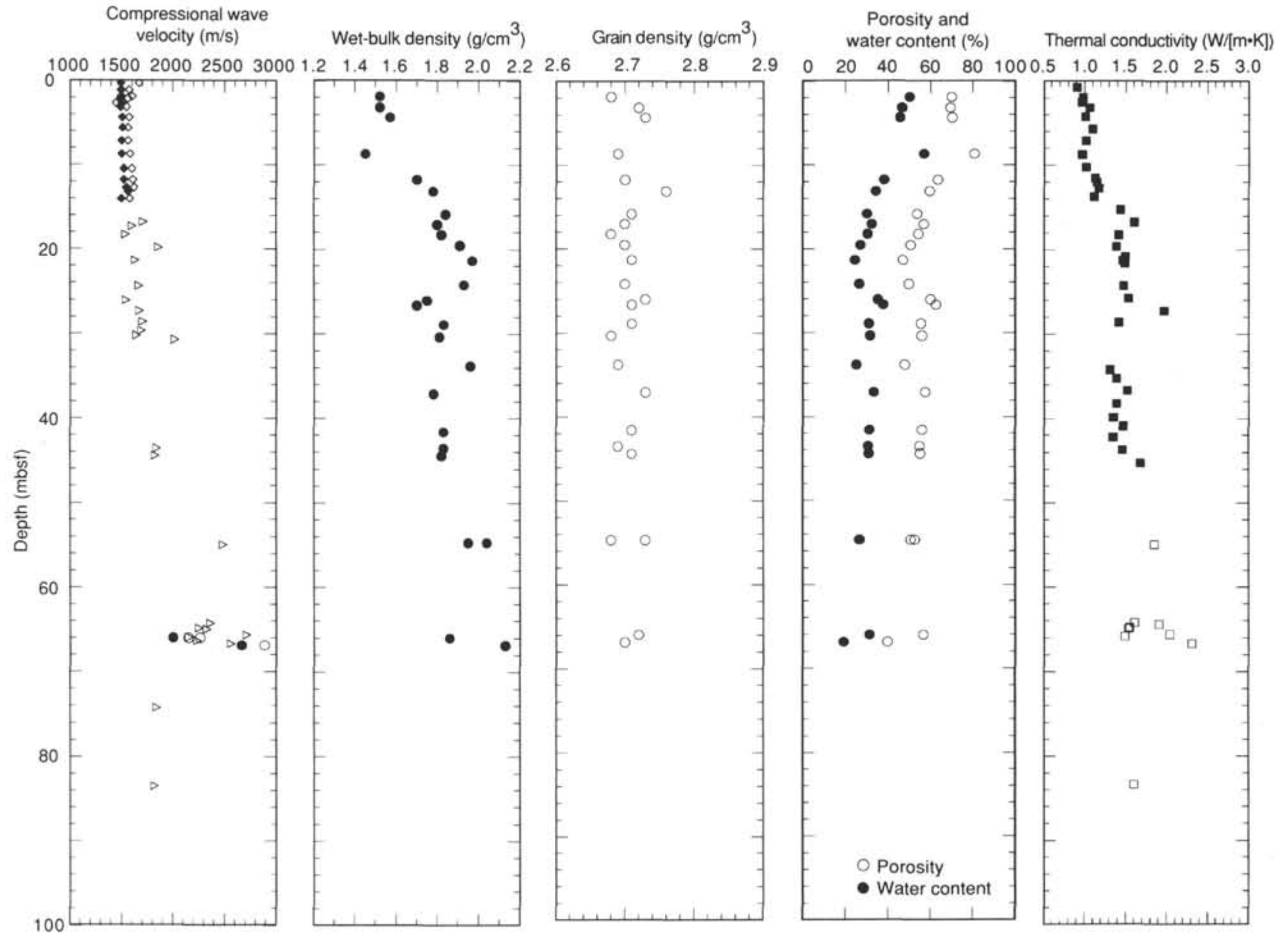

Figure 88. Compressional wave velocity, wet-bulk density, grain density, porosity and water content, and thermal conductivity vs. depth in Hole 858C. Open (transverse velocity) and solid (longitudinal velocity) diamonds in plot of compressional wave velocity are data measured by the digital sound velocimeter (DSV); open squares and open triangles are data from the Hamilton frame velocimeter (HFV) either measured on half-core pieces or taken as in-liner measurements in the c-direction (transverse); open and solid circles are measurements on cubes b- or c-directions and in a-direction, respectively. In thermal conductivity plot, open squares are half-space configuration and solid squares are full-space configuration.

gradient. Four zones were defined from the core to the margins of the vent field, and from deeper to shallower in the holes. Zone 1 is a chlorite-albite-quartz-pyrite assemblage that occupies the high-temperature core of the upflow zone. Epidote joins this assemblage in the deepest samples. Zone 2 is a quartz-zeolite-sulfide assemblage that occurs only in Hole 858F, above Zone 1 deep in the sediment at the center of the vent field. Zone 3 is an anhydrite-pyrite assemblage that forms above Zones 1 and 2. Zone 4 is a carbonate-pyrite assemblage that occurs near the seafloor and is thinner closer to the vent sites. The authigenic carbonate occurs as both nodules and cement. Calcite is the dominant carbonate mineral, but is locally superseded by ankerite at depth. Magnesium-rich clay minerals occur in the zone of carbonate alteration, but become more abundant in the anhydrite-pyrite zone. In Hole 858B intense alteration has formed pyritic massive sulfide with saponite. Authigenic chlorite is associated with quartz and analcime-wairakite replacing sand grains and forming a cement in altered sandstone in Zone 2. Chlorite is abundant in Zone 1.

Thermal alteration strongly affects the distribution of microfossils at Site 858. Both calcareous nannofossils and foraminifers are preserved to a depth of 111 mbsf in Hole 858A, whereas they are found no deeper than 13 mbsf in Holes 858B through 858F within the vent field. The preservation of microfossils is generally moderate to poor, and many specimens of both foraminifers and calcareous nannofossils are overgrown with calcite. Two planktonic foraminiferal zones and two calcareous nannofossil zones subdivide the fossiliferous portions of the holes. Planktonic foraminiferal Zone CD1, which is equivalent to the Holocene, was recognized in the top cores of Holes 858A through 858D, and material from the underlying Zone CD2 was recognized at each of these holes. Shore-based work will determine whether Zones CD3 to CD5 occur in Hole 858A. The calcareous nannofossil Zone NN21 was recognized in Holes 858A through 858D, and the *Emiliania huxleyi* Acme Zone was recognized only in Hole 858B, where we suspect that the base is shallow due to recrystallization of the delicate marker species.

Pore water was collected from both sediment and basalt at Site 858. Chlorinity ranged from the 540 mmol/kg of bottom seawater to as high as 660 mmol/kg; the latter value was found at only 3 mbsf in Hole 858D. The hot water that is venting has a chlorinity of about 600 mmol/kg. Chlorinity in all holes showed complex maxima and minima with depth that require lateral flow of water over a range of depths, from the upper few meters below seafloor in Hole 858D to more than 200 mbsf in Hole 858A. This lateral flow would result in mixing between hot water and local pore water in the subsurface, resulting in precipitation and other reactions. Within those depth intervals where chlorinity is high, deep within Holes 858A and 858F and shallow within Holes 858B and 858D, the pore water closely resembles that which is venting, and has about 80 mmol/kg calcium, 390 mmol/kg sodium, 16 mmol/kg potassium, and 1 mmol/kg dissolved silica. Magnesium at about

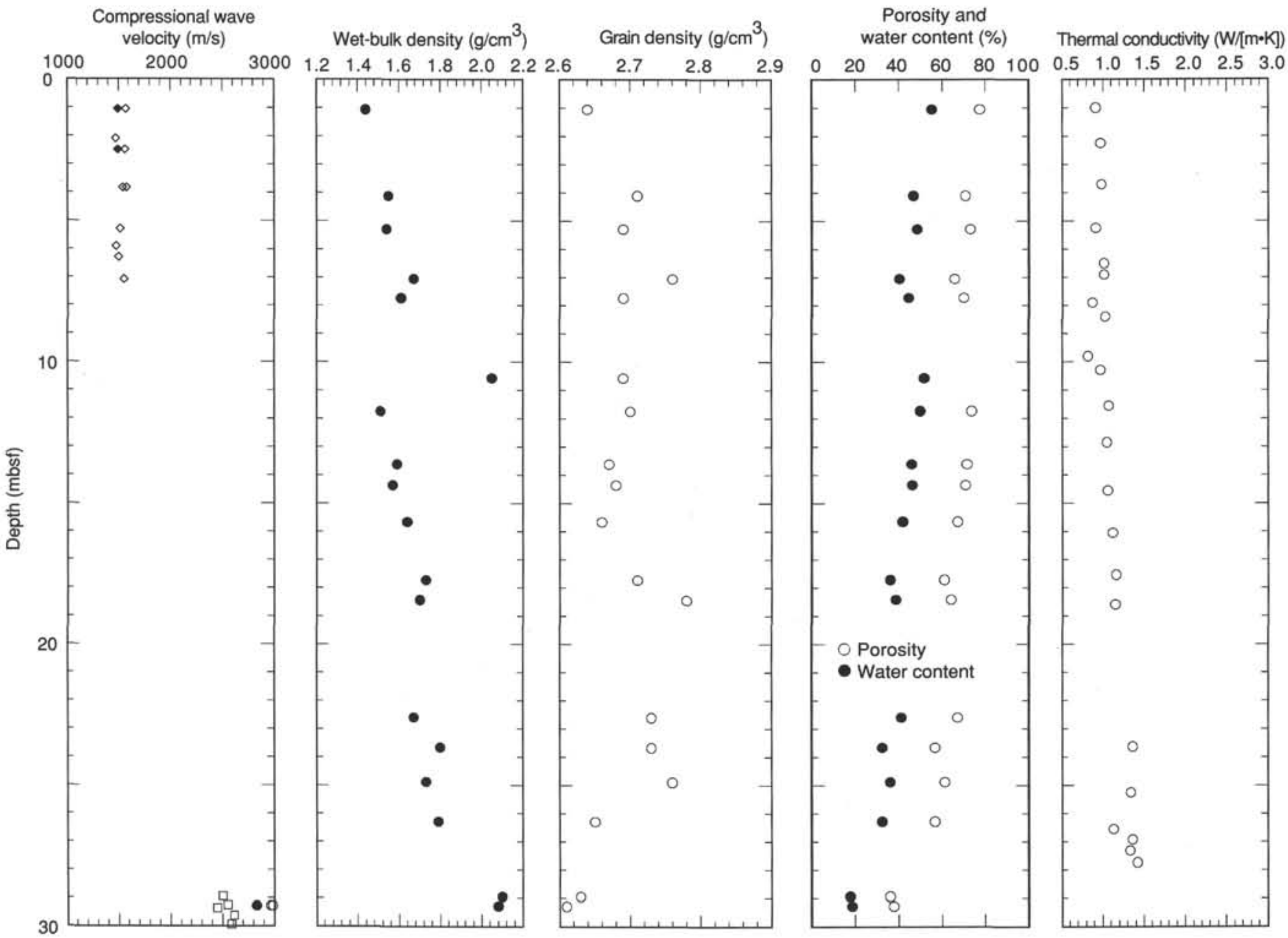

Figure 89. Compressional wave velocity, wet-bulk density, grain density, porosity and water content, and thermal conductivity vs. depth in Hole 858D. Open (transverse velocity) and solid (longitudinal velocity) diamonds in plot of compressional wave velocity are data measured by the digital sound velocimeter (DSV); open squares and open triangles are data from the Hamilton frame velocimeter (HFV) either measured on half-core pieces or taken as in-liner measurements in the c-direction (transverse); open and solid circles are measurements on cubes in b- or c-directions and in a-direction, respectively.

10 mmol/kg appears to be higher than in the vents. Sulfate varies from 0 to 5 mmol/kg in these intervals, alkalinity is surprisingly high at 2 to 7 mmol/kg, and pH varies from 7.2 to 7.9. Hydrogen sulfide concentrations as high as 1.5 mmol/kg were measured.

The gas concentrations C_1–C_3 follow geothermal gradients remarkably well for all of the Site 858 holes. The lowest thermal and methane gradients are observed in Holes 858A and 858C, which have comparable methane gradients. Much steeper methane gradients are observed in Holes 858B and 858D, where the thermal gradient is near 9°C/m. Alternatively, the observed methane gradients in Holes 858A through 858D could be explained by a source at depth and diffusion to the surface. This is not the case for either ethane or propane, whose profiles show a number of sharp discontinuities consistent with an *in-situ* sediment source. The C_1/C_2 ratios are low, suggesting that methane is thermogenic in these hot sediments. In Holes 858A, 858D, and the upper sections of Hole 858F, the C_1/C_2 ratio increases with depth, contrary to the normal decreasing trend observed at numerous DSDP sites but consistent with conversion of sedimentary organic matter, including kerogen and bitumens, to methane and graphite at very high temperature. Graphite may be present as a fine-grained black substance separated from many of the hydrothermally altered intervals. The appearance of CO_2 in several intervals where only traces of inorganic carbonate are present, but where organic carbon is still significant, suggests that the CO_2 is derived from organic carbon (i.e., kerogen) rather than from carbonate.

The petroleum source-rock potential is poor below the top 5 mbsf; total organic carbon is close to 0.1%. The concentrations of bitumen, based on the extract color and fluorescence intensities, are high and variable throughout the upper sections of all holes, suggesting that hydrocarbons are redistributed by fluid flow and temperature gradients. Black soot (carbonaceous particulate matter) occurs in the deeper intervals. Intervals showing either yellow or white fluorescence also typically show this black soot, suggesting that it is a kerogen residue formed in zones of hydrothermal flow. This flow also produces bitumens and causes them to migrate, and cracks kerogen and unexpelled bitumens to gas at higher temperatures. Hydrocarbons in the surficial intervals have high extract yields that reflect rapid maturation, probably resulting from high-temperature fluid flow at depth carrying petroleum upward. Hydrothermal petroleum occurs at shallow depths in all holes; accumulations are often associated with carbonate, which may have acted as a caprock. The present-day temperatures of the hydrothermal petroleum zones observed in Holes 858A through 858C, as estimated from downhole temperature data, are 3° to 70°C. These compare with the commonly cited temperature of 50°C for the onset and 80° to 110°C for the peak of oil generation. Coupled with the low bitumen concentrations at greater depth, this evidence suggests that oil formed at depth and migrated upward, where it was trapped. In Hole 858D, the zone with relatively high yields of petroleum, from 14 to 28 mbsf, is presently very hot: 208°C was measured at 21 mbsf. These bitumens probably could not survive

Table 40. Thermal conductivity, Hole 858C.

Sample (cm)	Depth (mbsf)	Full-space/ half-space (F/H)	Thermal conductivity (W/[m·K])
139-858C-			
1H-1, 75	0.75	F	0.91
1H-2, 50	2.00	F	0.98
1H-2, 100	2.50	F	0.97
1H-3, 18	3.18	F	1.06
2H-1, 75	4.25	F	1.01
2H-2, 70	5.70	F	1.10
2H-3, 60	7.10	F	1.02
2H-4, 75	8.75	F	0.97
2H-5, 70	10.20	F	1.02
2H-6, 50	11.50	F	1.13
2H-6, 100	12.00	F	1.15
2H-7, 23	12.73	F	1.18
3H-1, 75	13.75	F	1.12
3H-2, 75	15.25	F	1.44
3H-3, 75	16.75	F	1.61
3H-4, 75	18.25	F	1.42
3H-5, 64	19.64	F	1.39
3H-6, 32	20.82	F	1.50
3H-6, 75	21.25	F	1.47
3H-6, 113	21.63	F	1.49
5H-1, 75	24.25	F	1.48
5H-2, 75	25.75	F	1.54
5H-2, 75	25.75	F	1.54
5H-3, 75	27.25	F	1.97
5H-4, 60	28.60	F	1.42
6H-1, 120	34.20	F	1.31
6H-2, 75	35.25	F	1.39
6H-3, 65	36.65	F	1.52
6H-4, 75	38.25	F	1.39
6H-5, 85	39.85	F	1.35
6H-6, 40	40.90	F	1.47
7H-1, 70	42.20	F	1.35
7H-2, 70	43.70	F	1.46
7H-3, 75	45.25	F	1.68
11X-1, 44	54.94	H	1.85
12X-1, 23	64.23	H	1.61
12X-1, 42	64.42	H	1.91
12X-1, 77	64.77	H	1.55
12X-1, 94	64.94	H	1.54
12X-2, 10	65.60	H	2.04
12X-2, 36	65.86	H	1.49
12X-2, 119	66.69	H	2.31
14X-1, 1	83.41	H	1.60

Table 41. Index properties, Hole 858D.

Core, section, interval (cm)	Depth (mbsf)	Wet-bulk density (g/cm^3)	Grain density (g/cm^3)	Wet porosity (%)	Wet water content (%)	Void ratio
139-858D-						
1H-1, 105–107	1.07	1.44	2.64	77.5	55.3	3.44
1H-3, 112–115	4.12	1.55	2.71	70.8	46.7	2.43
1H-4, 80–83	5.30	1.54	2.69	73.1	48.5	2.71
1H-5, 106–110	7.06	1.67	2.76	65.7	40.4	1.92
1H-6, 25–28	7.75	1.61	2.69	69.9	44.6	2.33
2H-1, 128–131	10.58	1.50	2.68	75.4	51.5	3.06
2H-2, 95–98	11.75	1.51	2.70	73.6	50.0	2.79
2H-3, 133–136	13.63	1.59	2.69	72.0	46.3	2.57
2H-4, 57–60	14.37	1.57	2.68	70.8	46.3	2.43
2H-5, 36–39	15.66	1.64	2.66	67.2	41.9	2.05
2H-6, 93–96	17.73	1.73	2.71	61.0	36.0	1.56
2H-7, 14–16	18.44	1.70	2.78	64.0	38.6	1.78
4H-3, 107–110	22.61	1.67	2.73	67.0	41.2	2.03
4H-4, 64–67	23.68	1.80	2.73	56.8	32.3	1.32
4H-5, 35–38	24.89	1.73	2.76	61.3	36.2	1.58
4H-6, 26–29	26.30	1.79	2.65	56.6	32.3	1.30
6X-1, 15–17	28.95	2.10	2.63	36.1	17.6	0.56
6X-1, 48–50	29.28	2.08	2.61	37.8	18.6	0.61

Table 42. Compressional wave velocity (DSV), Hole 858D.

Sample (cm)	Depth (mbsf)	Longitudinal/ transverse (L/T)	DSV velocity (m/s)
139-858D-			
1H-1, 105	1.05	L	1494
1H-1, 105	1.05	T	1571
1H-2, 60	2.10	T	1473
1H-2, 99	2.49	L	1495
1H-2, 99	2.49	T	1564
1H-3, 84	3.84	T	1577
1H-3, 84	3.84	T	1541
1H-4, 79	5.29	T	1517
1H-4, 140	5.90	T	1476
1H-5, 30	6.30	T	1500
1H-5, 109	7.09	T	1552

Table 43. Compressional wave velocity (HFV), Hole 858D.

Core, section, interval (cm)	Depth (mbsf)	Direction (a, b, c)	HFV velocity (m/s)
139-858D-			
6X-1, 15–17	28.95	c	2505
6X-1, 46–48	29.26	c	2553
6X-1, 48–50	29.28	a	2829
6X-1, 48–50	29.28	b	2983
6X-1, 48–50	29.28	c	2967
6X-1, 56–58	29.36	c	2450
6X-1, 82–84	29.62	c	2615
6X-CC, 9–11	29.94	c	2587

Table 44. Thermal conductivity, Hole 858D.

Sample (cm)	Depth (mbsf)	Thermal conductivity (W/[m·K])
139-858D-		
1H-1, 100	1.00	0.91
1H-2, 75	2.25	0.97
1H-3, 70	3.70	0.98
1H-4, 75	5.25	0.91
1H-5, 50	6.50	1.01
1H-5, 90	6.90	1.01
1H-6, 40	7.90	0.87
1H-6, 90	8.40	1.03
2H-1, 50	9.80	0.82
2H-1, 100	10.30	0.97
2H-2, 75	11.55	1.07
2H-3, 55	12.85	1.05
2H-4, 75	14.55	1.06
2H-5, 75	16.05	1.12
2H-6, 75	17.55	1.16
2H-7, 30	18.60	1.15
4H-4, 59	23.63	1.36
4H-5, 71	25.25	1.34
4H-6, 52	26.56	1.13
4H-6, 88	26.92	1.36
4H-6, 128	27.32	1.33
4H-7, 20	27.74	1.42

Note: All measurements were made in the full-space configuration.

Table 45. Electrical resistivity, Hole 858D.

Sample (cm)	Depth (mbsf)	Electrical resistivity, seawater readings	Electrical resistivity, sample readings	Formation factor
139-858D-				
1H-3, 104	4.04	0.024	0.033	1.38
1H-4, 95	5.45	0.024	0.042	1.75
1H-5, 87	6.87	0.024	0.042	1.75
1H-6, 110	8.60	0.024	0.060	2.50
2H-3, 100	13.30	0.023	0.072	3.13
2H-4, 120	15.00	0.020	0.044	2.20
2H-5, 60	15.90	0.020	0.047	2.35
2H-6, 100	17.80	0.022	0.062	2.82
2H-7, 15	18.45	0.022	0.055	2.50

long at this temperature, suggesting that they have only recently either migrated or been generated there.

Total carbon varies from about 2.5% to 0.1% at Site 858 and in cooler zones consists of about equal proportions of organic and inorganic carbon. Above 160°C, carbonate disappears and carbon drops to 0.1%–0.2%.

Igneous rocks were recovered from the lower 48 m of Hole 858F (248.9–296.9 mbsf) and throughout the entire cored interval of Hole 858G (276.5–432.6 mbsf). All of the igneous rocks sampled from Site 858 except for a single basal unit of spherulitic diabase can be characterized as fine-grained basalts. The well-developed quench textures, local vesicularity, and presence of low-temperature alteration minerals (carbonate, celadonite, smectite) suggest that these rocks formed as extrusive massive flows. The basal unit is a very coarse-grained diabase to microgabbro (average grain size is >2.0 mm). Pale brown clinopyroxene crystals in this unit have well-developed spherulitic morphology. A very small quantity of metasiltstone or chert was recovered with the igneous rooks, suggesting that they represent basement rather than sills. The basalts contain sparse phenocrysts or microphenocrysts of plagioclase, olivine, and chromian spinel. They are chemically homogeneous and have N-MORB compositions. Their TiO_2 contents and Mg numbers suggest only modest crystal fractionation. The presence of olivine and chromian spinel suggests that the magmas from which they crystallized were only slightly evolved.

The interstitial plagioclase and mesostasis are extensively altered to chlorite, prehnite, epidote, and wairakite. These minerals also fill veins and vesicles. Ovoid mafic phenocrysts are pseudomorphed by saponite, chlorite, and actinolite. The metamorphic assemblages observed in Hole 858F are characteristic of upper zeolite (wairakite-chlorite) to greenschist (albite-epidote-chlorite-actinolite), with estimated alteration temperatures of 50°–300°C. Sulfide minerals are ubiquitous in the igneous rocks from Site 858 in quantities of 1%–5%. They are present in veins with epidote, quartz, chlorite, and zeolites. They also form ovoid porphyroblasts within the body of the rock by indiscriminately replacing igneous phases.

Paleomagnetic and other physical properties measurements were restricted to Holes 858A through 858D because of poor recovery from the other holes. The use of aluminum core liners at high-temperature Holes 858B and 858D precluded measurements of magnetic susceptibility and velocity. In Hole 858A, the magnetic intensity is higher within the upper 80 mbsf than below. Two possible reversed orienta-

Table 46. Index properties, Hole 858F.

Core, section, interval (cm)	Depth (mbsf)	Wet-bulk density (g/cm^3)	Grain density (g/cm^3)	Wet porosity (%)	Wet water content (%)	Void ratio
139-858F-						
4R-CC, 7–9	46.57	2.25	2.67	34.7	15.8	0.53
6R-CC, 4–6	65.64	2.46	2.53	10.3	4.3	0.11
9R-CC, 18–20	94.38	2.39	2.46	9.0	3.9	0.10
13R-CC, 7–9	132.97	2.10	2.77	40.4	19.7	0.68
15R-CC, 9–11	152.29	2.07	2.77	44.0	21.8	0.79
17R-CC, 7–9	171.67	2.21	2.71	29.4	13.6	0.42
18R-CC, 9–11	182.11	2.32	2.71	29.6	13.1	0.42
19R-1, 7–9	190.97	2.32	2.73	34.6	15.2	0.53
21R-1, 19–21	210.49	2.30	2.83	33.9	15.1	0.51
25R-1, 40–42	249.30	2.21	2.70	37.9	17.6	0.61
25R-1, 111–113	250.01	2.55	2.73	10.8	4.3	0.12
26R-1, 63–65	259.23	2.90	2.87	6.2	2.2	0.07
29R-1, 81–83	288.01	2.94	2.87	6.9	2.4	0.07

Table 47. Compressional wave velocity (HFV), Hole 858F.

Core, section, interval (cm)	Depth (mbsf)	Direction (a, b, c)	HFV velocity (m/s)
139-858F-			
2R-CC, 8–10	27.88	c	3531
4R-CC, 7–9	46.57	a	2673
4R-CC, 7–9	46.57	b	2906
4R-CC, 7–9	46.57	c	2939
4R-CC, 16–19	46.66	c	2777
4R-CC, 20–23	46.70	c	3728
6R-CC, 4–6	65.64	a	3942
6R-CC, 4–6	65.64	b	4141
6R-CC, 4–6	65.64	c	4177
9R-CC, 18–20	94.38	c	3371
9R-CC, 18–20	94.38	c	3786
13R-CC, 7–9	132.97	b	2649
18R-1, 56–59	181.86	c	2745
18R-CC, 7–13	182.09	c	2930
20R-CC, 7–10	200.67	c	3334
21R-1, 14–17	210.44	c	2698
21R-1, 21–24	210.51	c	2737
25R-1, 25–27	249.15	c	2604
25R-1, 40–42	249.30	a	2492
25R-1, 40–42	249.30	b	2126
25R-1, 40–42	249.30	c	2528
25R-1, 45–47	249.35	c	2742
25R-1, 85–88	249.75	c	4230
25R-1, 111–113	250.01	a	4040
25R-1, 111–113	250.01	b	4356
25R-1, 111–113	250.01	c	4152
25R-1, 113–115	250.03	c	4187
26R-1, 6–8	258.66	c	4202
26R-1, 22–24	258.82	c	5762
26R-1, 30–32	258.90	c	5929
26R-1, 43–45	259.03	c	5682
26R-1, 51–53	259.11	c	5611
26R-1, 61–63	259.21	c	5733
26R-1, 63–65	259.23	a	5728
26R-1, 63–65	259.23	b	5801
26R-1, 63–65	259.23	c	5531
26R-1, 74–76	259.34	c	5531
26R-1, 95–97	259.55	c	5575
26R-1, 110–112	259.70	c	5283
27R-1, 40–42	268.20	c	5475
28R-1, 1–3	277.51	c	4726
28R-1, 28–30	277.78	c	5234
28R-1, 45–47	277.95	c	5365
29R-1, 9–15	287.29	c	5960
29R-1, 23–34	287.43	c	5179
29R-1, 38–45	287.58	c	5883
29R-1, 50–55	287.70	c	5514
29R-1, 59–64	287.79	c	4687
29R-1, 64–69	287.84	c	4637
29R-1, 69–75	287.89	c	5480
29R-1, 75–86	287.95	c	5219
29R-1, 90–98	288.10	c	5903
29R-1, 98–105	288.18	c	5455
29R-1, 106–111	288.26	c	5288
29R-1, 118–122	288.38	c	5226

Table 48. Thermal conductivity, Hole 858F.

Core, section, interval (cm)	Piece	Depth (mbsf)	Thermal conductivity (W/[m·K])
139-858F-			
2R-CC, 8–10		27.88	1.5
9R-CC, 16–23		94.36	1.44
18R-CC, 7–13		182.09	1.4
21R-1, 14–25		210.44	1.32
25R-1, 22–30		249.12	1.7
26R-1, 4–10	1	258.64	1.
26R-1, 19–25	3	258.79	1.6
26R-1, 26–35	4	258.86	1.8
26R-1, 58–66	7B	259.18	1.58
26R-1, 90–102	11	259.50	1.5

Note: All measurements were made in the half-space configuration.

tions that did not change with AF demagnetization were observed at 15–17 mbsf and 20–21 mbsf, but only one of these could be duplicated on the archive half of the core, suggesting that they may be artifacts of drilling. There is no clear correlation between magnetic susceptibility and intensity. The lowest susceptibility value measured on Leg 139 was obtained on sediment from 13 to 18 mbsf in Hole 858C, from a zone rich in authigenic carbonate. Interbedded sequences of turbidites and pelagic clay were identified as at previous sites by their characteristic volume magnetic susceptibility of 0.002–0.003 interspersed with intervals up to one order of magnitude lower. Carbonate concentrations become more abundant with depth in Holes 858A (23.0–36.0 mbsf) and 858C (13.0–23.0 mbsf) and susceptibility decreases sharply. These occurrences suggest increased diagenetic and hydrothermal activity; the lack of a magnetic susceptibility signal may result from alteration of magnetite in the basal turbidites to iron sulfide.

Thermal conductivity is generally low normal in sediments recovered from all holes; isolated higher values were observed at depths where silicified or otherwise diagenetically altered sediments were encountered. Porosities at high-temperature locations (Holes 858B and 858D) do not differ significantly from those observed in Hole 858A and at Sites 856 and 857. This suggests that compaction, not diagenesis, plays the dominant role in the reduction of porosity in these sediments.

Most of the compressional wave velocity measurements were made on samples from Hole 858A, where recovery was good. Velocity anisotropy measured on unconsolidated to lithified sediment increased from 1% at the seafloor to a maximum value of 30% at 270 mbsf. The highest anisotropy was seen in claystone samples; fine-grained sandstone values are generally lower and average 10%.

The formation microscanner provided nearly continuous and clear images of the walls of Hole 858F. Numerous thin, rhythmically distributed bands of higher resistivity were imaged (expressed as light color) that are undoubtedly turbidite silt and sand layers. These contrast with the dark background produced by interbedded clay with higher porosity and lower electrical resistivity. The resolution of the turbidite beds in the resistivity log was sufficient to attempt a stratigraphic correlation between sections at this site and Site 857. Thicker sediment at the latter site suggests that Site 858 was topographically higher and received somewhat attenuated turbiditic beds. The lower 10 m of the logged interval (257.6 to 267 mbsf) is high-resistivity basalt that produces a light FMS image, with fractures seen as darker lines. The microscanner imaged two basalt units separated by a thin layer of sediment. The basalt units appear to be pillows with an extensive network of veins. The results of the resistivity, density, and natural gamma logs in Hole 858G indicate that most of the drilled section is basalt. The logging runs did not go to the bottom of Hole 858G because of excessive temperatures.

Seven deployments of temperature logging tools were made at four holes at Site 858. A deployment accident in Hole 858F led to a unintentional 19-hr temperature measurement with the GRC tool at

Table 49. Summary of logging operations at Site 858.

Deployment number	Begin/End Date, Time (PST)	Logging string/tools	Interval logged (mbsf)
858A-1	12 Aug., 1840 12 Aug., 2240	GRC high-temperature tool	70–264
858B-1	13 Aug., 2209 14 Aug., 0210	GRC high-temperature tool	Bottom-hole temperature at 37 mbsf
858F-1	18 Aug., 0811 19 Aug., 0400	GRC high-temperature tool	[a]Bottom-hole temperature at 264 mbsf
858F-2	18 Aug., 1645 18 Aug., 2200	Japex high-temperature tool	0–241
858F-3	19 Aug., 1245 19 Aug., 1830	Seismic stratigraphic DIT/LSS/NGT	29–299
858F-4	19 Aug., 2020 20 Aug., 0200	Formation microscanner FMS/GPIT/NGT	48–259
858G-1	3 Sept., 0532 3 Sept., 0840	GRC high-temperature tool	0–160, in casing
858G-2	6 Sept., 1052 6 Sept., 1452	GRC high-temperature tool	0–379
858G-3	7 Sept., 0740 7 Sept., 1400	Lithology/density DIT/HDLT/NGT	241–348
858G-4	7 Sept., 1758 7 Sept., 2200	GRC high-temperature tool	0–398

[a]The GRC high temperature tool accidently free-fell to the bottom of the hole, and was fished out about 19 hr later. The instrument still contained valid data and suffered only minor damage.

Table 50. Summary of operations and results of the 18 sediment temperature measurements made during coring at Holes 858A through 858E.

Core[a]	Depth[a] (mbsf)	Tool	Quality[b]	Temperature[c] (° C)	Comments
139-858A-					
3H	21.4	APC	Excellent	39.2 ± 0.3	
4H	30.9	APC	Excellent	55.3 ± 0.3	
5H	40.4	APC	Excellent	67.3 ± 0.3	
6H	[d]45.1–49.9	APC	Excellent	77.2 ± 0.5	Partial stroke
7H	[d]58.9–59.4	APC	Excellent	91.1 ± 0.5	Partial stroke
8H	[d]62.5–68.9	APC	Excellent	98.2 ± 0.5	Partial stroke
10P	74.4	WSTP	Good	97.1 ± 0.5	Low, in fill? Poor water sample
12X	92.4	WSTP	Good	119.5 ± 1.0	Low, in fill?
14X	111.7	WSTP	Very good	153.5 ± 0.5	
139-858B-3H	19.5	WSTP	Excellent	196.6 ± 0.5	Highest WSTP value ever measured
139-858C-					
2H	13.0	APC	Excellent	46.9 ± 0.3	
3H	22.5	APC	Excellent	67.3 ± 0.3	
4P	24.6	WSTP	Very good	71.3 ± 0.3	
5H	33.0	APC	Very good	92.0 ± 0.5	
7H	42.6	WSTP	Very good	122.2 ± 0.5	Disturbed
139-858D-					
2H	18.8	APC	Poor	>127	Too hot for tool electronics
3P	20.9	WSTP	Fair	~208	Disturbance when sampler opened
139-858E-1W	31.8	WSTP	Poor	?	Reentered Hole 858D, probe unsupported

[a]WSTP measurements were made after the core specified; for all WSTP measurements, the depth listed is 1.1 m greater than the maximum depth of this core.
[b]Quality is subjective and based on interpretations described in the text.
[c]Estimated error is based on a subjective assessment of deployment operations and how well recovered data fit a theoretical model.
[d]On partial stroke of APC, the first depth given was calculated from core recovery and is considered the best estimate of actual penetration; the second depth given is the maximum possible depth if the stroke was completed.

the bottom of Hole 858F. Extrapolation to equilibrium yields an estimated temperature of 250° to 260°C, similar to that of nearby vent water. During the 19 hr that the GRC tool was lost in Hole 858F, a temperature profile was measured with the JAPEX high-temperature tool. The temperatures and temperature gradients from this profile are much lower than the equilibrium conductive curve inferred from the measurement at the bottom of the hole. The fill at the bottom of the hole, in which the GRC tool was stuck, apparently approached equilibrium more rapidly than the water in the open hole. Three temperature profiles were also measured in Hole 858G with the GRC tool. The maximum temperature observed was 268°C at only 25 mbsf. Colder water near 100°C occupies the interval from 40 to 125 mbsf in Hole 858F; this fluid probably originated as cold bottom water drawn down into Hole 858F only 10 m away.

Temperature was measured in the sediment in Holes 858A through 858D. Gradients in the upper 10 to 100 mbsf vary from 1.7°C/m in Hole 858A, to 3°C/m in Hole 858C, to 10.6°C/m in Holes 858B and 858D. The temperature of 197°C measured with the WSTP at 19.5 mbsf in Hole 858B is the highest sediment temperature ever measured *in-situ* during the DSDP or ODP. Conductive heat flow calculated for Hole 858A is 1.9 W/m^2, although a Bullard plot of temperature vs. thermal resistance does not preclude transient or nonconductive thermal conditions. Conductive heat flow in Hole 858C is 3.3 W/m^2 but there is even more structure in the Bullard plot. Heat flow estimated from single measurements of sediment temperature in each of Holes 858B and 858D is 10.6 W/m^2. Shipboard results did not indicate active discharge of hot water from any of the holes, although venting was observed from Hole 858B two months after Leg 139 during a manned submersible study.

Special experiments in the cased deep Hole 858G were similar to those in Hole 857D and included packer experiments to determine bulk permeability and formation fluid pressure, and a flowmeter log to measure downhole flow and assess the fine-scale distribution of permeability. The packer was deployed three times within the casing at about 100 mbsf as a double-seal single packer. It measured an underpressure in the hole of about 0.5 MPa and a bulk permeability that is significantly lower than that found in Hole 857D. Accurate estimates of permeability will have to account for superimposed residual pressure decays from earlier pulse tests. The flowmeter tests did not resolve induced flow down Hole 858G following drilling, in contrast to the strong flow down Hole 857D. At the end of operations at Site 858, Hole 858G was sealed with a CORK that will allow long-term monitoring of downhole temperature and pressure and periodic fluid sampling.

REFERENCES

Bandy, O. L., 1960. The geological significance of coiling ratios in the foraminifer *Globigerina pachyderma* (Ehrenberg). *J. Paleontol.*, 34:671–681.

Bergen, F. W., and O'Neil, P., 1979. Distribution of Holocene foraminifera in the Gulf of Alaska. *J. Paleontol.*, 53:1267–1292.

Bird, D., and Helgeson, H., 1981. Chemical interaction of aqueous solutions with epidote-feldspar mineral assemblages in geologic systems: II. Equilibrium constraints in metamorphic/geothermal processes. *Am. J. Sci.*, 281:576–614.

Brassell, S. C., Eglinton, G., Marlowe, I. T., Pflaumann, U., and Sarnthein, M., 1986. Molecular stratigraphy: a new tool for climatic assessment. *Nature*, 320:129–133.

Bullard, E. C., 1939. Heat flow in South Africa. *Proc. R. Soc. London A*, 173:474–502.

————, 1954. The flow of heat through the floor of the Atlantic Ocean. *Proc. R. Soc. London A*, 222:408–429.

Claypool, G. E., 1975. *Manual on Pollution—Prevention and Safety* (3rd ed.). JOIDES J.

Curray, J. R., Moore, D. G., et al., 1982. *Init. Repts. DSDP*, 64 (Pt. 1): Washington (U.S. Govt. Printing Office).

Farrimond, P., Poynter, J. G., and Eglinton, G., 1990. A molecular stratigraphic study of Peru Margin sediments, Hole 686B, Leg 112. *In* Suess, E., von Huene, R., et al., *Proc. ODP, Sci. Results*, 112: College Station, TX (Ocean Drilling Program), 547–553.

Gartner, S., Jr., 1977. Calcareous nannofossils biostratigraphy and revised zonation of the Pleistocene. *Mar. Micropaleontol.*, 2:1–25.

Gieskes, J., and Peretsman, G., 1986. Water chemistry procedures aboard *JOIDES Resolution*—some comments. *Tech. Note No. 5*, Ocean Drilling Program.

Goldhaber, M. B., and Kaplan, I. R., 1974. The Sulfur Cycle. *In* Goldberg, E. D. (Ed.), *The Sea* (Vol. 5): New York (Wiley-Interscience), 569–655.

Goodfellow, W. D., and Blaise, B., 1988. Sulfide formation and hydrothermal alteration of hemipelagic sediment in Middle Valley, Northern Juan de Fuca Ridge. *Can. Mineral.*, 26:675–696.

Grimalt, J. and Albaiges, J., 1987. Sources and occurrence of C_{12}–C_{22} *n*-alkane distributions with even carbon-number preference in sedimentary environments. *Geochim. Cosmochim. Acta*, 51:1379–1384.

Horai, K., and Von Herzen, 1985. Measurement of heat flow on Leg 86 of the Deep Sea Drilling Project. *In* Heath, G. R., Burckle, L. H., et al., *Init. Repts. DSDP*, 86: Washington (U.S. Govt. Printing Office), 759–777.

Horner, D. R., 1951. Pressure build-up in wells. *Proc. Third World Pet. Congr.*, 2:501.

Hunt, J. M., 1979. *Petroleum Geology and Geochemistry:* San Francisco (W. H. Freeman).

Johnson, H. P., Franklin, J. M., and Currie, R. G., in press. SeaMARC IA Acoustic Imagery of the Middle Valley Area, northern Juan de Fuca Ridge. *Open-File Rep., Geol. Surv. Can.*

Karsten, J. L., Delaney, J. R., Rhodes, J. M., and Liias, R. A., 1990. Spatial and temporal evolution of magmatic systems beneath the Endeavour segment, Juan de Fuca Ridge: tectonic and petrological constraints. *J. Geophys. Res.*, 95:19235–19256.

Kawka, O. E., and Simoneit, B.R.T., 1987. Survey of hydrothermally-generated petroleums from the Guaymas Basin spreading center. *Org. Geochem.*, 11:311–328.

Kiyosu, Y., 1980. Chemical reduction and sulfur-isotope effects of sulfate by organic matter under hydrothermal conditions. *Chem. Geol.*, 30:47–56.

Kvenvolden, K. A., Rapp, J. B., Hostettler, F. D., Morton, J. L., King, J. D., and Claypool, G. E., 1986. Petroleum associated with polymetallic sulfide in sediment from Gorda Ridge. *Science*, 234:1231–1234.

Lachenbruch, A. H., and Brewer, M. C., 1959. Dissipation of the temperature effect in a well in Arctic Alaska. *U.S. Geol. Surv. Bull.*, 1083-C:73–109.

Lagoe, M. B., and Thompson, P. R., 1988. Chronostratigraphic significance of Late Cenozoic planktonic foraminifera from the Ventura Basin, California: potential for improving tectonic and depositional interpretation: *J. Foraminiferal Res.*, 18:250–266.

Liou, J. G., Kim, H. S., and Maruyama, S., 1983. Prehnite-epidote equilibria and their petrologic applications. *J. Petrol.*, 24:321–342.

Marlowe, I. T., Brassell, S. C., Eglinton, G., and Green, J. C., 1984. Long chain unsaturated ketones and esters in living algae and marine sediments. *Org. Geochem.*, 6:135–141.

Martini, E., 1971. Standard Tertiary and Quaternary calcareous nannoplankton zonation. *In* Farinacci, A. (Ed.), *Proc. 2nd Planktonic Conf. Roma:* Rome (Ed. Tecnosci.), 2:739–785.

Matthews, C. S., and Russell, D. G., 1967. *Pressure Buildup and Flow Tests in Wells.* SPE-AIME, Monogr. 1.

Pearce, J. A., and Cann, J. R., 1973. Tectonic setting of basic volcanic rocks determined using trace element analyses. *Earth Planet. Sci. Lett.*, 19:290–300.

Poynter, J. G., Farrimond, P., Brassell, S. C. and Eglinton, G., 1989. Molecular stratigraphic study of sediments from Holes 658A and 660A, Leg 108. *In* Ruddiman, W., Sarnthein, M. et al., *Proc. ODP, Sci. Results*, 108: College Station, TX (Ocean Drilling Program), 387–394.

Prahl, F. G., and Wakeham, S. G., 1987. Calibration of unsaturation patterns in long-chain ketone compositions for paleotemperature assessment. *Nature*, 330:367–369.

Rohr, K. M., Davis, E. E., and Hyndman, R. D., 1992. Multichannel seismic reflection profiles across Middle Valley, northern Juan De Fuca Ridge. *Geol. Surv. Can. Open-File Rep.* 2476.

Sautter, L. R., and Thunell, R. C., 1991. Planktonic foraminiferal response to upwelling and seasonal hydrographic conditions: sediment trap results from San Pedro Basin, Southern California Bight. *J. Foraminiferal Res.*, 21:347–363.

Simoneit, B.R.T., 1977. Diterpenoid compounds and other lipids in deep-sea sediments and their geochemical significance. *Geochim. Cosmochim. Acta*, 41:463–476.

————, 1978. The organic chemistry of marine sediments. *In* Riley, J. P., and Chester, R. (Eds.), *Chemical Oceanography* (Vol. 7) (2nd ed.): New York (Academic Press), 233–311.

————, 1985. Hydrothermal petroleum: genesis, migration and deposition in Guaymas Basin, Gulf of California. *Can. J. Earth Sci.*, 22:1919–1929.

———— (Ed.), 1990a. Organic matter in hydrothermal systems-maturation, migration and biogeochemistry. *Appl. Geochem.*, 5:1–248.

————, 1990b. Petroleum generation, an easy and widespread process in hydrothermal systems: an overview. *Appl. Geochem.*, 5:3–15.

Simoneit, B.R.T. and Lonsdale, P. F., 1982. Hydrothermal petroleum in mineralized mounds at the seabed of Guaymas Basin. *Nature*, 295:198–202.

Simoneit, B.R.T., Goodfellow, W. D., and Franklin, J. M., in press. Hydrothermal petroleum at the seafloor and organic matter alteration in sediments of Middle Valley, northern Juan de Fuca Ridge. *Applied Geochem.*

Taylor, B. E., 1990. Carbon dioxide and methane in hydrothermal vent fluids from Middle Valley. *Eos*, 71:1569.

Thunell, R. C., and Reynolds, L. A., 1984. Sedimentation of planktonic foraminifera: seasonal changes in species flux in the Panama Basin. *Micropaleontology*, 30:241–260.

Whelan, J. K., Hunt, J. M., Jasper, J., and Huc, A., 1984. Migration of C_1–C_8 hydrocarbons in marine sediments. *Org. Geochem.*, 6:683–694.

Ms 139A-108

NOTE: For all sites drilled, core description forms ("barrel sheets") and core photographs have been printed on coated paper and bound as Section 3, near the back of the book, beginning on page 573. Forms containing smear slide data are bound as Section 4, beginning on page 933. Thin-section data are given in Section 5, beginning on page 949.

Formation microscanner images for this site are presented on microfiche in the back of the book.

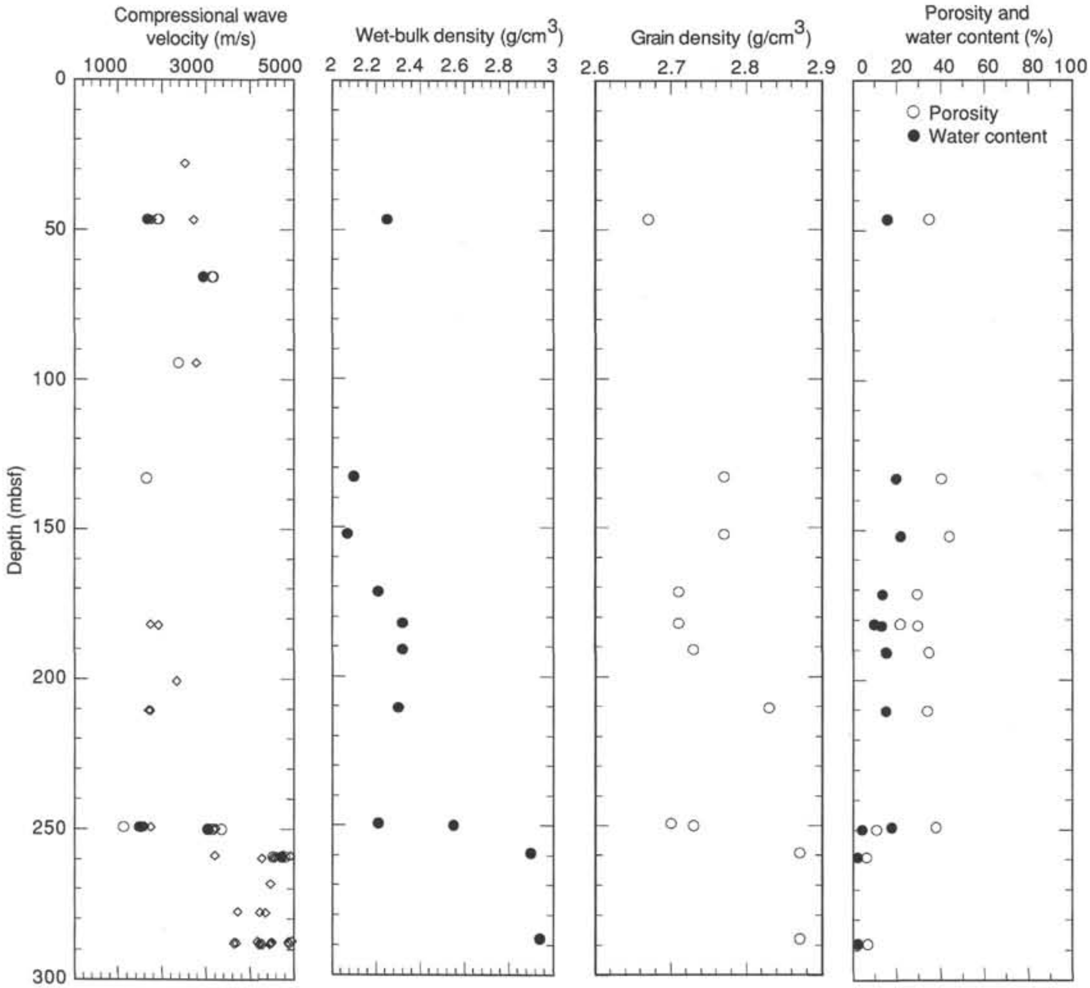

Figure 90. Compressional wave velocity, wet-bulk density, grain density, and porosity and water content vs. depth in Hole 858F. Open (transverse velocity) and solid (longitudinal velocity) diamonds in plot of compressional wave velocity are data measured by the digital sound velocimeter (DSV); open squares and open triangles are data from the Hamilton frame velocimeter (HFV) either measured on half-core pieces or taken as in-liner measurements in the c-direction (transverse); open and solid circles are measurements on cubes in b- or c-directions and in a-direction, respectively.

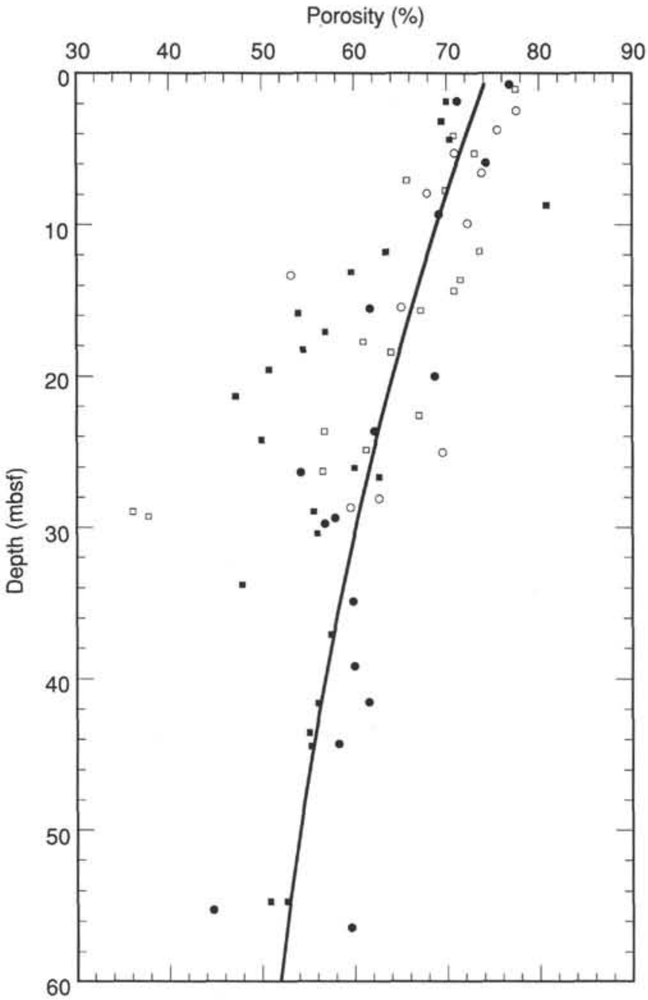

Figure 91. Comparison of porosity-depth profiles at Site 858 with data from Holes 858A (solid circles), 858B (open circles), 858C (solid squares), and 858D (open squares).

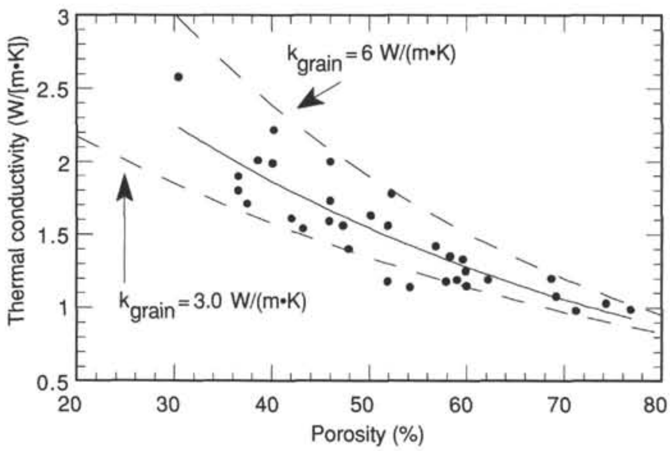

Figure 92. Correlation of thermal conductivity with porosity in Hole 858A. Dashed lines are calculated geometric-mean thermal conductivities for two different grain thermal conductivities. The solid line is the best-fit geometric mean grain thermal conductivity with a value of 3.9 W/(m·K). A value of 0.6 W/(m·K) was used as the thermal conductivity of seawater.

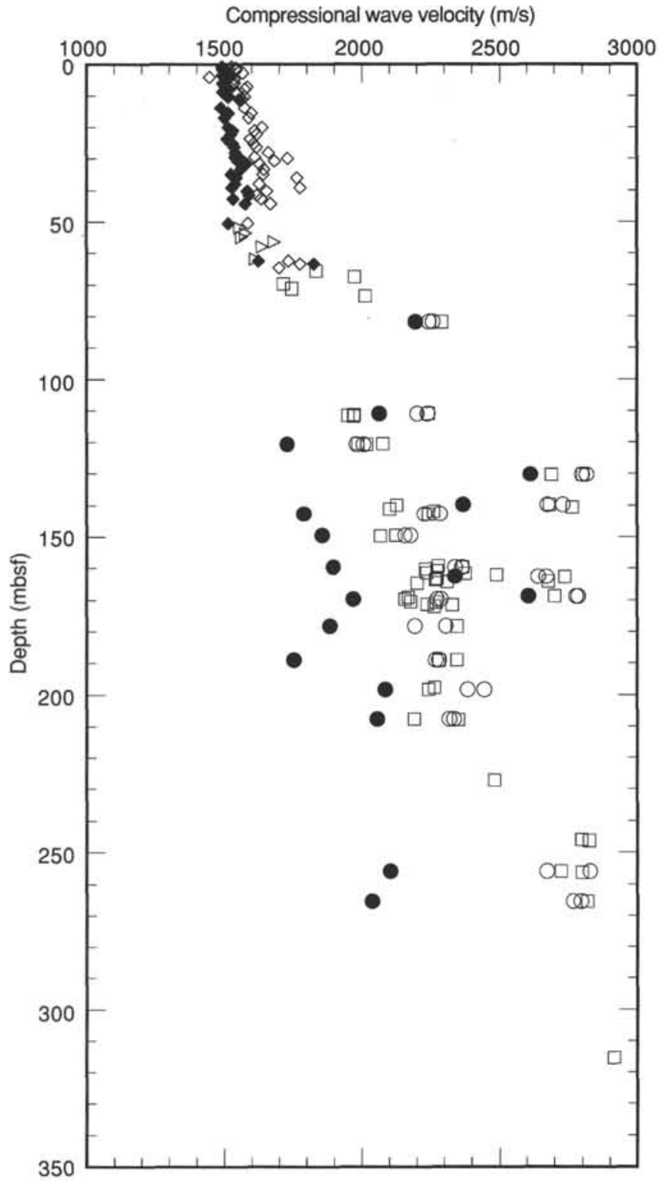

Figure 93. Measured compressional wave velocity in Hole 858A. Open (transverse velocity) and solid (longitudinal velocity) diamonds are velocities measured by the digital sound velocimeter (DSV); open squares and open triangles are data from the Hamilton frame velocimeter (HFV) either measured on half-core pieces or taken as in-liner measurements in the c-direction (transverse); open and solid circles are measurements on cubes in b- or c-directions and in a-direction, respectively.

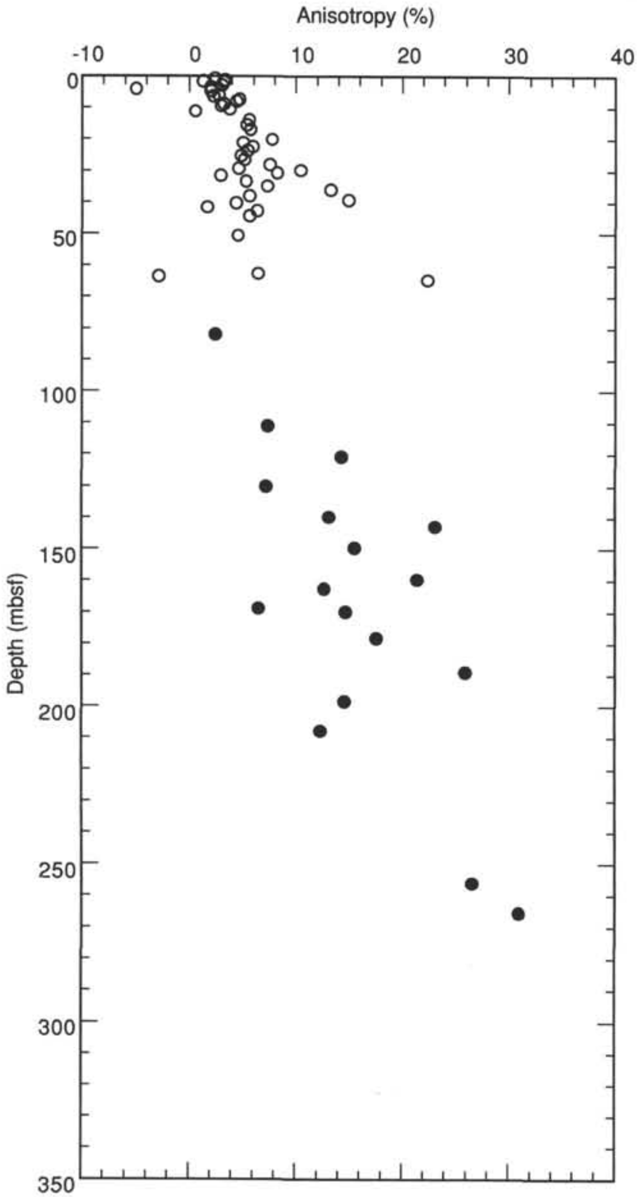

Figure 94. Compressional wave velocity anisotropy calculated from measurements with the DSV on half-round samples (unconsolidated sediments) and with the HFV on sample cubes from Hole 858A. Values for the sediments are shown as open circles, values for indurated sediments as solid circles.

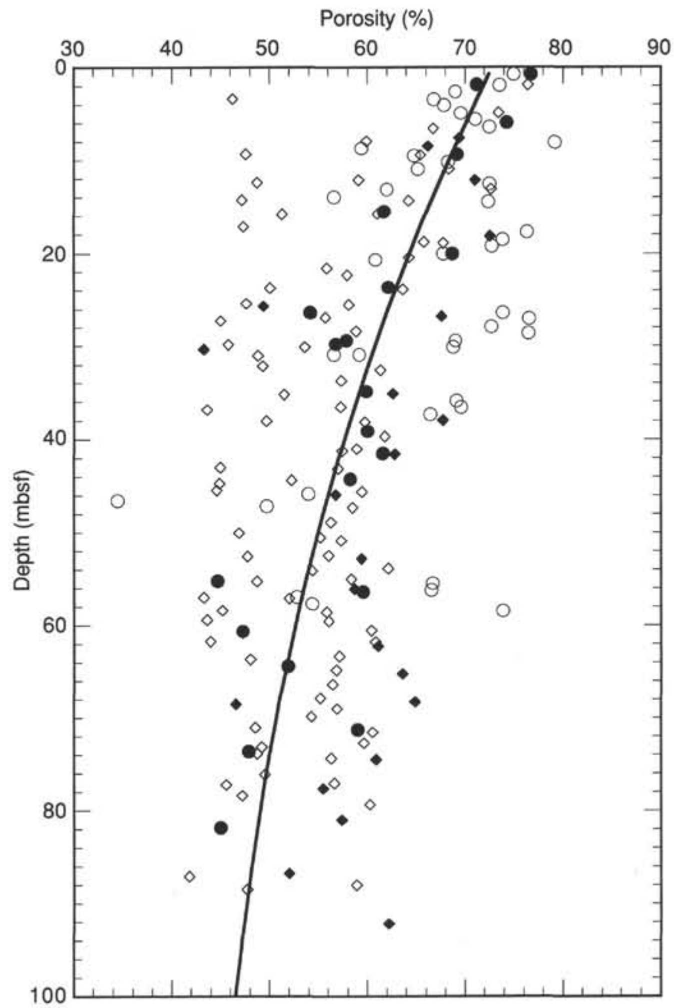

Figure 95. Intersite comparison of porosity-depth profiles from Holes 855A (open circles), 856A (open diamonds), 857A (solid diamonds), and 858A (solid circles). The heavy line is a third-order polynomial fit of the porosity-depth profile of Hole 858A, showing the decrease of porosity.

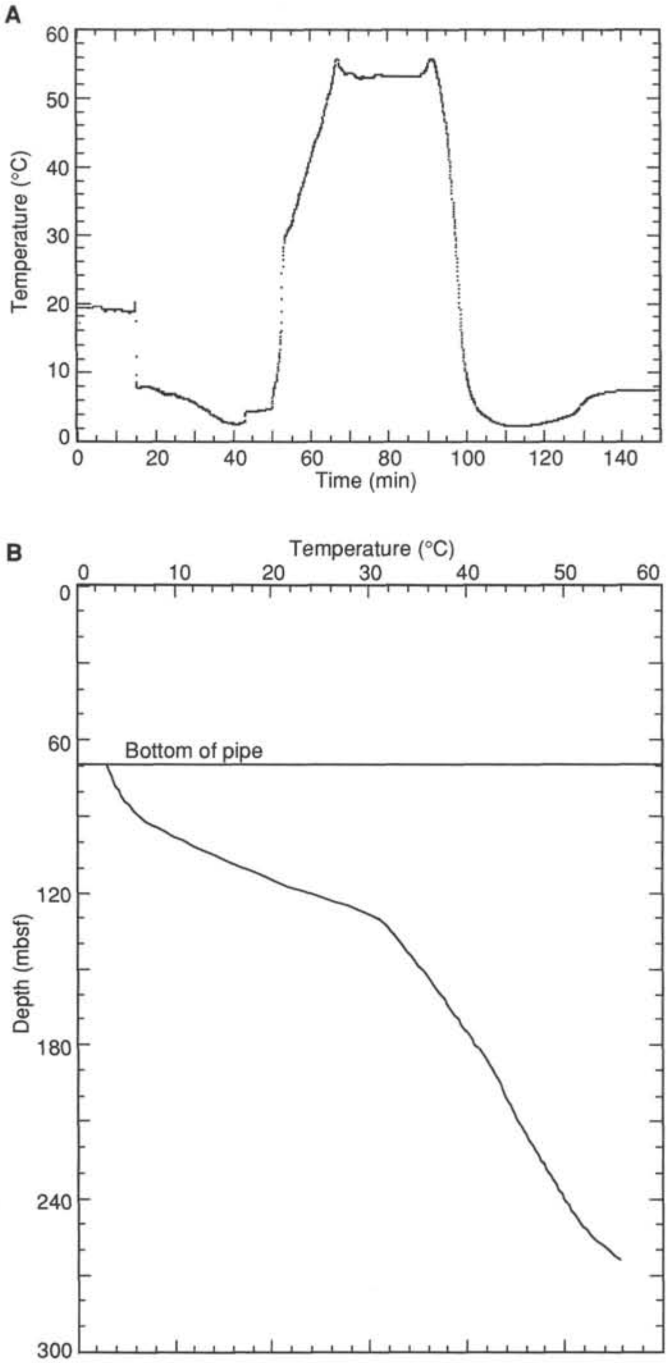

Figure 96. **A.** Temperature-time history recorded by the GRC high-temperature probe during a run in Hole 858A. **B.** Temperature vs. depth profile in Hole 858A.

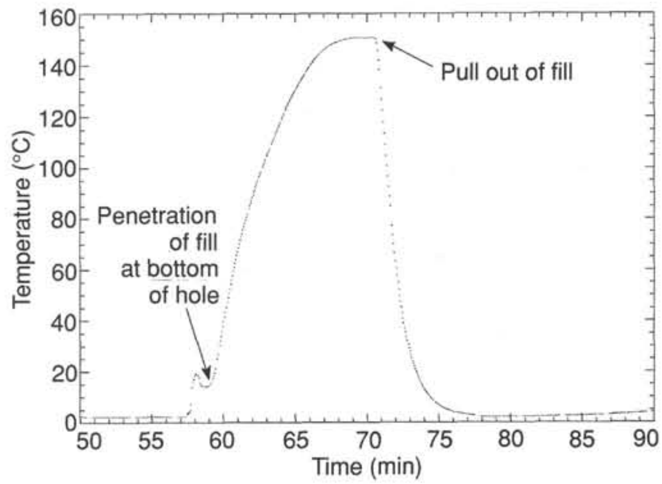

Figure 97. Temperature recorded by the GRC high-temperature probe in Hole 858B at a depth of 37 mbsf.

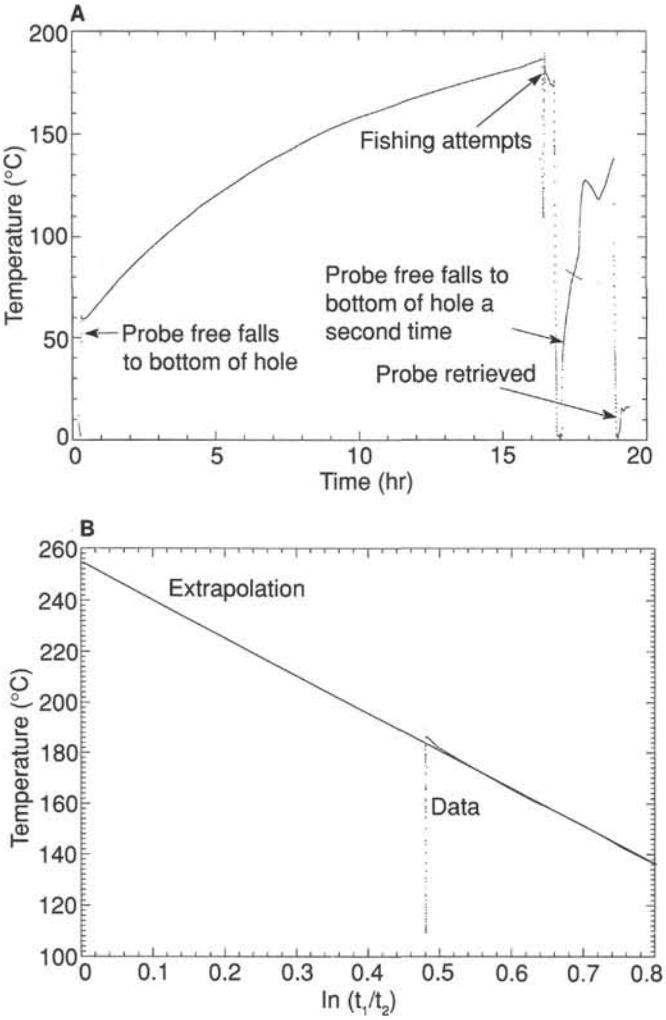

Figure 98. **A.** A 19-hr temperature history recorded by the GRC high-temperature tool after it fell to the bottom of Hole 858F. **B.** The temperature extrapolated to equilibrium using the model of Lachenbruch and Brewer (1959): $T(0,t) = A \times \ln(t_1/t_2)$, where t_1 is time measured from the time that circulation started and t_2 is the time measured from when circulation stopped.

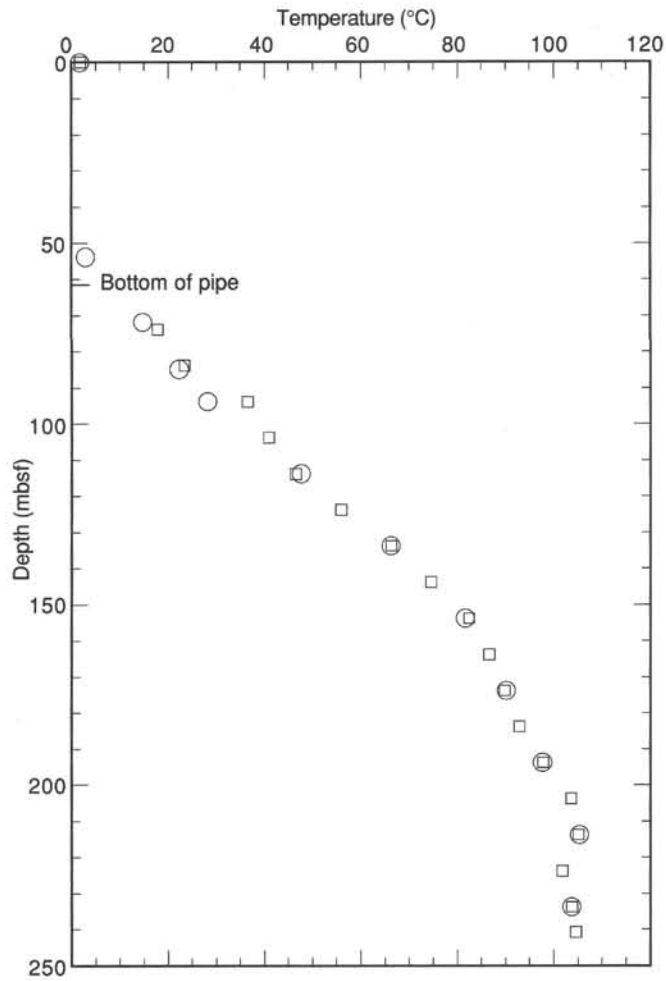

Figure 99. Temperature profile measured in Hole 858F with the JAPEX tool while the GRC probe was buried in fill at the bottom of the hole. Open squares denote logging down and open circles denote logging up.

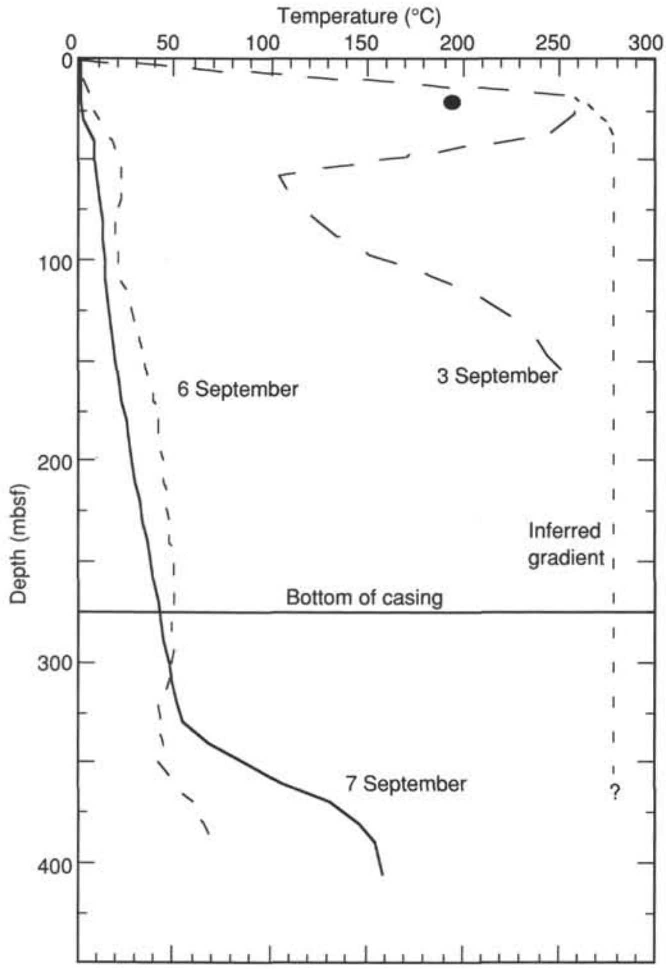

Figure 100. Three temperature profiles measured in Hole 858G. See Table 49 and text. The solid circle is the WSTP measurement made in Hole 858B. An inferred *in-situ* gradient below the upper 20 mbsf is also shown.

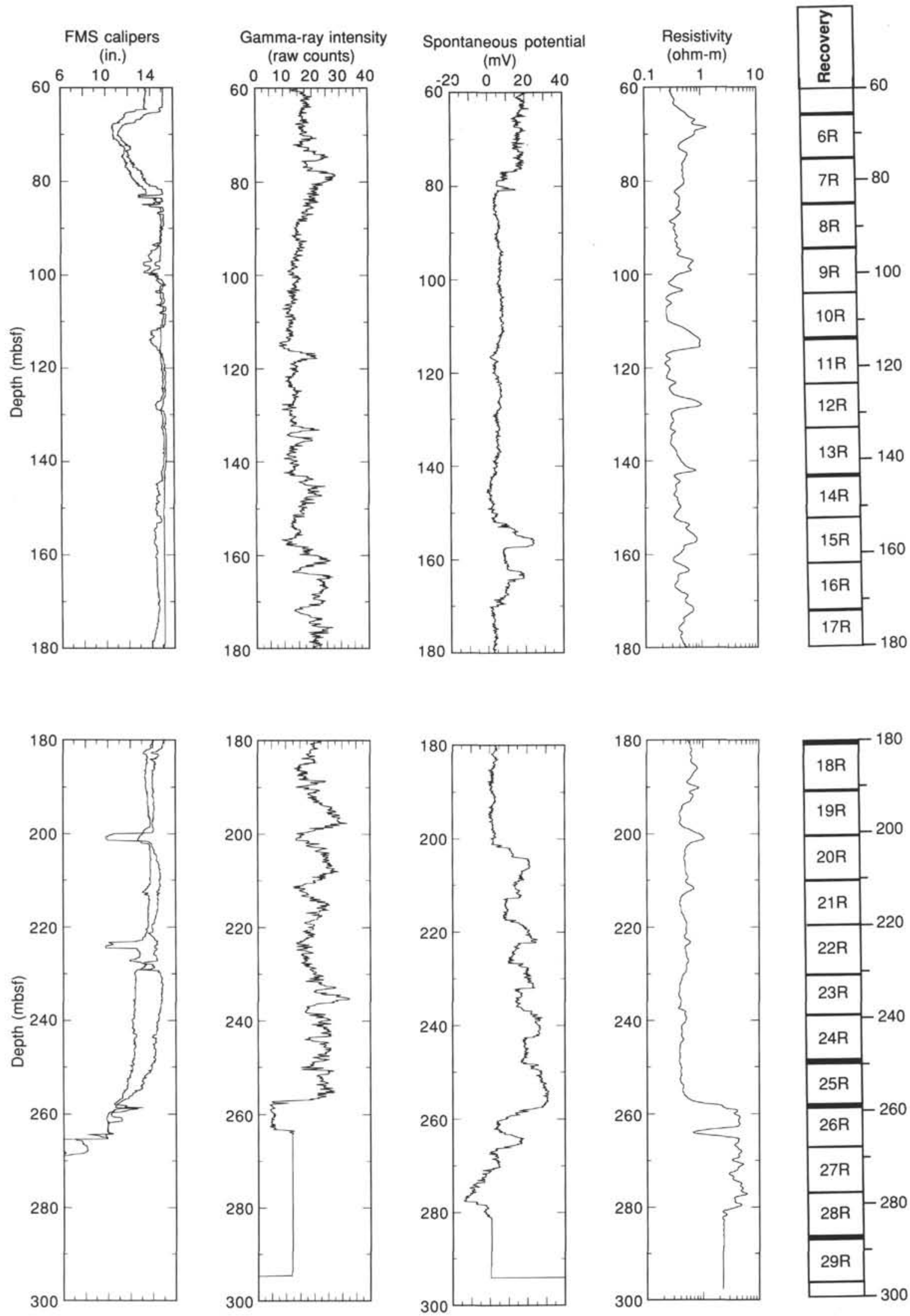

Figure 101. Summary plot of logging in Hole 858F. The caliper logs are from the formation microscanner log; the resistivity profile was made with the dual induction tool. Sonic results were noisy and are not included.

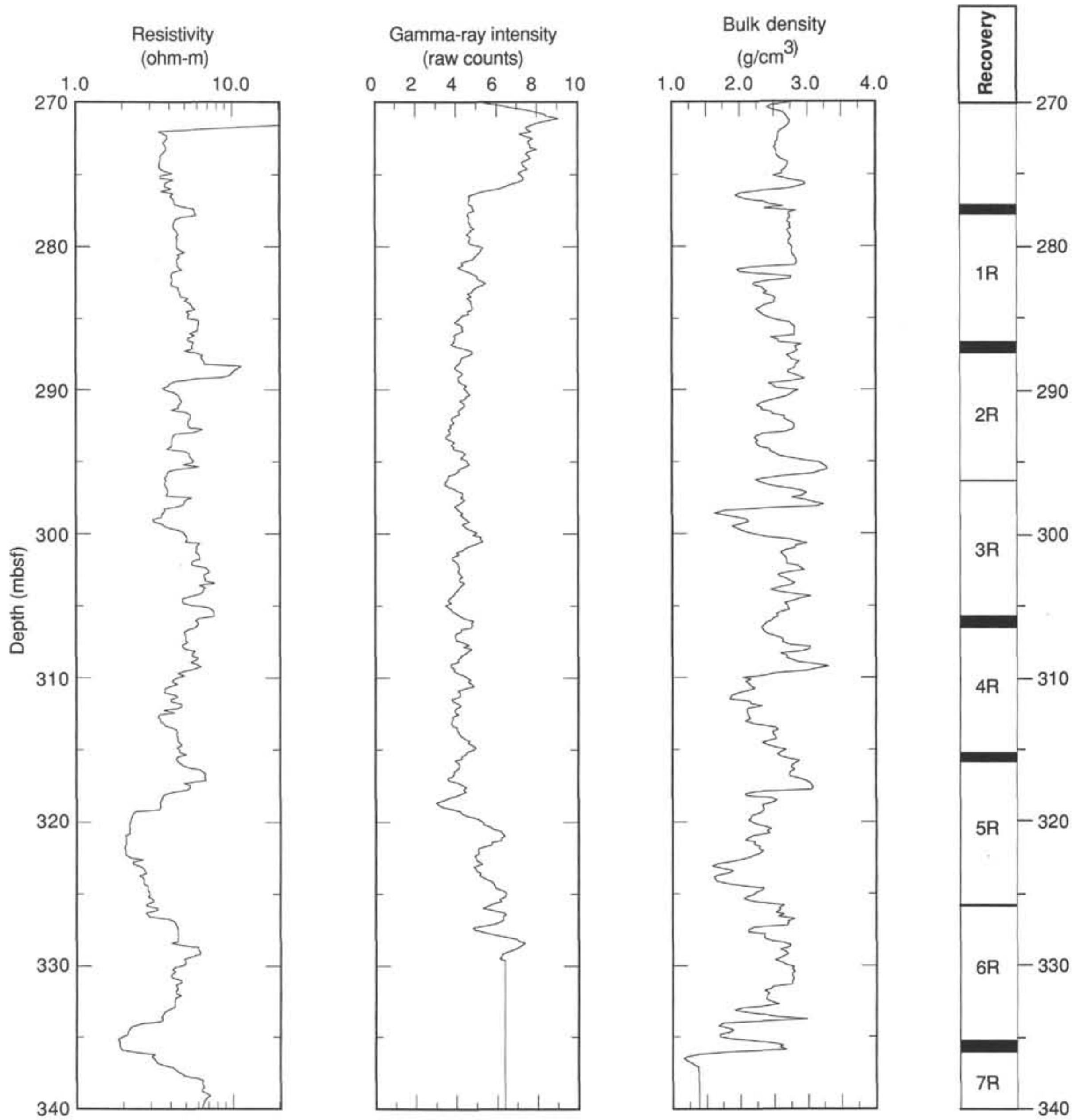

Figure 102. Summary plot of logging in Hole 858G.

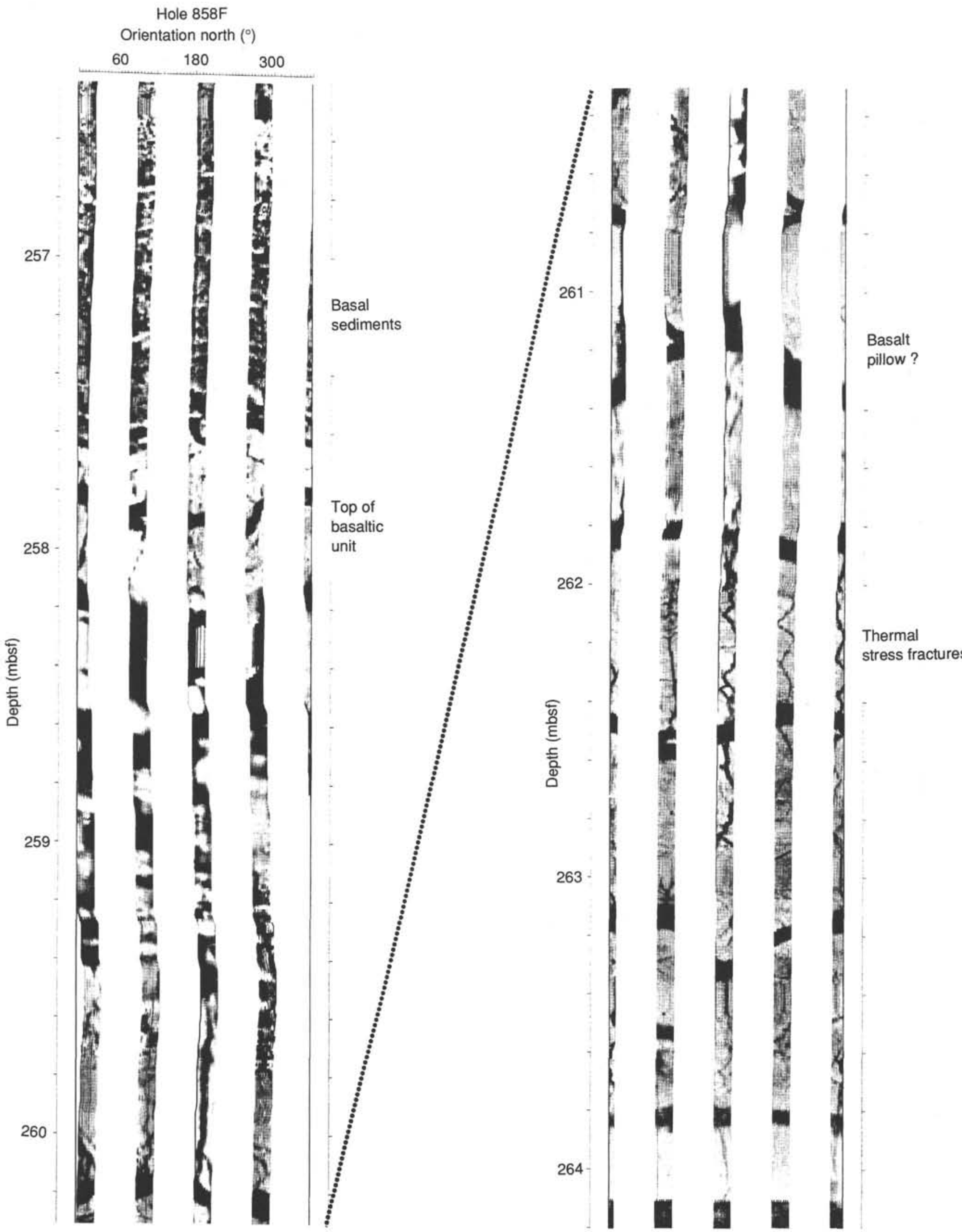

Figure 103. Formation microscanner image in the bottom of Hole 858F showing the contact between the sediments and the uppermost volcanic unit.

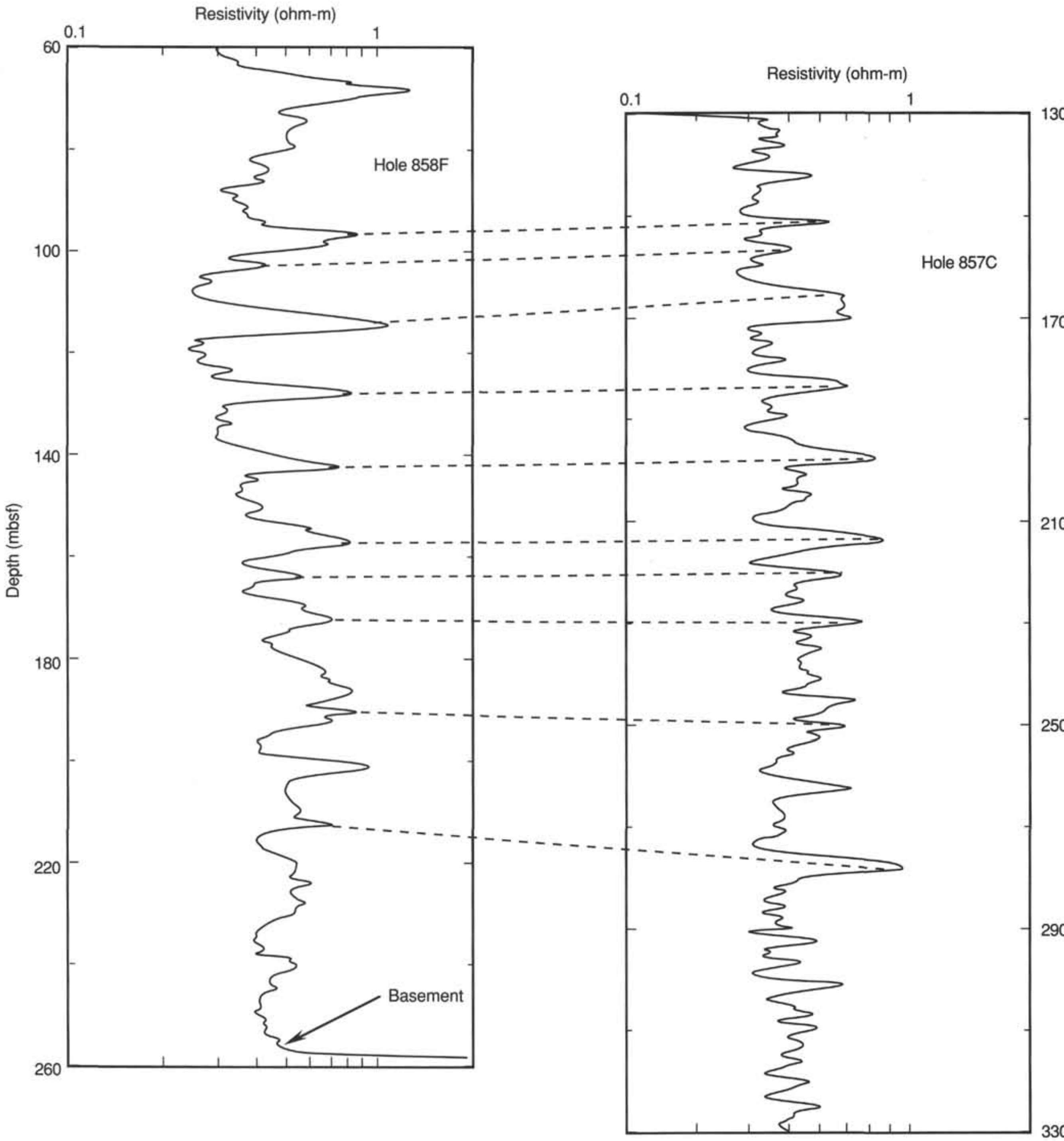

Figure 104. A comparison of the resistivity curves logged in Holes 858F with 857C. Note that the depth scales have been shifted to get the best correlation near the top of the section.

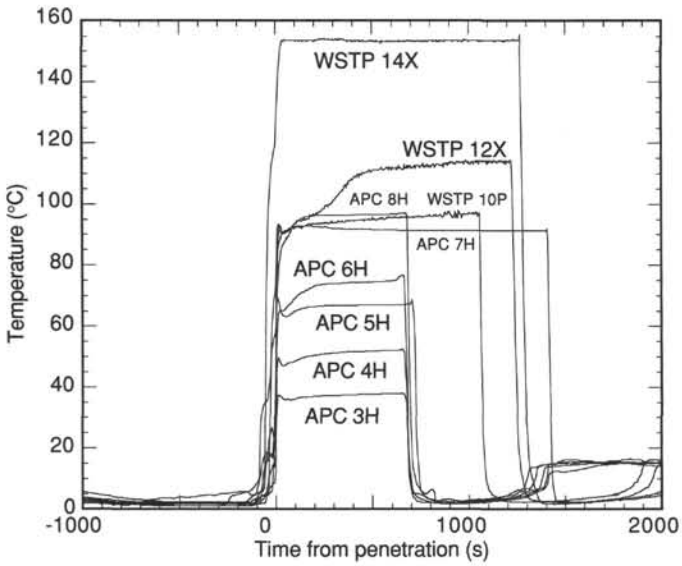

Figure 105. Temperature-time records for the six deployments of the APC temperature recorder and the three deployments of the WSTP in Hole 858A. Core numbers and letters are indicated.

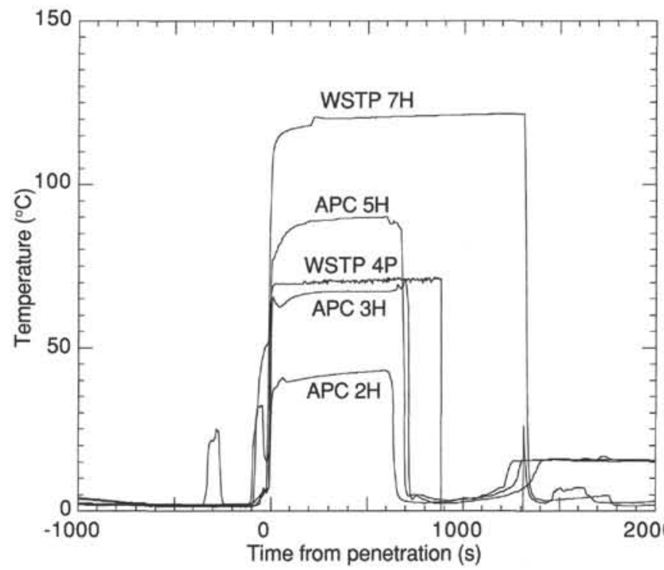

Figure 106. Temperature-time records for the three deployments of the APC temperature recorder and the two deployments of the WSTP in Hole 858C. Core numbers and letters are indicated.

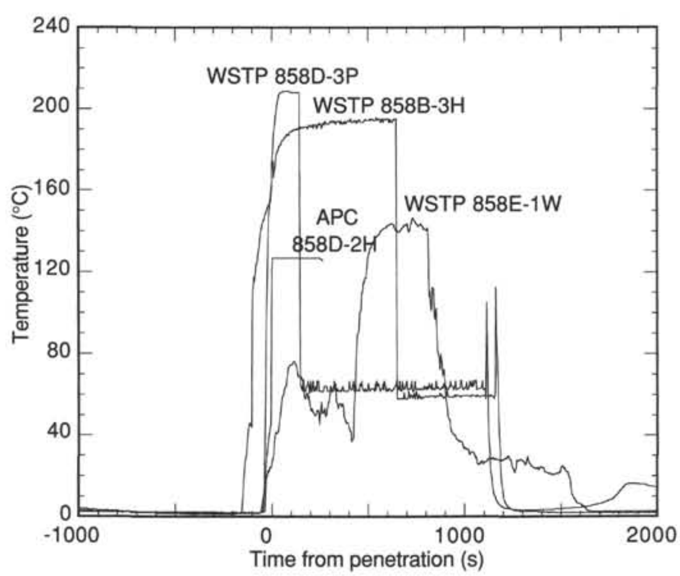

Figure 107. Temperature-time records for the single deployment of the APC temperature recorder and the three deployments of the WSTP under conditions of extremely high heat flow in Holes 858B, 858D, and 858E.

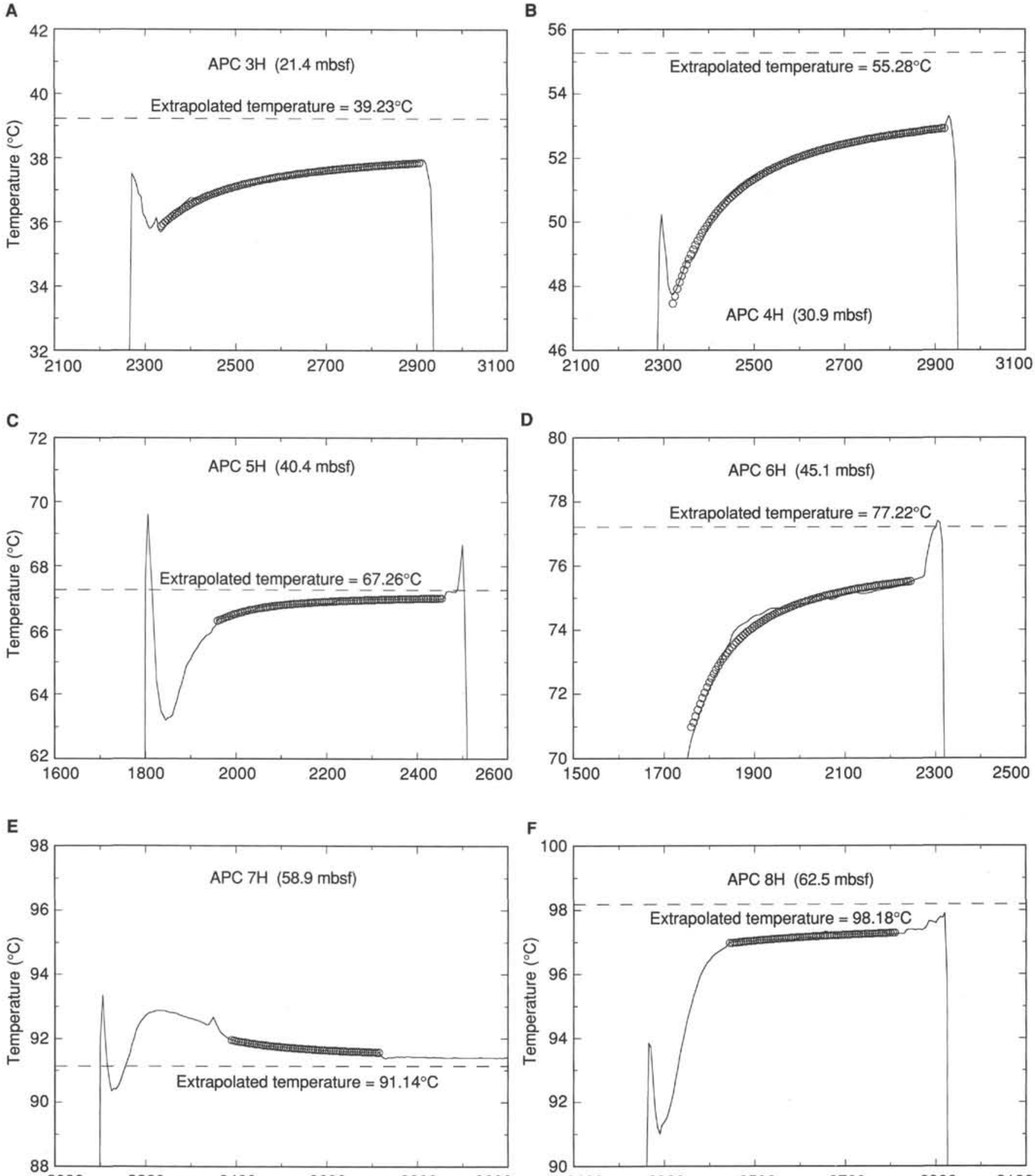

Figure 108. Temperatures measured with the APC tool during recovery of Cores 139-858A-3H, -4H, -5H, -6H, -7H, and -8H (**A–F**, respectively) and with the WSTP after recovery of Cores 139-858A-10P, -12X, and -14X (**G–I**, respectively), showing the best-fit theoretical decay curves and extrapolated *in-situ* temperatures. In each case, the solid line shows measured temperatures, circles indicate those that were fit to the theoretical decay curves, and the dashed line represents the extrapolated *in-situ* temperature.

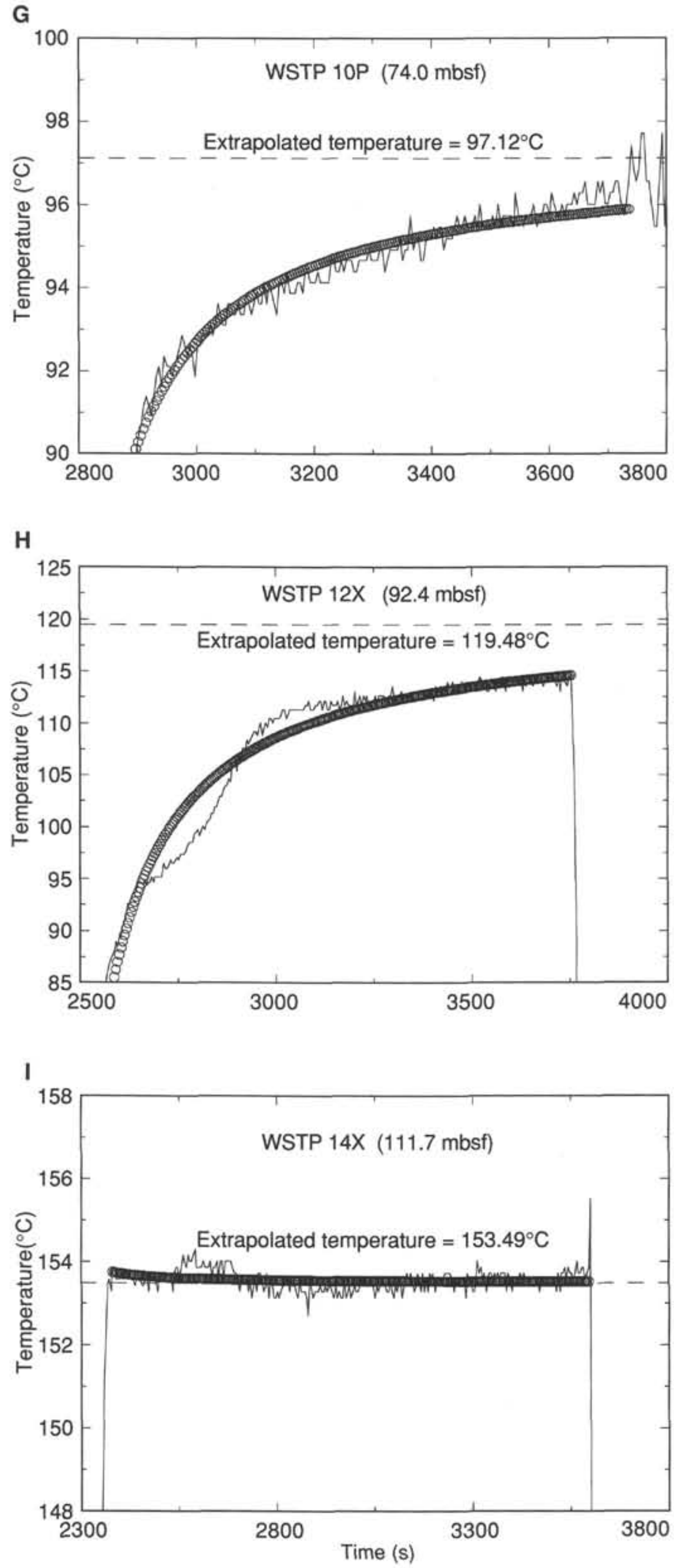

Figure 108 (continued).

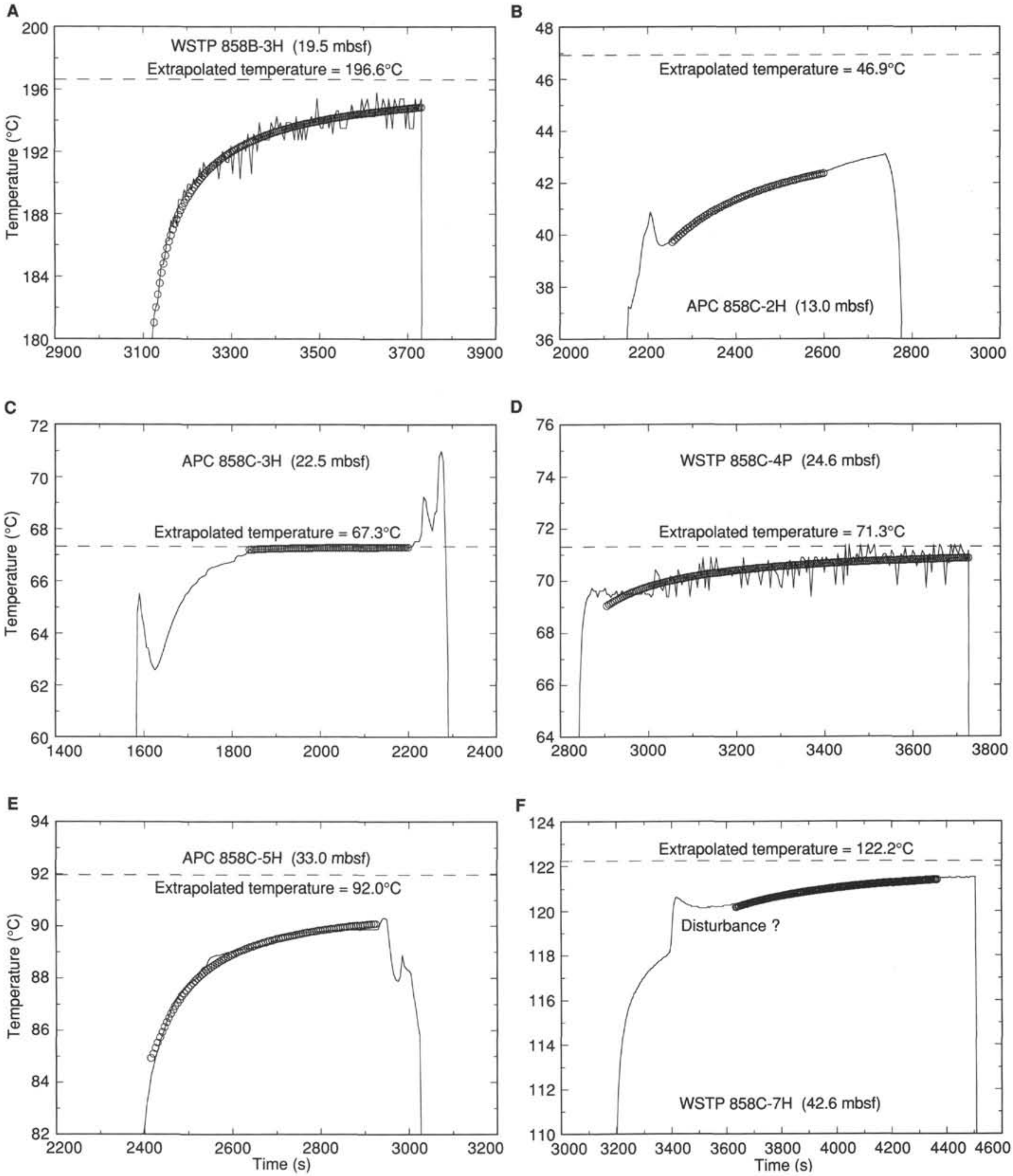

Figure 109. **A.** The high temperatures measured with the WSTP after recovery of Core 139-858B-3H, showing the best-fit theoretical decay curves and extrapolated *in-situ* temperatures. **B–F.** Temperatures measured with the APC tool and WSTP in Hole 858C showing the best-fit theoretical decay curves and extrapolated *in-situ* temperatures. Symbols as in Figure 108.

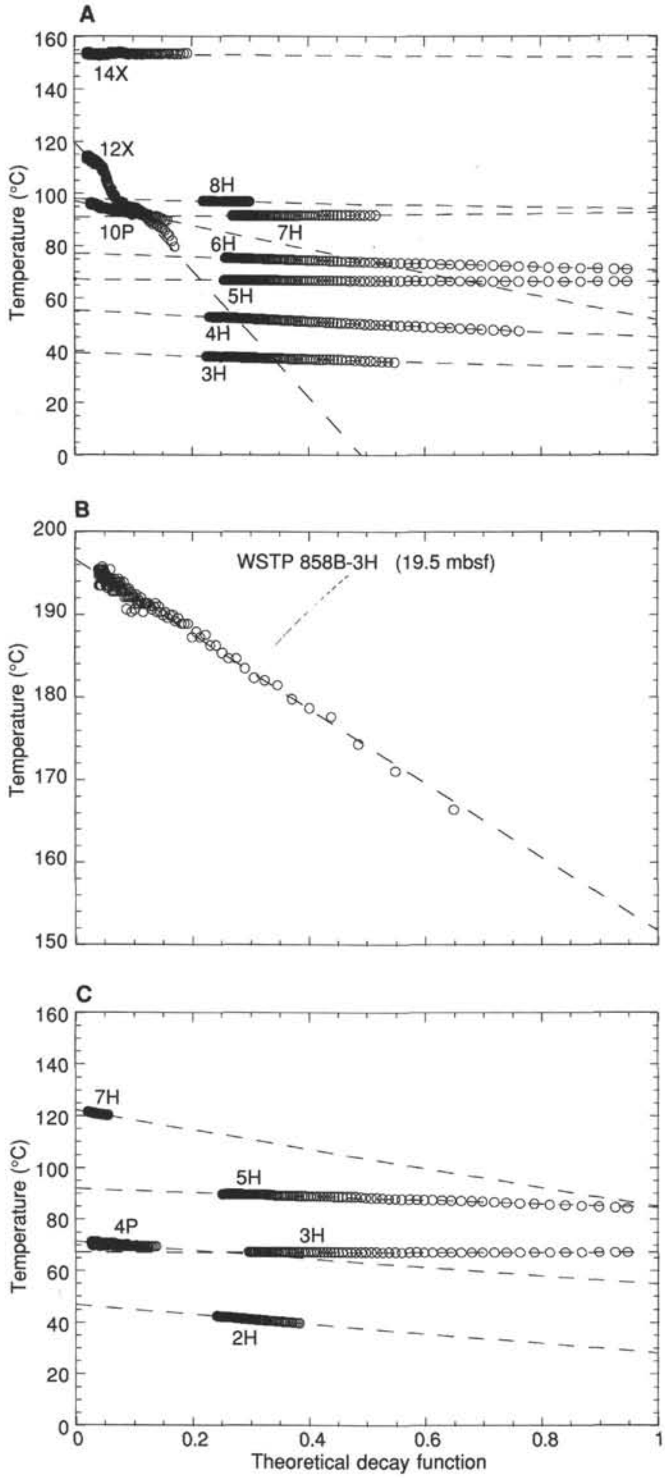

Figure 110. **A.** Temperatures measured in Hole 858A vs. the appropriate theoretical function that describes the approach with time of the annular APC cutting shoe or cylindrical WSTP to *in-situ* temperatures. The theoretical function is proportional to reciprocal time and therefore the estimated *in-situ* temperatures are given by the intercepts of the extrapolations of the linear trends of the measured data. **B.** Same plot for temperatures measured in Hole 858B. **C.** Same plot for temperatures measured in Hole 858C.

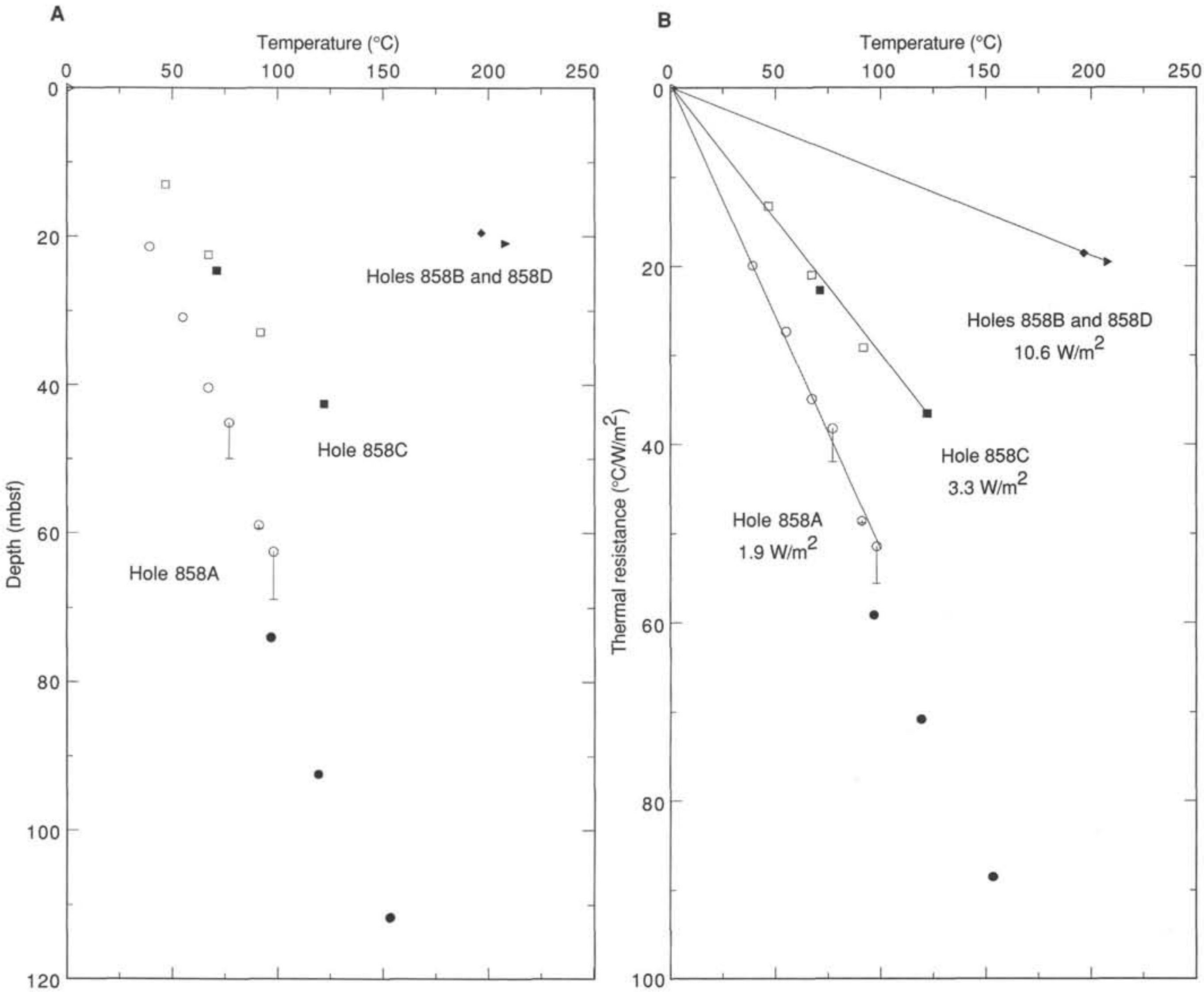

Figure 111. **A.** Estimated formation temperature in Holes 858A through 858D vs. depth. **B.** Bullard (1939) plots of temperature vs. cumulative thermal resistance. Circles denote data from Hole 858A; squares denote data from Hole 858C; the diamond and solid triangle denote Holes 858B and 858D, respectively; open triangle is the bottom-water temperature of 1.7°C. Open symbols are APC tool measurements; solid symbols are WSTP measurements. The deepest three APC tool measurements from Hole 858A followed incomplete stroke of the coring barrel, making identification of the actual penetration depths impossible. Likely depths (indicated by the open circles) were determined from core recovery; deeper depth limits, which would have been reached with full stroke, are also noted. The heat flow indicated for Holes 858B and 858D are limiting values only, assuming that heat transfer between the measurement points and the surface is conductive.

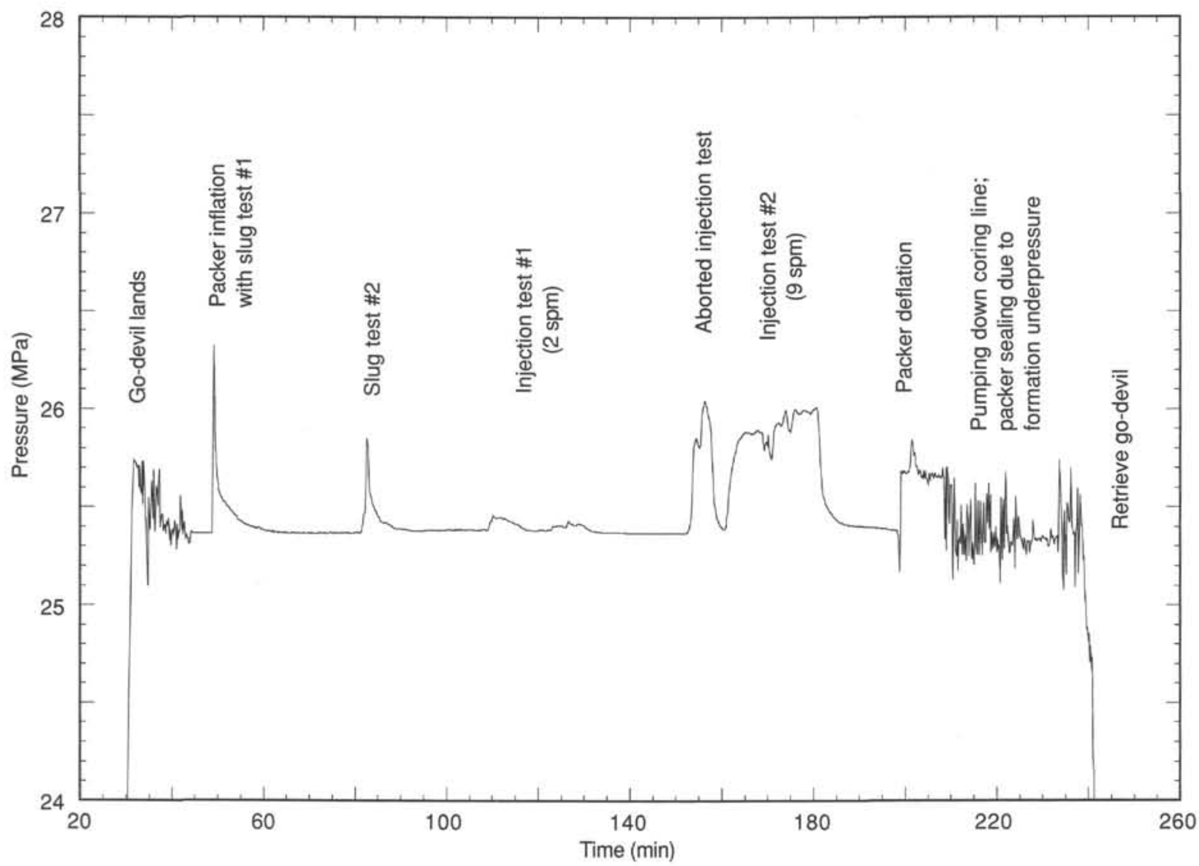

Figure 112. Annotated downhole pressure-time record collected with a GRC ERPG-300 recorder deployed within the first go-devil, with the packer set in casing at 104 mbsf, in Hole 858G.

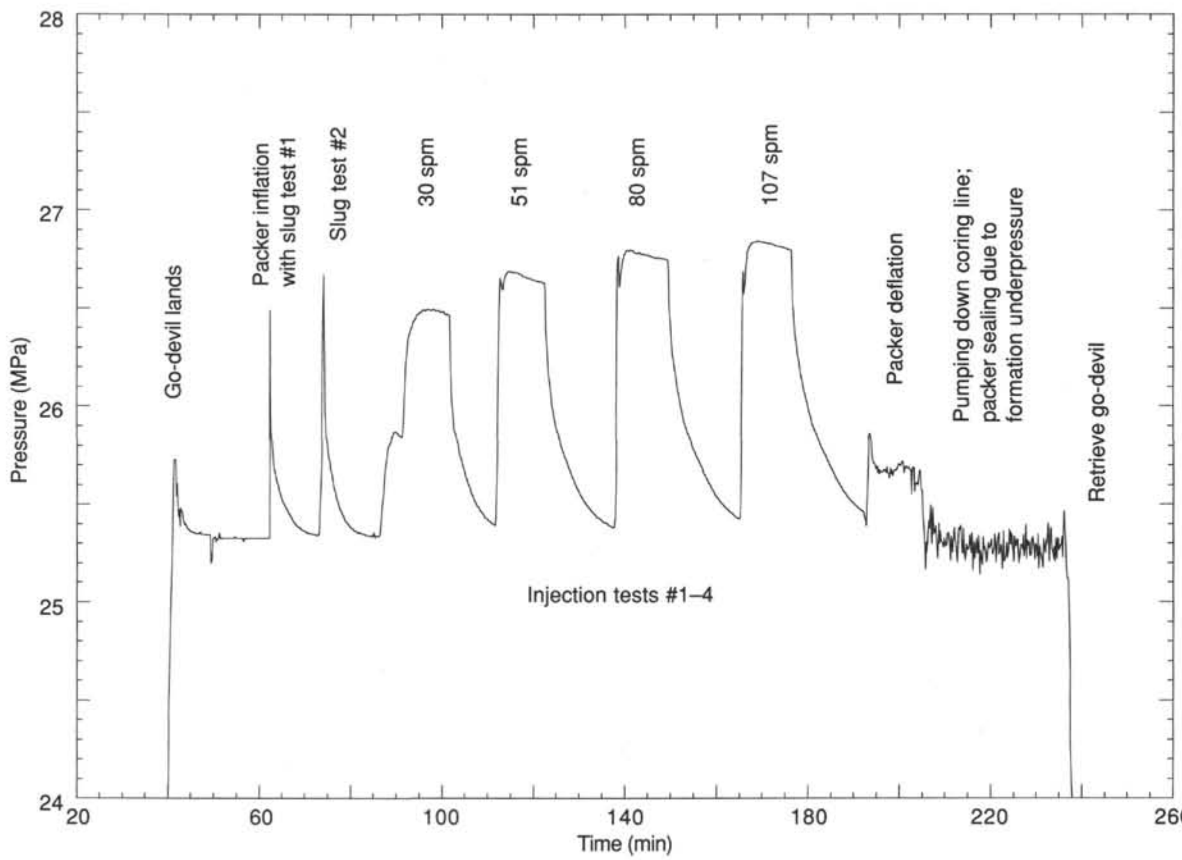

Figure 113. Annotated downhole pressure-time record collected with a GRC ERPG-300 recorder deployed within the second go-devil, with the packer set in casing at 104 mbsf, in Hole 858G.

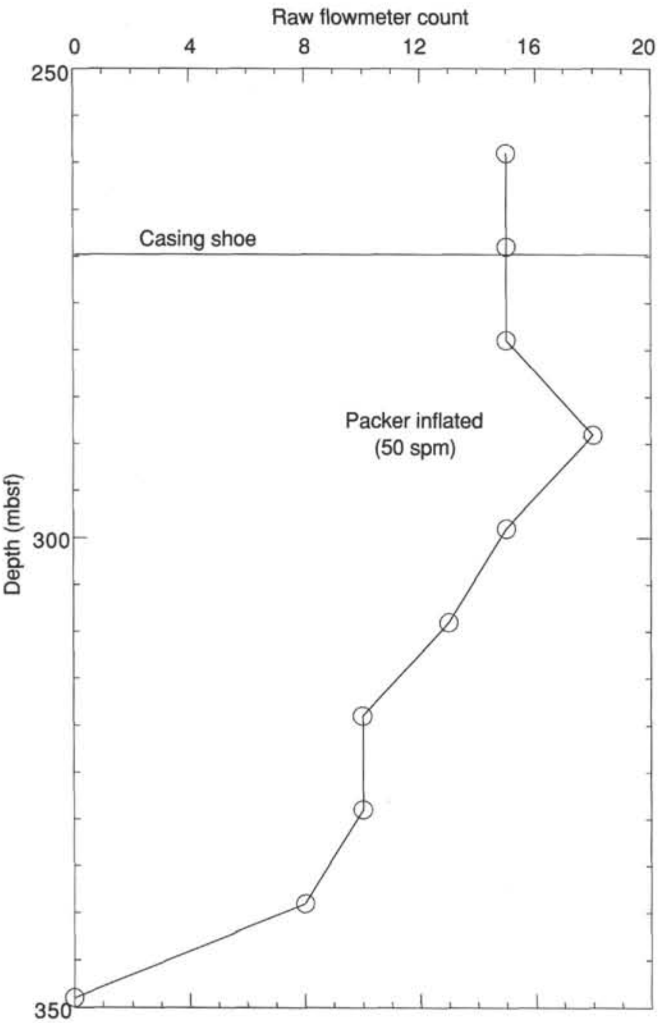

Figure 114. Preliminary determination of the variation of downhole flow readings collected during the flowmeter experiment in Hole 858G.

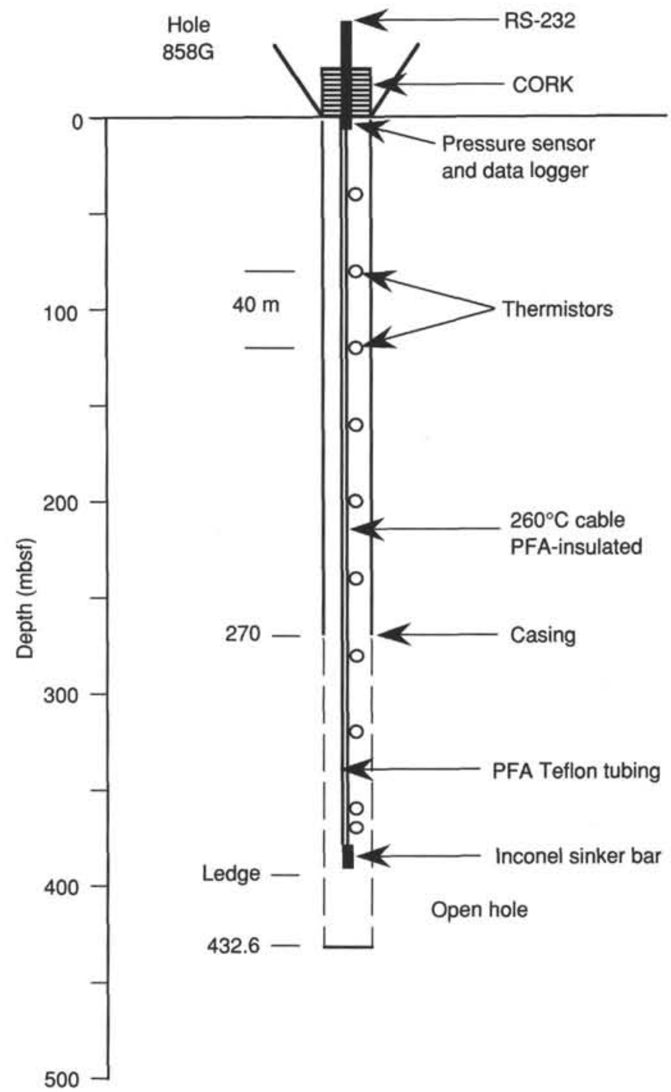

Figure 115. Schematic of the long-term instrumented borehole seal deployed in Hole 858G at the end of operations at the hole.

Hole 858F: Resistivity-Sonic-Natural Gamma Ray Log Summary

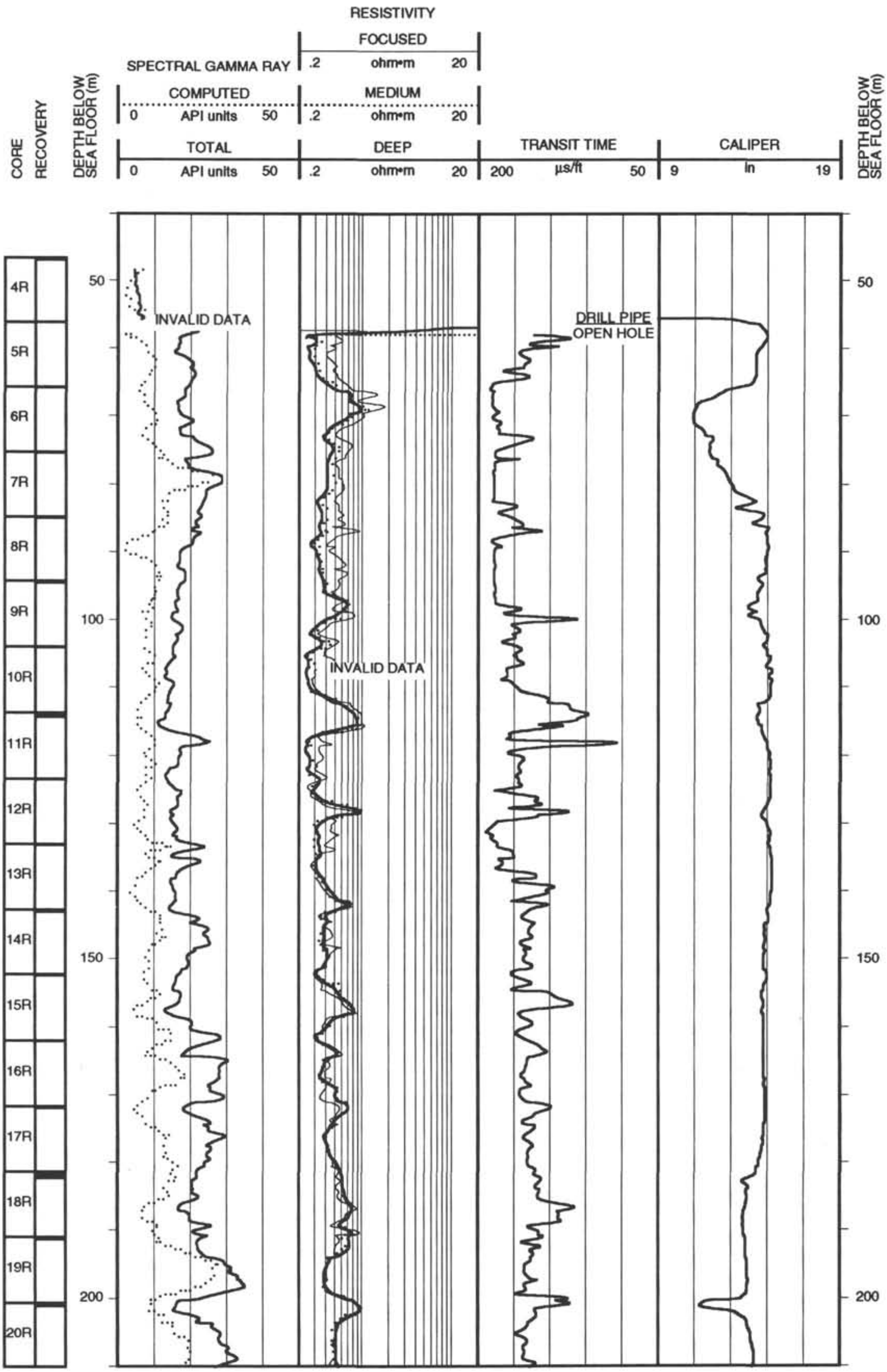

Hole 858F: Resistivity-Sonic-Natural Gamma Ray Log Summary (continued)

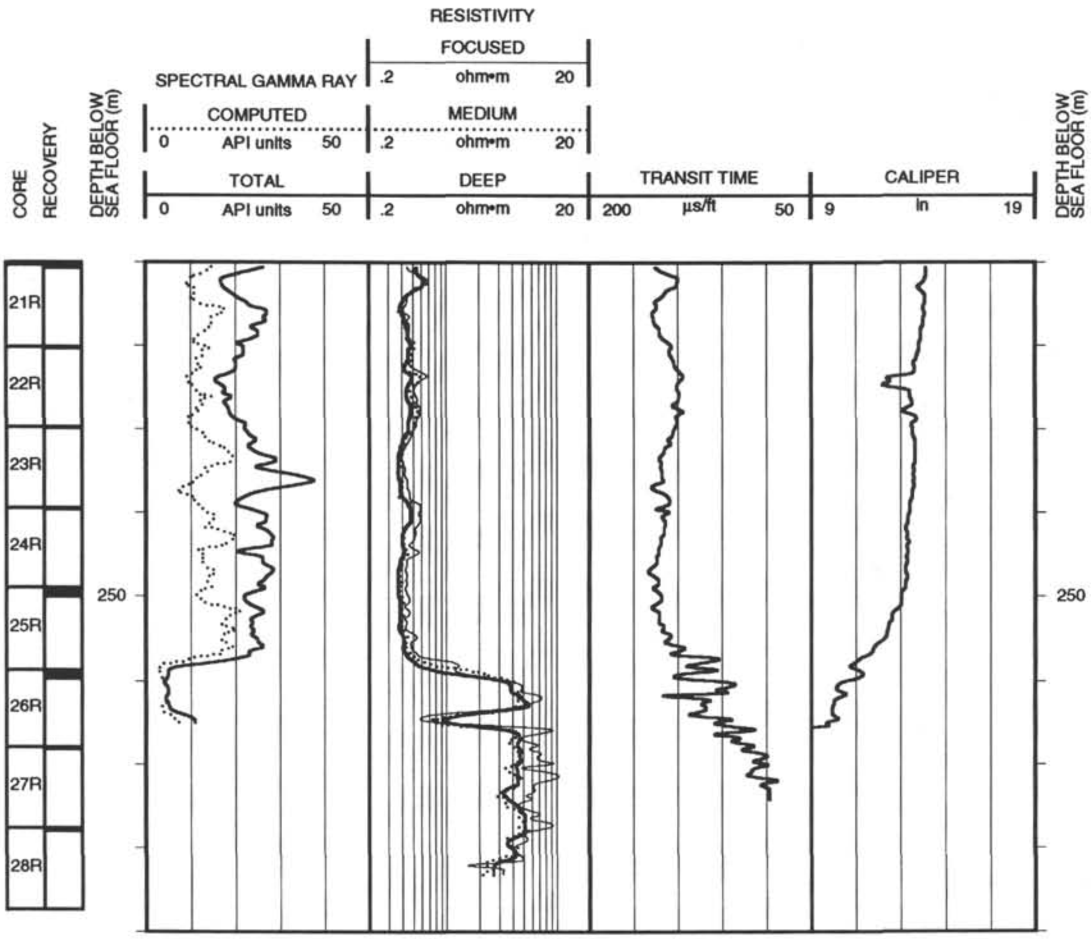

Hole 858F: Natural Gamma Ray Log Summary

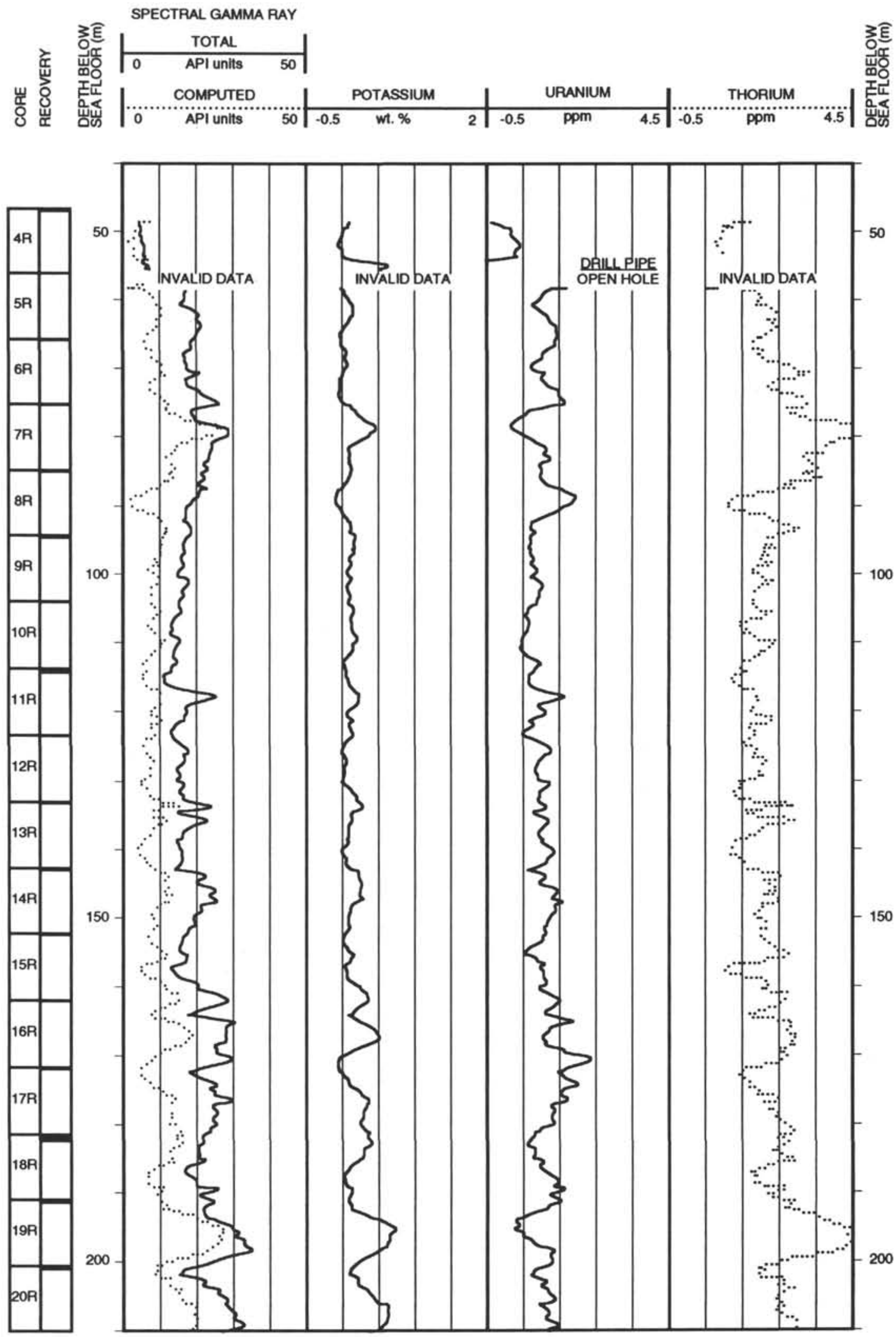

Hole 858F: Natural Gamma Ray Log Summary (continued)

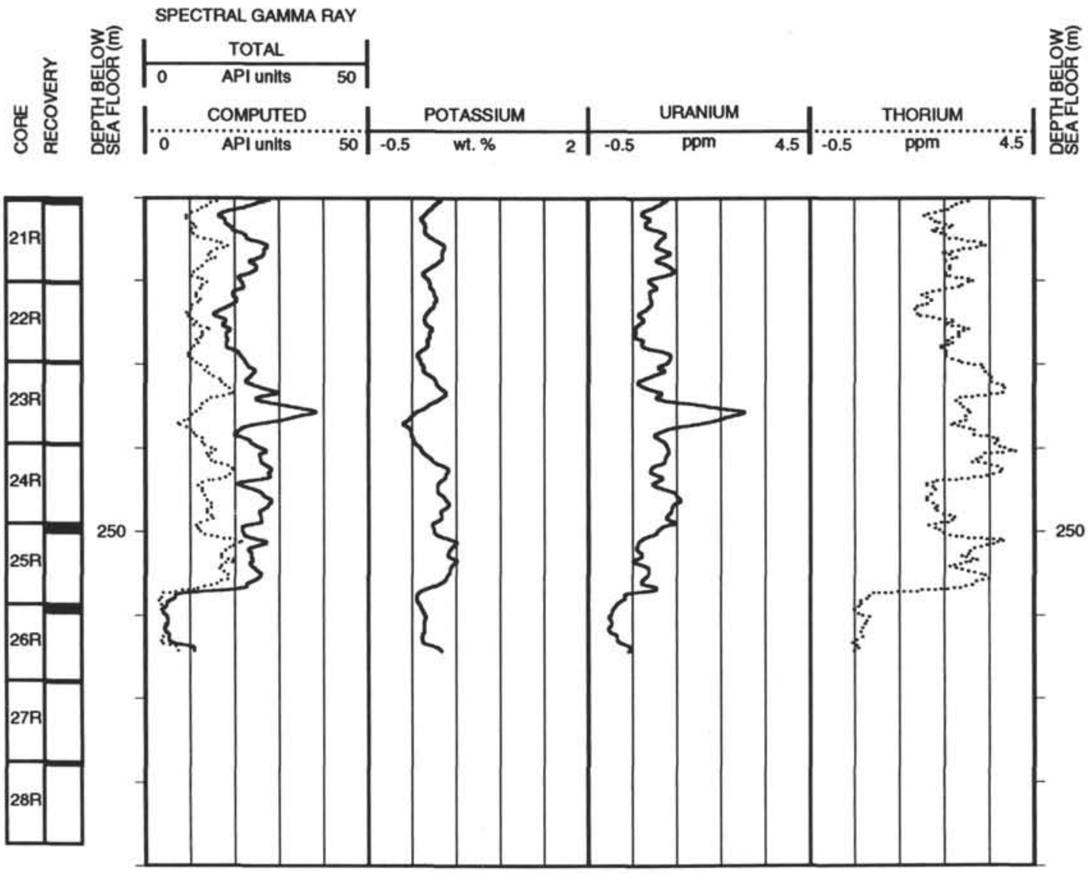

Hole 858G: Density-Natural Gamma Ray Log Summary

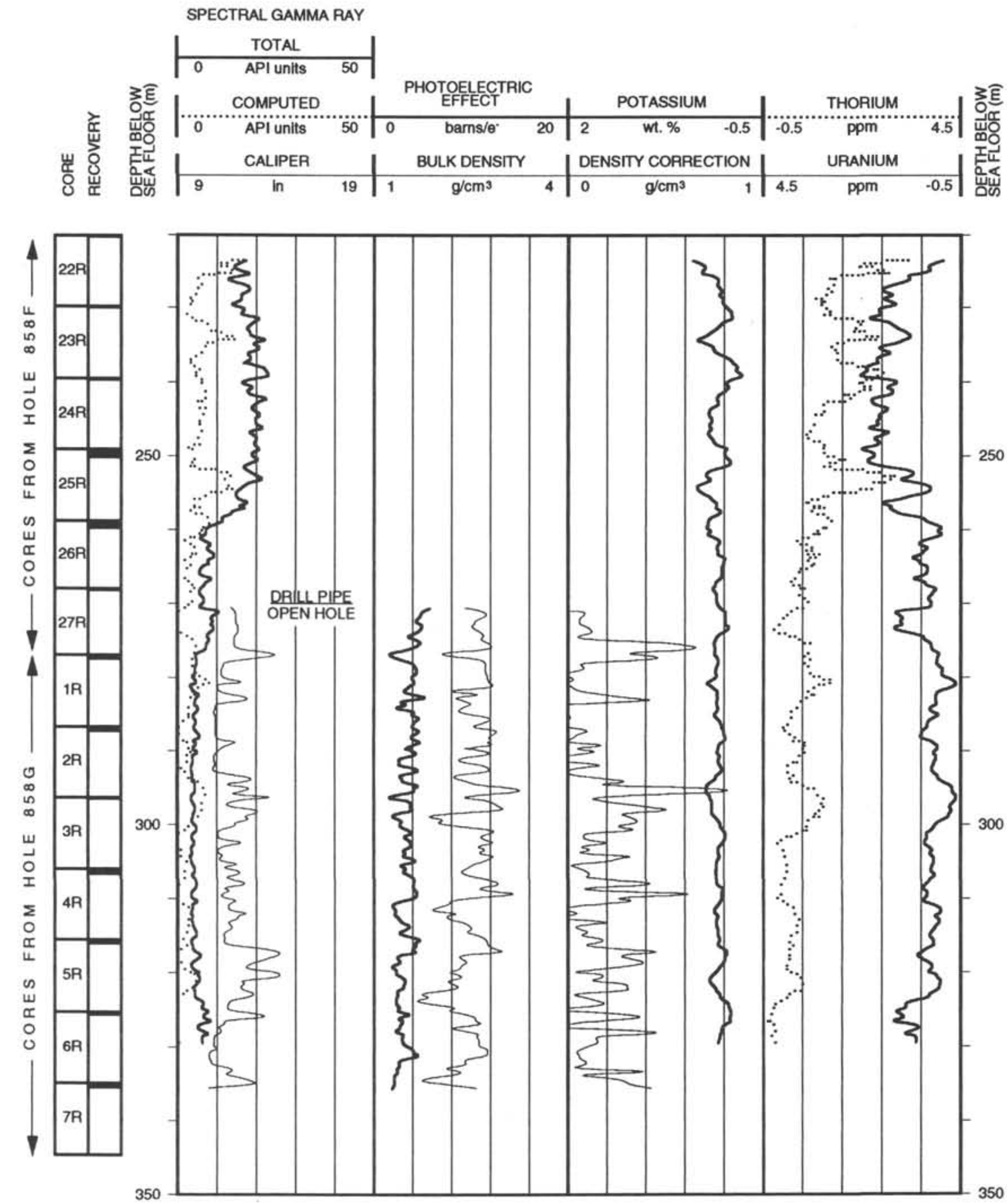

Hole 858G: Resistivity-Natural Gamma Ray Log Summary